Phage display and experimental brain therapeutics

A thesis submitted in accordance with the conditions governing candidates for the degree of Philosophiae Doctor in the University of Wales

By

Mathew Wayne Smith

(M.Pharm)

August 2009

Welsh School of Pharmacy

Cardiff University

ProQuest LLC
789 East Eisenhower Parkway
P.O. Box 1346
Ann Arbor, MI 48106-1346

Acknowledgements

I would firstly like to express my sincere gratitude to my supervisor Dr. Mark Gumbleton for his enthusiasm, encouragement and stewardship throughout my PhD – we have had great fun on this journey. I am grateful to the technical staff of the Welsh School of Pharmacy, and particularly Julian Menai-Purnell, for all the assistance rendered.

Sincere thanks to all members of the Gumbleton lab both past and present but especially Chris, Marc, Ghaith, Lee, Andrew and Dan who have helped to make my PhD studies both exciting and rewarding. Thanks also to all my friends outside of science who have helped keep me grounded.

Finally, this thesis is dedicated to my family: Keith, Tricia, Jonathan and Laura who have unfailingly supported me throughout my studies, sacrificing their time and goals so I can pursue mine.

Summary

Phage display, a powerful polypeptide display technology, affords the rapid identification of peptides and proteins that interact with a target of interest. The aims of the project were the phage display identification of peptides that interact with a druggable target in a brain disorder (glioblastoma multiforme) and the identification of peptides that serve as targeting vectors for brain delivery. Validation studies were undertaken to qualify the use of a cyclic-7mer peptide phage library against targets including streptavidin and paracetamol chosen as examples of a large complex and small simple molecule, respectively. With the aim of identifying peptide phages that bind to the luminal surface of brain microvasculature, a primary *in-vitro* porcine model of the blood-brain barrier (BBB) comprising primary brain capillary endothelial cells was established and characterised. An *in-vivo* phage display was undertaken in the rat with the aim of identifying peptide sequences that mediated translocation across the BBB into brain grey matter. A 7-mer cyclic peptide was identified with sequence AC-SYTSSTM-CGGGS that enhanced the uptake of phages into brain grey matter by 4-fold compared to control wild-type phages. This peptide may serve as a novel targeting vector for the delivery of a therapeutic cargo to the brain. Caveolin-1 was identified as a potential new therapeutic target in *in-vitro* models of grade IV astrocytomas (glioblastoma multiforme), with siRNA knockdown of caveolin-1 associated with reduced glioma cell proliferation and invasiveness. With the caveolin-1 scaffolding domain (aa 81-101 in the caveolin-1 protein) as a target, an *in-vitro* peptide phage selection was undertaken and identified a series of peptides that bind the scaffolding domain with high affinity. These peptides will serve as a template for the development of low molecular weight peptidomimetics that inhibit caveolin-1 function. In conclusion, the studies in this thesis have demonstrated the utility of phage display in experimental therapeutics of brain disorders.

Table of Contents

List of figures

List of tables

Chapter 1 Phage display and experimental brain therapeutics

1.1 CNS disorders

With an ageing population disorders of the brain and central nervous system (CNS) are increasingly prevalent[1, 2]; estimates suggest that one in every three individuals will suffer some brain disorder during their life[3]. Disorders of the CNS vary greatly in their epidemiology and aetiology but include CNS tumours, neuroAIDS, amyloidoses (Alzheimer's; prion disease), neurodegenerative diseases (Parkinson's; Huntingdon's; drug or alcohol abuse) and mood disorders (anxiety; depression; bipolar disease). Despite the increasing prevalence of CNS disorders, the rate at which new therapeutic entities for their treatment reach the market is significantly slower than for peripheral disorders[4]. This has been as a consequence of a poor understanding of many diseases of the brain and the blood-brain barrier (BBB), which restricts significant diffusional access to the brain. Classically, CNS drug discovery programs have concentrated either on the rational design of small lipophilic molecules that would be predicted on the basis of structure to result in a therapeutic response or the high-throughput functional screening of vast chemical libraries. In recent years however the molecular dissection of various central disorders has resulted in a shift in focus towards therapeutic biomacromolecules such as peptides, proteins, antibodies and nucleic material. For example various clinical trials are underway investigating amyloid-β immunotherapy with IgG for the treatment of Alzheimer's disease[5]. However access to the brain of these biologics is even more problematic than for small molecules because of the limiting nature of the BBB.

Phage display is a powerful combinatorial technology for the display of polypeptides on the surfaces of bacteriophages. Phage display libraries that are comprised of many billions of phages each displaying a unique polypeptide, show great utility for the discovery of peptides and antibodies that target vasculature to increase residency time at a tissue and as scaffolds for dug discovery. The research that follows in subsequent chapters of this thesis has been driven by an interest in utilizing phage display technology as a component in experimental therapeutics aimed at brain disorders. Specifically, to discover peptides that may promote macromolecule traversal across the BBB or to address issues surrounding the discovery of novel peptide brain therapeutics, particularly for gliomas (grade iv astrocytomas) within which a target protein, caveolin-1, has been identified for modulation.

1.2 Astrocytomas

Tumours of the central nervous system essentially fall into two categories, primary and secondary. Secondaries that originate from a primary tumour growing within the periphery are the most common CNS tumour type and are generally treated via surgical resection and chemotherapy directed against the primary tumour itself.

Primary brain tumours are subdivided into neuroepithelial tumours that arise from astrocytes or oligodendrocytes, the so-called glial tumours, or tumours arising from meningeal, germ or lymphatic tissue[6, 7]. Glial

tumours are the most abundant primary tumour type in the brain of which astrocytomas are the most common with estimates suggesting ~ 75% of all neuroepithelial tumours are astrocytomas. Histologically, gliomas can be distinguished as astrocytic, oligodendroglial or a heterogeneous mixture known as oligoastrocytomas. The grading of astrocytomas follows histological staging and is based on a four-tiered scheme established by the World Health Organisation[8-10] in 1993 that essentially reflects severity of disease from a benign to highly aggressive phenotype (see **Table 1.1**).

Table 1.1 World Health Organization classification of astrocytomas.

WHO Classification	Common nomenclature
Grade 1	Pilocytic astrocytoma
Grade 2	Diffuse or low-grade astrocytoma
Grade 3	Anaplastic (malignant) astrocytoma
Grade 4	Glioblastoma multiforme

The staging is associated with a number of histological features that include nuclear atypia, mitotic activity, angiogenic capacity and pseudopalisading necrosis, a feature specific to gliomas that is a particularly poor prognostic factor[7, 11]. Gliomas graded as 3 or 4 are exceptionally aggressive with median survival rates of 2-3 years and 9-12 months respectively[12]. Despite radical surgical resection combined with radio- and chemo-therapies 5-year survival rates for grade IV gliomas are reported to be 3% at best. The majority of gliomas arise in the frontal lobe[13] with computed tomography (CT) generally revealing distortion of lateral and third brain ventricles with significant displacement of both middle and anterior cerebral arteries. Factors that may indicate poor prognosis include advanced age, neurological deficits at presentation and partial surgical

resection due to the diffuse yet extensive (centimetres) infiltration of astrocytoma cells into healthy brain parenchyma that surrounds the tumour site. It remains a complex challenge to affect complete surgical resection without introducing severe neurological deficits. Surgical resection combined with radiotherapy and concurrent treatment with the chemotherapeutic agent temozolomide, an oral alkylating agent that methylates DNA, modestly extends life in grade 4 astrocytomas by 2-3 months compared to resection with radiotherapy alone, and is now the preferred treatment regimen in grade 4 astrocytomas[14]. The implantation of biodegradable polymer wafers impregnated with alkylating agents such as carmustine (Gliadel™) directly into the surgical cavity created when a tumour is excised has also proven relatively effective extending life by around 2 months[15], however significant migration of glial tumour cells often extends beyond the application area of wafers. It remains patently clear that there is a pressing need to design new treatment modalities and delivery systems to target high-grade astrocytomas since 6-month disease free progression has stalled at 31% in grade 3 tumours and < 15% in grade 4 tumours[16].

Gliomas share a number of features with non-brain cancers including invasion, angiogenesis, self-directed proliferation, evasion of apoptosis and avoidance of immune surveillance[17]. Whilst astrocytomas show significant heterogeneity, there appear to be a number of genetic anomalies that are common to grade 3 and 4 tumours. Grade 3 tumours show marked

anomalies in the retinoblastoma-associated cell-cycle regulatory pathways particularly mutations and deletions in the cyclin-dependent kinase inhibitor p16INK4A/CDKN2A and in the retinoblastoma susceptibility locus 1 (pRB1), as well as overexpression of cyclin- dependent kinase 4 (CDK4) and human double minute 2 (HDM2)[17, 18]. Chromosome 10, which houses tumour-suppressor phosphatase and tensin homolog (PTEN), is commonly deleted when grade 3 astrocytomas transform to grade 4[19]. In addition overexpression in a number of signal transduction pathways leads to uncontrolled cellular proliferation, survival and invasion. These pathways are generally associated with tyrosine kinases under the control of growth factors such as epidermal growth factor (EGF), platelet derived growth factor (PDGF), vascular endothelial growth factor (VEGF), hepatocyte growth factor/scatter factor (HGF/SF), caveolin and insulin-like growth factor (IGF)[19].

1.3 The Blood-Brain barrier

The blood-brain barrier serves to protect the central nervous system from potentially harmful endogenous and xenobiotic molecules[7, 20]. As a corollary it also shields the brain from therapeutic agents that may be effective in treating a wide variety of CNS disorders[7]. Whilst anatomically the BBB is comprised of endothelial cells that line brain microvasculature, the intimate association of astrocytes, pericytes and neuronal cells with the endothelia significantly modifies its functionality. It is clear that a highly restrictive paracellular pathway at the BBB significantly limits brain

infiltration to all but those drugs with physicochemical properties that afford the ready penetration of lipophilic cell membranes or those drugs that exploit endogenous active transport pathways that include solute carriers or endocytic pathways. Whilst it is apparent that the density of endocytic vesicles at the BBB ranks amongst the lowest reported for different endothelial cell types[21], endocytosis at the BBB is a critical pathway that mediates the uptake of nutrients essential for normal brain function and provides significant communicative links to the periphery. A number of strategies to exploit these pathways have already been explored using a diverse set of delivery vectors that includes hormones[22, 23], cytokines[24], cell penetrating peptides[25-27], transferrin and transferrin receptor antibodies (reviewed in [20, 28, 29]), nanoparticles[30-32], toxins and products of micro-organisms[20]. Whilst the field is still in its infancy with, to date, no delivery vector reaching the market, impressive results are beginning to accumulate and there is much excitement that these strategies will eventually provide a generic platform for the delivery of significant concentrations of chemotherapeutics as well as other CNS active drugs to their site of action in the brain.

1.4 Caveolae and caveolin

Caveolae, the predominant vesicle type at the BBB[33], were morphologically identified in the early 1950s by transmission electron microscopy[34, 35] and were first described as 'little caves' – vesicular invaginations of the plasmalemma 50 – 100 nm in diameter. It was later

recognised that caveolae also exist as highly-organised microdomains on the plasmalemma that are morphologically indistinguishable from 'normal' membrane[36]. Early references to these domains classified them as a subset of lipid rafts but this definition has been rescinded in recent years with evidence that certain probes localize to caveolae microdomains but not to lipid rafts[36, 37]. The relationship between the different forms of caveolae is not clearly understood and even within the same cell type caveolae may be morphologically diverse. Whilst caveolae are found on the surface of a wide range of cells they are particularly enriched on capillary endothelia, fibroblasts, adipocytes type I pneumocytes and muscle cells of all divisions i.e. cardio-, skeletal- and smooth- muscle cells. Caveolin-1 (22 KDa), the first product of the caveolin gene family to be identified[38, 39], is the major structural and functional element of caveolae. Although caveolin-1 is the signature biochemical marker within caveolae, the domains are similarly enriched in cholesterol, sphingomyelin and glycosphingolipids giving rise to detergent resistant areas of the plasmalemma. Further, a rich variety of cell surface receptors localise to caveolae domains and may initiate endocytic processes upon binding of their cognate ligand(s).

Caveolae and caveolin maintain a diverse set of functions that are still being uncovered but they clearly play a significant role in vesicular transport, homeostasis of cholesterol, compartmentalisation of signal transduction events and modulation of tumour growth, invasion and aggressiveness (for detailed reviews see [40-43]).

1.5 Polypeptide display systems

Display platforms that express recombinant polypeptides on their surface are an invaluable tool for the exploration of protein-protein interactions. To date at least five display platforms have been described: phage-, cell-, mRNA-, Ribosome- and DNA- display (**Figure 1.1**). These technologies share a common principle: a direct linkage between genotype and phenotype that affords identification of the displayed polypeptide by genomic sequencing (for a detailed review of these technologies see [44]). Of the five technologies described, it is probably phage display that has seen the most widespread application.

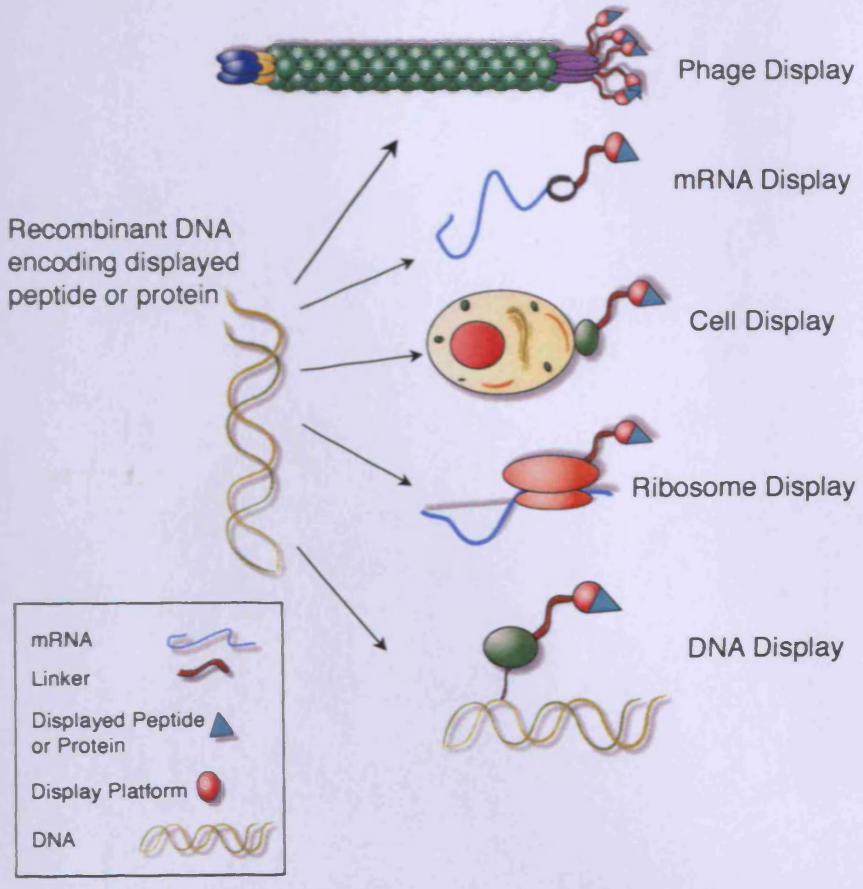

Figure 1.1 Polypeptide display technologies. Polypeptides encoded by recombinant genetic information can be expressed on a variety of biological scaffolds.

1.5.1 Phage Display

Phage display is a powerful combinatorial screening technology for the study of protein-protein, protein-peptide or protein-nucleic acid interactions. The filamentous bacteriophage readily accepts relatively sizeable insertions of additional genetic material into the genome that results in the display of foreign proteins or peptides as fusions with bacteriophage coat proteins. Phage libraries that contain a repertoire of many billions of clones each displaying a unique protein or peptide can be subjected to an affinity selection process against a target of interest. Those phage clones that display a protein that strongly interacts with the target can be recovered and amplified for further rounds of selection before the direct link between genotype and phenotype is exploited to identify the protein or peptide displayed. The initial invention of phage display was described in 1985 by George Smith of the University of Missouri in the seminal manuscript "Filamentous fusion phage: novel expression vectors that display cloned antigens on the virion surface"[45]. Little could George Smith have envisaged the power and application of phage display as a combinatorial screening technique for the exploration of protein-protein interactions or to probe and characterize a diverse set of biological and inert surfaces.

1.6 Phage Biology

1.6.1 Phage Structure

The filamentous phages f1, fd and M13 are part of the Inoviridae family of bacteriophages, belonging to the Inovirus genus and are characterized by semi-flexible filamentous virions with helical symmetry. Filamentous phages belong to the Ff class of organisms that infect *Escherichia coli* that harbour the F plasmid and whose surface therefore are decorated with multiple copies of the F-pilus. The genomes of M13, f1 and fd have been sequenced in their entirety and share approximately 98% homology[46-48] and unlike other members of the Ff phage class do not kill the host organism during their replicative life-cycle but slow the rate of multiplication by 25 – 50%[49, 50]. The physical dimensions of filamentous phages put them on the nano scale (6.5nm x 930nm) with a molecular weight of approximately 16.3 MDa and they are composed of as much as 87% protein by mass. Essentially the filamentous phages are comprised of a covalently closed circle of single stranded DNA some 6400-nucleotides in length housed in a protein capsid cylinder (see **Figure 1.2**).

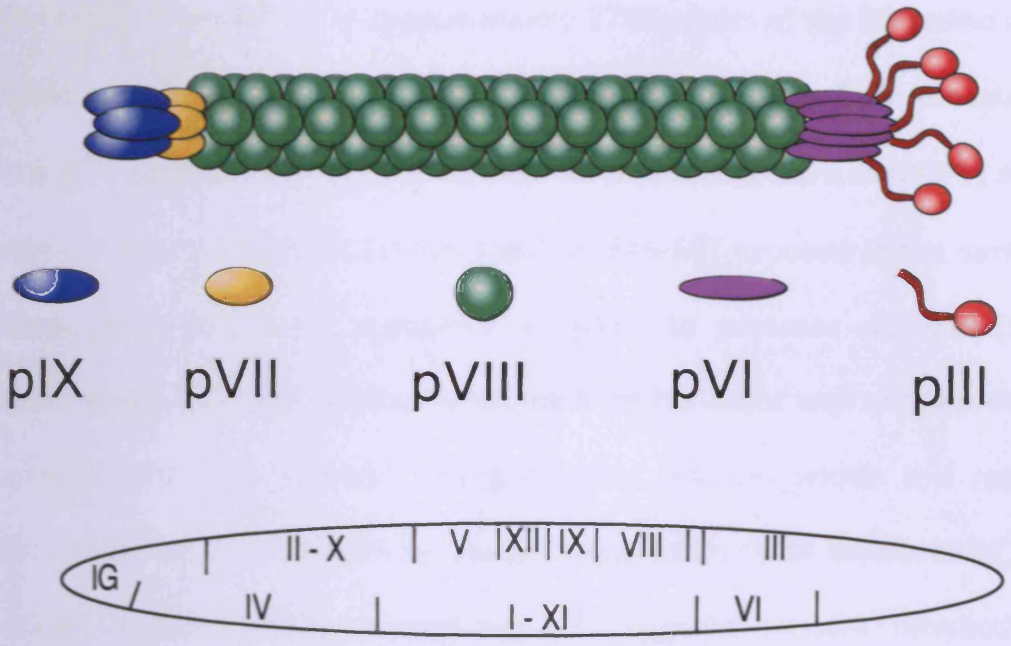

Figure 1.2 Schematic representation of the Ff bacteriophage virion. Schematic shows the location of the capsid proteins (Top) and the orientation of the genes encoding coat and other proteins around the single stranded DNA (Bottom).

The capsid, composed of five coat proteins, has numerous functions including protection of the genetic information as well as a role in virion replication which proceeds under the control of both phage capsid and host bacteria components (see **Table 1.2**)

Table 1.2 Filamentous phage genes and protein products.

Gene	Amino acid residues	MWt	Function	Location	Used for display
II	410	46,137	DNA replication	Cytoplasm	-
X	111	12,672	DNA replication	Cytoplasm	-
V	87	9,682	Binding ssDNA	Cytoplasm	-
VIII	50	5,235	Major capsid protein	Phage filament	Yes
III	406	42,522	Minor capsid protein	Phage terminus	Yes
VI	112	12,342	Minor capsid protein	Phage terminus	Yes
VII	33	3,599	Minor capsid protein	Phage terminus	Yes
IX	32	3,650	Minor capsid protein	Phage terminus	Yes
I	348	39,502	Assembly	Inner membrane	-
IV	405	43,476	Assembly	Inner membrane	-
XI	108	12,424	Assembly	Outer membrane	-

The capsid is composed of approximately 2700 copies of the 50-amino acid major coat protein pVIII which are oriented at a 20° angle from the lateral axis of the virion, overlapping to form an uninterrupted α-helix[51] with only the last five amino-terminal residues (46-50) exposed at the surface resulting in significant resistance of pVIII to protease digestion[52]. Residues 10-13 of the carboxy-terminus form the inner wall of the protein cylinder with four positively charged lysine residues within this region interacting with the negatively charged sugar-phosphate backbone of the ssDNA[53, 54]. pVIII monomers are held together through interactions between the residues that connect the amino and carboxy terminals of pVIII and form a stable inner core.

At one terminus of the phage are approximately 5 molecules each of pVII and pIX, two of the smallest ribosomally translated proteins thought to exist. Both their structure and arrangement at the blunt end of the phage remain unclear although efforts to model these proteins are underway [55, 56]. At the opposite end of the virion are approximately five copies each of pIII and pVI that account for around 2% of the phage length (10-16 nm). Whilst the structure and arrangement of pVI remains elusive pIII has been extensively characterized. In electron micrographs of the phage particle, pIII is seen to emanate at the 'pointy' end of the virion and is exposed on the surface as small 'knots' [57].

The coat protein pIII is the one most commonly utilised for display purposes and is comprised of three domains designated CT, N1 and N2 linked to each other by glycine rich spacers[58]. The 68-residue N1 domain is essential for bacterial infection, directing the phage ssDNA into the bacterial cytoplasm and for the insertion of coat proteins into the bacterial membrane ready for subsequent phage assembly. The N2 domain (130 residues) is responsible for binding to the bacterial F-pilus and thus initiates the infection process via formation of disulphide bridges between the phage and the bacterial cell[59, 60]. The surface exposure of these two domains makes them susceptible to protease digestion that renders the virion non-infectious[57, 61]. The carboxyl terminus CT (150 residues) which resides within the viral particle anchors pIII and helps mediate assembly termination and release of phage virions from the bacterial cell.

1.6.2 Phage Genome

Filamentous phage are particularly well suited for the display of foreign proteins since their genome tolerates relatively significant insertions of genetic material into non-essential regions, coat proteins can be modified without loss of infectivity, phage virions are stable to a wide range of environmental conditions including proteases[62], non-aqueous media[63], temperature and pH[45, 64] and since their propagation does not kill the bacterial host, phage can be produced in large quantities (~$1x10^{12}$ virions per ml). The ~ 6400 nucleotide phage genome contains nine genes encoding eleven proteins and a major non-coding region termed the

intergenic region (Ig) which is the site of origin for the synthesis of (+) and (-) complementary strands of phage DNA. The Ig region also contains a packaging signal (PS) that is essentially a seeding point around which the capsid is assembled.

The genes are arranged around the circular ssDNA according to their function in the phage life-cycle: proteins translated from genes II, X and V direct replication of the phage genome, genes VII, IX, VIII, III and VI encode the capsid proteins whilst genes I, XI and IV encode proteins that are involved with the phage assembly process in the bacterial cell membrane. Transcription, which proceeds counter clockwise using the (-) strand of the dsDNA intermediary of viral DNA replication begins at gene II. Differences in both promoter and ribosome binding strength and accessibility divide the genome into two transcription regions, the infrequently transcribed (genes III - IV) and the frequently transcribed (genes II - VIII). A weak termination signal (Rho-dependent) preceding gene I is transcription limiting whilst overlapping transcripts from multiple promoters and multiple RNA processing events increase the abundance of RNAs for genes closest to the terminator thus resulting in high levels of pV and pVIII, proteins required in the greatest abundance. Whilst there are few regions of the genome that do not encode a protein, antibiotic resistance cassettes can be inserted into the Ig region or between gene VIII and III but care must be taken not to disturb promoter or terminators as there is a precise

balance that must be maintained to allow production of phage virions without killing the bacterial host.

1.7 Phage Lifecycle

1.7.1 Infection

All filamentous phage utilize small hair like appendages on bacteria called pili as receptors for infection and whilst phage can infect cells that lack pili, the process is highly inefficient with estimates suggesting infection is 4-5 orders of magnitude less efficient than pilus mediated infection[65]. Infection is initiated when the N2 domain of pIII binds the tip of the pilus[59, 60]. The low copy number of pili per bacterial cell (up to 12 per cell[66]) means infection proceeds more efficiently with high multiplicity of infection and when there is high bacterial cell density. After the initial binding step, the pilus mechanically retracts[67, 68] drawing the pIII terminus of the phage (pointy end) into the bacterial periplasm. It remains to be elucidated whether the retraction is a response to phage binding or is part of the inherent retraction-assembly cycling of bacterial pili. Binding of N2 to the pilus appears to displace N1 from its normal interaction with N2 where it subsequently interacts with domain 3 of the bacterial protein TolA that extends into the periplasm from the bacterial cytoplasm[69, 70]. The precise molecular mechanism of the subsequent stages of infection remain to be fully elucidated however it is clear that there is some form of depolymerisation of the phage proteins pVIII, pVII and pIX, directed by Tol Q, R and A which are essential for phage infection[65, 69], followed by

translocation of the viral ssDNA into the cytoplasm. The exact role of Tol Q and R is unclear although it has been suggested that they interact to form some type of pore or channel through which the DNA translocates and this may be aided by the CT region of pIII.

A schematic of the DNA replication, protein synthesis pathways and protein location within the infected E. coli cell can be seen in **Figure 1.3** and is described in following sections..

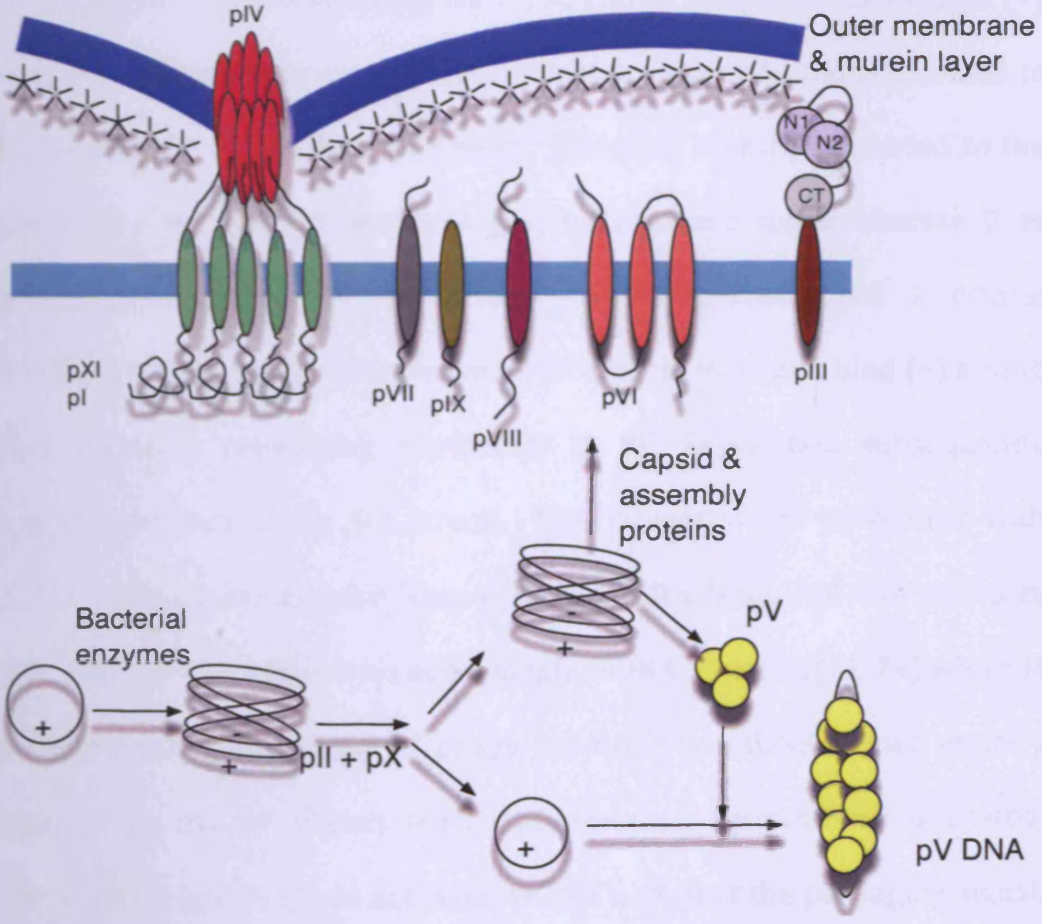

Figure 1.3 Schematic of the phage DNA replication, protein synthesis and protein location of the Ff filamentous bacteriophage following bacterial (E. coli infection).

1.7.2 Replication

After the phage (+) strand translocates into the bacterial cytoplasm, bacterial RNA and DNA polymerases mediate the production of the (-) strand. A bacterial topoisomerse II converts the dsDNA to a negatively charged, covalently closed supercoil designated the Replicative Form (RF) the (-) strand of which serves as a template for mRNA transcription which is then translated into the various phage proteins. pII cuts the (+) strand of the RF in the intergenic region yielding a primer that is elongated by bacterial DNA polymerase using the (-) strand as template. The original (+) strand is displaced as rolling-circle replication proceeds and is rejoined to form a circular ssDNA by pII. The (+) strand is then re-converted to the supercoiled RF by RNA and DNA polymerases and topoisomerase II as previously described. RF production continues thus until a critical threshold of pV is reached above which pV dimers form and bind (+) strand DNA physically preventing conversion to RF. Replication subsequently favours synthesis of the (+) strand. The interaction of pV-dimers with ssDNA collapses the circular strand into an 800 x 8 nm rod-like structure comprised of ~800 pV dimers and a single ssDNA molecule[71-74] which is the substrate for assembly of phage virions. The ssDNA is not entirely enclosed by the pV dimers with both terminal hairpins left uncoated, presumably because pV do not bind dsDNA such that the packaging signal, around which phage assembly occurs, is exposed[75].

1.7.3 Assembly

Those phage proteins not engaged in the cytoplasmic replication of the phage genome are synthesized and inserted into the cytoplasmic or outer membrane of the bacterial host[56]. Filamentous phage assembly is essentially a secretory process, assembly occurs within the cytoplasmic membrane and phages are extruded from the bacterial cell as they are assembled. Both pIII and pVIII are synthesised with an amino terminal signal peptide attached that directs insertion into the cytoplasmic membrane. The signal peptide is cleaved leaving the proteins to span the cytoplasmic membrane with their carboxy-terminals in the cytoplasm and amino-terminals in the periplasm. The remaining capsid proteins (pVI, pVII and pIX) are synthesized without signal peptides and the mechanism of membrane insertion and protein orientation is uncertain. Whilst pVI is hydrophobic and theoretically has three membrane spanning regions, pVII and pIX probably only have a single membrane spanning region[76]. Assembly only proceeds when the five capsid and three assembly proteins are present, there is a proton motive force, ATP and a bacterial Thioredoxin[77, 78]. The process is divided into five stages:

1. *Preinitiation:* characterized by the formation of an assembly site that is visible in electron micrographs as a close apposition of the cytoplasmic and outer membranes that resembles bacterial adhesion zones[79]. These are thought to be mediated by the

interaction of pIV oligomers in the outer membrane channel with pI and pXI on the cytoplasmic membrane to form a closed pore.

2. *Initiation:* in this step, pVII and pIX along with the first collection of pVIII oligomers interact with the PS to form the blunt end of the phage particle directed by the assembly helper protein pI. Although the exact details and order of association with PS remains unclear, it does appear that this initial assembly results in a conformational adjustment to pI allowing it to interact with the periplasmic terminus of pIV causing the channel to open and accept the developing phage assembly[80, 81]. The insertion of the phage into the open pore is essential in preventing 'bacterial bleed' which would lead to cell death. Mutations in pVII and pIX have been noted which results in the formation of an open pore that allows entry of foreign material into the cell and escape of bacterial elements from the cell which together results in growth inhibition[79].
3. *Elongation:* successive replacement of pV dimers with pVIII results in phage elongation and translocation across the cytoplasmic and outer membranes. Two interactions occur during this process: the cationic carboxy-terminals of pVIII interact with the sugar-phosphate backbone of the DNA and the central regions of pVIII interact with each other to 'seal' in the DNA.
4. *Pretermination:* in this penultimate step the membrane embedded pIII-pVI complex is incorporated onto the terminal end of the developing virion[82]. In the absence of pIII, the developing phage

particle remains anchored to the cell membrane giving opportunity for packaging of extra copies of the phage genome to yield polyphage which detach when pIII becomes available[83].

5. *Termination:* release of the phage is mediated through a conformational change in the 150 residue CT domain of pIII and more specifically a 121 residue subdomain starting at the carboxy-terminus is responsible for release of stable virions. A shorter 93-residue sequence affords release of the phage particle but results in a virion that is unstable to detergents.

1.8 Coat proteins used for display

Since the interaction of capsid proteins during assembly largely involves the hydrophobic regions that span the membrane, theoretically any protein or peptide attached to the periplasmic terminus of the capsid protein stands a reasonable chance of being displayed. Of course this is true only if it can be translocated across the cytoplasmic membrane and it does not hinder any of the processes during assembly. The first example was demonstrated by George Smith who fused EcoRI fragments to the amino-terminus of the pIII capsid protein[45]. These phages could be selected from a pool of phages in which they were the minority clones by affinity-purification against an EcoRI antibody adsorbed to culture plastics. The EcoRI displaying phages remained infective and could be amplified in *E. coli.* Iterative rounds of selection or panning as it has been termed significantly enriched for the EcoRI displaying phage. Whilst all of the five

capsid proteins have been used to display peptides or proteins their relative success and utility is variable. Display on the minor coat proteins pVIII and pIX[84] as well as pVI has been reported[85] but in the main successful display has primarily been achieved via fusions with pIII and pVIII.

1.8.1 pIII and pVIII display

Historically, pIII has been the most widely utilised capsid protein for display. Whilst display is limited to five copies of the peptide or protein per virion, large inserts do not appear to interfere with the assembly process although the larger the displayed protein the less infectious the phage virion becomes[45]. Generally, the genetic material encoding the peptide or protein is inserted in the phage genome between the signal sequence and the start of the N1 domain, although foreign proteins have been inserted between N1 and N2 and between N2 and CT[86]. Insertion at these alternate sites generally leads to a significant reduction in infectivity due to steric hindrance of the interaction of N1 and N2 with the pilus. Display between N1 and N2 is however particularly advantageous when protease resistant peptides are required since cleavage of the displayed peptide will render the phage particle non-infectious[86, 87].

The inherently greater number of pVIII proteins on the virion surface offers the opportunity to display many more units of foreign protein per phage particle. Insertion of small DNA sequences encoding 6-8 residues between

the pVIII signal peptide and the amino terminal coding region leads to display on virtually all copies of pVIII (~2700)[88-90]. However larger inserts are not well tolerated presumably because the resulting phage assembly will not fit through the pIV channel or pVIII is not efficiently translocated to the bacterial membrane[56], in such cases a 'phagemid' system is required[91, 92].

The classification of phage vectors (see **Table 1.3**), as described by George Smith[93], is essentially based on the coat protein used for display, whether the protein is displayed on all copies of the capsid protein and whether the recombinant protein is encoded by the phage genome or plasmid (phagemid).

Table 1.3 Classification of phage display systems (adapted from [94]).

Vector type	Coat protein	All or some copies of coat protein display	Phage or Phagemid
Type 3	pIII	All	Phage
Type 8	pVIII	All	Phage
Type 33	pIII	Some	Phage
Type 88	pVIII	Some	Phage
Type 3+3	pIII	Some	Phagemid
Type 8+8	pVIII	Some	Phagemid

The expression characteristics of the displayed polypeptide is largely determined by the parental phage used in the library for example a wild-type phenotype (M13KE) whose genome is intact save for the coat protein gene which is altered for display, a neutered phage that is propagated as a plasmid under antibiotic selection (f88-4) and a true phagemid (pComb3) that only carries the encoded polypeptide, the gene for the coat protein used for display and a phage origin of replication.

1.9 Wild-type phage vector M13KE

The studies conducted in this thesis have utilized Type 3 display with the M13KE vector. In many ways this is the simplest phage display vector since the function of the wild-type parent phage is largely maintained. The genetic information encoding the protein to be displayed is inserted into the region of the genome that encodes the carboxy terminus of the coat protein's leader sequence and the amino terminus of the mature capsid protein. This leads to display at the amino terminal of the capsid protein. Whilst this vector can be used to produce type 8 vectors, as previously described displayed peptides will by necessity be very short (6-8 residues). M13KE can be utilized to display large proteins such as scFV and Fab fusions but are almost exclusively used to produce pIII libraries displaying peptides up to 30 amino-acids in length[95]. Larger proteins probably interfere with insertion of pIII into the membrane for assembly, reduce infectivity through steric hindrance of the pIII-pilus interaction and are more susceptible to both protease degradation and misfolding.

M13KE, derived from M13mp19[96, 97], contains a lacZ gene that produces blue plaques on plates containing 5-Bromo-4-chloro-3-indolyl-β-D-galactoside (X-gal) and isopropyl-β-D-thiogalactopyranoside (IPTG). KpnI and EagI restrictions sites in gene III make it easy to splice the recombinant peptide gene into the vector. M13KE clones amplify to quite significant titers of 10^{13}-10^{14} virions.ml^{-1} without antibiotic selection and generate RF DNA in sufficient quantities in liquid culture to afford DNA sequencing of

the genome to allow identification of the displayed peptides. Unfortunately, libraries derived from M13KE are invariably contaminated with vanishingly small quantities of the wild-type parent phage (no KpnI or EagI restriction site; clear plaques on IPTG/X-gal plates) which, in the absence of a well defined target interaction, may overcome the library population with successive selection rounds due to an advantageous infectivity since pIII is not occupied with displayed peptide. That said, M13KE has excellent infectivity with nearly 100% of the phage selected in any given round amplified in bacterial culture assuming they are infected at the correct multiplicity of infection. This is particularly critical in early rounds of panning where a given clone is represented with a low frequency in the library population. For example the commercially available New England Biolabs Ph.D.™-C7C library contains 1.28×10^9 unique clones and a panning study utilizes 2×10^{11} phage virions such that each clone is present at a frequency of ~ 160. Clearly if the recovery of a given clone is only 1% in the first round of panning this represents a single copy of the clone – using M13KE phage ensures this single copy will be amplified.

1.10 Applications of phage display

The studies conducted in this thesis that involve phage display are based on the New England Biolabs Ph.D.™ peptide libraries and therefore the remainder of this introduction will discuss the applications and limitations of peptide libraries and more specifically Type 3 vectors i.e. a peptide

expressed on each of the five copies of pIII, in the identification of peptides that interact with a given target.

1.10.1 Applications of phage display in disease therapeutics

The aim of many phage display selection projects is to derive a peptide that interacts with a druggable target to affect a therapeutic response. One advantage of phage libraries is that they can be used to investigate several orders of magnitude more entities than a chemical library that is limited to a few thousand clones. Unfortunately, affinity selection strategies in phage display are generally not designed to select for clones that elicit a biological response as a result of a binding interaction. More generally it is simply the binding event itself that is the intended outcome. As a result further selection is often required to identify those clones within the binding population that meet some user defined requirement such as activity as an agonist[98-100] or antagonist[101-103]. Bonetto and co-workers[104] for example isolated a series of 31 peptides that bound melanocortin-1 receptor and subsequently assessed their capacity to stimulate the receptor. Among the 31 peptides investigated, they found two peptides were weak agonists (EC_{50} 11 – 16 μM), two peptides were strong agonist (EC_{50} 14 – 25 nM) and one peptide was a partial antagonist (IC_{50} 36 μM).

Whilst to date no phage derived product has reached market, there are a number of clinical trials currently being undertaken using peptides derived from phage display: DX-88 (Ecallantide) from Dyax Corp is a highly specific

and potent inhibitor of kallikrein (K_i ~ 20 - 40 pM)[105-107]. Kallikrein is a key molecule in the regulation of inflammatory and blood clotting processes and plays a role in a number of autoimmune and inflammatory conditions. Dyax have successfully completed phase 3 trials of DX-88 in the treatment of hereditary angiodema (HAE) and phase I/II trials for the prevention of blood loss in on-pump coronary artery bypass graft (CABG) surgery; Compstatin (Potentia Pharmaceutics Inc.) [108, 109], a cyclic 13mer peptide originally identified from phage display, is a selective and potent inhibitor (K_d ~ 0.13 μM) of C3 protein in the complement cascade and will shortly enter clinical trials for the treatment of age-related macular degeneration. The development of Compstatin benefited from a multidisciplinary optimisation of the binding affinity of the original peptide to C3 through chemical, biophysical, and computational approaches; CIBG-300 (Center of Genetic Engineering and Biotechnology, Havana), is an inhibitor of Protein kinase CK2 phosphorylation. Overexpression of CK2 has been shown to be both oncogenic and tumorigenic. Early phase clinical trials of CIGB-300 have shown 75% of volunteers with microinvasive or preinvasive cervical cancers experience a significant reduction in lesion volume and 19% of the volunteers exhibited complete histological regression [110].

Despite these promising reports, the role of peptides as drugs in their own right is still in its infancy primarily because delivery and pharmacological issues such as poor oral stability and rapid degradation generally limit their

use. An exciting solution to these issues is to identify peptides that interact with a target and then design low molecular weight peptidomimetics from these lead peptides through *in-silico* molecular modelling and molecular dynamics. Hao and co-workers[111] have identified cyclic 7mer peptides to Cysteine-rich intestinal protein 1 (CRIP1), a biomarker for the early detection of breast, cervical and pancreatic cancers, that bind with modest affinities (kd ~ 30-60 μM). The lead candidate peptide was molecularly modelled and docked with CRIP1. Using the resultant data, the peptide was re-engineered *in-silico* to improve the docking. The resultant amino-acid sequence was synthesized and its binding affinity characterized. The K_d was found to be ~ 2.6 μM, a 10-fold greater affinity than the initial lead peptide. Extending these *in-silico* modelling simulations may afford the rational design of low molecular weight peptidomimetics based on the initial peptide.

1.10.2 Applications of phage display in drug delivery

Phage display is routinely employed to identify polypeptides that bind to cell surface receptors and proteins for the purpose of enhancing drug delivery to a particular tissue type. This is feasible because vascular beds in normal and pathological conditions are highly specialised landscapes that can be mapped using phage display technologies[112-115]. Whilst the selected polypeptides may not be entirely specific for a particular organ or tissue type they may prove useful in delivering therapeutic concentrations of a drug or a gene to its site of action. A variety of phage display selection

techniques can be used to identify targeting or homing polypeptides. If the identity of a surface receptor or epitope of interest is known and it can be purified or recombinantly expressed then it can be attached to a support and selected against *in-vitro*. The receptor is either immobilised on a solid support or exposed to phage library in a soluble form with subsequent capture via an affinity tag. Many examples of these techniques can be found in the literature against a staggering diversity of targets too numerous to mention here but are covered in detail in a number of excellent review articles[44, 116-120].

More recently selections have been made *in-vitro* on normal and malignant cell cultures. This strategy has the advantage that prior knowledge of the identity of a receptor on the cell surface need not be known. Subtractive selection strategies where library is exposed first to normal cells or malignant cells not associated with the primary tumour before exposure to primary malignant cells aids the identification of polypeptides specific for the tumour cell of interest. Hong and Clayman[121] used a 12-mer peptide library to screen *in-vitro* human head and neck squamous cell cancers (HHNSCC) and identified a peptide sequence that internalizes into HHNSCCs but not human prostate carcinoma, astrocytoma or human colon carcinoma cell lines; the peptide translated to the *in-vivo* environment with fluorescent labelled peptide observed to accumulate in tumour tissue implanted in mice. Similarly identified peptides have been reported for tumours associated with the liver[122, 123], colon[124], prostate[125] and

stomach[126]. It is of course not just malignancies that can be targeted in this way, normal cell cultures are amenable to selection processes as well and significant efforts have been invested in isolating peptides that may cross biological barriers. Unfortunately, cellular internalisation of macromolecules is not a simple issue and intracellular delivery remains a complex challenge.

Many researchers forego *in-vitro* selections and inject a phage library directly into animal models. In common with selections against *in-vitro* cell cultures *in-vivo* phage display does not require a pre-existing knowledge of a receptor to be targeted but affords an unbiased and internally controlled selection process that identifies phage-displayed peptides that home to a particular tissue. Essentially, a phage library is injected into the animal and allowed to circulate for sufficient time to ensure adequate exposure of vascular beds to phages. A saline perfusion is often used to remove phages remaining in the circulation before the tissue of interest is extracted and the phages within it recovered. Peptides have been identified in this way that home to a range of normal and diseased tissues including heart[127], kidney[114], lung[128], skin[129], pancreas[130], gastro-intestinal tract[131-134], uterus[135], adrenal gland[135], prostate[136], breast[137] and adipose tissue[138]. Researchers have sought to extend the utility of *in-vivo* phage display derived peptides to monitor disease progression. A recent report[139] used phage display identified peptides to monitor the progression of a pancreatic cancer model from a benign to a

metastatic stage. RIP1-Tag2 is a transgenic model of islet cell carcinoma and the research group hypothesised that the vasculature in pre-malignant lesions differs significantly from an established tumour. By undertaking phage selection processes at each stage of tumour progression the group were able to isolate stage specific peptides that differentiated between the vasculature of pre-malignant angiogenic islets and established tumour. Further, a number of the peptides identified selectively homed to pancreatic tumours but not tumours growing under the skin.

It may prove possible to use phage libraries to isolate patient specific peptides either by using excised pathological tissue as target or by intravenous administration of peptide phage libraries directly into the patient. Some pioneering work has already been conducted in this field[113] where a cancer patient on life-support but with no brain stem activity was injected with a 7-mer cyclic phage library and after 15 minutes circulation time bone marrow, white adipose, skeletal muscle, prostate and skin tissue was biopsied. A number of identical tripeptide motifs were found to accumulate in all tissues analysed but some tripeptide motifs were found to home to a single tissue. These data reflect current knowledge that certain vascular markers are ubiquitously expressed whilst others are tissue-specific.

1.10.3 Phage therapy

So far this introduction has been concerned with utilizing phage virions solely as vectors for the selection of polypeptides that interact with target. However, it would be imprudent to ignore the potential uses of phage as therapeutics in their own right. Phage therapy entered the public consciousness in 1925 with the publication of the Pullitzer prize winning novel Arrowsmith by Sinclair Lewis[140]. The book culminates with the discovery of a phage that kills bacteria responsible for the pathogenesis of bubonic plague.

The origins of phage therapy probably date to the late 19th century with the observation of a heat labile, filterable antibacterial that killed *Vibrio cholerae* in the Jumna and Ganges rivers[141]; two years later, the same effect was observed for *Bacillus subtilis*. The exact identity of this antibacterial remained elusive however until 1915 when Frederick Twort observed a glassification of micrococci on standard agar culture plates and suggested this was the result of some form of acute infectious disease[142]. Felix d'Herelle[143] coined the term plaque to describe this glassification or as we now interpret it a clearing of a bacterial lawn that indicates bacterial infection with phages. D'Herelles observation that patients who recover more rapidly from dysentery and typhoid have higher faecal phage titers paved the way for the commercialization of bacteriophage preparations through the Societe Francaise de Teintures Inoffensives pour

Cheveux (The French Society for Safe Hair Colouring or L'Oreal as it is known today)[144].

Whilst other companies including Eli Lilly became involved in the commercialization of phage products, the advent of modern antibacterial therapy in the 1930s all but bankrupted the science of phage therapy although the Eliava Institute of Bacteriophage, Microbiology and Virology in Tblisi, Georgia continued and continues to invest in the development of phage therapies[145]. Antibiotic resistance has led to a resurgent interest in research and development of phage therapeutics and at least eight commercial enterprises are involved in the development of clinically relevant phage medicines. Most phage, have a specific affinity for only a small group of bacteria predicated by the interaction of phage components (such as pIII on M13) with bacterial surface receptors. Upon interaction, the viral DNA is translocated into the bacterial cell for transcription where lytic or lysogenic replication may occur. Lytic phages replicate and assemble and then 'burst' from the host cell resulting in cell death. This is the result of hydrophobic pore formation by holins that allow access of lysins and endolysins to the petidoglycans in the bacterial membrane[146, 147]. In the lysogenic lifecycle, bacteriophage DNA becomes integrated in the host bacterium's genome. This newly generated material termed a prophage is replicated during cell division. The lysogenic lifecycle is shifted to a lytic one when exposed to some external trigger, such as UV radiation.

Lytic phage are in many ways an ideal antibacterial agent - they are target specific and the > 1 x 10^8 species of phage probably means there is a phage therapeutic for every bacterial species, they kill bacteria rapidly and amplify at the site of infection and are relatively inexpensive to produce. Further, the FDA recognize that humans ingest vast quantities of phages on a daily basis and tacitly accept that they are safe for oral administration[148]. It is perhaps topical administration however that has seen the most interest with the application of cocktails of phage to chronic wounds either as simple suspensions or incorporated into some form of dressing system such as a biodegradable polymer infused with phage and antibiotics [149]. The systemic administration of phage therapeutics is complicated by an inadequate knowledge of the pharmacokinetic and pharmacodynamic properties of most phage species with many studies indicating that the timing of administration is critical for infection control[150, 151]. Attaching phage display derived peptides that target particular organs to a therapeutic phage through recombinant techniques may afford site-specific delivery of the phages and negates some of the pharmacokinetic issues associated with phage therapy. Recent reports suggest that phages, which are naturally immuno-stimulatory[152, 153], may also be useful as vaccine delivery vehicles either by vaccinating with phages displaying the antigen[118, 154] or by utilizing phages to deliver a DNA expression cassette integrated into the phage genome[152, 155-157].

1.11 Scope of thesis

The increasing prevalence of CNS and brain disorders has intensified the requirements for novel therapeutic and targeting entities. Peptides are increasingly finding utility as novel therapeutics to treat a wide range of diseases and disorders and have also shown promise in enhancing macromolecular drug transport across biological barriers. Phage display libraries afford the rapid identification of peptides that interact with a target of interest and may find significant utility in addressing issues surrounding drug discovery and drug delivery. Therefore, the research that follows in this thesis is driven by an objective to explore the relevance of phage display identified peptides as experimental therapeutics in brain disorders.

The objective in Chapter 2 was in-house validation of a commercially available cyclic 7mer peptide phage display library. The library was validated against two molecules, streptavidin and paracetamol. Streptavidin is a large macromolecule routinely used to ensure the integrity of a phage library and as such the amino acid sequences of peptides that bind streptavidin have been widely reported. Paracetamol (4-AAP) is a low molecular weight species with two closely related structural isomers. Paracetamol is a simple model but represents a difficult target since it is comprised of few functional groups for peptide interaction. Nevertheless it provides a system in which to examine the capacity of phage display to isolate peptides that distinguish between very small structural variations.

Chapter 3 details the establishment and characterization of a BBB model comprised of primary porcine brain microvascular capillary endothelial cells. The phenotypic characteristics of the model were compared to primary rat and a variety of immortalized BBB cell lines as well as published *in-vivo* data. The established model along with two immortalized BBB cell lines from mouse and rat origins were exposed to phage library in an effort to identify peptides that would bind to brain microvasculature to increase the residency time at the BBB *in-vivo*.

Chapter 4 expands upon the phage display work in chapter 3, seeking to identify peptides that mediate, in a sequence specific manner, the *in-vivo* traversal of phages across the BBB. Rats were injected with phage library and, after a brief circulation time to allow displayed peptides to direct phages into the brain, the brains were excised, white matter and capillaries depleted and the phages in the brain parenchyma recovered and examined. The capacity of identified peptides to mediate traversal across the BBB was explored by co-injecting rats with peptide phages and insertless phages and determining subsequent tissue distribution profiles. Finally a physiologically based pharmacokinetic model was designed to contextualize the *in-vivo* data.

The objective of chapter 5 was to examine the role of caveolin-1 in the induction of an aggressive phenotype within *in-vitro* models of glioblastoma multiforme (grade iv astrocytoma); overexpression of caveolin-1 has been observed to positively correlate with an aggressive

phenotype in a variety of cancers. The expression levels of caveolin-1 and a series of downstream signalling markers were examined in four human glioblastoma multiforme cell lines. Subsequently, the effects of siRNA knockdown of caveolin-1 and inhibition of key molecules (mTOR and ERK) in the caveolin-1 signalling pathway, on invasion and proliferation were determined.

Given that overexpression of caveolin-1 in glioblastoma multiforme appears to drive an aggressive phenotype and that the actions of caveolin-1 are primarily mediated through a caveolin scaffolding domain (CSD) within caveolin-1, in chapter 6, peptides were identified via phage display that bind CSD. The binding of identified peptides to CSD was further characterized by enzyme linked immunosorbant assay.

Reference List

1. MacDonald, B.K., et al., *The incidence and lifetime prevalence of neurological disorders in a prospective community-based study in the UK.* Brain, 2000. **123 (Pt 4)**: p. 665-76.
2. Hirtz, D., et al., *How common are the "common" neurologic disorders?* Neurology, 2007. **68**(5): p. 326-37.
3. Regier, D.A., et al., *One-month prevalence of mental disorders in the United States. Based on five Epidemiologic Catchment Area sites.* Arch Gen Psychiatry, 1988. **45**(11): p. 977-86.
4. Pardridge, W.M., *Drug delivery to the brain.* J Cereb Blood Flow Metab, 1997. **17**(7): p. 713-31.
5. Nitsch, R.M. and C. Hock, *Targeting beta-amyloid pathology in Alzheimer's disease with Abeta immunotherapy.* Neurotherapeutics, 2008. **5**(3): p. 415-20.
6. DeAngelis, L.M., *Brain tumors.* N Engl J Med, 2001. **344**(2): p. 114-23.
7. Kleihues, P., et al., *The WHO classification of tumors of the nervous system.* J Neuropathol Exp Neurol, 2002. **61**(3): p. 215-25; discussion 226-9.
8. Nakazato, Y., *[The 4th Edition of WHO Classification of Tumours of the Central Nervous System published in 2007].* No Shinkei Geka, 2008. **36**(6): p. 473-91.
9. Louis, D.N., et al., *The 2007 WHO classification of tumours of the central nervous system.* Acta Neuropathol, 2007. **114**(2): p. 97-109.
10. Fuller, G.N. and B.W. Scheithauer, *The 2007 Revised World Health Organization (WHO) Classification of Tumours of the Central Nervous System: newly codified entities.* Brain Pathol, 2007. **17**(3): p. 304-7.
11. de Vries, N.A., et al., *Blood-brain barrier and chemotherapeutic treatment of brain tumors.* Expert Rev Neurother, 2006. **6**(8): p. 1199-209.
12. Scott, C.B., et al., *Validation and predictive power of Radiation Therapy Oncology Group (RTOG) recursive partitioning analysis classes for malignant glioma patients: a report using RTOG 90-06.* Int J Radiat Oncol Biol Phys, 1998. **40**(1): p. 51-5.
13. Larjavaara, S., et al., *Incidence of gliomas by anatomic location.* Neuro Oncol, 2007. **9**(3): p. 319-25.
14. Stupp, R., et al., *Radiotherapy plus concomitant and adjuvant temozolomide for glioblastoma.* N Engl J Med, 2005. **352**(10): p. 987-96.
15. Brem, H., et al., *Placebo-controlled trial of safety and efficacy of intraoperative controlled delivery by biodegradable polymers of*

chemotherapy for recurrent gliomas. The Polymer-brain Tumor Treatment Group. Lancet, 1995. **345**(8956): p. 1008-12.

16. Wong, E.T., et al., *Outcomes and prognostic factors in recurrent glioma patients enrolled onto phase II clinical trials.* J Clin Oncol, 1999. **17**(8): p. 2572-8.
17. Sathornsumetee, S. and J.N. Rich, *New treatment strategies for malignant gliomas.* Expert Rev Anticancer Ther, 2006. **6**(7): p. 1087-104.
18. Houillier, C., et al., *Prognostic impact of molecular markers in a series of 220 primary glioblastomas.* Cancer, 2006. **106**(10): p. 2218-23.
19. Sathornsumetee, S., et al., *Molecularly targeted therapy for malignant glioma.* Cancer, 2007. **110**(1): p. 13-24.
20. Smith, M.W. and M. Gumbleton, *Endocytosis at the blood-brain barrier: from basic understanding to drug delivery strategies.* J Drug Target, 2006. **14**(4): p. 191-214.
21. Stewart, P.A., *Endothelial vesicles in the blood-brain barrier: are they related to permeability?* Cell Mol Neurobiol, 2000. **20**(2): p. 149-63.
22. Pardridge, W.M., *Transport of insulin-related peptides and glucose across the blood-brain barrier.* Ann N Y Acad Sci, 1993. **692**: p. 126-37.
23. Boado, R.J., Y. Zhang, and W.M. Pardridge, *Humanization of anti-human insulin receptor antibody for drug targeting across the human blood-brain barrier.* Biotechnol Bioeng, 2007. **96**(2): p. 381-91.
24. Banks, W.A., *Blood-brain barrier transport of cytokines: a mechanism for neuropathology.* Curr Pharm Des, 2005. **11**(8): p. 973-84.
25. Mazel, M., et al., *Doxorubicin-peptide conjugates overcome multidrug resistance.* Anticancer Drugs, 2001. **12**(2): p. 107-16.
26. Rousselle, C., et al., *Enhanced delivery of doxorubicin into the brain via a peptide-vector-mediated strategy: saturation kinetics and specificity.* J Pharmacol Exp Ther, 2001. **296**(1): p. 124-31.
27. Rousselle, C., et al., *New advances in the transport of doxorubicin through the blood-brain barrier by a peptide vector-mediated strategy.* Mol Pharmacol, 2000. **57**(4): p. 679-86.
28. Pardridge, W.M., *Brain drug development and brain drug targeting.* Pharm Res, 2007. **24**(9): p. 1729-32.
29. Pardridge, W.M., *Drug targeting to the brain.* Pharm Res, 2007. **24**(9): p. 1733-44.
30. Kreuter, J., *Influence of the surface properties on nanoparticle-mediated transport of drugs to the brain.* J Nanosci Nanotechnol, 2004. **4**(5): p. 484-8.

31. Kreuter, J., *Nanoparticulate systems for brain delivery of drugs.* Adv Drug Deliv Rev, 2001. **47**(1): p. 65-81.

32. Kreuter, J., *Drug targeting with nanoparticles.* Eur J Drug Metab Pharmacokinet, 1994. **19**(3): p. 253-6.

33. Smith, M., Y. Omidi, and M. Gumbleton, *Primary porcine brain microvascular endothelial cells: biochemical and functional characterisation as a model for drug transport and targeting.* J Drug Target, 2007. **15**(4): p. 253-68.

34. Palade, G.E., *An electron microscope study of the mitochondrial structure.* J Histochem Cytochem, 1953. **1**(4): p. 188-211.

35. Yamada, E., *The fine structure of the gall bladder epithelium of the mouse.* J Biophys Biochem Cytol, 1955. **1**(5): p. 445-58.

36. Couet, J., et al., *Cell biology of caveolae and caveolin.* Adv Drug Deliv Rev, 2001. **49**(3): p. 223-35.

37. Sowa, G., M. Pypaert, and W.C. Sessa, *Distinction between signaling mechanisms in lipid rafts vs. caveolae.* Proc Natl Acad Sci U S A, 2001. **98**(24): p. 14072-7.

38. Kurzchalia, T.V., P. Dupree, and S. Monier, *VIP21-Caveolin, a protein of the trans-Golgi network and caveolae.* FEBS Lett, 1994. **346**(1): p. 88-91.

39. Kurzchalia, T.V., et al., *VIP21, a 21-kD membrane protein is an integral component of trans-Golgi-network-derived transport vesicles.* J Cell Biol, 1992. **118**(5): p. 1003-14.

40. Campbell, L., M. Gumbleton, and K. Ritchie, *Caveolae and the caveolins in human disease.* Advanced Drug Delivery Reviews, 2001. **49**(3): p. 325-335.

41. Fielding, C.J. and P.E. Fielding, *Caveolae and intracellular trafficking of cholesterol.* Advanced Drug Delivery Reviews, 2001. **49**(3): p. 251-264.

42. Schnitzer, J.E., *Caveolae: from basic trafficking mechanisms to targeting transcytosis for tissue-specific drug and gene delivery in vivo.* Advanced Drug Delivery Reviews, 2001. **49**(3): p. 265-280.

43. Goetz, J.G., et al., *Caveolin-1 in tumor progression: the good, the bad and the ugly.* Cancer Metastasis Rev, 2008. **27**(4): p. 715-35.

44. Sergeeva, A., et al., *Display technologies: application for the discovery of drug and gene delivery agents.* Adv Drug Deliv Rev, 2006. **58**(15): p. 1622-54.

45. Smith, G.P., *Filamentous fusion phage: novel expression vectors that display cloned antigens on the virion surface.* Science, 1985. **228**(4705): p. 1315-7.

46. van Wezenbeek, P.M., T.J. Hulsebos, and J.G. Schoenmakers, *Nucleotide sequence of the filamentous bacteriophage M13 DNA genome: comparison with phage fd.* Gene, 1980. **11**(1-2): p. 129-48.

47. Hill, D.F. and G.B. Petersen, *Nucleotide sequence of bacteriophage f1 DNA.* J Virol, 1982. **44**(1): p. 32-46.

48. Beck, E. and B. Zink, *Nucleotide sequence and genome organisation of filamentous bacteriophages f1 and fd.* Gene, 1981. **16**(1-3): p. 35-58.

49. Brown, L.R. and C.E. Dowell, *Replication of coliphage M-13. I. Effects on host cells after synchronized infection.* J Virol, 1968. **2**(11): p. 1290-5.

50. Hoffmann Berling, H. and R. Maze, *Release of Male-Specific Bacteriophages from Surviving Host Bacteria.* Virology, 1964. **22**: p. 305-13.

51. Marvin, D.A., *Filamentous phage structure, infection and assembly.* Curr Opin Struct Biol, 1998. **8**(2): p. 150-8.

52. Terry, T.D., P. Malik, and R.N. Perham, *Accessibility of peptides displayed on filamentous bacteriophage virions: susceptibility to proteinases.* Biol Chem, 1997. **378**(6): p. 523-30.

53. Marvin, D.A., et al., *Molecular models and structural comparisons of native and mutant class I filamentous bacteriophages Ff (fd, f1, M13), If1 and IKe.* J Mol Biol, 1994. **235**(1): p. 260-86.

54. Greenwood, J., G.J. Hunter, and R.N. Perham, *Regulation of filamentous bacteriophage length by modification of electrostatic interactions between coat protein and DNA.* J Mol Biol, 1991. **217**(2): p. 223-7.

55. Makowski, L., *Terminating a macromolecular helix. Structural model for the minor proteins of bacteriophage M13.* J Mol Biol, 1992. **228**(3): p. 885-92.

56. Endemann, H. and P. Model, *Location of filamentous phage minor coat proteins in phage and in infected cells.* J Mol Biol, 1995. **250**(4): p. 496-506.

57. Gray, C.W., R.S. Brown, and D.A. Marvin, *Adsorption complex of filamentous fd virus.* J Mol Biol, 1981. **146**(4): p. 621-7.

58. Stengele, I., et al., *Dissection of functional domains in phage fd adsorption protein. Discrimination between attachment and penetration sites.* J Mol Biol, 1990. **212**(1): p. 143-9.

59. Kremser, A. and I. Rasched, *The adsorption protein of filamentous phage fd: assignment of its disulfide bridges and identification of the domain incorporated in the coat.* Biochemistry, 1994. **33**(46): p. 13954-8.

60. Deng, L.W., P. Malik, and R.N. Perham, *Interaction of the globular domains of pIII protein of filamentous bacteriophage fd with the F-pilus of Escherichia coli.* Virology, 1999. **253**(2): p. 271-7.

61. Armstrong, J., R.N. Perham, and J.E. Walker, *Domain structure of bacteriophage fd adsorption protein.* FEBS Lett, 1981. **135**(1): p. 167-72.

62. Salivar, W.O., H. Tzagoloff, and D. Pratt, *Some Physical-Chemical and Biological Properties of the Rod-Shaped Coliphage M13.* Virology, 1964. **24**: p. 359-71.

63. Olofsson, L., et al., *Filamentous bacteriophage stability in non-aqueous media.* Chem Biol, 2001. **8**(7): p. 661-71.

64. Harrison, J.L., et al., *Screening of phage antibody libraries.* Methods Enzymol, 1996. **267**: p. 83-109.

65. Russel, M., et al., *Low-frequency infection of F- bacteria by transducing particles of filamentous bacteriophages.* J Bacteriol, 1988. **170**(11): p. 5312-6.

66. Jacobson, A., *Role of F pili in the penetration of bacteriophage fl.* J Virol, 1972. **10**(4): p. 835-43.

67. Novotny, C.P. and P. Fives-Taylor, *Effects of high temperature on Escherichia coli F pili.* J Bacteriol, 1978. **133**(2): p. 459-64.

68. Novotny, C.P. and P. Fives-Taylor, *Retraction of F pili.* J Bacteriol, 1974. **117**(3): p. 1306-11.

69. Riechmann, L. and P. Holliger, *The C-terminal domain of TolA is the coreceptor for filamentous phage infection of E. coli.* Cell, 1997. **90**(2): p. 351-60.

70. Lubkowski, J., et al., *The structural basis of phage display elucidated by the crystal structure of the N-terminal domains of g3p.* Nat Struct Biol, 1998. **5**(2): p. 140-7.

71. Gray, C.W., *Three-dimensional structure of complexes of single-stranded DNA-binding proteins with DNA. IKe and fd gene 5 proteins form left-handed helices with single-stranded DNA.* J Mol Biol, 1989. **208**(1): p. 57-64.

72. Guan, Y., H. Zhang, and A.H. Wang, *Electrostatic potential distribution of the gene V protein from Ff phage facilitates cooperative DNA binding: a model of the GVP-ssDNA complex.* Protein Sci, 1995. **4**(2): p. 187-97.

73. Olah, G.A., et al., *Structures of fd gene 5 protein.nucleic acid complexes: a combined solution scattering and electron microscopy study.* J Mol Biol, 1995. **249**(3): p. 576-94.

74. Skinner, M.M., et al., *Structure of the gene V protein of bacteriophage f1 determined by multiwavelength x-ray diffraction on the*

selenomethionyl protein. Proc Natl Acad Sci U S A, 1994. **91**(6): p. 2071-5.

75. Bauer, M. and G.P. Smith, *Filamentous phage morphogenetic signal sequence and orientation of DNA in the virion and gene-V protein complex.* Virology, 1988. **167**(1): p. 166-75.

76. Welsh, L.C., et al., *Structure of the capsid of Pf3 filamentous phage determined from X-ray fibre diffraction data at 3.1 A resolution.* J Mol Biol, 1998. **283**(1): p. 155-77.

77. Russel, M. and P. Model, *Sequence of thioredoxin reductase from Escherichia coli. Relationship to other flavoprotein disulfide oxidoreductases.* J Biol Chem, 1988. **263**(18): p. 9015-9.

78. Feng, J.N., M. Russel, and P. Model, *A permeabilized cell system that assembles filamentous bacteriophage.* Proc Natl Acad Sci U S A, 1997. **94**(8): p. 4068-73.

79. Lopez, J. and R.E. Webster, *Assembly site of bacteriophage f1 corresponds to adhesion zones between the inner and outer membranes of the host cell.* J Bacteriol, 1985. **163**(3): p. 1270-4.

80. Russel, M., N.A. Linderoth, and A. Sali, *Filamentous phage assembly: variation on a protein export theme.* Gene, 1997. **192**(1): p. 23-32.

81. Marciano, D.K., M. Russel, and S.M. Simon, *An aqueous channel for filamentous phage export.* Science, 1999. **284**(5419): p. 1516-9.

82. Rakonjac, J., J. Feng, and P. Model, *Filamentous phage are released from the bacterial membrane by a two-step mechanism involving a short C-terminal fragment of pIII.* J Mol Biol, 1999. **289**(5): p. 1253-65.

83. Rakonjac, J. and P. Model, *Roles of pIII in filamentous phage assembly.* J Mol Biol, 1998. **282**(1): p. 25-41.

84. Gao, C., et al., *Making artificial antibodies: a format for phage display of combinatorial heterodimeric arrays.* Proc Natl Acad Sci U S A, 1999. **96**(11): p. 6025-30.

85. Jespers, L.S., et al., *Surface expression and ligand-based selection of cDNAs fused to filamentous phage gene VI.* Biotechnology (N Y), 1995. **13**(4): p. 378-82.

86. Krebber, C., et al., *Selectively-infective phage (SIP): a mechanistic dissection of a novel in vivo selection for protein-ligand interactions.* J Mol Biol, 1997. **268**(3): p. 607-18.

87. Spada, S., C. Krebber, and A. Pluckthun, *Selectively infective phages (SIP).* Biol Chem, 1997. **378**(6): p. 445-56.

88. Iannolo, G., et al., *Modifying filamentous phage capsid: limits in the size of the major capsid protein.* J Mol Biol, 1995. **248**(4): p. 835-44.

89. Malik, P., et al., *Role of capsid structure and membrane protein processing in determining the size and copy number of peptides displayed on the major coat protein of filamentous bacteriophage.* J Mol Biol, 1996. **260**(1): p. 9-21.

90. Petrenko, V.A., et al., *A library of organic landscapes on filamentous phage.* Protein Eng, 1996. **9**(9): p. 797-801.

91. Bass, S., R. Greene, and J.A. Wells, *Hormone phage: an enrichment method for variant proteins with altered binding properties.* Proteins, 1990. **8**(4): p. 309-14.

92. Breitling, F., et al., *A surface expression vector for antibody screening.* Gene, 1991. **104**(2): p. 147-53.

93. *Surface display and peptide libraries. Cold Spring Harbor Laboratory, April 4-7, 1992. Proceedings.* Gene, 1993. **128**(1): p. 1-144.

94. Smith, G.P. and V.A. Petrenko, *Phage Display.* Chem Rev, 1997. **97**(2): p. 391-410.

95. Kay, B.K., et al., *An M13 phage library displaying random 38-amino-acid peptides as a source of novel sequences with affinity to selected targets.* Gene, 1993. **128**(1): p. 59-65.

96. Messing, J., et al., *Filamentous coliphage M13 as a cloning vehicle: insertion of a HindII fragment of the lac regulatory region in M13 replicative form in vitro.* Proc Natl Acad Sci U S A, 1977. **74**(9): p. 3642-6.

97. Messing, J., *New M13 vectors for cloning.* Methods Enzymol, 1983. **101**: p. 20-78.

98. Lin, B., et al., *A step-wise approach significantly enhances protein yield of a rationally-designed agonist antibody fragment in E. coli.* Protein Expr Purif, 2008. **59**(1): p. 55-63.

99. McConnell, S.J., et al., *Isolation of erythropoietin receptor agonist peptides using evolved phage libraries.* Biol Chem, 1998. **379**(10): p. 1279-86.

100. Skelton, N.J., et al., *Amino acid determinants of beta-hairpin conformation in erythropoeitin receptor agonist peptides derived from a phage display library.* J Mol Biol, 2002. **316**(5): p. 1111-25.

101. Robinson, S.A. and S.A. Rosenzweig, *Paradoxical effects of the phage display-derived peptide antagonist IGF-F1-1 on insulin-like growth factor-1 receptor signaling.* Biochem Pharmacol, 2006. **72**(1): p. 53-61.

102. Wu, X., et al., *Isolation of a novel basic FGF-binding peptide with potent antiangiogenetic activity.* J Cell Mol Med, 2008.

103. Serrati, S., et al., *TGFbeta1 antagonistic peptides inhibit TGFbeta1-dependent angiogenesis.* Biochem Pharmacol, 2008.

104. Bonetto, S., I. Carlavan, and D. Baty, *Isolation and characterization of antagonist and agonist peptides to the human melanocortin 1 receptor.* Peptides, 2005. **26**(11): p. 2302-13.

105. Zingale, L.C., et al., *Successful resolution of bowel obstruction in a patient with hereditary angioedema.* Eur J Gastroenterol Hepatol, 2008. **20**(6): p. 583-7.

106. Lehmann, A., *Ecallantide (DX-88), a plasma kallikrein inhibitor for the treatment of hereditary angioedema and the prevention of blood loss in on-pump cardiothoracic surgery.* Expert Opin Biol Ther, 2008. **8**(8): p. 1187-99.

107. Lehmann, A., *Ecallantide (Dyax/Genzyme).* Curr Opin Investig Drugs, 2006. **7**(3): p. 282-90.

108. Sahu, A., D. Morikis, and J.D. Lambris, *Compstatin, a peptide inhibitor of complement, exhibits species-specific binding to complement component C3.* Mol Immunol, 2003. **39**(10): p. 557-66.

109. Ricklin, D. and J.D. Lambris, *Compstatin: a complement inhibitor on its way to clinical application.* Adv Exp Med Biol, 2008. **632**: p. 273-92.

110. Perea, S.E., et al., *CIGB-300, a novel proapoptotic peptide that impairs the CK2 phosphorylation and exhibits anticancer properties both in vitro and in vivo.* Mol Cell Biochem, 2008. **316**(1-2): p. 163-7.

111. Hao, J., et al., *Identification and rational redesign of peptide ligands to CRIP1, a novel biomarker for cancers.* PLoS Comput Biol, 2008. **4**(8): p. e1000138.

112. Zurita, A.J., W. Arap, and R. Pasqualini, *Mapping tumor vascular diversity by screening phage display libraries.* J Control Release, 2003. **91**(1-2): p. 183-6.

113. Arap, W., et al., *Steps toward mapping the human vasculature by phage display.* Nat Med, 2002. **8**(2): p. 121-7.

114. Pasqualini, R. and E. Ruoslahti, *Organ targeting in vivo using phage display peptide libraries.* Nature, 1996. **380**(6572): p. 364-6.

115. Ruoslahti, E., *Specialization of tumour vasculature.* Nat Rev Cancer, 2002. **2**(2): p. 83-90.

116. Rowley, M.J., K. O'Connor, and L. Wijeyewickrema, *Phage display for epitope determination: a paradigm for identifying receptor-ligand interactions.* Biotechnol Annu Rev, 2004. **10**: p. 151-88.

117. Stefanidakis, M. and E. Koivunen, *Peptide-mediated delivery of therapeutic and imaging agents into mammalian cells.* Curr Pharm Des, 2004. **10**(24): p. 3033-44.

118. Wang, L.F. and M. Yu, *Epitope identification and discovery using phage display libraries: applications in vaccine development and diagnostics.* Curr Drug Targets, 2004. **5**(1): p. 1-15.

119. Hartley, O., *The use of phage display in the study of receptors and their ligands.* J Recept Signal Transduct Res, 2002. **22**(1-4): p. 373-92.

120. Koivunen, E., et al., *Identification of receptor ligands with phage display peptide libraries.* J Nucl Med, 1999. **40**(5): p. 883-8.

121. Hong, F.D. and G.L. Clayman, *Isolation of a peptide for targeted drug delivery into human head and neck solid tumors.* Cancer Res, 2000. **60**(23): p. 6551-6.

122. Du, B., et al., *In vitro panning of a targeting peptide to hepatocarcinoma from a phage display peptide library.* Biochem Biophys Res Commun, 2006. **342**(3): p. 956-62.

123. Jia, W.D., et al., *A novel peptide that selectively binds highly metastatic hepatocellular carcinoma cell surface is related to invasion and metastasis.* Cancer Lett, 2007. **247**(2): p. 234-42.

124. Zhang, Y., et al., *Panning and identification of a colon tumor binding peptide from a phage display peptide library.* J Biomol Screen, 2007. **12**(3): p. 429-35.

125. Popkov, M., C. Rader, and C.F. Barbas, 3rd, *Isolation of human prostate cancer cell reactive antibodies using phage display technology.* J Immunol Methods, 2004. **291**(1-2): p. 137-51.

126. Zhang, K.D., et al., *[Screening and identification of phage-displayed polypeptides specifically binding to human gastric cancer with high metastatic potential to peritoneum].* Zhonghua Zhong Liu Za Zhi, 2005. **27**(7): p. 397-400.

127. Zhang, L., J.A. Hoffman, and E. Ruoslahti, *Molecular profiling of heart endothelial cells.* Circulation, 2005. **112**(11): p. 1601-11.

128. Wu, M., et al., *Mapping alveolar binding sites in vivo using phage peptide libraries.* Gene Ther, 2003. **10**(17): p. 1429-36.

129. Chen, Y., et al., *Transdermal protein delivery by a coadministered peptide identified via phage display.* Nat Biotechnol, 2006. **24**(4): p. 455-60.

130. Yao, V.J., et al., *Targeting pancreatic islets with phage display assisted by laser pressure catapult microdissection.* Am J Pathol, 2005. **166**(2): p. 625-36.

131. Kang, S.K., et al., *Identification of a peptide sequence that improves transport of macromolecules across the intestinal mucosal barrier targeting goblet cells.* J Biotechnol, 2008. **135**(2): p. 210-6.

132. Duerr, D.M., S.J. White, and H.J. Schluesener, *Identification of peptide sequences that induce the transport of phage across the*

gastrointestinal mucosal barrier. J Virol Methods, 2004. **116**(2): p. 177-80.

133. Higgins, L.M., et al., *In vivo phage display to identify M cell-targeting ligands.* Pharm Res, 2004. **21**(4): p. 695-705.

134. Hui, X., et al., *Specific targeting of the vasculature of gastric cancer by a new tumor-homing peptide CGNSNPKSC.* J Control Release, 2008. **131**(2): p. 86-93.

135. Kolonin, M.G., et al., *Synchronous selection of homing peptides for multiple tissues by in vivo phage display.* FASEB J, 2006. **20**(7): p. 979-81.

136. Newton, J.R., et al., *In vivo selection of phage for the optical imaging of PC-3 human prostate carcinoma in mice.* Neoplasia, 2006. **8**(9): p. 772-80.

137. Essler, M. and E. Ruoslahti, *Molecular specialization of breast vasculature: a breast-homing phage-displayed peptide binds to aminopeptidase P in breast vasculature.* Proc Natl Acad Sci U S A, 2002. **99**(4): p. 2252-7.

138. Kolonin, M.G., et al., *Reversal of obesity by targeted ablation of adipose tissue.* Nat Med, 2004. **10**(6): p. 625-32.

139. Yang, W., et al., *TMTP1, a novel tumor-homing peptide specifically targeting metastasis.* Clin Cancer Res, 2008. **14**(17): p. 5494-502.

140. Lewis, S., *Arrowsmith.* 1925, New York: Harcourt, Brace & Co.

141. Hankin, E., *The bactericidal action of the waters of the Jumna and the Ganges on Vibrio cholerae.* Ann Inst Pasteur, 1896. **10**: p. 511.

142. Twort, F.W., *THE ULTRA-MICROSCOPIC VIRUSES.* The Lancet, 1921. **198**(5108): p. 204-204.

143. Publications, s., *On an invisible microbe antagonistic toward dysenteric bacilli: brief note by Mr. F. D'Herelle, presented by Mr. Roux.* Research in Microbiology, 2007. **158**(7): p. 553-554.

144. Sulakvelidze, A., Z. Alavidze, and J.G. Morris, Jr., *Bacteriophage therapy.* Antimicrob Agents Chemother, 2001. **45**(3): p. 649-59.

145. Kutateladze, M. and R. Adamia, *Phage therapy experience at the Eliava Institute.* MÈdecine et Maladies Infectieuses, 2008. **38**(8): p. 426-430.

146. Srividhya, K.V. and S. Krishnaswamy, *Subclassification and targeted characterization of prophage-encoded two-component cell lysis cassette.* J Biosci, 2007. **32**(5): p. 979-90.

147. Borysowski, J., B. Weber-Dabrowska, and A. Gorski, *Bacteriophage endolysins as a novel class of antibacterial agents.* Exp Biol Med (Maywood), 2006. **231**(4): p. 366-77.

148. Abuladze, T., et al., *Bacteriophages reduce experimental contamination of hard surfaces, tomato, spinach, broccoli, and ground beef by Escherichia coli O157:H7.* Appl Environ Microbiol, 2008. **74**(20): p. 6230-8.

149. Markoishvili, K., et al., *A novel sustained-release matrix based on biodegradable poly(ester amide)s and impregnated with bacteriophages and an antibiotic shows promise in management of infected venous stasis ulcers and other poorly healing wounds.* Int J Dermatol, 2002. **41**(7): p. 453-8.

150. Payne, R.J. and V.A. Jansen, *Pharmacokinetic principles of bacteriophage therapy.* Clin Pharmacokinet, 2003. **42**(4): p. 315-25.

151. Payne, R.J., D. Phil, and V.A. Jansen, *Phage therapy: the peculiar kinetics of self-replicating pharmaceuticals.* Clin Pharmacol Ther, 2000. **68**(3): p. 225-30.

152. Clark, J.R. and J.B. March, *Bacterial viruses as human vaccines?* Expert Rev Vaccines, 2004. **3**(4): p. 463-76.

153. Kleinschmidt, W.J., R.J. Douthart, and E.B. Murphy, *Interferon production by T4 coliphage.* Nature, 1970. **228**(5266): p. 27-30.

154. Irving, M.B., O. Pan, and J.K. Scott, *Random-peptide libraries and antigen-fragment libraries for epitope mapping and the development of vaccines and diagnostics.* Curr Opin Chem Biol, 2001. **5**(3): p. 314-24.

155. Clark, J.R. and J.B. March, *Bacteriophage-mediated nucleic acid immunisation.* FEMS Immunol Med Microbiol, 2004. **40**(1): p. 21-6.

156. March, J.B., J.R. Clark, and C.D. Jepson, *Genetic immunisation against hepatitis B using whole bacteriophage lambda particles.* Vaccine, 2004. **22**(13-14): p. 1666-71.

157. Jepson, C.D. and J.B. March, *Bacteriophage lambda is a highly stable DNA vaccine delivery vehicle.* Vaccine, 2004. **22**(19): p. 2413-9.

Chapter 2 Phage display method development

2.1 Introduction

2.1.1 General principles of phage display panning studies

The objective of any phage display selection process is to reduce the initial phage library (10^9 unique clones represented by 100 – 200 copies of each clone) to a small population of phages that have an increased 'suitability' for a user defined requirement such as a binding interaction, a targeting moiety, agonism or antagonism of a biological or chemical event etc[1]. After the initial selection, the phages are amplified in a bacterial host such that each clone in the population is now represented by many millions of copies. These amplified phage clones can then be subjected to iterative rounds of selection to further enrich the pool for those phage clones that are the 'fittest' for the chosen criterion. A generalised panning experiment is detailed in **Figure 2.1**.

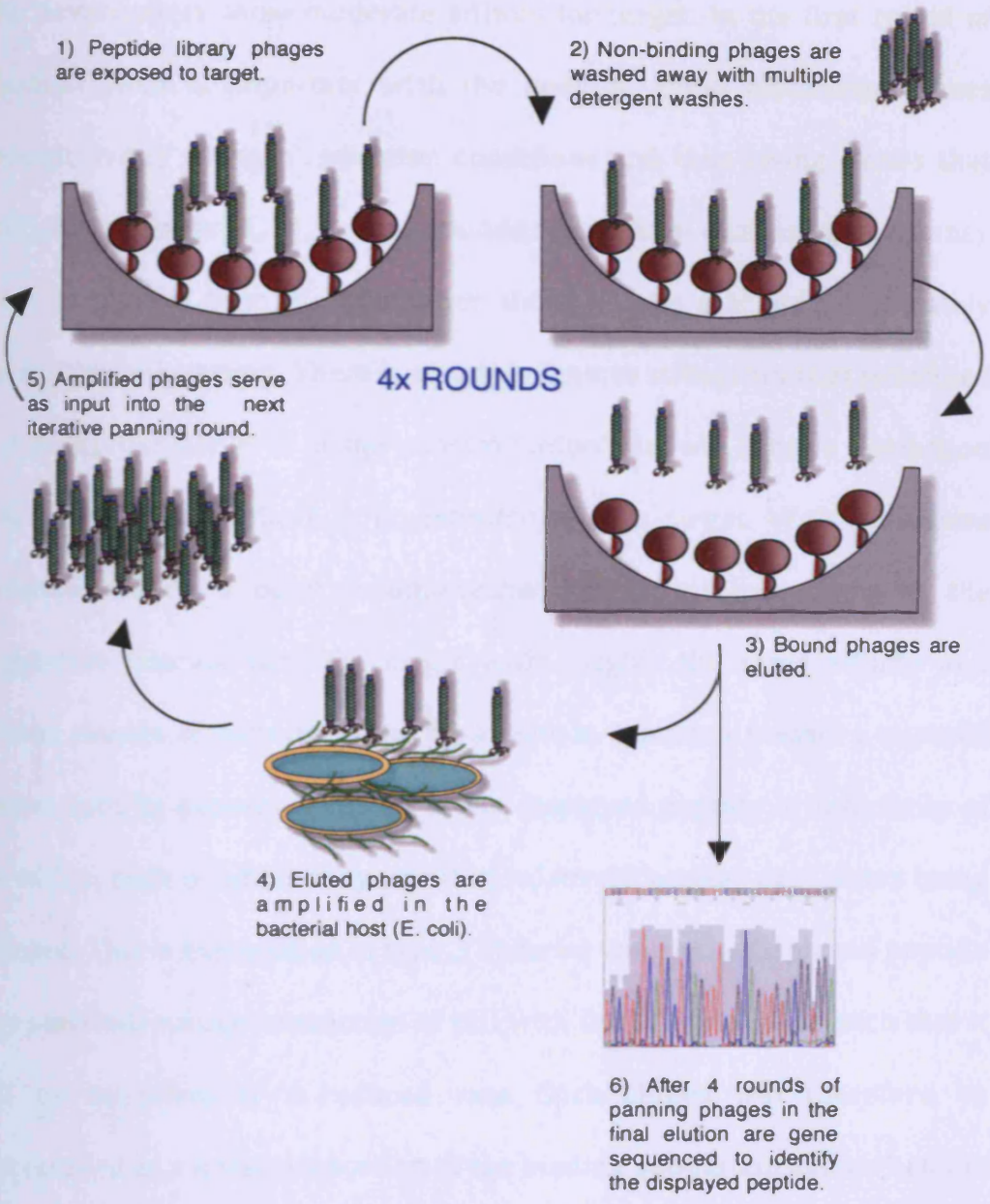

Figure 2.1 Schematic of a generic phage display panning strategy.

Any phage selection process is essentially governed by two factors: yield and stringency[1]. Yield is the number of phages within the population that interact with the target and 'survive' the selection process. This is determined by stringency, the property that discriminates clones that interact with target with high affinity from the rest of the population, which

may nevertheless show moderate affinity for target. In the first round of selection yield is important with the need to avoid discarding clones through overly stringent selection conditions and thus losing clones that interact with target[1, 2]. In later rounds of selection increasing stringency helps to remove from the population those phages that only moderately interact with the target. There is an upper limit to stringency that is defined by a background level of phage 'contamination' that will survive a selection process even when there is no interaction with target. With successive selection rounds a point is approached where all the clones in the population interact with the target with roughly the same affinity and further rounds of panning result in a shift in selection pressure towards factors such as expression levels of the displayed peptide or infectivity of the virion, both of which may result in relatively weaker candidates being selected. This is exemplified in type 3 libraries where the displayed peptide may sterically hinder interaction of pIII with the bacterial pilus such that it will be amplified at a reduced rate. Such clones will therefore be represented as a lower proportion of the binding population even when the displayed peptide has greater affinity for target than other clones in the population.

2.1.2 Affinity selection

Phage display libraries can be screened or 'panned' against a diverse range of molecules and surfaces including peptides, proteins, nucleic acid material[3, 4], cells[5-7], tissues[8, 9], whole organisms[10-13] and low

molecular weight entities[14, 15]. Irrespective of target, by far the most common selection pressure utilised in the screening of library against target is the affinity of a given polypeptide displayed on the phage clone for a target molecule. A generalised schematic of a phage panning procedure can be seen in **Figure 2.1**. Essentially the target is exposed to the phage library for a period of time to allow interaction between the displayed peptide and target. Those phage clones with an affinity for the target (usually a tiny proportion of the parent library) are captured on the surface of the target and those that do not bind or have limited affinity for the target are washed away. The bound phage are recovered into solution using an elution strategy that may include non-specific disruption of phage-target bonds (e.g. low pH washes)[16] or a specific elution with either excess free target or with a cognate ligand(s) for the target[17-20]. In each case, the eluate contains a sub-population of phage clones from the original library that have an increased affinity for the target. The eluted phages, which remain infective, are subsequently amplified in the host bacterium to afford iterative rounds of panning to further enrich for the highest affinity binders. After 3-4 rounds of selection, the phage clones in the final eluate are propagated on a clonal basis before the relevant coding region in the viral DNA is sequenced to determine the peptide displayed.

2.1.3 Target presentation

The majority of phage display panning experiments are designed against targets immobilised to a solid support such as derivatised or activated

polystyrene surfaces, activated dextrans, epoxide beads, paramagnetic beads, nitrocellulose membranes, derivatised biosensor chips or permeable beaded agarose gels. A variety of techniques have been employed to affect this immobilisation including cross-linking of $-NH_2$, -SH or -CHO to modified or activated surfaces, non-covalent adsorption to a hydrophobic surface, attachment through a molecular tag such as biotin, GST or His(6) which bind their cognate binding partner and capture of IgG-Fc fusions to anti-Fc antibody (**Table 2.1**).

***Table 2.1** Example immobilization matrices used for target presentation in phage binding selections.*

Capture Matrix	Immobilization mechanism	Issues
Maxisorp (Nunc)	Non-specific adsorbance	Matrix binders
Covalink (Costar)	Cross-linking of -SH, -CHO or $-NH_2$ to activated surface	Matrix binders, limited capacity
Oxirane acrylic beads (Sigma)	Cross-linking of $-NH_2$ or -SH to epoxide	Matrix binders
Biosensor chip (Biacore, QCM)	Cross-linking of -SH, -CHO or $-NH_2$ to modified dextran	Matrix binders, limited capacity
Avidin coated plates/beads (Promega, Nunc)	Capture of biotinylated target via avidin-biotin interaction	Peptidergic biotin binders
Ni^{2+} or antibody plates/beads (Qiagen)	$(His)_6$ interaction with Ni^{2+} or antibody	Ni^{2+} or antibody binders; $(His)_6$ binders

Panning methodologies against immobilised target are generally classified as one- or two- step selection procedures. In one-step selections the phage library is directly exposed to immobilized target whilst in two-step selections the target, fused to an affinity tag, is initially exposed to the library in a solution or suspension phase, then in a second step, the phage-target-tag complex is reacted with a surface decorated with a molecule that captures the complex via the attached affinity tag. Two-step selection

generally results in considerably lower yields but favours monovalent interactions and selections based on binding affinity and kinetics rather than avidity where multiple peptide copies interact with target[21-24].

2.1.3.1 Elution

After washing away non-binding and weakly binding phage clones with a detergent buffer, the binding phage must be recovered for amplification. Non-specific elution strategies seek to weaken phage-target interactions, exploiting, without loss of infectivity, the robustness of the phage particle to a wide-range of conditions including extremes of pH, temperature and exposure to proteases[1]. Alternatively, the binding phage clones may be competitively eluted with excess free target or specifically eluted with a cognate ligand[17-20], the latter is particularly effective when the target is presented within a crude mixture of related or unrelated 'contaminants' since the ligand will displace only those phages that bind the target. However, careful consideration of binding kinetics must be given when using competitive ligand elution since it is a two-stage process requiring first the spontaneous dissociation of the phage clone from target followed by occupation within the target by the competitive ligand. Clearly, each process will have its own k_{on}/k_{off} with typically a reduction in k_{off} for the phage clone an indicator of increased affinity for target. If the incubation period with the competitive ligand is too short, those phage clones with highest affinity will not be eluted. Conversely, a long incubation time will

not discriminate between high and low affinities since essentially all the binding clones will be displaced.

Whilst it would seem logical that directly adding bacterial host cells to the phage-target-support complex would be the optimal recovery strategy, it is apparent that only 1-10% of the clones recovered by elution are recovered by direct bacterial infection[1]. As the iterative panning rounds are completed, the progress of affinity selection can be quantitatively monitored with techniques such as enzyme-linked immunosorbant assay, surface plasmon resonance[25] or quartz crystal microbalances.

2.1.4 Technology validation

In preparation for panning studies against targets involved in the pathobiogenesis of glioma and for the discovery of peptides that cross the BBB to deliver novel therapies into the brain, a series of phage display studies were designed to validate the phage library and phage selection strategies. Two targets were utilised for this preliminary validation exercise, streptavidin a 53 KDa tetrameric protein and 4-acetamidophenol (4-AAP; paracetamol) a low molecular weight species. Some consideration will now be giving to the selection of these targets and issues of panning against them.

2.1.4.1 Streptavidin

Streptavidin is a ~ 53 KDa tetrameric protein purified from the bacterium Streptomyces *avidinii*. The incredible high affinity of the vitamin biotin

(244 Da) for streptavidin (Kd ~ 10^{-14} M)[26] has intrigued researchers for many years and the interaction has found application in a diverse range of biomedical and biotechnological fields[27]. Through technologies such as phage display, streptavidin has also proven particularly amenable to the discovery of peptide ligands that interact with the biotin binding pocket[28-30]. The ready crystallisation of apostreptavidin (streptavidin without biotin bound) and complexes of streptavidin with biotin or streptavidin with novel peptide ligands[30], has made streptavidin an ideal model for the exploration of the structural determinants of high affinity peptide-ligand pairs. The availability of a diverse range of streptavidin derivatised supports coupled with the knowledge of linear and cyclic peptide sequences that bind streptavidin[28, 31] makes the molecule an ideal starting point to examine new libraries and to test selection strategies before panning against the desired target.

2.1.4.2 4-AAP

Peptides that bind low molecular weight organic species would have significant application in such areas as therapeutics, biosensing and neutralisation and sensing applications in the environmental and chemical sciences. However, the scientific literature only has a few accounts of phage-peptide interactions with non-proteinaceous low molecular weight targets[32-34]. The slow progress in identifying peptides that bind low molecular weight species either from phage display or other combinatorial peptide technologies is largely associated with complex issues of

immobilising the low molecular weight entity without chemically occupying one of the limited recognition groups on the molecule itself. To overcome these issues, it was hypothesised that insoluble complexes of a molecule could be panned against and then manipulated with the insoluble complexes washed and, together with binding phages, captured by centrifugation techniques. The advantage of this approach should be that the surface of the molecule is entirely exposed with no functional groups occupied or lost through attachment to a surface, affinity tag or carrier protein. The disadvantage is that peptide-phage may not bind the molecule once in solution.

The molecule 4-acetamidophenol (molecular weight 151.17 Da) was chosen as the low molecular weight target because it is a relatively simple molecule with two structural isomers (**Figure 2.2**) 2- and 3-acetamidophenol (2-AAP; 3-AAP) that differ only in the orientation of the hydroxyl group around the benzene ring.

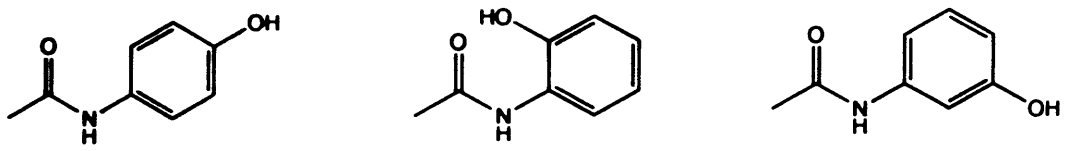

N-(4-hydroxyphenyl)acetamide
4-acetamidophenol
Paracetamol

N-(2-hydroxyphenyl)acetamide
2-acetamidophenol

N-(3-hydroxyphenyl)acetamide
3-acetamidophenol

Figure 2.2 Structure of 4-acetamidophenol and its isomers 2-acetamidophenol and 3-acetamidophenol.

As secondary objectives to panning against 4-AAP, isolating a peptide that can discriminate 4-AAP from 2-AAP and 3-AAP would serve as proof of

principle for a new panning strategy against insoluble complexes. Further, such a peptide may be of practical value since 4-AAP, the most commonly administered analgesic in the UK, accounts for more than 70,000 cases of overdose annually and 15% of all drug related poisoning deaths[35]. A peptide that binds 4-AAP may therefore find utility for diagnostic sensing or as a therapeutic antidote in its own right.

2.1.5 Objectives

In this section of the thesis a series of discrete phage display panning strategies were employed to identify cyclic peptide(s) that bind to streptavidin and to the low molecular weight organic species 4-AAP. In streptavidin panning studies, streptavidin was immobilised on both a solid plastic support and on paramagnetic beads. Functionality of identified peptides was investigated using ELISA.

In the case of 4-AAP, occupancy of one of the limited functional groups on the molecule, through attachment to a solid support, was avoided by panning against insoluble complexes of 4-AAP. To further enrich for high affinity 4-AAP binders, a deletion step to remove peptide phage that bound the isomers 2-AAP and 3-AAP was also included. The functionality of identified peptide phage particles that bind 4-AAP was examined with respect to altering the diffusion capacity of 4-AAP and with respect to attenuating the cellular toxicity of 4-AAP in an *in-vitro* hepatocyte cell model.

The chapter is divided into two sections, one for streptavidin with specific materials and methods, results and discussion and one for 4-AAP with specific materials and methods, results and discussion. A section detailing general phage methods precedes the specific sections.

2.2 Materials & Methods – Phage Display

2.2.1 Materials

Sodium chloride (NaCl); magnesium chloride ($MgCl_2$); IPTG; X-gal; nuclease free water; propan-2-ol; sodium bicarbonate ($NaHCO_3$); and ethanol were obtained from Fisher Scientific (Loughborough, UK). Tween 20 was obtained from Amersham (Little Chalfont, UK). Agarose was obtained from Bioline (London, UK). Big dye v3.1 and 5x sequencing buffer were obtained from Applied Biosystems (Warrington, UK). Luria-Bertani (LB) broth; LB agar; bovine serum albumin (BSA); Trizma (Tris-HCl); tetracycline; dimethyl formamide; sodium azide (NaN_3); glycine-HCl and PEG-8000 were obtained from Sigma-Aldrich (Dorset, UK). SuperBlock™ blocking buffer (guaranteed biotin free) was obtained from Pierce (Northumberland, UK).

2.2.2 Phage library

The Ph.D.™-C7C cyclised 7-mer disulphide constrained peptide-phage library (New England Biolabs, Hitchin, UK) was used for all panning experiments. This library represents 1.2 x 10^9 unique genotypes encoding random cyclised peptides fused to the pIII coat protein of the filamentous phage M13. The general motif of the displayed peptide is $^{N'}$AC-XXXXXXX-

$CGGGS^{C}$ where X_7 represents a unique 7-mer peptide, the two cysteine residues cyclise the peptide and GGGS is a short amino acid spacer that links the peptide to the N terminus of the phage pIII coat protein.

2.2.3 Phage display media and solutions

- **LB Medium:** 10 g Bacto-Tryptone, 5 g yeast extract, 5 g NaCl, ddH_2O to 1 L.
- **IPTG/X-gal:** 1.25 g IPTG, 1g X-gal in 25 ml dimethyl formamide.
- **LB/IPTG/Xgal Plates:** LB medium + 15 $g.L^{-1}$ agar. Autoclave, cool to ~ 60°C and add 1 ml IPTG/X-gal. Aseptically dispense into 90 mm petri dishes (12 ml per dish). Store plates at 4°C in the dark.
- **Agarose Top:** 10 g Bacto-Tryptone, 5 g yeast extract, 5 g NaCl, 1 g $MgCl_2.6H_2O$, 7 g agarose. Autoclave, dispense into 50 ml aliquots. Store solid at room temperature, melt in microwave as needed.
- **Tetracycline Stock:** 20 $mg.ml^{-1}$ in ethanol.
- **Blocking buffer:** 0.1 M $NaHCO_3$ (pH 8.6), 5 $mg.ml^{-1}$ BSA, 0.02% NaN_3.
- **TBS:** 50 mM Tris-HCl (pH 7.5), 150 mM NaCl.
- **TBS-T:** TBS + 0.1% v/v Tween or TBS + 0.5% v/v Tween.
- **Glycine elution buffer:** 0.2 M Glycine-HCl (pH 2.2), 0.1% w/v BSA.
- **PEG/NaCl:** 20% w/v polyethylene glycol–8000, 2.5 M NaCl.
- **Iodide Buffer:** 10 mM Tris-HCl (pH 8.0), 1 mM EDTA, 4 M NaI.

2.2.4 Maintenance of the bacterial host used for phage propagation

The male specific coliphage M13 readily propagates in the ER2738 (F'; Tet^R) strain of *E. coli* which is supplied by New England Biolabs with the Ph.D.™C7C library. The F plasmid within ER2738 houses a mini-transposon that confers tetracycline resistance affording the selection of *E. coli* colonies that express the F-pilus when cultured using selective medium. In all phage studies detailed in this thesis M13 were propagated within cultures inoculated from tetracycline doped LB agar plates streaked with glycerol stocks of ER2738. Plates were streaked at the beginning of the week, inverted and incubated at 37°C overnight and then stored at 4°C wrapped in parafilm; plates were discarded after 7 days.

2.2.5 Phage amplification and purification

Fourteen hours before phage propagation, a single colony of ER2738 was picked from ER2738 streak plates and deposited in 10 ml of LB broth and incubated at 37°C for 14 hrs. A 2 ml aliquot of the culture was then added to 18 ml of LB broth in a 250 ml Erlenmeyer flask and the phage to be propagated was added to this culture. The flask was sealed with aluminium foil and incubated for 4.5 hours at 37°C with gentle orbital shaking (150 rpm). The amplified culture was transferred to a 50 ml centrifuge tube and centrifuged at 7500g (15 mins; 4°C). The supernatant was collected in a fresh 50 ml centrifuge tube and re-centrifuged. The upper 90% (18 ml) of this second supernatant was aspirated and transferred to a fresh 50 ml centrifuge tube containing 3ml PEG/NaCl; this solution was incubated for 1

hr at 4°C after which a precipitate was observed. The solution was then centrifuged at 7500 g (15 mins; 4°C) and the supernatant discarded. The tube was briefly re-centrifuged (1 min) and residual supernatant aspirated. The phage pellet was suspended in 1 ml TBS and the phage re-precipitated through addition of 200 µl of PEG/NaCl (1 hour; 4°C). The precipitate was pelleted by centrifugation (14,000 g; 10 mins; 4°C) and the supernatant discarded; after a 1 min re-centrifugation, residual supernatant was discarded. Finally, the phage pellet was suspended in 200 µl of TBS containing 0.02% NaN_3 and stored at 4°C for up to 1 month after which any unused material was transferred to 50% glycerol stock and stored at -80°C for up to 2 years.

2.2.6 Phage plaque formation assay

Phages in amplified stocks and panning elutions were quantified using bacterial titration. Phages were serially diluted (1:10) in LB broth (10^8 - 10^{11} for amplified stocks; 10^1 - 10^4 for eluates) before 10 µl was transferred to 190 µl of ER2738 (OD_{600} ~ 0.5) and incubated at room temperature for 5 mins. A 3 ml aliquot of molten agarose top was dispensed into a 15ml centrifuge tube (one tube for each serial dilution) and the phage culture added. After gentle mixing, the molten agarose top was carefully poured onto pre-warmed LB-agar plate containing IPTG/X-gal; plates were inverted and incubated overnight at 37°C and then inspected for phage numbers. Library phage are derived from M13mp9 and carry the LacZα gene producing blue colonies in the presence of IPTG/X-gal, insertless

phages, used in some studies detailed in the thesis, appear as clear plaques on IPTG/X-gal plates.

2.2.7 Gene sequencing

The linkage of genotype with phenotype in phage display was exploited to identify the amino-acid sequence of the displayed peptide. Essentially, phages were amplified on a clonal basis, DNA extracted and subjected to PCR amplification followed by automated dye-labelled dideoxynucleotide sequencing to determine the DNA sequence encoding the displayed peptide.

2.2.7.1 Phage plaque amplification and DNA extraction

Using a sterile 1 ml pipette tip, individual plaques of phages were picked from phage titer plates bearing < 100 colonies. Each harvested plaque was deposited into 3ml of a culture of ER2738 (OD600 ~ 0.5); all phages within a single isolated (well separated) plaque have the same genome and hence display the same peptide. After cultures were incubated for 4.5 hours (37°C, 150 rpm orbital shaking), 1 ml of supernatant was dispensed into a microcentrifuge tube. The *E. coli* were pelleted (14,000g, 10 mins, 4°C) and the supernatant aspirated and added to a fresh microcentrifuge tube containing 200 µl of PEG/NaCl. Phages were precipitated for 10 minutes at room temperature and then pelleted by centrifugation (14,000g, 10 mins, 4°C). The supernatant was discarded and the phage pellet suspended in 100 µl iodide buffer and 250 µl of ethanol. A 10 min incubation at room

temperature precipitates phage ssDNA leaving the phage protein coat in solution. The DNA was pelleted by centrifugation (14,000 g, 10 mins, 4°C) and then briefly washed in 180 µl of 70% ethanol. Finally the DNA was suspended in 30 µl of molecular grade H_2O.

2.2.7.2 PCR

A 5 µl aliquot of DNA obtained in 2.2.7.1 was added to a PCR tube containing 0.30 µl Big Dye v3.1 (dye-labelled dideoxynucleotides), 2 µl 5x sequencing buffer, 1.6 µl primer (1 $pmol.\mu l^{-1}$; sequence $^{5'}CCCTCATAGTTAGCGTAACG^{3'}$) and 1.1 µl ddH_2O. Dye-labelled dideoxynucleotides were incorporated and amplified using a PCR cycle reaction comprising denaturation at 96°C for 30 sec, annealing at 50 °C for 15 sec, extension at 60°C for 4 mins repeated for a total of 31 cycles. Upon completion of reaction, PCR product was precipitated with 90 µl of 70% isopropanol (15 mins; room temperature) and then pelleted by centrifugation (14,000g; 4°C; 30 mins). The pellet was washed 2x with 180 µl of 70% isopropanol and then dried briefly under vacuum. The DNA pellet was sequenced on an ABI Prism 3100 Genetic Analyzer (Medical Genetics department, Cardiff University or Biosciences department, Cardiff University) and chromatograms were processed using 4Peaks (A. Griekspoor and Tom Groothuis, mekentosj.com). A BLAST search of the SWISSPROT database (http://www.ncbi.nlm.nih.gov/blast/) was performed to identify homologies between displayed peptides and known

peptide sequences. Peptide sequence alignment was performed using Clustal W using default settings (www.ebi.ac.uk/clustalw).

2.2.8 Statistical analysis

Statistical analysis was performed using Graphpad Prism (Graphpad Software; California, USA). Results were expressed as mean ± standard deviation (SD) unless otherwise stated. Statistical significance between multiple groups was assessed using a two-way ANOVA followed by a post hoc Bonferroni test. Single group differences were determined using a one-way ANOVA followed by Dunnett's post hoc. $P < 0.05$ was considered significant.

2.3 Streptavidin Panning

2.3.1 Materials & Methods

2.3.1.1 Materials

Nunc Immobilizer™- streptavidin plates (Cat No 436014) were obtained from Fisher Scientific (Loughborough, UK). Streptavidin paramagnetic particles (SA-PMPs) were obtained from Promega (Southampton, UK).

2.3.1.2 Panning studies

To validate the use of the phage library in our laboratory a series of panning studies were conducted against streptavidin. The literature has reported peptides isolated from phage display libraries that bind streptavidin[28] and a consensus motif appears to be the tripeptide motif HPQ. Two strategies were employed to select peptides:

- Strategy 1: Ph.D.™-C7C library exposed to streptavidin covalently attached to a 96 well plate.
- Strategy 2: Ph.D.™-C7C library exposed to paramagnetic beads coated in Streptavidin.

This was to determine whether selections against the same target presented in different ways yielded the same or similar peptides.

Strategy 1: Non-specific binding sites were blocked by incubating streptavidin coated wells with SuperBlock™ for 1 hour. After aspirating blocking buffer and washing 6x with TBS-T (0.5%) the streptavidin target was exposed to 2 x 10^{11} pfus of Ph.D.™-C7C. Following a 1 hr incubation at room temperature on an orbital shaker (150 rpm), non-binding phages were aspirated and discarded. The streptavidin was washed 10x with TBS-T (0.5%) to remove those phages that bind with limited affinity. Phages binding with higher affinity were eluted using 3x glycine elution buffer washes. The elutions were either pooled (i.e. all three glycine elutions combined) or only the third glycine elution was collected. In both cases the phages in the elution were amplified, purified and titered as previously described to serve as input into the next iterative panning round. A total of three panning rounds were completed for each of the two experiments after which a selection of colonies from the final panning round were gene sequenced.

Strategy 2: 10 mg of SA-PMPs were dispensed into a microcentrifuge tube and were washed 3x with 1 ml of TBS (pelleted using a neodymium rare

earth magnet between washes). The SA-PMPs were then suspended in 100 µl of TBS containing 2 x 10^{11} pfus of PhDC7C™ library. After a 1 hr incubation (room temperature: 18 – 24°C; gentle rocking: 50 rpm) the SA-PMPs were pelleted using a rare earth magnet and the supernatant aspirated and discarded. The SA-PMPs were washed 10x with TBS-T (0.5%) before being exposed to 3x 5 minute glycine elutions (200 µL) during which the SA-PMPs were sonicated. The glycine elutions were neutralized, pooled and amplified to serve as input into the next iterative panning round. A total of three panning rounds were completed after which a selection of colonies were randomly selected from the third glycine elution from round three and gene sequenced.

2.3.1.3 ELISA analysis of a streptavidin binding phage clone

A phage based ELISA was developed to quantitatively assess the interaction of a streptavidin binding phage clone with a streptavidin coated surface. A 100 µl aliquot of TBS containing 1 x 10^{10} pfus of either streptavidin binding phages or insertless phages was added to streptavidin coated wells of a 96 well microtiter plate; some wells had been exposed to a 10- or 100- fold excess of biotin for 15 minutes prior to addition of phages. After 1 hr the supernatant was aspirated and the wells washed 6x with TBS-T (0.5%). To each well was added 200 µl of a 1:5000 dilution of HRP-anti-M13 mAb in TBS-T (0.5%). After 1 hour, the wells were washed 3x with ddH_2O and then exposed to 100µl of HRP substrate (o-phenylenediamine (OPD) in TBS).

After 15 minutes the OPD was quenched with 50 µl of 2.5 M H_2SO_4 and the optical absorbance at 492 nm recorded.

2.3.2 Results

2.3.2.1 Analysis of phage recovery and peptide sequences in streptavidin phage studies

Streptavidin was immobilised on two different supports for panning experiments, a plastic 96 well microtiter plate (Strategy 1) and on paramagnetic particles (Strategy 2). **Figure 2.3** shows the recovery of library phages from strategies 1 and 2 respectively. In both strategies a significant enrichment for binding phages was observed with progressive rounds of panning. In contrast, in strategy 1, in studies where library phages were substituted for insertless phages, the number of insertless phages recovered did not increase in progressive rounds. In strategy 1, two experiments were undertaken where either the three glycine elutions were pooled and amplified for input in the subsequent panning round, or glycine elution 3 alone was amplified to serve as input in the subsequent panning round. The results indicate that recovery is marginally greater when amplifying glycine elution 3 (round 3) alone but the number of phages recovered in each experiment is within the same order of magnitude and therefore the difference has limited practical significance.

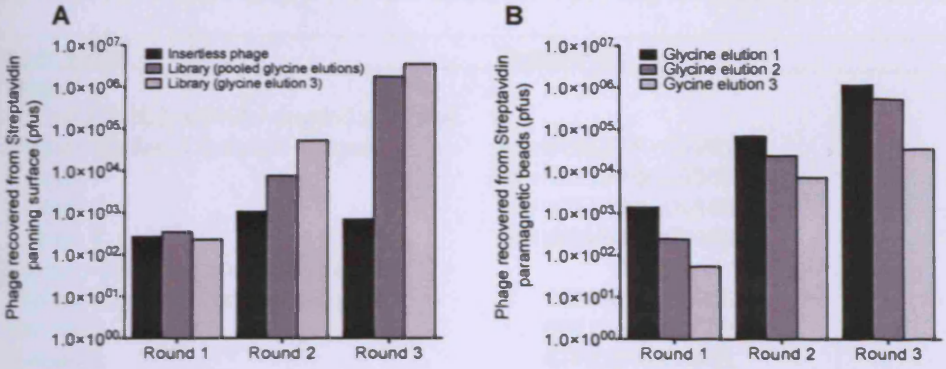

Figure 2.3 Phage recovered in glycine elutions from streptavidin coated plastic support (A) or from SA-PMPs (B). Increasing recovery of library peptide phage but not insertless phages is observed with progressive panning rounds in (A) indicating enrichment of streptavidin binding species in the library population.

The HPQ motif previously reported as a high affinity binder to strepatavidin was identified in all panning studies and the majority (87%) of the colonies sequenced (see **Table 2.2**). Of note, there was significant commonality between sequences identified in strategies 1 and 2 with all clones displaying the generic peptide motif AC-G$X_1X_2X_3$HPX_4-CGGGS where X_1 = T/S/W, X_2 = H/F/Y/W, X_3 = L/I/W/F AND X_4 = Q/M/L.

Table 2.2 Sequences of displayed peptides identified in panning studies against streptavidin.

Sample name	Sequence
Strategy1	
SA coated plastic support – pooled elutions	
Glycine elution 3 (pooled sample)	AC-GTHLHPP-CGGGS
Colony 1	AC-GTFIHPQ-CGGGS
Colony 2	AC-GTFIHPQ-CGGGS
Colony 3	AC-GSYWHPQ-CGGGS
SA coated plastic support – elution 3	
Glycine elution 3 (pooled sample)	AC-GTFIHPL-CGGGS
Colony 1	AC-GTFIHPQ-CGGGS
Colony 2	AC-GTFIHPM-CGGGS
Colony 3	AC-GSYWHPM-CGGGS
Strategy 2	
SA-PMPs	
Colony 1	AC-GSYWHPQ-CGGGS
Colony 2	AC-GSYWHPQ-CGGGS
Colony 3	AC-GTYFHPQ-CGGGS
Colony 4	AC-GSYWHPQ-CGGGS
Colony 5	AC-GSYWHPQ-CGGGS
Colony 6	AC-GNWIHPQ-CGGGS
Colony 7	AC-GSYWHPQ-CGGGS
Colony 8	AC-GSYWHPQ-CGGGS

2.3.2.2 ELISA analysis of a streptavidin binding peptide phage

Confirmation of the binding of peptide phage to strepatavidin was undertaken using ELISA. Phages displaying peptide AC-**GSYWHPQ**-CGGGS, identified in both strategies 1 and 2, or insertless phages were exposed to a strepatvidin coated plate in the presence or absence of biotin. **Figure 2.4** shows that the binding of AC-**GSYWHPQ**-CGGGS phages to streptavidin is significantly greater than insertless phages (~ 85 fold greater) and that this binding can be prevented by blocking streptavidin sites with excess biotin. In contrast biotin does not affect the binding of insertless phages to streptavidin.

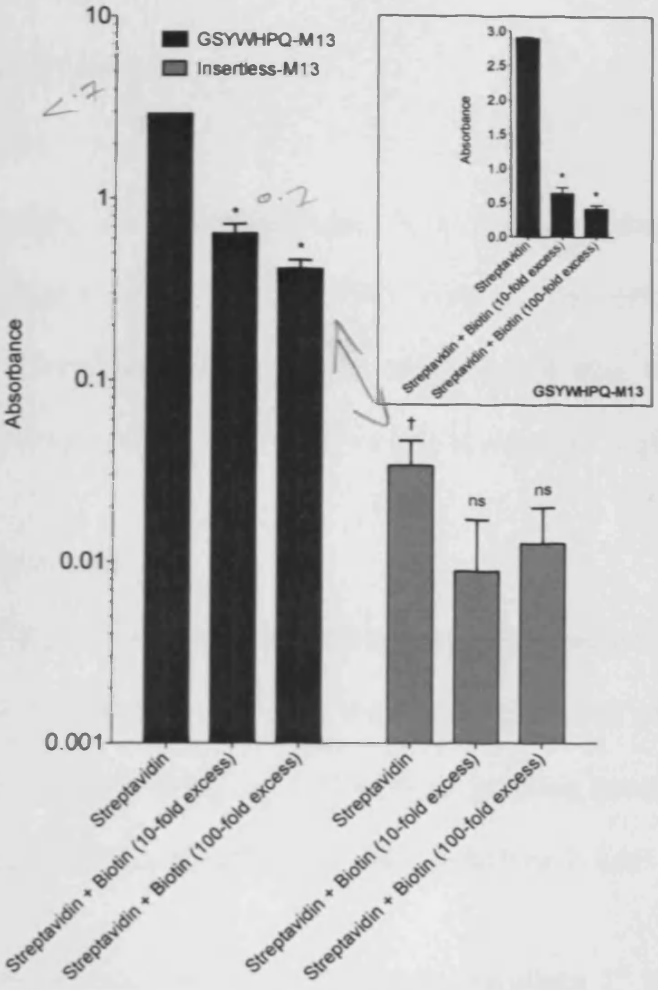

*Figure 2.4 ELISA confirmation of the binding of a phage clone displaying peptide sequence AC-**GSYWHPQ**-CGGGS to streptavidin. For the same phage input, the absorbance produced with AC-**GSYWHPQ**-CGGGS virions (a direct measure of the number of phage binding) is ~ 85 fold greater than insertless phage. Blocking AC-**GSYWHPQ**-CGGGS binding sites with biotin, either in 10- or 100- fold excess, significantly reduces the level of Pep-strep-1 binding by 4.5- and 7.1- fold respectively; in contrast biotin had no effect on the binding of insertlesss phages to streptavidin. Inset: data for AC-**GSYWHPQ**-CGGGS presented on a linear scale highlights the reduction in binding when binding sites on streptavidin are blocked with biotin. Data are mean ± SD (n=3). * represents a statistically significant difference(P < 0.05) compared to streptavidin alone; † represents a statistically significant difference (P < 0.05) between insertless phage and AC-**GSYWHPQ**-CGGGS binding to streptavidin alone; ns represents no statistically significant difference (P > 0.05) compared to streptavidin alone.*

2.4 4-AAP Panning

2.4.1 Materials & Methods

2.4.1.1 Materials

4-acetamidophenol; 2-acetamidophenol and 3-acetamidophenol were obtained from Sigma-Aldrich (Dorset, UK). Acetonitrile (HPLC grade) and Nucleopore track-etched polycarbonate filters (pore size 0.1μm; 13mm diameter) were obtained from Fisher Scientific (Loughborough, UK).

2.4.1.2 Panning studies

The Ph.D.™-C7C library was used for all panning experiments against 4-AAP and its structural isomers 2-AAP and 3-AAP. A schematic of the panning experiments can be seen in **Figure 2.5**, with all panning conducted against suspensions of insoluble complexes of 4-AAP, 3-AAP or 2-AAP.

The panning was divided into: (i) "Isolation strategy 1" involving four rounds of panning against 4-AAP (rounds 1-4): undertaken with the objective of isolating a pool of peptide phage library members that bind with high affinity to 4-AAP. (ii) (rounds 5-6) "Isolation strategy 2" involving an additional two rounds of panning: undertaken to delete from the 4-AAP binding pool those phage also binding to the structural isomers 2-AAP and 3-AAP. The initial input to round 5 comprised phages from the final (3rd) glycine elution step of panning round 4 from "Isolation strategy 1". At the end of each round in "Isolation strategy 2" a further panning against 4-AAP as target was undertaken to augment the 4-AAP selection.

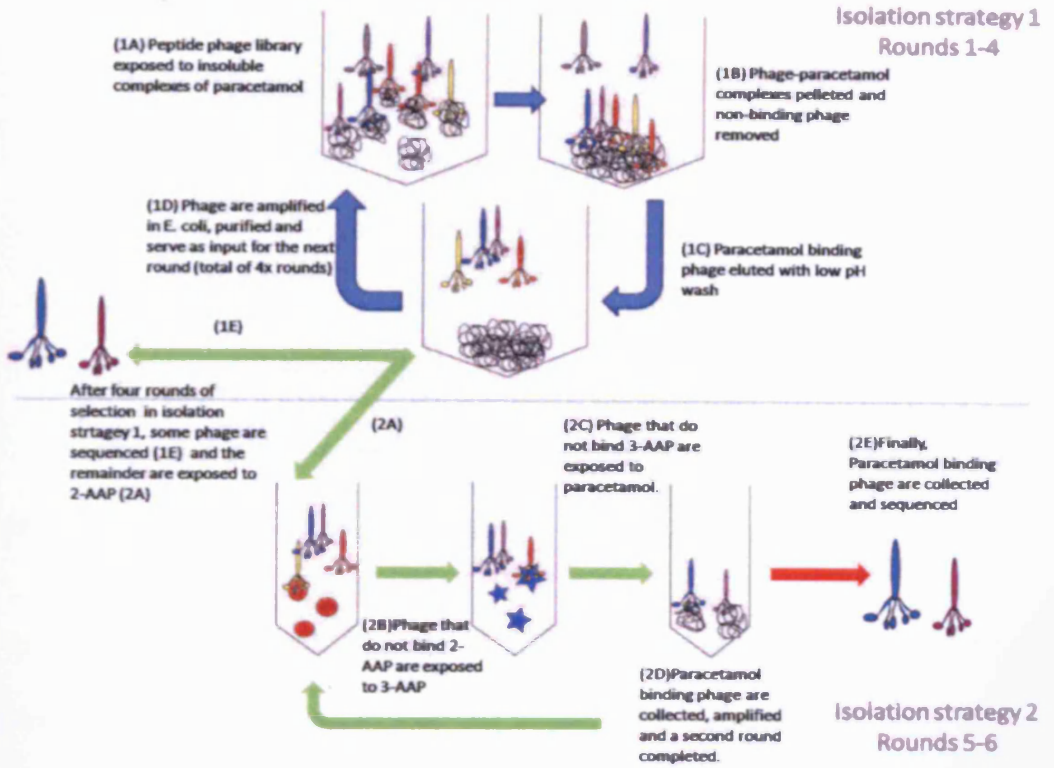

Figure 2.5 Schematic of phage panning experiments. In "Isolation strategy 1" the aim was to isolate a pool of clones enriched with peptide phage that bind 4-AAP. The Ph.D.™-C7C library was exposed to insoluble complexes of 4-AAP. The third glycine elution was collected and the phage amplified in E. coli and a further 3 rounds of panning completed (4 rounds in total). Some peptide phages collected in Round 4 were sequenced. The remainder were used as input for "Isolation strategy 2". In "Isolation strategy 2" peptide phages that bound the isomers 2-AAP and 3-AAP were deleted from the 4-AAP binding pool by two additional rounds of exposure to insoluble complexes of 2-AAP and 3-AAP. Peptide-phage that did not bind 2-AAP or 3-AAP were collected and then exposed to 4-AAP to augment the 4-AAP binding population (Rounds 5-6).

For "Isolation strategy 1" 4-AAP was suspended at 500 mg.ml^{-1} in 4 ml TBS and incubated for 1 hr at 37°C with 2 x 10^{11} plaque forming units (pfu) of the Ph.D.™-C7C phage library. After incubation the 4-AAP was pelleted by centrifugation (10,500g; 10 mins) and the non-binding phages in the supernatant discarded. The 4-AAP pellet was then washed 6x with TBS-T (0.5%) with the 4-AAP pelleted and supernatant discarded between each

wash. The 4-AAP binding phages were then eluted with 3x 5 min 200 µl glycine buffer elutions with the 4-AAP pelleted between each elution. The third glycine elution, containing the highest affinity binders, was collected, amplified and purified serving as input for the next iterative round of panning. After four such rounds of panning within "Isolation strategy 1" an aliquot of the 4th round binders (3rd glycine elution) were gene sequenced. The remainder of the phage (3rd glycine elution) was amplified and served as the input into "Isolation strategy 2".

In "Isolation strategy 2" a total of 2 x 10^{11} pfus of phage from round 4 were exposed to a suspension of 2-AAP (500 $mg.ml^{-1}$; total volume 4ml) for 1 hr at 37°C after which the isomer was pelleted and the supernatant, containing 2-AAP non-binding peptide-phage, transferred to a suspension of 3-AAP (500 $mg.ml^{-1}$; total volume 4ml) for 1 hr at 37°C. The 3-AAP was subsequently pelleted and the supernatant, now containing phages that do not bind either 2-AAP or 3-AAP, were transferred to a suspension of 4-AAP (500 $mg.ml^{-1}$; total volume 4ml) for 1 hr at 37°C. Following this, the 4-AAP was pelleted, the pellet washed 6x with TBS-T (0.5%) and 3x low pH glycine elutions completed with the third glycine elution collected and amplified. A second panning round against 2-AAP, 3-AAP and 4-AAP was repeated before gene sequencing to identify 4-AAP binding peptide sequences.

2.4.1.3 4-AAP permeability studies

The effect of a peptide phage isolated in the panning procedure upon the diffusion of 4-AAP across a semi-permeable membrane was examined; this was used as one functional endpoint to assess peptide phage binding to 4-AAP. Permeability studies were conducted in 1 ml Franz cell diffusion apparatus with the donor and receiver chambers separated by a semi-permeable membrane (Nucleopore track-etched polycarbonate filters, 100 nm pore size). Phages were found to be incapable of penetrating this membrane to any great extent - after 4 hrs less than 1×10^{-6} % of the phage pfu loaded in the donor chamber (1×10^{11} pfus) was able to penetrate to the receiver chamber.

The study was initiated by adding 200 µl of a 4-AAP solution (100 µM in TBS) into a Franz cell donor chamber either alone or with a binding peptide phage PARA-061 that had been isolated in the 4-AAP phage panning procedure (strategy 1 and 2); 4-AAP was pre-exposed to phages for 30 mins prior to loading. As a control, the effect upon 4-AAP diffusion of a non-binding peptide phage clone, NB-062 (AC-**HKSSPHQ**-CGGGS; from panning washings) was examined. The phage virions were incubated in a 1:1 stoichiometric ratio with 4-AAP molecules. Since each phage can display up to five copies of the peptide, this equates to a maximum of 5 peptide copies per 4-AAP molecule. At predetermined time points following the start of the permeability experiment 200 µl samples of the receiver chamber were collected and 4-AAP quantified by HPLC-UV. Receiver chamber sample

volume was replenished with an equal volume of TBS. The cumulative membrane transport of 4-AAP as a function of time was determined and the apparent permeability coefficients (ρ) calculated using equation 2.1.

$$\frac{dM}{dt} = \rho \times A \times Co \qquad \textbf{Equation 2.1}$$

Where *dM/dt* represents the rate of change in cumulative mass of 4-AAP transferred from donor – receiver, *A* represents the area of the Nucleopore membrane (0.95 cm^2) and *Co* is the original concentration of 4-AAP in the donor chamber (100 μM).

2.4.1.4 HPLC quantification of 4-AAP

To determine 4-AAP and 3-AAP concentrations, HPLC-UV was undertaken using a HP1050 HPLC system with a Varian Pursuit XRs analytical (5μm) C18 (150 mm x 4.6 mm) column. Elution was performed with a mobile phase of 50:50 acetonitrile:H_2O at a flow rate of 1ml.min^{-1}; the injection volume was 50 μl. The concentration of compounds was determined by UV detection (wavelength 550nm) against linear ($r^2 > 0.99$) calibration curves. The limit of detection for each compound was ~ 2 μM. Calibration standards in the range 2-100 μM were prepared for each compound and run on each day of analysis. The relative standard deviation for within day and between day precision was less than 10%. The accuracy was determined by subtracting the measured concentration from its nominal value; the mean relative error (M.R.E.) of the difference from theoretical was less than 10%.

2.4.1.5 *In-vitro* hepatotoxicity assays

As a second assessment of the functionality of the selected 4-AAP binding peptide phage clone PARA-061, an examination was made of the *in-vitro* modulation of 4-AAP induced hepatotoxicity. Preliminary *in-vitro* toxicity studies were undertaken to determine the most efficient method of monitoring 4-AAP toxicity and its attenuation in the hepatocarcinoma cell line Hep3B. Appendix 1 details the growth characterisation of the Hep3B cell line and investigations into the time and concentration dependent hepatotoxicity of 4-AAP and its attenuation with the sulphydryl group donor N-acetylcysteine (NAC) within Hep3B cells. These studies included micrographic monitoring of confluent monolayers of Hep3B, MTT (3-(4,5-dimethyethiazol-2-yl)-2,5-diphenyltetrazolium bromide) assessment of mitochondrial dehydrogenase activity, measurement of lactate dehydrogenase (LDH) leakage from the cell and determination of intracellular levels of reactive oxygen species. All measures of toxicity showed 4-AAP to be hepatotoxic in a time and concentration dependent manner.

MTT, a colorimetric assay widely used to assess cell viability and proliferation, distinguishes viable cells from non-viable through the reduced activity of mitochondria in non-viable cells. Mitochondrial activity is monitored through the reduction of the water-soluble yellow tetrazolium salt MTT to an insoluble blue formazan salt. The method used was based on

that first detailed by Mosmann *et al* [36] and later by Plumb et al[37] but with modifications.

Hep3B cells were seeded in a 96 well plate at a density of $3x10^4$ cells.cm^{-2} until 80% confluent. The cells were exposed to varying concentrations of 4-AAP (5, 20 or 40 mM) or 3-AAP (1, 5, 10, 20 or 50 mM) ± the sulphydryl group donor N-acteylcysteine (NAC; 10 mM) for 5, 24 or 48 hours. At the indicated time intervals, media was aspirated from each well and replaced with 200 µl of fresh media. A 50 µl aliquot of MTT stock (2 $mg.ml^{-1}$ MTT in culture medium) was immediately added to each well. The plate was wrapped in aluminium foil and incubated for 4 hours at 37°C. The media was then aspirated and 200 µl of DMSO added to each well to permeabilise the cell membrane and release the intracellular formazan dye. Immediate addition of 25 µl of Sorensen's glycine buffer (0.1M glycine; 0.1M NaCl; pH 10.5) fully solubilised the formazan dye. The absorbance was immediately measured spectrophotometrically at 570 nm using an Anthos htll microtiter reader. Background absorbance of DMSO controls was subtracted from sample absorbance. Cells exposed to culture medium alone were used as reference for 100% viability and to which all experimental variables were compared.

MTT was used to assess the phage modulation of *in-vitro* hepatotoxicity and was chosen over other measurements of hepatotoxicity (LDH leakage, generation of reactive oxygen species and intracellular levels of

glutathione) because the culture format in the MTT study means that phages can be incubated in a physiologically relevant stoichiometric ratio with 4-AAP. MTT assays were undertaken following a five hour incubation of Hep3B cells with 40 mM 4-AAP in the presence or absence of the 4-AAP binding peptide phage clone PARA-061, the non-binding peptide phage clone NB-062 or NAC (10 mM). The phage virions were incubated in a 1:100 stoichiometric ratio with 4-AAP molecules i.e. 1 peptide for every 20 4-AAP molecules; the phage numbers used reflects the maximum phage pfus that can be obtained with amplification.

2.4.2 Results

2.4.2.1 Analysis of phage recovery and peptide sequences in 4-AAP studies

The details of the panning scheme to select peptide phages that bind 4-AAP are outlined in **Figure 2.5**. The strategy enabled the selection of peptides that specifically bound 4-AAP but not its isomers 2-AAP and 3-AAP. Prior to panning studies, the solubility of 4-AAP and its isomers in the TBS panning buffer was determined using HPLC-UV, the results of which confirmed that 500 mg of the respective isomer in 4ml TBS resulted in adequate formation of insoluble complexes (data not shown).

Analysis of phage titer in "Isolation strategy 1" rounds 1-3 showed that the percentage of phage input recovered in the 3rd glycine elution progressively decreased (**Figure 2.6**). However, at panning round 4 the phage recovered in the 3rd glycine elution showed a small relative increase of 20% compared

to glycine wash 3 in round 3 (5000 pfus recovered cf 4000 pfus) suggesting enrichment of a 4-AAP binding population. A sequential isolation strategy was then adopted ("Isolation strategy 2") to augment selection of 4-AAP binding phage through the deletion of peptide-phage clones that also bound the isomers 2-AAP and 3-AAP. In the initial round of panning in "Isolation strategy 2" (round 5 of the overall scheme) with an input of $1x10^{11}$ pfus from round 4 only 100 phage clones were recovered in the third glycine elution. This dramatic reduction in recovery in round 5 is not unexpected since the isomers only differ in the orientation of the hydroxyl and amide groups on the benzene ring and one would not anticipate many peptide sequences could distinguish this orientation. However, with an input of $1x10^{11}$ pfus into round 6, an enrichment in the population of 4-AAP specific binders was evidenced by a 10-fold increase in recovered peptide-phage clones in glycine elution 3 (**Figure 2.6**).

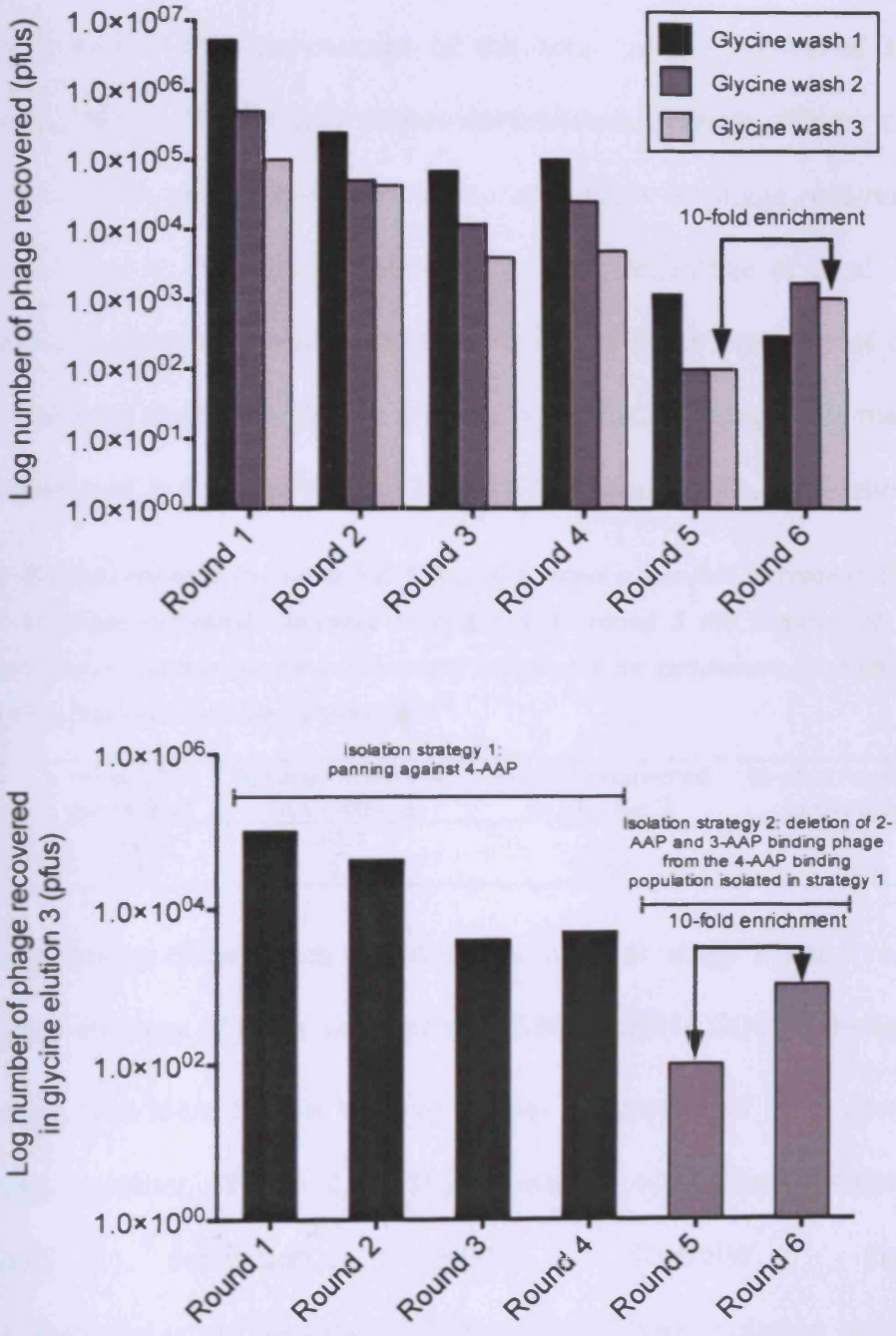

Figure 2.6 Phage recovered in panning isolations. (A) Phage recovered in glycine elutions 1-3 reduces for rounds 1-3 and then increases in round 4 indicating enrichment of 4-AAP binding phage. Deletion of 2-AAP and 3-AAP binding phage in round 5 dramatically reduces phage recovery. In round 6 enrichment of a 4-AAP binding population is evidenced by increased recovery in glycine elutions 2 and 3. (B) Phage recovered in glycine elution 3 in all panning rounds. These elutions were amplified to serve as input in the subsequent panning round.

Expressing the number of phage recovered in each glycine elution in rounds 5 and 6 as a percentage of the total clones recovered in the respective round (**Table 2.3**) shows enrichment for high affinity clones, since in addition to an increase in the total number of phage recovered in round 6, there is a significant increase in the percentage of total clones recovered in glycine elutions 2 & 3 i.e. in round 5 the majority of clones were recovered in glycine elution 1 (~ 86%) whilst in round 6 the majority were recovered in glycine elutions 2 & 3 (~ 56% and 33.9% respectively).

***Table 2.3** Phages recovered in rounds 5 & 6. Round 6 shows a two-fold increase in the total number of phage recovered compared to round 5. In round 5 the majority of phages recovered were in glycine elution 1. Conversely in round 6 an enrichment for high affinity binders was observed in glycine elutions 2 & 3.*

	Total pfus recovered	% pfus recovered in Glycine 1	% pfus recovered in Glycine 2	% pfus recovered in Glycine 3
Round 5	1400	85.7	7.1	7.1
Round 6	3100	9.7	56.45	33.9

After sequencing clones from round 4 ("Isolation strategy 1") and round 6 ("Isolation strategy 2"), the sequence $^{N'}$AC-**NPNNLSH**-CGGGS$^{C'}$, designated PARA-061, was identified in both strategies suggestive of its presence in high copy number (**Table 2.4**). This sequence was taken forward for functional evaluation. Whilst ClustalW analysis (http://www.ebi.ac.uk/clustalw/) of clones from both isolation strategies did not highlight any common motifs, analysis of their primary amino acid sequences (**Table 2.5**) revealed the peptides to largely comprise hydrophilic amino acid residues (47%) with asparagine, threonine, serine and glutamine the most frequent.

Table 2.4 Amino acid sequences of 4-AAP binding peptide-phage clones analysed on completion of Isolation strategies 1 and 2.

Peptide sequences of phage clones binding to 4-AAP with unknown isomer binding status	**Peptide sequences of phage clones binding to 4-AAP with 2-AAP and 3-AAP isomer binding phage clones deleted**
Isolation strategy 1, round 4 (Sample of five peptide phages randomly selected from phage plaques)	**Isolation strategy 2, round 6** (Sample of twenty-one peptide phages randomly selected from phage plaques)
AC-NPNNLSH-CGGGS *(PARA-061)*	AC-NPNNLSH-CGGGS *(PARA-061)*
AC-KNFTHTD-CGGGS	AC-RAPSQTV-CGGGS
AC-TTASGAR-CGGGS	AC-DGNSRTQ-CGGGS
AC-TDLLPRH-CGGGS	AC-TTLTKTF-CGGGS
AC-PTAPLHM-CGGGS	AC-TLRSATA-CGGGS
	AC-SHLHSPL-CGGGS
	AC-ENTQKNS-CGGGS
	AC-SQGRLGQ-CGGGS
	AC-DRNGSNA-CGGGS
	AC-SQHSSRS-CGGGS
	AC-LNSHLQT-CGGGS
	AC-RTTSDAL-CGGGS
	AC-TSDWRLH-CGGGS
	AC-WNQGMRA-CGGGS
	AC-KQQMEPA-CGGGS
	AC-VLHKGFQ-CGGGS
	AC-SPWQHKN-CGGGS
	AC-THSLTIQ-CGGGS
	AC-ADKQTTL-CGGGS
	AC-MHGDSAV-CGGGS
	AC-NQPNIRH-CGGGS

Detailed analysis of the physicochemical properties of the round 6 peptides (**Table 2.5**) shows they can essentially be separated into two distinct groups – those with a pI between 6.7 and 8 (~ 48%) and those with a pI of either 10.1 or 11 (~ 43%) indicating that the panning strategy employed has led to the isolation of peptides with a bimodal pattern of physicochemical properties.

Table 2.5 Physicochemical properties of 4-AAP binding phage clones sequenced from round 6. All the peptides sequenced are essentially hydrophilic and with the exception of peptide sequence MHGDSAV, the sequences fall into two distinct physicochemical groupings, those with isoelectric point (pI) of 6.7 – 8 and those with isoelectric points of 10.1 -11.

Sequence	Net Charge at pH7.0	pI	Average hydrophilicity	Percentage hydrophilic residues
AC-MHGDSAV-CGGS	-0.9	4.9	-0.1	29%
AC-ADKQTTL-CGGS	0	6.7	0.4	43%
AC-DGNSRTQ-CGGS	0	6.8	0.9	71%
AC-DRNGSNA-CGGS	0	6.8	0.9	71%
AC-RTTSDAL-CGGS	0	6.8	0.5	43%
AC-ENTQKNS-CGGS	0	6.9	0.9	86%
AC-KQQMEPA-CGGS	0	6.9	0.7	57%
AC-TSDMRLH-CGGS	0.1	7.8	0	43%
AC-NPNNLSH-CGGS	0.1	7.8	-0.2	57%
AC-LNSHLQT-CGGS	0.1	7.8	-0.5	43%
AC-THSLTIQ-CGGS	0.1	7.8	-0.6	29%
AC-SHLHSPL-CGGS	0.2	8	-0.6	29%
AC-TTLTKTF-CGGS	1	10.1	-0.4	14%
AC-VLHKGFQ-CGGS	1.1	10.1	-0.4	29%
AC-SPWQHKN-CGGS	1.1	10.1	0	57%
AC-RAPSQTV-CGGS	1	11	0.2	14%
AC-TLRSATA-CGGS	1	11	0	29%
AC-SQGRLGQ-CGGS	1	11	0.3	57%
AC-SQHSSRS-CGGS	1.1	11	0.6	86%
AC-HNQGMRA-CGGS	1	11	-0.3	43%
AC-NQPNIRH-CGGS	1.1	11	0.2	57%
MEAN	**0.43**	**8.63**	**0.12**	**47%**

A search of the SWISSPROT database with the BLAST search engine to identify short nearly exact matches to known proteins and peptides did not reveal any homologies of note. This is probably to be expected since a literature search did not reveal any natural peptide or protein motifs known to bind 4-AAP.

2.4.2.2 4-AAP permeability studies

To assess the capacity of the phage peptide clone PARA-061 to bind 4-AAP, the permeability of 4-AAP across an inert semi-permeable membrane (0.1 µm pore diameter) was determined following pre-incubation of the 4-AAP

with the PARA-061 clone. The 4-AAP in solution was pre-exposed to PARA-061 (stoichiometric ratio of one phage particle per 4-AAP molecule) for 30 mins after which the PARA-061/4-AAP solution was loaded into the donor chambers of Franz cell diffusion apparatus. The permeability of 4-AAP under these conditions was compared to the permeability of an equimolar dose of 4-AAP alone, and the permeability of an equimolar dose of 4-AAP pre-exposed to, and co-loaded with, phage clone NB-062. The diffusion of 4-AAP was not rate-limited by the Nucleopore membrane (0.1 μm pore size) as evidenced by a similar 4-AAP permeability across Nucleopore membranes with a 3 μm pore diameter (data not shown). **Figure 2.7** shows that the control phage NB-062 had no effect ($p > 0.05$) on 4-AAP permeability with 4-AAP permeability co-efficients of 77.05 ± 4.49 and 76.87 ± 4.56 $x10^{-6}$ $cm.s^{-1}$ when incubated respectively with and without NB-062. However, when 4-AAP was exposed to the 4-AAP peptide-phage clone PARA-061, the permeability coefficient was significantly reduced ($p < 0.05$) to 59.54 ± 3.38 $x10^{-6}$ $cm.s^{-1}$ representing an approximate 20% reduction compared to both 4-AAP alone and to 4-AAP exposed to NB-062.

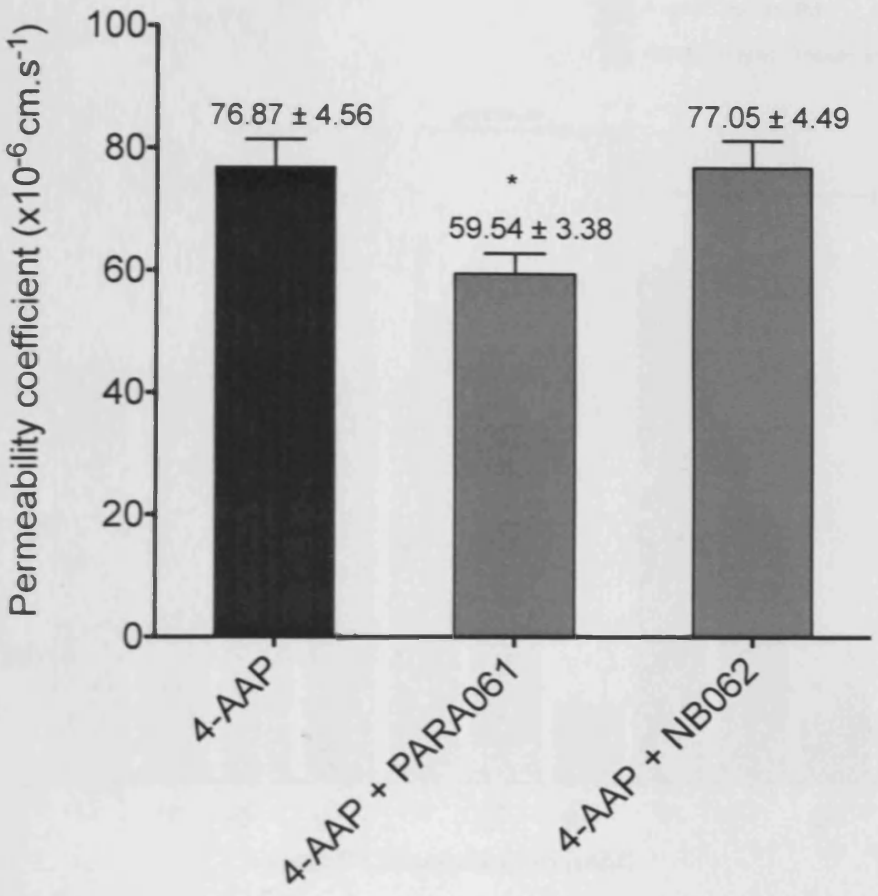

*Figure 2.7 Permeability of 4-AAP through a nucleopore membrane (100nm pore size) placed between the donor and receiver chambers of a Franz cell. Permeability experiments showed that PARA-061, but not peptide-phage clone NB-062, significantly ($p < 0.05$) reduced 4-AAP permeability. * Signifies statistically significant difference ($p < 0.05$) compared to any of the other treatments. DATA are mean ± SEM for three separate experiments. ($n = 8$ for each experiment).*

2.4.2.3 *In-vitro* hepatotoxicity assays

Figure 2.8 highlights the time and concentration dependent toxicity of 4-AAP on Hep3B cells as determined by MTT assay.

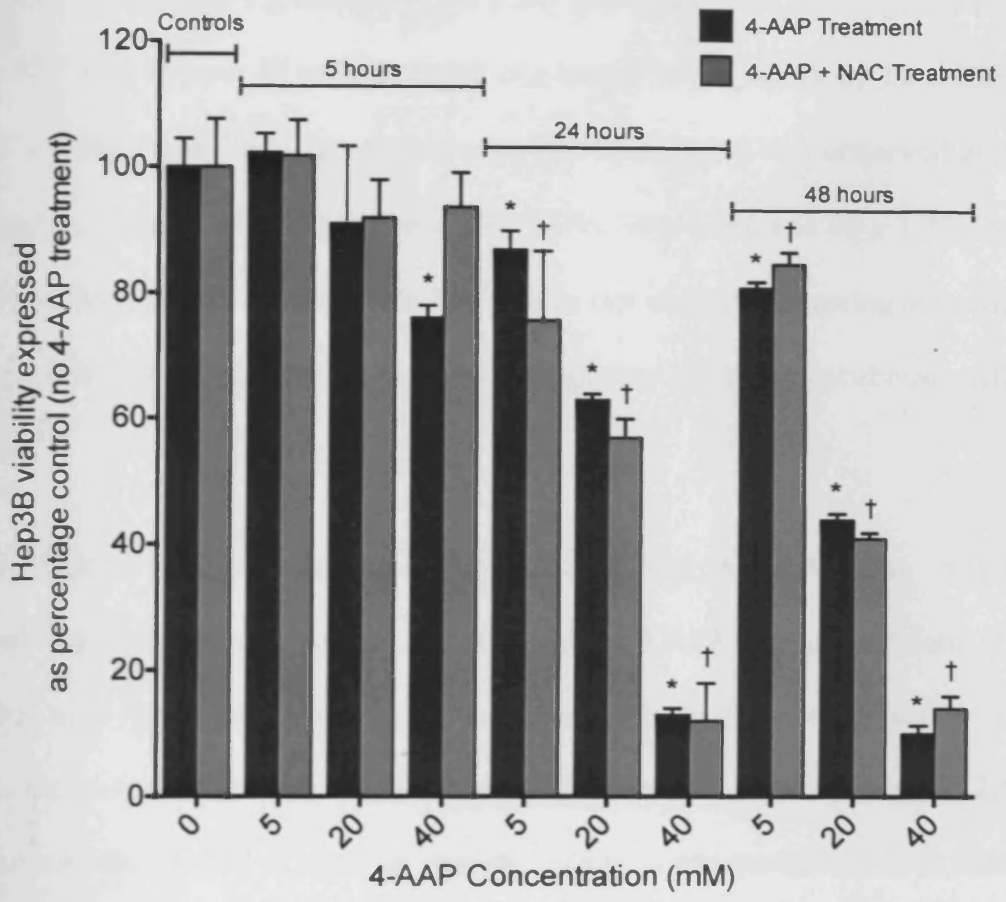

*Figure 2.8 Mitochondrial dehydrogenase activity of Hep3B cells exposed to 4-AAP. Results expressed as percentage of controls where controls are either no treatment or cells exposed to NAC (10 mM) alone. Hep3B cells exposed to 4-AAP showed a time and concentration dependent toxicity. A 5 hr exposure to 40 mM 4-AAP led to a significant ($p < 0.05$) 24% reduction in cell viability that was prevented by co-incubation with NAC. DATA are mean ± SD (n=4). * Signifies statistically significant difference ($p < 0.05$) compared to no treatment cells. † Signifies statistically significant difference ($p < 0.05$) compared to cells exposed to NAC alone.*

After five hours exposure to a 40 mM concentration of 4-AAP, a significant ($p < 0.05$) 24 ± 2.1% reduction in cell viability was observed. The loss in viability could be prevented by co-incubation with 10 mM NAC. Exposure to lower concentrations of 4-AAP (5 and 20 mM) for 5 hours did not cause any significant ($p > 0.05$) loss in cell viability. In cells exposed to 4-AAP for 24

hours cell viability significantly ($p < 0.05$) decreased with concentrations of 4-AAP at 5, 20 and 40 mM resulting in a loss of cell viability by 13 ± 3.0%, 27 ± 1.0% and 87 ± 1.1% respectively. The same trend was observed at 48 hours exposure with respectively, 19 ± 1.0%, 56 ± 1.0% and 90 ± 1.3% loss in viability compared to control. The loss in cell viability following exposure to 4-AAP for 24 and 48 hrs could not be prevented by co-incubation with NAC.

In order to analyse whether PARA-061 is specific for 4-AAP, an *in-vitro* functional assessment of its interaction with 3-AAP was undertaken and this was achieved through measurement of Hep3B cell viability on exposure to 3-AAP with the MTT assay. Preliminary studies (**Figure 2.9**) showed that 3-AAP is toxic to Hep3B cells in a concentration- and time-dependent manner. However, co-incubating hepatocytes exposed to 3-AAP with NAC for 5 hours abrogated toxicity at all 3-AAP concentrations investigated. After 24 hour exposure, 3-AAP induced toxicity was greater than toxicity at 5 hours and could not be prevented by co-incubation with NAC at any concentration investigated.

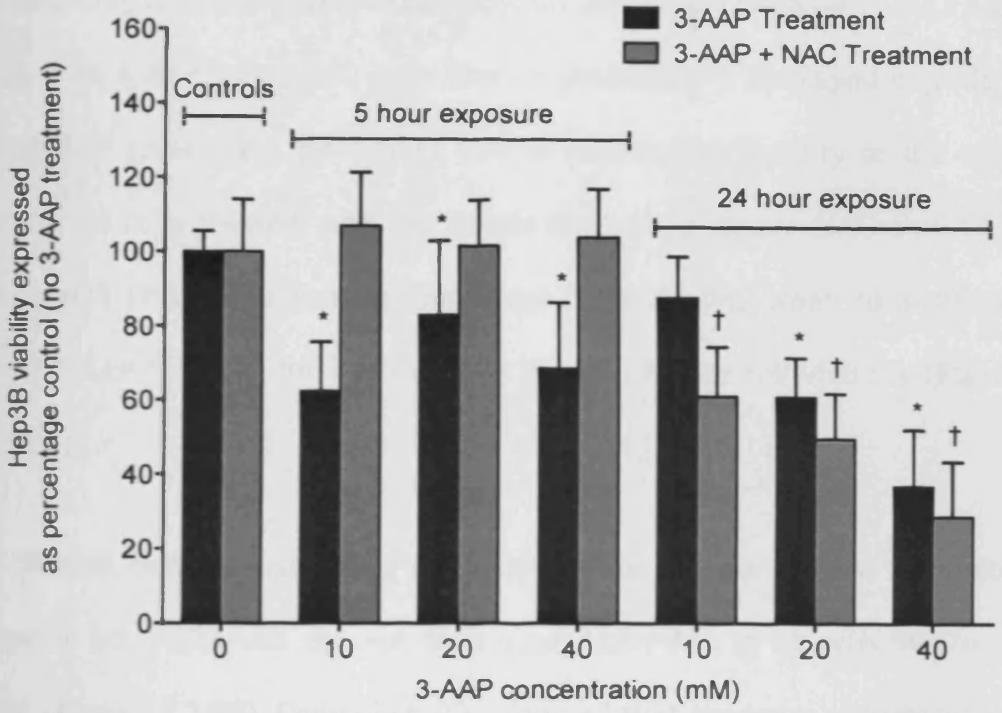

Figure 2.9 Mitochondrial dehydrogenase activity in Hep3B cells exposed to 3-AAP with results expressed as mean absorbance at 570 nm as percentage control where control is either no treatment or exposure to NAC (10 mM) *alone. 3-AAP is toxic to Hep3B cells in a time and concentration dependent manner. A 5 hr exposure to 10, 20 or 40 mM 3-AAP led to a significant ($p < 0.05$) reduction in cell viability that was prevented by co-incubation with NAC. Exposures for 24 hours also resulted in loss in cell viability but this loss could not be prevented by co-incubation with NAC. DATA are mean ± SD (n=4). * Signifies statistically significant difference ($p < 0.05$) compared to no treatment cells. † Signifies statistically significant difference ($p < 0.05$) compared to cells exposed to NAC alone.*

2.4.2.4 Phage modulation of *in-vitro* hepatotoxicity

The functionality of the 4-AAP peptide-phage binding clone PARA-061 was assessed by examining its *in-vitro* effectiveness in preventing hepatocyte toxicity following exposure of Hep3B to toxic concentrations of 4-AAP. The MTT study results detailed above indicated exposure to 40 mM 4-AAP for 5 hours was optimal to test the effectiveness of the PARA-061 clone in

minimising loss of hepatocyte viability. Co-incubation of phage clone PARA-061 with 4-AAP, in a 1:100 ratio (that is potentially 1 displayed peptide to 20 4-AAP molecules), prevented loss in hepatocyte viability to the same extent as cells treated with the sulphydryl group donor NAC and 4AAP (**Figure 2.10A**). The non-binding phage clone NB-062 when co-incubated with 4-AAP (40 mM) for 5 hrs did not prevent loss in cell viability (**Figure 2.10A**).

In Hep3B cells exposed to 3-AAP (40mM for 5 hours), NAC abrogated toxicity but PARA-061 did not indicating PARA-061 to be selective for 4-AAP (**Figure 2.10B**). Control studies showed that exposure of hepatocytes to $1x10^{11}$ phages did not result in toxicity (**Figure 2.10C**).

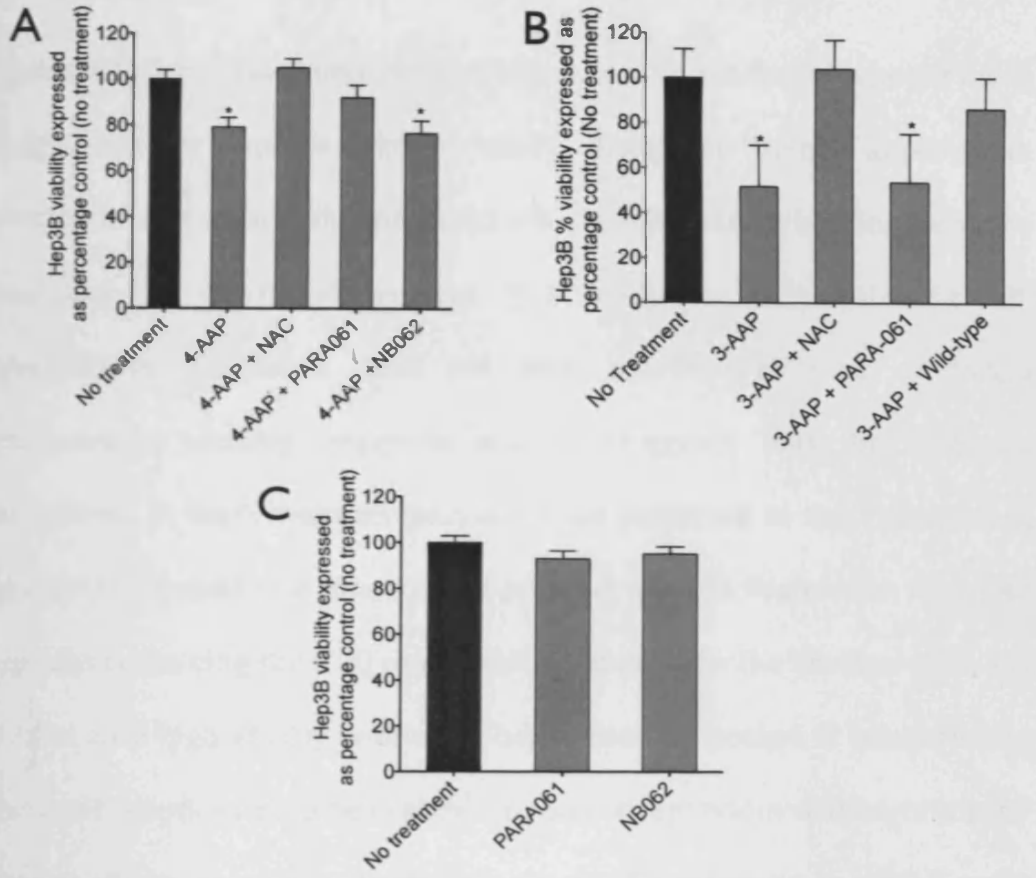

*Figure 2.10 Mitochondrial dehydrogenase activity of Hep3B cells exposed to 4-AAP or 3-AAP with results expressed as mean absorbance at 570nm as percentage control where control is either no treatment or exposure to N-acetylcysteine (NAC) alone. (A) In Hep3B cells exposed to 4-AAP (40 mM for 5 h) and co-incubated with peptide-phage PARA-061, 4-AAP induced hepatotoxicity was prevented. In contrast, co-incubation with phage clone NB-062 did not prevent 4-AAP induced hepatotoxicity. Data are mean ± SEM for three separate experiments where n = 6-8 for each experiment. * Signifies statistically significant difference ($p < 0.05$) compared to no treatment control cells and binding phage clone PARA-061. (B) In Hep3B cells exposed to 3-AAP (40 mM for 5 h) and co-incubated with peptide-phage PARA-061, hepatotoxicity could not be prevented in contrast to cells co-incubated with NAC. Data are mean ± SD (n=4). * Signifies statistically significant difference ($p <0.05$) compared to no treatment control cells. (C) Exposure of Hep3B cells to phage clones PARA-061 or NB-062 did not result in any loss in cell viability. Results are presented as mean ± SD (n = 4).*

2.5 Discussion

Successfully identifying peptide motifs that bind to a target of interest using phage display requires careful study design to select appropriate conditions that ultimately will discriminate high affinity binding peptides from the rest of the phage pool. It is clear that a 'one-size fits all' experimental procedure does not exist and factors such as target presentation, washing protocols, elution stringency must be diligently considered. In many ways streptavidin is an exception to this rule since it appears to be amenable to a range of panning methodologies that will yield peptides containing the HPQ motif widely reported in the literature[28, 31] to bind with high affinity within the biotin binding pocket. It is interesting that cyclic peptides have been shown to bind streptavidin with significantly greater affinity than their linear counterpart. For example at pH 7.3 cyclic ^{C}AECHPQFCIEGRK$^{N'}$ (Kd = 0.023 μM) binds streptavidin with ~ 7000 fold greater affinity than linear ^{C}AEFSHPQNTCIEGRK$^{N'}$ (K_d = 160 μM)[30]. This is not as a consequence of interaction of the cysteine residues with streptavidin, although they are surface exposed, rather it reflects a decrease in entropy of unbound cyclic versus unbound linear peptide.

The ready success in identifying peptides that bind to macromolecules such as streptavidin is in sharp contrast to the difficulties in selecting against low molecular weight species. It is clear that peptides and proteins can form strong interactions with small molecules such as those formed during the *in-vivo* generation of antibodies against haptens - low molecular weight

molecules conjugated to carrier proteins such as albumin. Whilst antibody phage display has been used to identify antibodies to haptens [32, 34, 38-41], to date no peptide isolation has been reported. The primary obstacle in these selections is presenting the target to the peptide phage particles without occupying one of the limited functional groups within the molecule through immobilisation strategies or introducing a significant chemical functionality such as linker groups or affinity tags that peptide phage may bind to preferentially. Insoluble complexes of low molecular weight molecules whilst having a heterogeneous and indeed non-defined surface should nevertheless display the various functional groups of the parent molecule and therefore represent a target against which phage display selection can be undertaken. The studies have shown that our in-laboratory phage display protocols can effectively identify peptides that bind large complex biomacromolecules and small molecules with limited functional groups.

Whilst the primary aim of these studies was validation, there were some interesting consequences of note particularly with respect to 4-AAP. Specifically, the peptide identified against 4-AAP may find use in the diagnosis or treatment of 4-AAP induced hepatotoxicity. 4-AAP is metabolised by the hepatic cytochrome P450 system and specifically isoenzyme CYP2E1(10). In therapeutic doses of 4-AAP ~ 4% is converted through CYP2E1 to a toxic intermediary *N*-acetyl-*p*-benzoquinone imine (NAPQI) which is sequestered through the oxidation of reduced

glutathione. In overdose, stores of reduced glutathione are quickly depleted and NAPQI accumulates forming adducts to cellular macromolecules by covalent binding through cysteine groups which disrupts protein conformation and function. The clinical antidote of choice is the sulfydryl group donor N-acetylcysteine (NAC). The administration of NAC is often reserved until laboratory based diagnostic tests confirm overdose, primarily because some 3-6% of patients suffer severe anaphylactic reactions on intravenous administration. Standard laboratory based determinations of 4-AAP concentration in patient blood samples can take many hours and with the window of opportunity for successful treatment with NAC a maximum of 24 hours after ingestion, delays in sample processing or in patients presenting many hours after overdose may result in an ineffective reversal of poisoning. Point of care tests[42] would have significant advantage in the rapid diagnosis of 4-AAP overdose using pin prick volumes of blood on a sensing platform, in much the same way as glucose levels are monitored in diabetes. Very early stage development of a 4-AAP biosensor based on the peptide identified in these studies are underway using molecularly imprinted polymers (MIPs)[43]. A peptide-MIP sensing platform is not without precedent, Itoda and co-workers[44] identified a peptide against glucose oxidase using phage display and produced a simple polymeric system with the peptide conjugated to the polymer; an increase in the binding affinity of the peptide in the conjugate for glucose oxidase was observed compared to peptide alone[44].

It is interesting to hypothesise the use of a phage based medicine for the treatment of 4-AAP overdose. As will be shown in Chapter 5, following intravenous administration M13 phage primarily accumulate in the liver[45, 46], the site of 4-AAP toxicity, and would therefore act as a rudimentary delivery vector for a therapeutic moiety which in this case could be a peptide that binds 4-AAP. The modest amelioration of cell toxicity demonstrated by the peptide sequence identified in the studies in section 2.4.2.4 may be improved by re-engineering the phage to display the peptide on the pVIII phage protein thus exposing ~ 200 – 300 copies on the phage surface compared to 5 in the library used. Whilst the intravenous administration of phages in man may not receive approval until sometime in the future, phage based medicines delivered orally are tacitly accepted as safe by the FDA[47] with few apparent adverse reactions and this should go some way to accelerating studies in man.

The studies in this chapter have demonstrated that with the correct strategy phage display technologies can be utilized to identify peptides that bind large complex biomacromolecules and small, simple molecules with limited functional groups. Whilst the strategy of using insoluble complexes as the panning target may or may not prove appropriate for a wide range of similar molecules, peptides that are functional with respect to such molecules and that can be identified by display approaches is an original finding [14]. Peptides generated in this way will serve as recognition motifs

within the next generation of hybrid polymeric molecular sensors or as therapeutics in their own right.

Reference List

1. Smith, G.P. and V.A. Petrenko, *Phage Display.* Chem Rev, 1997. **97**(2): p. 391-410.

2. Yu, L., et al., *Phage display screening against a set of targets to establish peptide-based sugar mimetics and molecular docking to predict binding site.* Bioorg Med Chem, 2009. **17**(13): p. 4825-32.

3. Wolcke, J. and E. Weinhold, *A DNA-binding peptide from a phage display library.* Nucleosides Nucleotides Nucleic Acids, 2001. **20**(4-7): p. 1239-41.

4. Cheng, X., B.K. Kay, and R.L. Juliano, *Identification of a biologically significant DNA-binding peptide motif by use of a random phage display library.* Gene, 1996. **171**(1): p. 1-8.

5. Doorbar, J. and G. Winter, *Isolation of a peptide antagonist to the thrombin receptor using phage display.* J Mol Biol, 1994. **244**(4): p. 361-9.

6. Goodson, R.J., et al., *High-affinity urokinase receptor antagonists identified with bacteriophage peptide display.* Proc Natl Acad Sci U S A, 1994. **91**(15): p. 7129-33.

7. Barry, M.A., W.J. Dower, and S.A. Johnston, *Toward cell-targeting gene therapy vectors: selection of cell-binding peptides from random peptide-presenting phage libraries.* Nat Med, 1996. **2**(3): p. 299-305.

8. Odermatt, A., et al., *Identification of receptor ligands by screening phage-display peptide libraries ex vivo on microdissected kidney tubules.* J Am Soc Nephrol, 2001. **12**(2): p. 308-16.

9. Maruta, F., et al., *Use of a phage display library to identify oligopeptides binding to the lumenal surface of polarized endothelium by ex vivo perfusion of human umbilical veins.* J Drug Target, 2003. **11**(1): p. 53-9.

10. Arap, W., et al., *Steps toward mapping the human vasculature by phage display.* Nat Med, 2002. **8**(2): p. 121-7.

11. Kolonin, M., R. Pasqualini, and W. Arap, *Molecular addresses in blood vessels as targets for therapy.* Curr Opin Chem Biol, 2001. **5**(3): p. 308-13.

12. Kolonin, M.G., et al., *Synchronous selection of homing peptides for multiple tissues by in vivo phage display.* FASEB J, 2006. **20**(7): p. 979-81.

13. Pasqualini, R. and E. Ruoslahti, *Organ targeting in vivo using phage display peptide libraries.* Nature, 1996. **380**(6572): p. 364-6.

14. Smith, M.W., et al., *Phage display identification of functional binding peptides against 4-acetamidophenol (Paracetamol): an exemplified approach to target low molecular weight organic molecules.* Biochem Biophys Res Commun, 2007. **358**(1): p. 285-91.

15. Yu, X., et al., *Screening of phage displayed human liver cDNA library against dexamethasone.* J Pharm Biomed Anal, 2007. **45**(5): p. 701-5.

16. Smith, G.P., *Filamentous fusion phage: novel expression vectors that display cloned antigens on the virion surface.* Science, 1985. **228**(4705): p. 1315-7.

17. Oldenburg, K.R., et al., *Peptide ligands for a sugar-binding protein isolated from a random peptide library.* Proc Natl Acad Sci U S A, 1992. **89**(12): p. 5393-7.

18. O'Neil, K.T., et al., *Identification of novel peptide antagonists for GPIIb/IIIa from a conformationally constrained phage peptide library.* Proteins, 1992. **14**(4): p. 509-15.

19. Blond-Elguindi, S., et al., *Affinity panning of a library of peptides displayed on bacteriophages reveals the binding specificity of BiP.* Cell, 1993. **75**(4): p. 717-28.

20. Dennis, M.S. and R.A. Lazarus, *Kunitz domain inhibitors of tissue factor-factor VIIa. II. Potent and specific inhibitors by competitive phage selection.* J Biol Chem, 1994. **269**(35): p. 22137-44.

21. Lowman, H.B., *Bacteriophage display and discovery of peptide leads for drug development.* Annu Rev Biophys Biomol Struct, 1997. **26**: p. 401-24.

22. Muller, K.M., K.M. Arndt, and A. Pluckthun, *Model and simulation of multivalent binding to fixed ligands.* Anal Biochem, 1998. **261**(2): p. 149-58.

23. Bass, S., R. Greene, and J.A. Wells, *Hormone phage: an enrichment method for variant proteins with altered binding properties.* Proteins, 1990. **8**(4): p. 309-14.

24. Wells, J.A. and H.B. Lowman, *Rapid evolution of peptide and protein binding properties in vitro.* Curr Opin Biotechnol, 1992. **3**(4): p. 355-62.

25. Finucane, M.D., et al., *Core-directed protein design. I. An experimental method for selecting stable proteins from combinatorial libraries.* Biochemistry, 1999. **38**(36): p. 11604-12.

26. Green, N.M., *Avidin and streptavidin.* Methods Enzymol, 1990. **184**: p. 51-67.

27. Laitinen, O.H., et al., *Brave new (strept)avidins in biotechnology.* Trends Biotechnol, 2007. **25**(6): p. 269-77.

28. Katz, B.A., *Binding to protein targets of peptidic leads discovered by phage display: crystal structures of streptavidin-bound linear and cyclic peptide ligands containing the HPQ sequence.* Biochemistry, 1995. **34**(47): p. 15421-9.

29. Katz, B.A., *Streptavidin-binding and -dimerizing ligands discovered by phage display, topochemistry, and structure-based design.* Biomol Eng, 1999. **16**(1-4): p. 57-65.

30. Katz, B.A. and R.T. Cass, *In crystals of complexes of streptavidin with peptide ligands containing the HPQ sequence the pKa of the peptide histidine is less than 3.0.* J Biol Chem, 1997. **272**(20): p. 13220-8.

31. Giebel, L.B., et al., *Screening of cyclic peptide phage libraries identifies ligands that bind streptavidin with high affinities.* Biochemistry, 1995. **34**(47): p. 15430-5.

32. Alvarez-Rueda, N., et al., *Generation of llama single-domain antibodies against methotrexate, a prototypical hapten.* Mol Immunol, 2007. **44**(7): p. 1680-90.

33. Moghaddam, A., et al., *Selection and characterisation of recombinant single-chain antibodies to the hapten Aflatoxin-B1 from naive recombinant antibody libraries.* J Immunol Methods, 2001. **254**(1-2): p. 169-81.

34. Moghaddam, A., et al., *Identification of scFv antibody fragments that specifically recognise the heroin metabolite 6-monoacetylmorphine but not morphine.* J Immunol Methods, 2003. **280**(1-2): p. 139-55.

35. Fagan, E. and G. Wannan, *Reducing paracetamol overdoses.* BMJ, 1996. **313**(7070): p. 1417-8.

36. Mosmann, T., *Rapid colorimetric assay for cellular growth and survival: application to proliferation and cytotoxicity assays.* J Immunol Methods, 1983. **65**(1-2): p. 55-63.

37. Plumb, J.A., R. Milroy, and S.B. Kaye, *Effects of the pH dependence of 3-(4,5-dimethylthiazol-2-yl)-2,5-diphenyl-tetrazolium bromide-formazan absorption on chemosensitivity determined by a novel tetrazolium-based assay.* Cancer Res, 1989. **49**(16): p. 4435-40.

38. McKenzie, K.M., et al., *Identification and characterization of single chain anti-cocaine catalytic antibodies.* J Mol Biol, 2007. **365**(3): p. 722-31.

39. Persson, H., J. Lantto, and M. Ohlin, *A focused antibody library for improved hapten recognition.* J Mol Biol, 2006. **357**(2): p. 607-20.

40. Strachan, G., et al., *Rapid selection of anti-hapten antibodies isolated from synthetic and semi-synthetic antibody phage display libraries expressed in Escherichia coli.* FEMS Microbiol Lett, 2002. **210**(2): p. 257-61.

41. Krykbaev, R.A., et al., *Phage display-selected sequences of the heavy-chain CDR3 loop of the anti-digoxin antibody 26-10 define a high affinity binding site for position 16-substituted analogs of digoxin.* J Biol Chem, 2001. **276**(11): p. 8149-58.

42. Dale, C., et al., *Assessment of a point-of-care test for paracetamol and salicylate in blood.* QJM, 2005. **98**(2): p. 113-8.

43. Piletsky, S.A., N.W. Turner, and P. Laitenberger, *Molecularly imprinted polymers in clinical diagnostics--future potential and existing problems.* Med Eng Phys, 2006. **28**(10): p. 971-7.

44. Itoda, K., E. Tamiya, and K. Yokoyama, *Evaluation of the molecular recognition of peptide-conjugated polymer.* Anal Sci, 2003. **19**(1): p. 185-7.

45. Zou, J., et al., *Biodistribution of filamentous phage peptide libraries in mice.* Mol Biol Rep, 2004. **31**(2): p. 121-9.

46. Molenaar, T.J., et al., *Uptake and processing of modified bacteriophage M13 in mice: implications for phage display.* Virology, 2002. **293**(1): p. 182-91.

47. Abuladze, T., et al., *Bacteriophages reduce experimental contamination of hard surfaces, tomato, spinach, broccoli, and ground beef by Escherichia coli O157:H7.* Appl Environ Microbiol, 2008. **74**(20): p. 6230-8.

Chapter 3 Establishment of an *in-vitro* primary porcine blood-brain model for the phage display identification of peptides that bind brain microvasculature

3.1 Introduction

3.1.1 The Blood-Brain Barrier

The delivery of therapeutic macromolecules into the central nervous system and particularly into the brain remains a significant challenge for the Pharmaceutical Sciences. This is as a consequence of the cellular interplay between capillary endothelial cells, astrocytes, pericytes and neurones in the cerebral microvasculature that results in a complex and restrictive three-dimensional architecture termed the blood-brain barrier (BBB)[1-3]. The BBB essentially serves to isolate the brain in a discrete and highly-regulated compartment that is protected both physically and biochemically from the fluctuating milieu of the systemic circulation. Non-fenestrated endothelial cells continuously lining the brain microvasculature coupled with the expression of intercellular tight junctions (zonulae occludentes) and a relative paucity of endothelial vesicles prevents significant solute entry into the brain with even small lipophilic molecules that readily partition across lipid membranes often excluded by active efflux transport mechanisms or by metabolic enzymes.

3.1.2 Brain microenvironment

The role of the brain microenvironment in the development of a fully differentiated BBB cannot be overstated. Elegant transplantation studies in the early 1980s[4] revealed that implants of avascular tissue fragments from 3-day-old quail brain into the coelomic cavity of chick embryos were infiltrated by vasculature arising from the gut and yet developed a

functional BBB phenotype. Conversely, blood vessels infiltrating avascular embryonic quail somites implanted into brain ventricles of the chick lost their barrier properties despite the brain origin of the endothelial cells invading. In another series of transplantation studies [5, 6], mouse brain tissue transplanted onto the embryonic chorioallantoic membrane of the chick egg becomes vascularised by chick blood vessels that, although normally leaky, begin to express BBB markers. Together these studies imply that properties of the brain tissue itself must direct the development and maintenance of brain microvasculature. Histological studies[7] have revealed close association of brain capillary endothelia with a number of cell types and cell processes that include perivascular endfeet of astrocytic glia, pericytes, microglia and neuronal projections that in combination induce the fully differentiated BBB phenotype (**Figure 3.1**).

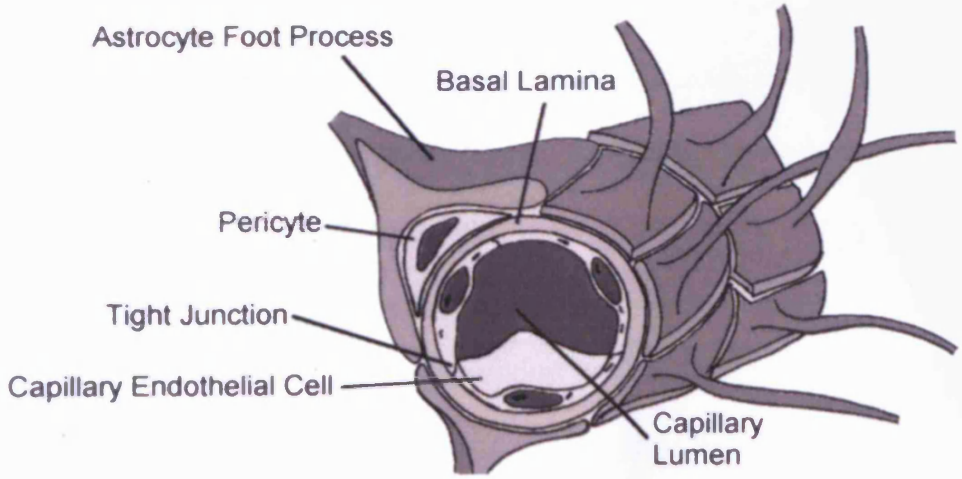

Figure 3.1 Schematic representation of the cellular architecture at the blood-brain barrier. Although the primary anatomical barrier is the continuous lining of brain microvasculature with non-fenestrated endothelial cells, it is the complex and dynamic interaction of endothelial cells with astrocytes, pericytes and neurons that provide the fully differentiated and competent BBB neurovascular unit (adapted from [8]).

3.1.3 Astrocytes

Astrocytes, the foot processes of which form a network of fine lamellae that envelop more than 99% of the abluminal surface of brain microvascular endothelia[9], have long been recognised to play a key role in the differentiation of the BBB. Whilst astrocytes do not in themselves constitute a cellular barrier as evidenced by the passage of horseradish peroxidase between astrocytic cell junctions[10], they significantly enhance the restrictive paracellular barrier of BBB endothelium. In studies that complement those of Stewart and Wiley, Janzer and Raff [11] demonstrated primary rat astrocytic tissue when implanted in the anterior chamber of the eye in adult syngeneic rats becomes vascularised by leaky vessels originating from the iris that develop a restrictive phenotype upon infiltration of the astrocytes. More recently *in-vitro* studies have shown that culturing primary brain microvascular endothelial cells in apposition to primary astrocytes or astroglioma cell lines results in restoration of an endothelial phenotype that more closely resembles the *in-vivo* BBB. This is evidenced by increases in transendothelial electrical resistance (TEER) and decreases in permeability to classical paracellular probes such as sucrose and mannitol [12-15]. It is interesting to note that in the developing embryo CNS capillaries only begin to display barrier properties after astrocyte differentiation[16]. Clear lines of evidence now exist that astrocytes regulate many BBB features including the regulation of tight junctions[17-20], the up-regulation and polarized localization of transporters that include the multi-drug resistance transporter P-

glycoprotein (P-gp)[21], the principal brain glucose transporter GLUT-1 and the system-L and system-A amino acid transporters as well as a number of key metabolic enzyme systems[22, 23]. Such effects are partially explained by the release of soluble astrocytic paracrine factors, the precise identity of which remains elusive but is thought to include transforming growth factor-β (TGFβ)[24], glial derived neurotrophic factor (GDNF)[25, 26], basic fibroblast growth factor (bFGF)[20], IL-6 and hydrocortisone[27]. Further efforts to understand the effects of astrocytes on the development of a fully differentiated BBB phenotype are ongoing with particular emphasis on co-culture models of primary brain endothelia with astrocytes and brain endothelia cultured in astrocyte conditioned media (ACM). It is clear however that BBB induction by glial cells is both complex and highly regulated and significant communication between endothelium and glial cells is essential.

3.1.4 Pericytes

The pericyte is a specialized smooth muscle cell at the BBB located on the abluminal microvascular surface and separated from the endothelia and astrocytic foot processes by a basal lamina readily penetrated by pericytic projections. Whilst the primary role of pericytes appears to be provision of vasodynamic capacity and structural integrity they play a key role in new vessel formation during brain development and also appear to contribute towards auto-regulation of blood flow distribution[28, 29]. Pericytes, like astrocytes, do not constitute an intrinsic permeability barrier but express a

significant range of metabolizing enzymes that include gamma glutamyl transpeptidases[30], glutamylaminopeptidases[31], aminopeptidases A and N[32] and glutamic acid decarboxylase[33] which indicates a role as an enzymatic barrier particularly with respect to peptides. In addition, pericytes may also be the most potent initiator of CNS immunity via antibody dependant phagocytosis[34]. Evidence is beginning to emerge that pericytes play a limited role in influencing BBB paracellular permeability with *in-vitro* models of brain endothelial cells cultured with pericytes demonstrating an up-regulation of the tight junctional protein occludin[35] and a decrease in permeability to the paracellular marker sodium fluorescein[36].

3.1.5 BBB Models

One of the aims of this thesis is the phage display identification of peptides that increase brain uptake of a therapeutic cargo. There are two ways in which this may be accomplished: (i) identification of peptides that essentially adhere to brain microvasculature to increase the residency time of a therapeutic cargo at the BBB, or (ii) identification of peptides that stimulate an endocytotic or transcytotic event to carry the cargo across the BBB. This chapter is concerned with the identification of peptides that adhere to vasculature as in (i) and a phenotypically representative *in-vitro* model of the BBB would afford selection of such peptides. This model needs to accurately represent polarized transport systems and metabolic and signaling pathways that are evident *in-vivo*. It is also important for the

phage display studies that the model accurately reflects the significant paracellular restrictiveness at the BBB, not because of an interest in transendothelial solute screening, but because the studies in this chapter will seek to identify phages that bind surface element(s) on the luminal membrane and not the basal membrane; the latter would be inaccessible *in-vivo* due to the presence of highly-restrictive tight junctions.

Whilst a range of immortalized BBB cells lines are available both commercially and from academia (**Table 3.1**), in general their value would be limited in phage studies by intercellular junctions that are leaky and a poorly differentiated phenotype compared to their *in-vivo* counterpart particularly with respect to their receptor and transporter profile.

***Table 3.1** Immortalized brain capillary endothelial cell lines reported in the literature from academic and commercial laboratories (updated and adapted from [37]).*

Species	Cell line	Nature of transformation	Ref
Human	SV-HCEC	SV40 T antigen	[38]
	HBEC-51	SV40 T antigen	[39]
	BB19	SV40 T antigen	[40]
	NKIM-6	pLXSN16E6E7	[41]
	hCMEC/D3	SV40 T antigen	[42]
Mouse	MBEC	SV40 T antigen	[43]
	S5C	Adenovirus E1A gene	[44]
	TM-BBB4	SV40 T antigen	[45]
	b.End3	Polyoma virus middle T-antigen	[46]
	b.End5	Polyoma virus middle T-antigen	[46]
Rat	RBE4	Adenovirus E1A gene	[47]
	GPNT	SV40 T antigen	[48]
	CR3	SV40 T antigen	[49]
	GP8.3	SV40 T antigen	[50]
	RBEC1	SV40 T antigen	[51]
	RCE-T1	Rous sarcoma virus	[52]
Bovine	t-BBEC-117	SV40 T antigen	[20]
	SV-BEC	SV40 T antigen	[53]
	BBEC-SV	SV40 T antigen	[54]
Porcine	PBMEC/C1-2	SV40 T antigen	[55]

Primary BBB models, which are more challenging to isolate and maintain, are more closely related to the *in-vivo* phenotype. Whilst brain microvascular endothelial models isolated from bovine brains are the most fully characterised[56, 57], apprehension over bovine spongiform encephalopathy (BSE) has resulted in changes to the law regarding handling of neural tissue from bovine sources that has dissuaded many researchers from its use. Efforts have been underway to isolate primary brain endothelia from other animal species including rat[58] and guinea pigs[59] with some success but generally the yield of cells (~1-2 million per brain) is insufficient to allow for large scale, high throughput permeability experiments. More recently primary human BBB models have been investigated but have so far proven leaky in comparison to other primary systems[60, 61]. Further, primary human cell models will face difficulties in obtaining a reliable and ethical supply of fresh human brain tissue.

3.1.6 Requirements of an *in-vitro* cell model of the BBB

Whilst *in-silico* and experimentally determined drug physicochemical properties have been used to give a gross indication of the interaction of vectors and therapeutics with the BBB [62-73], they frequently do not correlate with *in-vivo* therapeutic effects. Essentially this is because such predictors are based exclusively on the potential of the candidate molecule to undergo passive diffusion processes which, in its simplest form, is related to molecular size and lipophilicity and does not account for metabolic systems or transporters (both influx and efflux) present within

the microvasculature. Whilst *in-vitro* BBB models may not fully represent the *in-vivo* phenotype they provide a system to mechanistically explore various aspects of BBB drug transport, fundamental biological and pathological processes and metabolic systems in addition to screening for transendothelial solute diffusion. As first described by Gumbleton and Audus[37], *in-vitro* BBB models should meet a number of criteria:

I. *The model should display a restrictive paracellular pathway.* The *in-vivo* blood-brain barrier is highly effective in limiting transendothelial transport of solutes and any *in-vitro* model must have a restrictive paracellular pathway if it is to discriminate between candidate molecules displaying low, moderate or high BBB permeability with sufficient sensitivity. Moreover the relative permeability of high brain extraction molecules, such as the benzodiazepines, compared to low brain extraction molecules, such as sucrose and mannitol, indicates the discriminative power of the model in terms of paracellular and transcellular diffusion routes. BBB models that do not display suitable paracellular restrictiveness for transendothelial solute screening, for example immortalized BBB cell lines, may still provide useful data on kinetic uptake of molecules into brain endothelial cells and may afford dissection of endocytic pathways within them.

II. The model should have a cellular architecture that is comparable with the in-vivo BBB. Gross morphology including cell dimensions, volume and surface area of cell-cell interaction must retain parity with *in-vivo*

architecture. Further, expression and activity of metabolic enzymes and complexity of tight junctional elements must also be maintained.

III. *The model should retain functional expression of key BBB transporters.* The emerging role of efflux transporters in the expulsion of a diverse range of xenobiotics from brain endothelia as well as the importance of nutrient transporters that maintain brain homeostasis predicate a representative expression and distribution of such transporters in any *in-vitro* BBB model. Whilst the specificity of a molecule for a given transporter can be determined in cell models distinct from BBB endothelia, for example polarized transfer across the MDR1 transfected MDCK cells[74], it is critical to establish the quantitative relationship between *in-vitro* and *in-vivo* transporter function and this is more closely served by a representative *in-vitro* BBB phenotype.

IV. *The model should be easy to isolate and maintain in culture.* To facilitate high-throughput studies the model should ideally be isolated in large unit volume and retain phenotypic stability with a high number of population doublings. The failure of continuous cell lines to demonstrate a representative BBB phenotype necessitates a strategy to preserve the isolated primary cell line for long periods of time without loss in function to facilitate investigations over extended periods of time.

3.1.7 Objectives

This current work was focused on developing a consistent and effective isolation protocol for the culture of primary porcine brain microvascular

capillary endothelial cells (PBMVECs) to afford the phage display selection of peptides that bind the luminal membrane of brain microvasculature. PBMVECs were isolated from the whole brain of pigs by a procedure that essentially involved enzymatic digestions to produce a crude suspension of grey matter and microvessels. The microvessels were then separated by density centrifugation and subsequently enzymatically digested to yield capillary endothelial cells. Assessment of restrictive barrier properties including permeability to paracellular and transcellular probes validated the model; the inductive influence of astrocytes and astrocytic co-factors was also explored. Whilst the isolation protocol was loosely based on the methods described by Frank et al[75], significant modifications to the isolation and culture procedures were undertaken in these studies. Finally, a series of panning experiments against PBMVECs and the immortalised BBB cells lines b.End3 and RBE4 were conducted in an effort to identify peptides that bind brain microvascular endothelia.

3.2 Materials

3.2.1 Cell culture

Dulbecco's modified Eagle's medium (DMEM) containing 25 mM HEPES; DMEM:F12; M199; Trypsin-EDTA; sodium pyruvate; heat inactivated fetal bovine serum (FBS); heat inactivated fetal horse serum (FHS); Penicillin G (100 unit per ml); Streptomycin (100μg per ml) and L-glutamine 200mM (x100) were obtained from Invitrogen, (Paisley, UK). Non-essential amino acids; hydrocortisone and 2-mercaptoethanol were obtained from Sigma-

Aldrich Chemical Co., (Poole, UK). All cell culture plastics and Transwell™ inserts were obtained from Corning Costar, (High Wycombe, UK).

3.2.2 Isolation materials

Dispase Type II; collagenase-dispase (*Vibrio alginolyticus/Bacillus polymyxa*) and rat tail collagen type I were obtained from Roche, (East Sussex, UK). Percoll (1.219 g/ml density) was obtained from Pharmacia, (Buckinghamshire, UK).

3.2.3 cAMP Modulators

CPT-cAMP (8-(4-chlorophenylthio)-adenosine 3′, 5′-cyclic monophosphate) was obtained from Sigma-Aldrich Chemical Co., (Poole, UK). Ro20-1724, a phosphodiesterase inhibitor, was obtained from Calbiochem, (Nottingham, UK).

3.2.4 Uptake and transport studies

[6,6(n)-^{3}H]sucrose and [2-^{14}C]diazepam were obtained from Amersham Life Science, (Little Chalfont, UK). OptiPhase HiSafe3™ liquid scintillation fluid was obtained from Fisher Scientific Chemicals, (Loughborough, UK). Rhodamine-123 (2-[6-Amino-3-imino-3H-xanthen-9-yl]-benzoic acid methyl ester) and Verapamil hydrochloride were obtained from Sigma-Aldrich Chemical Co., (Poole, UK).

3.2.5 Electron microscopy

Neutrally-buffered 2% osmium tetroxide in veronal acetate buffer and Araldite (CY212) resin were obtained from TAAB Laboratories Equipment

Ltd., (Aldermaston, UK).

3.2.6 Western analyses

DC protein assay kit was obtained from Bio-Rad, (Hertfordshire, UK). Rabbit polyclonal caveolin-1 antibody was obtained from BD Transduction Laboratories, (Oxford, UK). Swine anti-rabbit HRP-conjugated IgG reporter antibody and rabbit anti-mouse HRP-conjugated IgG reporter antibody were obtained from Dako, (Cambridge, UK). Rainbow™ molecular weight marker and Hyperfilm ECL™ were obtained from Amersham Life Science (Little Chalfont, UK). Super Signal Ultra™ was obtained from Pierce, (Chester, UK).

3.2.7 RT-PCR

Ultraspec™ DEPC treated water was obtained from Biogenesis (Poole, UK). Random hexamer primers (pdN6) was obtained from Amersham Life Science (Little Chalfont, UK). Dithiotheritol (DTT); first strand RT buffer (x5); moloney murine leukaemia virus reverse-transcription (MMLV-rt); deoxynucleotide triphosphate monomers (dNTPs) and forward and reverse primers were obtained from Invitrogen, (Paisley, UK). RNAsin was obtained from Promega, (Southampton, UK). PCR reaction buffer (x10); $MgCl_2$ and Taq polymerase were obtained from Qiagen Ltd (Crawley, UK). 100 bp DNA molecular weight marker ladder was obtained from ABGene, (Surry, UK). Ethidium bromide was obtained from Sigma-Aldrich Chemical Co., (Poole, UK).

3.3 Methods

3.3.1 Cell lines

The rat C6 glioma cell line (passages 18-23) was seeded at $1x10^4$ cells.cm^{-2} and maintained in culture medium comprising M199 supplemented with 10% heat inactivated FBS, and the antibiotics penicillin G (100 units/ml) and streptomycin sulfate (100 μg/ml). The mouse brain microvascular cell line b.End3 (passages 27-33) was seeded at a density of 0.5×10^4 cells.cm^{-2} and maintained in culture medium comprising DMEM supplemented with 10% heat inactivated FBS, and the antibiotics penicillin G (100 units/ml) and streptomycin sulfate (100 μg/ml), 1% w/v non-essential amino acids, glutamine (2 mM), 2-mercaptoethanol (5 μM) and sodium pyruvate (1 mM). The rat brain microvascular cell line RBE4 was seeded at a density of $1x10^4$ cells.cm^{-2} and maintained in culture medium comprising Ham's F10 and αMEM (1:1, v/v) supplemented with 10% FBS, 1 ng.ml^{-1} basic fibroblast growth factor (bFGF), 300 mg.ml^{-1} Geneticin and 1 ng.ml^{-1} glutamine. The human epidermal squamous carcinoma cell line A431 (passage 27) and the Monkey African Green kidney cell line MA104 (passages 16-23) were seeded at densities of 4×10^4 cells.cm^{-2} and 3×10^4 cells.cm^{-2} respectively and were maintained in culture medium comprising DMEM supplemented with 10% heat inactivated FBS, and the antibiotics penicillin G (100 units/ml) and streptomycin sulfate (100 μg/ml), 1% w/v non-essential amino acids and glutamine (2 mM). All cultures were maintained at 37°C in a humidified atmosphere (5% CO_2/95% air) and culture medium replenished every 48 hours.

3.3.2 PBMVEC and RBMVEC isolation and culture mediums

- **Preparation medium:** M199, 100 $\mu g.ml^{-1}$ Penicillin, 100 $\mu g.ml^{-1}$ streptomycin.
- **Culture medium:** 90% M199, 10% fetal horse serum, 100 $\mu g.ml^{-1}$ Penicillin, 100 $\mu g.ml^{-1}$ streptomycin.
- **Freezing medium:** 70% M199, 20% horse serum, 10% DMSO.
- **Switch medium:** DMEM:Hams-F12 (1:1 v/v), 100 $\mu g.ml^{-1}$ Penicillin, 100 μg.ml-1 streptomycin, 550 nM hydrocortisone.
- **'BBB isolation buffer':** 1.3 M NaCl; 50 mM KCl; 16 mM $Na_2HPO_4.2H_2O$; 10 mM $NaH_2PO_4.2H_2O$; 130 mM HEPES; 55mM Glucose.
- **Continuous percoll gradient (ρ = 1.032g/ml):** 30% percoll (ρ = 1.129g/ml), 10% M199, 10% 'BBB isolation buffer', 50% PBS.
- **Discontinuous percoll gradient:** see **Table 3.2.**

Table 3.2 Recipe for 'light' and 'heavy' components of discontinuous percoll gradient. The 'light' component is gently layered onto the 'heavy' component to give a sharp interface between the two components.

	'Light Percoll'	'Heavy Percoll'
Percoll	2.72 ml	6.49 ml
Horse serum	50 μl	50 μl
ddH_2O	6.28 ml (with phenol red)	2.51 ml
'BBB isolation buffer'	1 ml	1 ml
Final Volume	10 ml	10 ml

3.3.3 Porcine brain capillary endothelial cell isolation procedure

The isolation protocol developed in Cardiff is largely based upon the methods described in the pioneering work of Franke[75] but with significant modifications:

1. The intact heads from pigs aged less than 5 months old were obtained from an abattoir immediately following termination (< 10 mins after death) and transported to the laboratory within 30 mins.
2. The brains from four heads were surgically removed by making a vertical incision in the skin from the forehead to the nose to expose the skull, which was subsequently opened with a surgical cutter (MSxe 636 II, C&E Fein Gmbh & Co. KG, Stuttgart, Germany) to reveal the brain. The brains were carefully removed by hand, whilst wearing sterile gloves, and submerged in sterile ice cold (4-8°C) PBS for 5 mins.
3. The meninges and large surface vessels were carefully removed from the brain using a sterile scalpel and forceps and were discarded.
4. The accessory organs (cerebellum, brain stem, hypothalamus etc) and white matter i.e. leaky tissue were carefully dissected away from the cortical grey matter and discarded.
5. The grey matter was then minced to a fine paste (~ 1 mm^3 pieces) using a stainless steel rolling multi-blade cutter.
6. The paste was transferred to a sterile container and suspended to 200 ml in preparation medium containing dispase type II at a final concentration of 0.5% w/v.
7. The resultant suspension was incubated for 2 hours at 37°C with gentle shaking (125 rpm) on a Mini Orbital Shaker SO5 (Bibby Sterilin Ltd., Staffordshire, UK). The end point of the enzymatic

digestion was visually identified by dipping a sterile glass rod into the suspension, withdrawing the rod and identifying red microvessels attached to the glass. The digestion was terminated by putting the suspension on ice for 5 mins.

8. The suspension was divided equally between two centrifuge bottles each containing 150 ml 30% percoll stock solution (ρ = 1.032g.ml^{-1}) and centrifuged for 10 mins (6000g, 4°C) using a swing-out Avanti J-25 centrifuge (Beckman Coulter Inc., California, USA).
9. The floating layer containing cell debris, fats, myelin etc, was carefully aspirated and discarded and the remaining suspension was centrifuged at 1700g for 10 min at 4°C. At this stage observation of the bottom of the flask revealed vibrant red streaks of microvessels.
10. The supernatant was carefully aspirated and the microvessel pellet suspended to a final volume of 20 ml with pre-warmed (37°C) culture medium containing 1mg.ml^{-1} (0.1% w/v) collagenase-dispase II from *Vibrio alginolyticus/Bacillus polymyxa*. The suspension was incubated for 45 – 75 mins at 37°C with gentle orbital shaking (125 rpm). After 45 mins, the suspension was observed microscopically every 10 minutes until clusters of microvascular cells were observed. Over-digestion occurs when the clusters break up and result in a population of single cells that when cultured do not form monolayers.
11. To remove any remaining undigested vessels, the digestion was filtered through 180 μm nylon mesh.

12. The cell clusters were pelleted by centrifugation (185g, 4°C) for 10 mins and the supernatant discarded.
13. The pellet was suspended in 20 ml of culture medium and a final purification was completed by carefully layering the suspension on a discontinuous percoll gradient, prepared from 10 ml of a light percoll suspension (ρ = 1.03 $g.ml^{-1}$) layered on 10 ml of a heavy percoll suspension (ρ = 1.07 $g.ml^{-1}$), and centrifuging for 10 mins (1300g, 4°C).
14. The capillary endothelia fraction, appearing as a band at the sharp interface of the percoll gradients (ρ ~ 1.05 g/ml), was carefully needle aspirated in a volume of approximately 2ml taking care to avoid shear stresses. A pellet at the bottom of the heavy percoll was observed to contain erythrocytes and a 'floating' layer contained other debris.
15. The aspirated fraction was washed in 20ml of culture medium and after removing a small aliquot for cell counting (~ 100 µl) was centrifuged for 10 minutes (1300g, room temperature).
16. A typical isolation from four brains yielded ~ 100 million endothelial cells. The cells were either used immediately after isolation or were frozen. Frozen vials of cells, containing 5-6 million cells, were prepared by suspending the cells in freezing medium and cooled to -80°C over 2 hours and then transferred to a cryofreezer (-130°C).

3.3.4 RBMVEC isolation

The isolation of primary rat brain microvascular endotheilal cells (RBMVECs) largely paralleled the isolation of PBMVECs but with modifications:

1. Terminally anaesthetised rats (male SD; 350 – 450 g) were decapitated and the brains carefully removed by making a vertical incision in the skin from the forehead to the nose to expose the skull. A scissors was then used to crack open the skull before blunt forceps were used to carefully remove the brain.
2. The meninges and large surface vessels were carefully removed from the brain using a sterile scalpel and forceps and were discarded.
3. The accessory organs (cerebellum, brain stem, hypothalamus etc) and white matter i.e. leaky tissue were carefully dissected away from the cortical grey matter and discarded.
4. The grey matter was then cut to a fine paste (~ 1 mm^3 pieces) using a scalpel.
5. The paste was transferred to a sterile 50 ml centrifuge tube and suspended to 8 ml in preparation medium containing dispase type II at a final concentration of 2.5% w/v.
6. The resultant suspension was incubated for 2 hours at 37°C with gentle shaking (125 rpm) on a Mini Orbital Shaker SO5 (Bibby Sterilin Ltd., Staffordshire, UK). In common with the PBMVEC

isolation, the end point of the enzymatic digestion was visually identified by dipping a sterile glass rod into the suspension to observe microvessels.

7. The suspension was layered on top of a 30% percoll stock solution (20ml; ρ = 1.032g.ml^{-1}) and centrifuged for 10 mins (6000g, 4°C) using a swing-out Avanti J-25 centrifuge (Beckman Coulter Inc., California, USA).
8. The floating layer containing cell debris, fats, myelin etc, was carefully aspirated and discarded and the remaining suspension was centrifuged at 1700g for 10 min at 4°C. At this stage observation of the bottom of the centrifuge tube revealed vibrant red streaks of microvessels.
9. The supernatant was carefully aspirated and the microvessel pellet suspended to a final volume of 5 ml with pre-warmed (37°C) culture medium containing 1mg.ml^{-1} (0.1% w/v) collagenase-dispase II from *Vibrio alginolyticus/Bacillus polymyxa*. The suspension was incubated for 45 – 60 mins at 37°C with gentle orbital shaking (125 rpm). The suspension was observed microscopically every 10 mins from 45 mins onward until clusters of microvascular cells were observed.
10. The cell clusters were pelleted by centrifugation for 10 mins (185g, 4°C) and the supernatant discarded.
11. The pellet was suspended in 10 ml of culture medium and a final purification was completed by carefully layering the suspension on

top of a 30% percoll stock solution (20ml; ρ = 1.032g.ml^{-1}) and centrifuging for 10 minutes (700g, 4°C).

12. The supernatant was aspirated and discarded and the capillary endothelia fraction, appearing as a pellet at the bottom of the tube, was suspended in PBMVEC growth medium and centrifuged 185g for 10 mins.
13. The supernatant was once again aspirated and discarded and the endothelial cells suspended in PBMVEC growth medium supplemented with puromycin (4 μg.ml^{-1}) before seeding onto culture plastics.
14. A typical isolation from two brains yielded ~ 1 million endothelial cells. Isolated cells were cultured immediately after isolation.

3.3.5 Preparation of culture surfaces

Pilot studies showed that an extracellular matrix of rat tail collagen type I (RTCI) was essential for the growth of PBMVECs and RBMVECs; without this basal lamina, cell attachment was very poor and cells never reached confluency. A 1 mg.ml^{-1} stock solution of RTCI was prepared by dissolving lyophilised collagen in 0.2% v/v sterile acetic acid. This stock was stored at 4°C for up to 6 months. All culture surfaces were coated to a final concentration of 3 μg.cm^{-2} by diluting the RTCI stock solution with sterile water to volumes indicated in **Table 3.3**.

Table 3.3 Collagen coating of cell culture surfaces for PBMVEC attachment.

Culture surface	Surface area (per unit)	Volume RTCI stock	Volume of dilute RTCI solution added to surface
T75 flask	75 cm^2	225 µl	1000 µl
T25 flask	25 cm^2	75 µl	500 µl
6 well plate	10 cm^2	30 µl	500 µl
24 well plate	1.8 cm^2	5.4 µl	200 µl per well
Large inserts	4.7 cm^2	14 µl	600 µl per insert
Small inserts	0.33 cm^2	1 µl	60 µl per insert

The RTCI solution was applied to the surface and incubated at 37°C for 3 hours before being dried under laminar flow at room temperature for 18 hours. Surfaces were washed 3x with PBS to remove any residues of acetic acid and stored at 2 – 8°C for up to 4 weeks.

3.3.6 Astrocyte co-culture and production of astrocyte conditioned medium

Astrocyte co-culture system comprised growth of the astroglioma cell line C6 on a 24 or 6 well plate (basal chamber) until confluent (2-3 days) after which PBMVECs or RBMVECs were grown on Transwell™ inserts suspended above the C6 culture (apical chamber).

Astrocyte conditioned medium comprised 50% C6 medium (C6 cells grown to confluence, medium replaced with M199 and collected after 24 hours), 50% 'double strength' culture medium - M199 supplemented with the antibiotics penicillin G (200 units/ml) and streptomycin sulfate (200 µg/ml) and 20% heat inactivated fetal horse serum.

Astrocyte conditioned switch medium comprised 50% C6 medium (C6 cells grown to confluence, media replenished with DMEM:F12 and collected

after 24 hours), 50% DMEM:F12; final medium supplemented with 550 nM hydrocortisone.

Any other additions to these specialist media are explicitly stated where appropriate in the text.

3.3.7 Culture and sub-cultivation of porcine brain microvascular capillary endothelial cells

A frozen vial of PBMVECs was removed from the cryofreezer and rapidly thawed (< 5 mins) in a water bath (37°C). The cells were suspended to 10 ml in culture medium and centrifuged at 185g for 5 min. The PBMVEC pellet was suspended in culture medium and deposited onto RTCI coated T25-flask, multiwell plates or Transwell™ inserts. After 48 hours, the cells were washed vigorously 3x with PBS to remove cell detritus and the medium was replaced; microscopic examination at this early stage of growth showed islands of endothelial cells. In certain studies indicated in the text 1st passage cultures were used. For these studies, after 6 days *in-vitro* (80-90% confluency) PBMVECs were sub-cultivated. Briefly, the cells were washed 3x with PBS (37°C) and then exposed to Trypsin/EDTA for 30 seconds. Since endothelial cells are easily damaged during excessive exposure to trpysin, the cells were constantly visualized with a reverse phase-contract microscope until they began to detach from the culture surface, normally within 3 minutes. The detaching cells were collected in 10ml of culture medium and centrifuged for 5 mins (185g). The pellet was resuspended in culture medium and seeded at a density of 5 x 10^4 cells.cm^{-2}

on RTCI coated Transwell™ inserts. Primary cultures of brain microvascular endothelial cells are recognised to undergo phenotypic drift upon sub-cultivation and therefore 1st passage cells were not further sub-cultured.

3.3.8 Effects of astrocyte co-culture and astrocyte conditioned medium on alkaline phosphatase activity in PBMVECs

The responsiveness of PBMVECs to astrocytic induction was determined by measuring alkaline phosphatase activity in the presence and absence of astrocyte co-culture and astrocyte conditioned medium. Assessment of ALP activity on the apical (luminal) membrane of PBMVECs was undertaken using protocols previously described[20] but with modifications. Specifically, frozen PBMVECs were grown to confluence ± C6 co-culture in PBMVEC growth medium (7 days) followed by switch medium (24 hours) or in astrocyte conditioned medium (7 days) followed by astrocyte conditioned switch medium (24 hours). Confluent monolayers were washed 3x with PBS then incubated (up to 40 min, 37°C) with 1 ml of 10 mM ρ-nitrophenyl phosphate in 0.7 M 2-amino-2-methyl-1-propanol and 1 mM $MgCl_2$ (pH 10.2). Termination of reaction was achieved through addition of 200 µl of 1 N NaOH. After transferring 200 µl of supernatant to a 96 well plate, ρ-nitrophenol levels were determined by UV/VIS spectrometry (405 nm) to afford determination of alkaline phosphatase activity.

3.3.9 Permeability of PBMVECs and RBMVECs to paracellular and transcellular probes

Assessment of the permeability of PBMVECs and RBMVECs to the hydrophilic paracellular probe [^{3}H]sucrose and to the lipophillic trancellular probe [^{14}C]diazepam was carried out day 7 post seeding on 6.5 mm Transwell™ Clear inserts and 24 hours post media switch to fully express BBB properties (8 days total growth *in-vitro*). Thirty minutes before commencing the study, medium in the apical and basal chambers of Transwell™ inserts was removed and replaced with serum-free DMEM:F12. Probe transport in the apical to basal direction (A – B) was initiated by adding 200 µl of DMEM:F12 (serum free) containing 0.5 µCi (0.018 MBq) each of [^{3}H]sucrose (0.1 pmol) and [^{14}C]diazepam (0.1 nmol) to the apical chamber affording sucrose-diazepam data for a given study to reflect transport across the exact same monolayer. At predetermined time points (5, 10, 20, 30, 45, 60 and 90 min), 200 µl samples were collected from the basal chamber and replenished with fresh DMEM:F12 (serum free). Quantitation of radiolabeled probe accumulation in the basal chamber was determined using liquid scintillation (Wallac 1409, PerkinElmer Life Sciences, Boston, MA, USA).

Cumulative transport of probes as a function of time in the A – B direction was determined and the apparent permeability coefficients (ρ) $x10^{-6}$ $cm.s^{-1}$ calculated using **Equation 3.1**:

$$\frac{dM}{dt} = \rho \times A \times Co \qquad \text{Equation 3.1}$$

Where d*M*/d*t* represents the rate of change in cumulative mass of probe transferred from A – B; *A* represents the area of the Transwell™ membrane and *Co* is the original concentration of radio-labelled probe in the apical (donor) chamber (assumed to remain constant; <5% loss).

3.3.10 Ultra-structural morphology of PBMVECs

Light micrographs of confluent monolayers of PBMVECs were recorded after 7 days *in-vitro* using an Olympus IX50 inverted microscope with image acquisition via an Olympus DP10 automated digital processor. Qualitative assessment of cellular gross morphology and vesicular populations within PBMVECs grown on Transwell™ inserts was examined by transmission electron microscopy (T.E.M.). PBMVECs were grown from frozen stocks either in PBMVEC culture medium (7 days) followed by PBMVEC switch medium (24 hours) or with C6 co-culture. Cells were fixed and embedded for T.E.M. using methods previously described[76]. Specifically, Transwell™ insert membranes were fixed for 1 hour at room temperature with 1% glutaraldehyde and then post-fixed with neutrally-buffered osmium tetroxide in veronal acetate buffer for 1 hour at room temperature. Post-fixed membranes were dehydrated using 100% ethanol and then embedded in Araldite (CY212) resin. Sections of 70 nm depth were mounted on mesh copper grids and contrasted with saturated uranyl acetate and Reynolds' lead citrate. T.E.M. examination and image

acquisition was conducted in a Philips CM12 transmission electron microscope at an accelerating voltage of 80kV.

3.3.11 P-gp expression in PBMVECs

3.3.11.1 P-gp immunoblot analysis

Confluent monolayers of PBMVECs grown from frozen stocks were harvested and processed for Western blotting; an in-depth list of materials and a complete procedure for Western blotting is detailed in Chapter 5. Cells were collected in lysis buffer (50 mM Tris (pH 7.5), 1% Triton-X, 5 mM EGTA, 150 mM NaCl, 60 mM n-octyl-glucoside) containing protease inhibitors and incubated at 4°C for 20 min. Total protein in the lysed sample was measured using a Bio-Rad protein assay kit with an equal mass of protein (10 μg) loaded onto and resolved by 7.5% SDS-PAGE before being electro-blotted (0.2 μm pore diameter). Pre-stained molecular weight markers were run concurrently in order to determine molecular size. The primary antibody probe (monoclonal P-gp C219 antibody, ID Labs, Inc. Ontario, Canada) was diluted 1:100 and incubated with the membrane for 16h at 4°C. The membrane was washed 3x in TBS-T(0.5%) and then incubated with a 1:2000 dilution of the secondary reporter antibody (HRP conjugated rabbit anti-mouse, Dako, Cambridge, UK) for 1 hour at room temperature. The membrane was washed 6x with TBS-T(0.5%) before the chemiluminescent signal was generated and recorded onto Hyperfilm ECL. Image acquisition was undertaken on GS-700 densitometer with Molecular Analyst Software (Bio-Rad, Hemel Hempstead, UK).

3.3.11.2 Rhodamine-123 accumulation-retention

A rhodamine-123 transport assay was used to assess the functional expression of P-gp within PBMVEC cultures amplified from frozen stocks. Confluent monolayers of PBMVECs (day 8 post-seeding, 7 days growth medium then switch to serum free medium containing 550 nM hydrocortisone for 24 hours prior to study) were washed 3x with PBS and the cells disaggregated by trypsin/EDTA. The cells were suspended (5×10^5 cells.ml^{-1}) in DMEM containing 1% FBS and the fluorescent probe rhodamine-123 (0.2 μg.ml^{-1}), in the presence or absence of the P-gp inhibitor verapamil (40 μM). The cells were incubated on an orbital shaker for 1 hr at 37°C - this phase representing cellular accumulation of rhodamine-123. At the end of the incubation the cell suspension was centrifuged (100g for 5 min), washed 3x in PBS and 50% of the population aliquoted and put on ice ready for flow cytometric analysis. The remaining 50% of the cell population was suspended in fresh DMEM (1% FBS) ± verapamil (40 μM) but devoid of rhodamine-123. Efflux of intracellular rhodamine-123 accrued within the cells during the accumulation phase proceeded over a 2 h incubation period at 37°C, after which the cells were washed in PBS and aliquoted for flow cytometric analysis; this population represents rhodamine-123 cellular retention. The cellular associated fluorescence of rhodamine-123 was collected on a FACScan flow cytometer using the FL-1 band pass filter.

3.3.12 mRNA expression of key BBB components in PBMVECs and RBMVECs

3.3.12.1 Total RNA extraction

Total RNA was harvested from PBMVEC monolayers grown from frozen stocks cultured to day 8 post-seeding (7 days astrocyte conditioned growth medium followed by 24 hour exposure to astrocyte conditioned switch medium). RNA was harvested with an RNEasy (Protect) Kit (Qiagen, West Sussex, UK) according to the manufacturers protocol. Specifically, cells were cultured in 6-well plates and lysed *in-situ* with 350 µl of Qiagen lysis buffer. The lysate was collected with a rubber policeman and after passing through a sterile 20-gauge needle five times to ensure complete homogenization, was transferred to a microcentrifuge tube. The lysate was treated with 350 µl of 70% v/v ethanol and mixed well by pipetting. The lysate was transferred to an RNEasy spin column and centrifuged 15 sec at 8000 g with the flow-through discarded. The RNA trapped on the silica membrane of the spin column was washed with a series of proprietary buffers followed by centrifugation (15 sec, 8000 g) to remove contaminants. Finally the RNA was eluted by loading 30 µl RNAse/DNAse free water onto the column, centrifuging (15 sec, 8000 g) and collecting the flow-through. The extracted RNA was quantified and its purity assessed by UV spectrophotometry (Genequant Pro, Amersham, UK) at 260 nm and 280 nm.

3.3.12.2 Reverse transcriptase polymerase chain reaction (RT-PCR)

RNA extracted in 3.3.12.1 was used in reverse transcriptase polymerase chain reaction (RT-PCR). Reverse transcription (RT) reaction mixture and thermocycling program are show in **Table 3.4** and **Table 3.5** respectively.

Table 3.4 Reverse transcription mixture.

RT component (20 µl total volume)	Volume (µl)
dNTP's (10 µM)	2.0
DTT (0.1 M)	2.0
First strand buffer (5x)	4.0
MMLV-rt (200 U.µl^{-1})	1.0
pdN6 (50 ng.µl^{-1})	2.0
RNA (1 µg.µl^{-1})	1.0
RNAsin	0.5
Ultraspec™ DEPC treated water	7.5

Table 3.5 Thermocycling program.

Thermocycling step	Temperature (°C)	Time (min)
1. Denaturing	95	5
2. Incubation	4	5
3. Addition of MMLV-rt & RNAsin		
4. Binding	25	10
5. Extension	42	42
6. Denaturing and termination	95	5

RT mix was stored at -20°C until required for polymerase chain reaction. PCR amplification primers were designed using the web based design program Primer 3 (http://frodo.wi.mit.edu/cgi-bin/primer3/primer3_www.cgi). Primer pairs were designed to have between 18 and 27 bases with an optimal melting point (Tm) of 60°C (range 57°C to 63°C) and with a GC content between 45% and 60%. Primer-dimers were avoided by ensuring 3'- and 5'- ends of the forward and reverse primers were not complementary.

Table 3.6 highlights the accession number for porcine mRNA (*Sus scrofa*) and primer sequences for the genes studied, principally tight junctional elements (Zonulae occludens 1 (ZO-1), Claudin-1, Claudin-3, Claudin-5 and occludin), efflux transporters (P-glycoprotein (MDR-1), brain multidrug resistance protein (BMDP) and the multidrug resistance associated proteins, MRP-1 & MRP-2) and nutrient transporters and receptors (organic cation transporter 1 (OCT-1), organic anion-transporting polypeptide A & C (OATP-A & OATP-C), GLUT-1 the principal brain glucose transporter, neutral amino acid transporter 1 (NAA-1), cationic amino acid transporter 1 (CAA-1) and Leptin receptor).

Table 3.6 RT-PCR for tight junction elements, carrier mediated transporters and hormone receptors in primary porcine brain microvascular endothelial cells grown from frozen stocks to confluence (7 days) using astrocyte conditioned growth media followed by a 24 hr switch to serum free astrocyte conditioned media containing hydrocortisone (550 nM). The table shows the GenBank mRNA accession number for primer design, primer sequence and expected size of PCR product.

Gene Product	Access. No.	Primer Sequence	Size (bp)
Tight junctional components			
Claudin-1	AJ318102	F: ctgccccagtggaagattta R: caacagtggccacaaagatg	223
Claudin-3	AY625258	F: ccagatgcagtgcaaagtgt R: acgatggtgatcttggcttt	180
Claudin-5	AJ318103	F: aaggtgtacgactcggtgct R: gccgcctgtgagagctac	174
ZO-1	AJ318101	F: cagcacagtgcctaaagctg R: gtgggaggatgctgttgtct	230
Occludin	U79554	F: ggcctgcaggagtacaagag R: tccgcagatcccttaacttg	161
Transporters			
GLUT-1	X17058	F: cttcactgtcgtgtcgctgt R: cacgatgctcaggtaggaca	154
NAA-1	AY375264	R: caatgtggagctgaaagcag F: cagccaggatcaaagagagg	161
CAA-1	AY371320	F: catcaaaaactggcagctca R: tggtagcgatgcagtcaaag	185
OCT-1	AY238476	F: ctcgaagaggaggtcgtcac R: cggtcgatgatgaggagaat	236
OATP-A	Goh et al[77]	F: ccatgctcacacaaatagagagac R: gatgccaacaaaagtccaat	520
OATP-C	Goh et al[77]	F: aggtattctaaagaaact R: ctgaccatactgttgctctac	744
Hormone receptors			
Leptin receptor	NM_001024587	F: ccggaatgatgcaggtctat R: gaaatggtttcaggctccaa	249
Drug resistance transporters			
BMDP	NM_214010	F: ttatccgtggtgtgtctggt R: cacgatgctcaggtaggaca	175
MDR-1	AF403245	F: atggcagtgggacaggttag R: ggtcgagtggggtagttgaa	188
MDR-1 (human)	Goh et al[77]	F: ggcatttacttcaaacttgtc R: gcttggtgaggatctctccagctttg	502
MRP-1	AF403246	F: gcagatcacgcgatacttga R: gtccaggtcgtctcggtaac	219
MRP-2	Goh et al[77]	F: aaatgtgtcttttcctgg R: taagattctgaagaggcgattt	325
Positive Control			
B-actin	Goh et al[77]	F: actatcggcaatgagcggttc R: agagccaccaatccacacaga	288

An examination for key BBB transporter mRNA transcripts was also made in RBMVECs (**Table 3.7**).

Table 3.7 RT-PCR for carrier mediated transporters including drug resistance transporters in freshly isolated primary rat brain microvascular endothelial cells grown to confluence (7 days) using astrocyte conditioned growth media followed by a 24 hr switch to serum free astrocyte conditioned media containing hydrocortisone (550 nM). The table shows the GenBank mRNA accession number for primer design and primer sequence.

Gene Product	Access. No.	Primer Sequence
Transporters		
GLUT-1	NM_138827	F: gcctgagaccagttgaaagc
		R: gagtgtccgtgtcttcagca
OCT-1	NM_012697	F: ctcccatctatgtgggcatc
		R: ctggttccagtccacctcat
OATP1	50572	F: atcagtttcatctactcacttacagcc
		R: agaaacaggaaatgacacaggagtgag
OATP2	NM_131906	F: ctcatattcaggggcttca
		R: gttcggtggcaaacagttct
PEPT1	NM_057121	F: ccagctgacaagcataaacg
		R: cccacactagaagggtgtgc
PEPT2	NM_031672	F: cgggtctgctaagtttgagg
		R: caagctagcctctggattgg
Drug resistance transporters		
MDR-1a	S96559	F: catccagaacgcagacttga
		R: ctcgcatggtcacagttcat
MDR-1b	X61104	F: accatccagaacgcagactt
		R: acctcaaatactcccagctca
MRP-1	AY170916	F: gcgatcacccatgagtttct
		R: ggatgatgatgacagctcca
MRP-2	NM_012833	F: gacggttggattctgtcacc
		R: cacctgttggaggtaatccag
Positive Control		
B-actin	NM_031144	F: agccatgtacgtagccatcc
		R: ctctcagctgtggtggtgaa

Polymerase chain reaction mix and thermocycling program are detailed in **Table 3.8** and **Table 3.9** respectively.

Table 3.8 Polymerase chain reaction mixture.

PCR component (23.7 µl total volume)	Volume (µl)
dNTP's (5 µM)	2.5
Forward primer (10 pmol.µl^{-1})	2.5
Reverse primer (10 pmol.µl^{-1})	2.5
$MgCl_2$ (25 mM)	1.0
RT mix (100 ng.µl^{-1})	1.0
Taq polymerase buffer (10x)	2.5
Taq polymerase (5 Units.µl^{-1})	0.2
Ultraspec™ DEPC treated water	11.5

Table 3.9 Thermocycling program.

Thermocycling step (30 cycles)	Temperature (°C)	Time (sec)
1. Denaturing	94	30
2. Annealing	60	45
3. Chain extension	72	45

To examine PCR products, samples were electrophoresed (90 volts, 1.5 hrs) through a 2% agarose gel containing 1 µg.ul^{-1} ethidium bromide and visualized under UV light. Negative controls comprised RT-PCR reactions minus cDNA and/or primers.

3.3.13 Effects of C6 co-culture on caveolin-1 expression in PBMVECs

Cryopreserved PBMVECs were grown to confluence on Transwell™ inserts with either PBMVEC growth medium followed by PBMVEC switch medium, astrocyte co-culture (C6 grown on the floor of basal chamber) or astrocyte side-by-side culture (C6 grown on underside of insert direct in apposition to PBMVECs). Cells were processed for Western analysis for caveolin-1 and its phosphorylated form. Cell harvest and processing was completed using standard protocols as previously described in section 3.3.11.1 and in detail in chapter 5. The primary antibody probe was a rabbit anti-caveolin-1

polyclonal antibody diluted 1:4000. Incubation of the primary antibody with the membrane was for 16 hrs at 4°C. The secondary reporter antibody, a HRP conjugated swine anti-rabbit diluted 1:2000, was incubated with the membrane for 1 hr at room temperature. Chemiluminescence signal was generated and recorded onto Hyperfilm ECL. Image acquisition was on a GS-700 densitometer with Molecular Analyst Software (Bio-Rad, Hemel Hempstead, UK).

3.3.14 Identification of cell-surface binding phage

A schematic of the biopanning procedure can be seen in **Figure 3.2.** In total four rounds of phage display were conducted against confluent monolayers of either mouse (b.End3), rat (RBE4) or porcine (PBMVECs) brain microvascular endothelia. Cells were cultured until confluent on 60 mm Petri dishes before incubation with blocking buffer (1% w/v BSA in PBS) for 60 mins at 4°C to reduce non-specific binding. The blocking buffer was aspirated and the cells were exposed to 2 x 10^{11} plaque forming units of Ph.D.™-C7C library in a total volume of 1ml ice-cold DMEM for 1 hr at 4°C; incubation at 4°C was to inhibit endocytosis and thus prevent phage internalization. The supernatant, containing phages that do not bind to cells, was aspirated and discarded. Phages that bind with limited affinity were removed with 10x TBS-T(0.5%) washes. Membrane bound phages were recovered from the cell surface with 3x glycine buffer elutions. The third eluate was neutralized with glycine neutralization buffer then amplified in *E. coli*. After purifying and titering the phage as previously

described (Chapter 2) an aliquot constituting 2 x 10^{11} pfus of phages served as input for the next iterative round of panning; in total four rounds of panning were completed against each cell line before the identity of the displayed peptides were determined by gene sequencing using standard Big Dye v3.1 chemistry on an ABI Prism 3100 genetic analyzer.

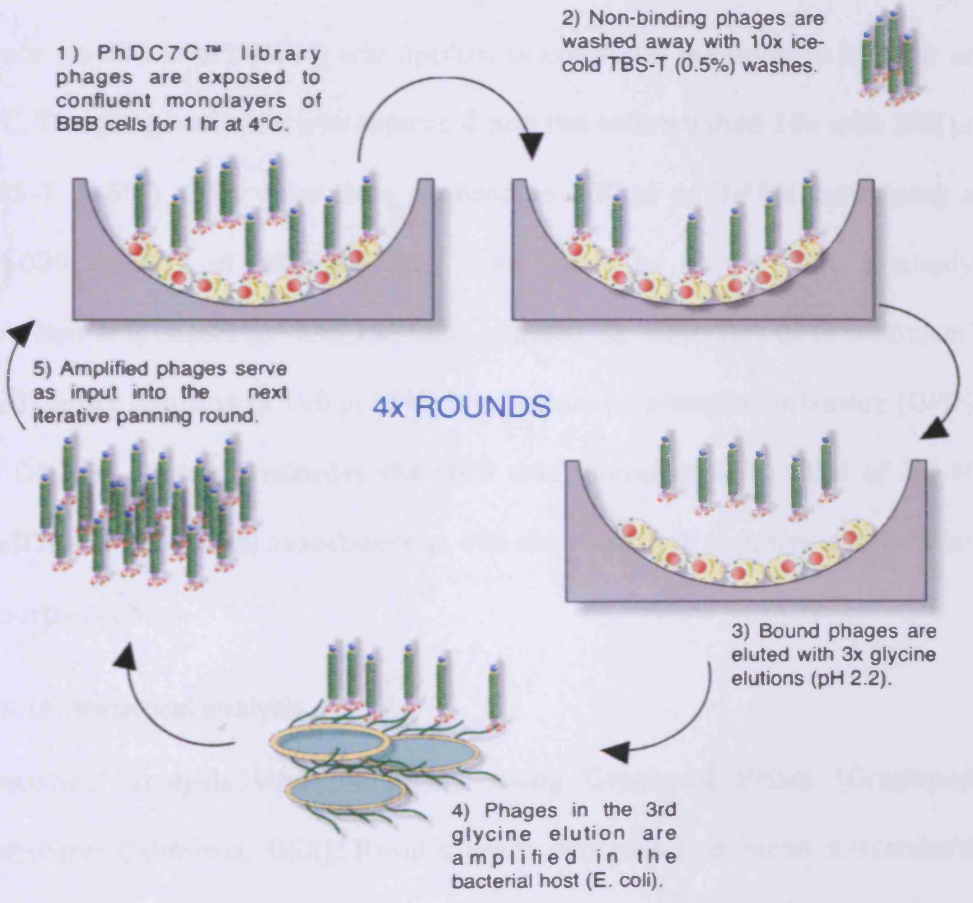

Figure 3.2 Schematic representation of the biopanning procedure used to isolate peptide-phages from the PhDC7C™ library that bind in-vitro blood-brain barrier microvascular endothelia. In total, three cell lines were explored: (i) primary porcine brain microvascular endothelial capillary cells (ii) the mouse brain microvascular endothelia cell line b.End3 and (iii) the rat brain microvascular endothelia cell line RBE4.

3.3.15 ELISA analysis

To monitor for phage enrichment at each panning round, ELISA analysis was undertaken. Essentially, phages from the amplified 3rd glycine elution from rounds 1-3 were applied to confluent monolayers of the respective BBB microvascular endothelial cell culture and the extent of binding determined through ELISA. Specifically 2 x 10^{11} pfus of amplified phage stock (in 100 µl of DMEM) was applied to confluent monolayers for 1 hr at 4°C. The phage solution was aspirated and the cells washed 10x with 200 µl TBS-T (0.5%). Cells were then exposed to 100 µl of DMEM containing a 1:5000 dilution of HRP/anti-M13 mAb for 1 hr at 4°C. The antibody solution was aspirated and the cells washed 3x with 300 µl of deionised H_2O before addition of 100 µl of HRP substrate (o-phenylenediamine (OPD) in DMEM). After 15 minutes the OPD was quenched with 50µl of 2.5 M H_2SO_4 and the optical absorbance at 492 nm recorded; negative control was insertless phage.

3.3.16 Statistical analysis

Statistical analysis was performed using Graphpad Prism (Graphpad Software; California, USA). Results were expressed as mean ± standard deviation (SD) unless otherwise stated. Statistical significance between multiple groups was assessed using a two-way ANOVA followed by a post hoc Bonferroni test. Single group differences were determined using a one-way ANOVA followed by Dunnett's post hoc or by two-tailed Student's t-test. $P < 0.05$ was considered significant.

3.4 Results

3.4.1 Ultra-structural morphology of PBMVECs

Prior to the studies described in section 3.3 a significant number of preliminary investigations and observations were undertaken to progress the establishment of the isolation protocol and maintenance of the resultant cultures. Notably, the source and activity of the digestive enzymes dispase II and dispase-collagenase, the composition of the collagen matrix (type I vs IV), the mass of collagen coated per unit area, the technical procedure for coating and the substitution of horse serum for bovine serum all significantly improved the model quality i.e. growth to confluency without significant visual contamination with non-endothelial cells. In addition small but nevertheless incremental improvements in the model were achieved by investigating seeding density, freezing and thawing processes and the composition of astrocyte conditioned media. Together these investigations formed the groundwork for a robust and reproducible isolation protocol that yields ~ 25 million primary microvascular capillary endothelial cells per brain, sufficient to culture 100 cm^2 at a density of 250 K cells.cm^{-2}. Cells cryopreserved in M199 supplemented with 20% horse serum and 10% DMSO could be rescued from frozen and cultured without apparent phenotypic drift (gross morphology and permeability to radiolabeled probes) at least 1 year from cryopreservation. Freshly isolated, frozen primary and first passage PBMVECs attained confluency within 7 days of seeding ($2.5x10^5$ cells.cm^{-2}) with a doubling time estimated

to be ~ 36 hr. Growth rate was not affected by astrocyte co-culture or astrocyte conditioned medium. In the first 48 hours after seeding, PBMVECs preferentially grew as microvascular endothelial islands gradually expanding to form confluent monolayers with an elongated 'spindle' like morphology (**Figure 3.3A & Figure 3.3B**) that is characteristic of brain microvascular endothelia. PBMVECs cultured from cryopreserved stocks imaged under T.E.M. maintain a squamous morphology (perinuclear thickness ~ 2 μm) extending peripherally to thin attenuations (~ 0.3 μm) (**Figure 3.3C**) that overlap neighbouring cells and are locked together via morphologically evident tight junctional complexes (**Figure 3.3D**). Non-coated membrane invaginations (average diameter 60 - 80 nm) morphologically consistent with caveolae could be observed at both the basolateral and apical domains of the cell (**Figure 3.3E**), the numerical density and topography of which did not alter significantly when exposed to astrocyte co-culture or astrocyte conditioned medium (data not shown). This was true even when C6 astrocytes were cultured in direct apposition with PBMVECs (side-by-side co-culture) separated only by a thin porous membrane (0.4 μm or 3 μm pore size) that afforded direct physical contact between astroglial endfeet and PBMVECs. In a limited number of micrographs electron dense membrane invaginations that are characteristic of clathrin coated pits could be observed (**Figure 3.3F**) but these were observed with an apparent lower numerical density relative to caveolae.

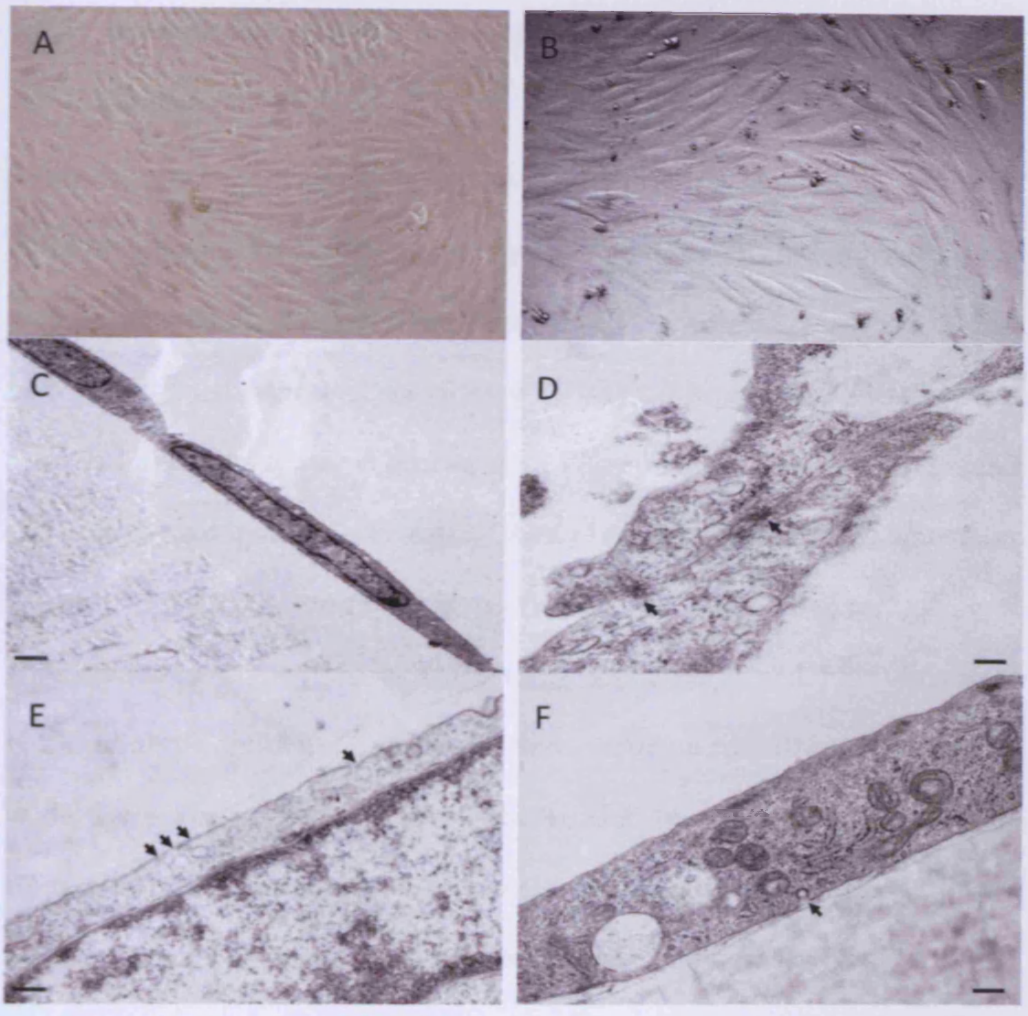

Figure 3.3 Microscopy of PBMVECs (day 7, confluent monolayer) grown on Transwell™ clear membrane inserts. (A & B) Light micrographs (x200 and x500 magnification respectively) revealing a characteristic elongated "spindle" like morphology. (C) Ultrustructural transmission electron microscopic (T.E.M.) image highlighting the squamous morphology of PBMVEC cell monolayers; bar = 200 µm. (D) Monolayers of PBMVECs cultured in the presence of C6 cells retain a squamous morphology, display vesicles on the apical and basal membrane (denoted by dashed arrows) and additionally yield the generation of tight junctional complexes (denoted by solid arrows); bar = 200 nm. (E) T.E.M. analysis of the apical plasmalemma of PBMVECs reveals the presence of non-coated invaginations (denoted by solid arrows) and non-coated intracellular vesicles (denoted by dashed arrow) both of which are morphologically consistent with caveolae; bar = 200 nm. (F) T.E.M. of the apical plasma membrane showing a single invagination consistent with the electron rich coat of a clathrin coated pit (denoted by arrow); bar = 200 nm.

3.4.2 Upregulation of alkaline phosphatase in PBMVECs by C6 conditioned media

In-vivo brain microvascular endothelia expresses significant levels of alkaline phosphatase [78], a recognised marker of the microvascular endothelial cell phenotype. Reductions in ALP synthesis result in a loss of expression on the luminal membrane within 48 hours of *in-vitro* culture. Studies have shown that exposure of *in-vitro* primary brain microvascular cultures to astrocytic cells re-establishes ALP synthesis[79]. To determine whether PBMVECs were responsive to astrocytes or to astrocyte conditioned medium, luminal ALP activity was determined. PBMVECs were cultured until confluent (7 days) in either astrocyte conditioned medium or with astrocyte co-culture after which ALP levels were compared to untreated cells. Untreated cells and cells cultured in astrocyte conditioned medium displayed a low level of constitutive ALP activity (**Figure 3.4A**). However, co-culturing PBMVECs with C6 astrocytes led to significant increases in ALP activity with the earliest time point (10 mins) showing a six-fold increase in ALP activity compared to untreated cells and to cells exposed to astrocyte factors (**Figure 3.4B**). Over the time course of the experiment the ALP activity in the C6 astrocyte co-culture group declined, as a result of both ALP exhaustion and the absence of C6 cells whilst conducting the experiment but still remained significantly higher than untreated cells (**Figure 3.4B**). These results indicate that astrocytes influence the BBB phenotype of endothelial cells *in-vitro* but astrocyte

conditioned medium is incapable of mimicking co-culture in re-establishing ALP expression.

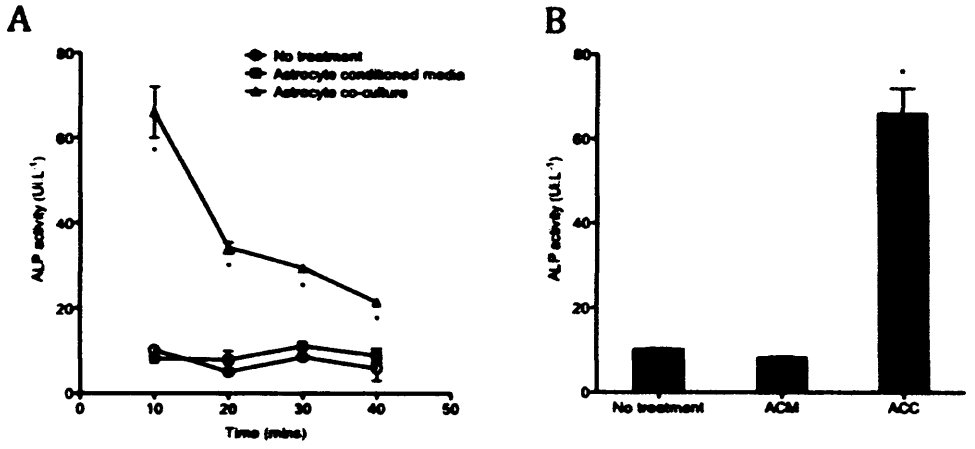

*Figure 3.4 Alkaline phosphatase activity on the luminal membrane of PBMVECs. (A) The constitutive expression of ALP in untreated cells and cells exposed to astrocytic factors in the form of astrocyte conditioned medium (ACM) is low. Co-culturing PBMVECs with C6 astrocytes leads to a significant upregulation in ALP activity that diminishes with time as C6 are withdrawn at the commencement of the study but remains significantly higher than untreated cell and cells exposed to astrocytic conditioned medium. (B) At the first time point in the study (10 min) PBMVECs co-cultured with C6 astrocytes have 6-7 fold greater ALP actitvity than untreated cells and cells exposed to astrocyte conditioned medium. Data are mean ± SD (n =6). * signifies a statistically significant (P < 0.05) difference compared to untreated cells.*

3.4.3 Expression of vesicle associated proteins in PBMVECs

Whilst caveolae appear to be the predominant morphologically evident vesicle type within *in-vivo* brain microvasculature, as previously discussed, intact tissue studies indicate a much lower numerical density of vesicles in the BBB compared to peripheral capillary beds[80]. To determine if the low-density of vesicles reported within brain microvasculature reflects reduced caveolin-1 expression, caveolin-1 comprising the major structural and functional protein of caveolae, an examination of caveolin-1 levels in

PBMVECs was undertaken. **Figure 3.5** shows immunoblots of caveolin-1 from lysates retrieved from a range of porcine and rat tissues as well as from freshly isolated porcine brain microvascular endothelia, cryopreserved primary cultured PBMVECs (approximately 1 month post cryopreservation), 1st passage PBMVECs and from two epithelial cell lines, A431 and MA104, widely used in caveolae research. Initial observations revealed whole brain tissue from both rat and porcine species contained low to neglible levels of caveolin-1 compared to lung tissue when loaded at equivalent milligrams of total protein (**Figure 3.5A**). This is to be expected as the microvasculature comprises < 0.1% of brain tissue volume, although it is recognised that caveolin-1 is present not only in brain endothelial cells but also astrocytes and some specific neuronal populations [81, 82] but still combined these constitute a very small fraction of total brain tissue volume. In stark contrast, the expression of caveolin-1 within freshly isolated PBMVECs approximated (per mg of total protein) that of both MA104 and A431, cells that are recognised to express abundant quantities of caveolin-1 (**Figure 3.5A**). Comparison of the levels of caveolin-1 in freshly isolated brain microvascular cells and cells grown in primary culture (from frozen stocks) or cells taken through a single passage revealed no difference in caveolin-1 expression (**Figure 3.5B**). Curiously, cryopreserved and first passage PBMVEC cells displayed a significantly greater degree of phosphorylated caveolin-1 compared to freshly isolated cells (**Figure 3.5B**).

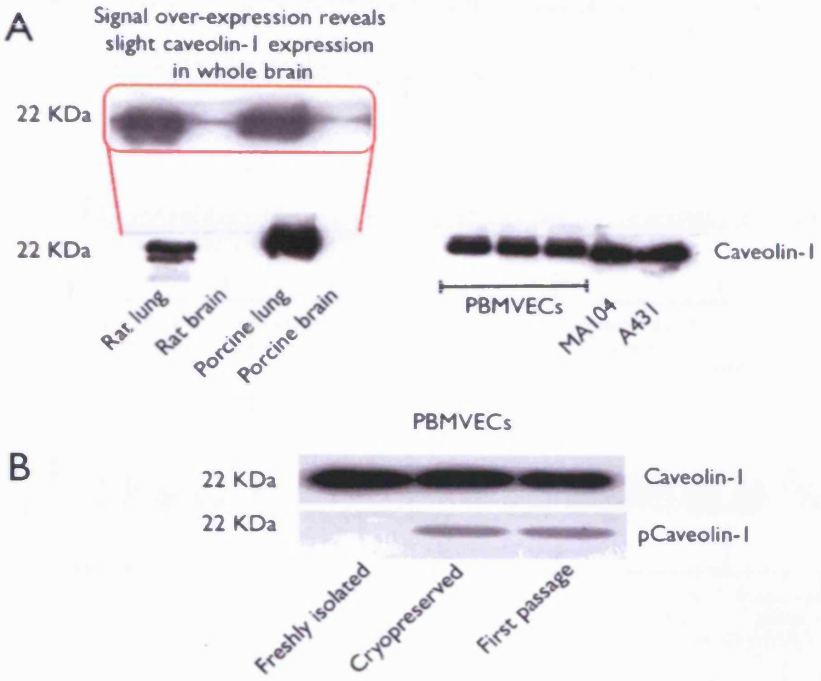

Figure 3.5 Western blot analysis of caveolin-1 in whole tissues, PBMVEC cells and model caveolin-1 cell lines A431 and MA104. (A) Porcine and rat whole lung tissue shows considerable expression of caveolin-1, but significantly there is little expression in whole brain tissues. Freshly isolated porcine brain microvascular endothelia, lysed immediately after isolation, shows a significant expression of caveolin-1, comparable with that of A431 and MA104, cell lines widely used in the study of caveolae and caveolin. (B) Consistent expression of caveolin-1 is confirmed in freshly isolated, primary and 1st passage cultures of PBMVECs. Caveolin-1 in its phosphorylated (activated) state was observed in PBMVECs and 1st passage culture but not freshly isolated endothelia. All lanes were loaded with equivalent total protein (10 μg).

Neither astrocyte co-culture nor astrocyte conditioned medium had any effect on the expression of caveolin-1 or phosphorylated caveolin-1 (pCaveolin-1) in primary PBMVECs grown from cryopreserved stocks (**Figure 3.6**). This was true even when C6 astrocytes were grown in direct apposition to PBMVECs by growing C6 cells on the underside of Transwell™

inserts (0.4 μm and 3.0 μm pore size) such that astrocytic endfeet could invade the Transwell™ and intimately contact the endothelial cells.

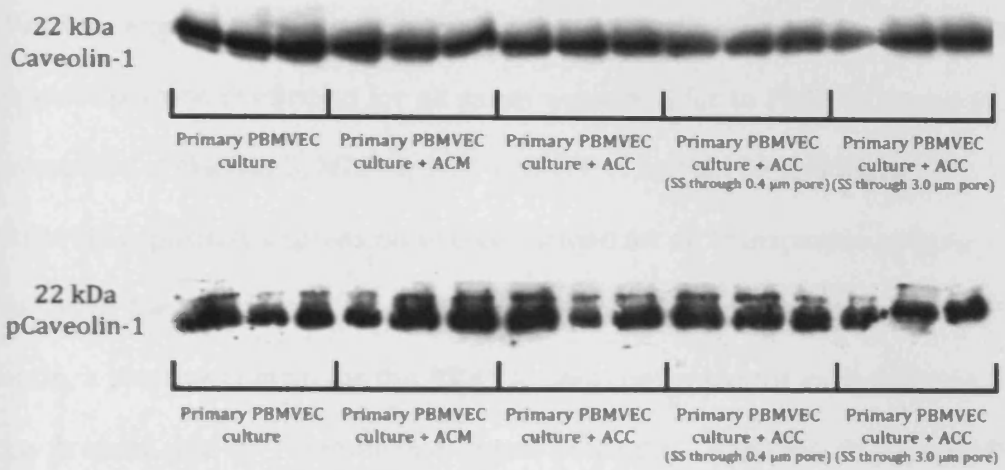

Figure 3.6 Western blot analysis of caveolin-1 and phosphorylated (activated) caveolin-1 (pCaveolin-1) in cryopreserved PBMVECS co-cultured with astrocytes (ACC) or exposed to astrocyte conditioned medium (ACM). Neither ACC nor ACM had any effect on expression of caveolin-1 or its activated phosphorylated form. This was true even when astrocytes were grown in direct apposition to PBMVECs in a 'side-by-side' culture system (SS) that allows astrocytic endfeet to invade the Transwell™ membrane and intimately interact with the basal membrane of PBMVECs.

3.4.4 mRNA expression of key BBB components in PBMVECs and RBMVECs

Confirmation of mRNA expression of tight junctional components and carrier transporters in PBMVECs cultured from frozen stocks of PBMVECs was accomplished by undertaking RT-PCR upon RNA extracted from confluent monolayers of PBMVECs (three separate isolations) exposed to C6 astroglial factors during culture; the analysis was limited to genes that have been identified in the pig genome and can be found in the pig database at http://www.ncbi.nlm.nih.gov/projects/genome/guide/pig/.

Table 3.6 and **Table 3.7** details mRNA accession number (Genbank) used for PCR primer design for PBMVECs and RBMVECs respectively, the primer sequences subsequently designed and the expected PCR product size. Positive expression of tight junctional elements and transporter mRNA transcripts was confirmed for all genes examined for in PBMVECs with the exception of claudin-3, MRP-2, OCT-1, OATP-A and OATP-C (**Figure 3.7**). In RBMVECs, positive expression was confirmed for all transporters examined for with the exception of OCT-1 and OATP2 .The house-keeping gene β-actin, a positive control for the RT-PCR, was confirmed for each PCR run to be present and of reproducible signal strength. Negative PCR controls comprised minus RT enzyme and minus cDNA. An absence of genomic DNA contamination was confirmed for each sample.

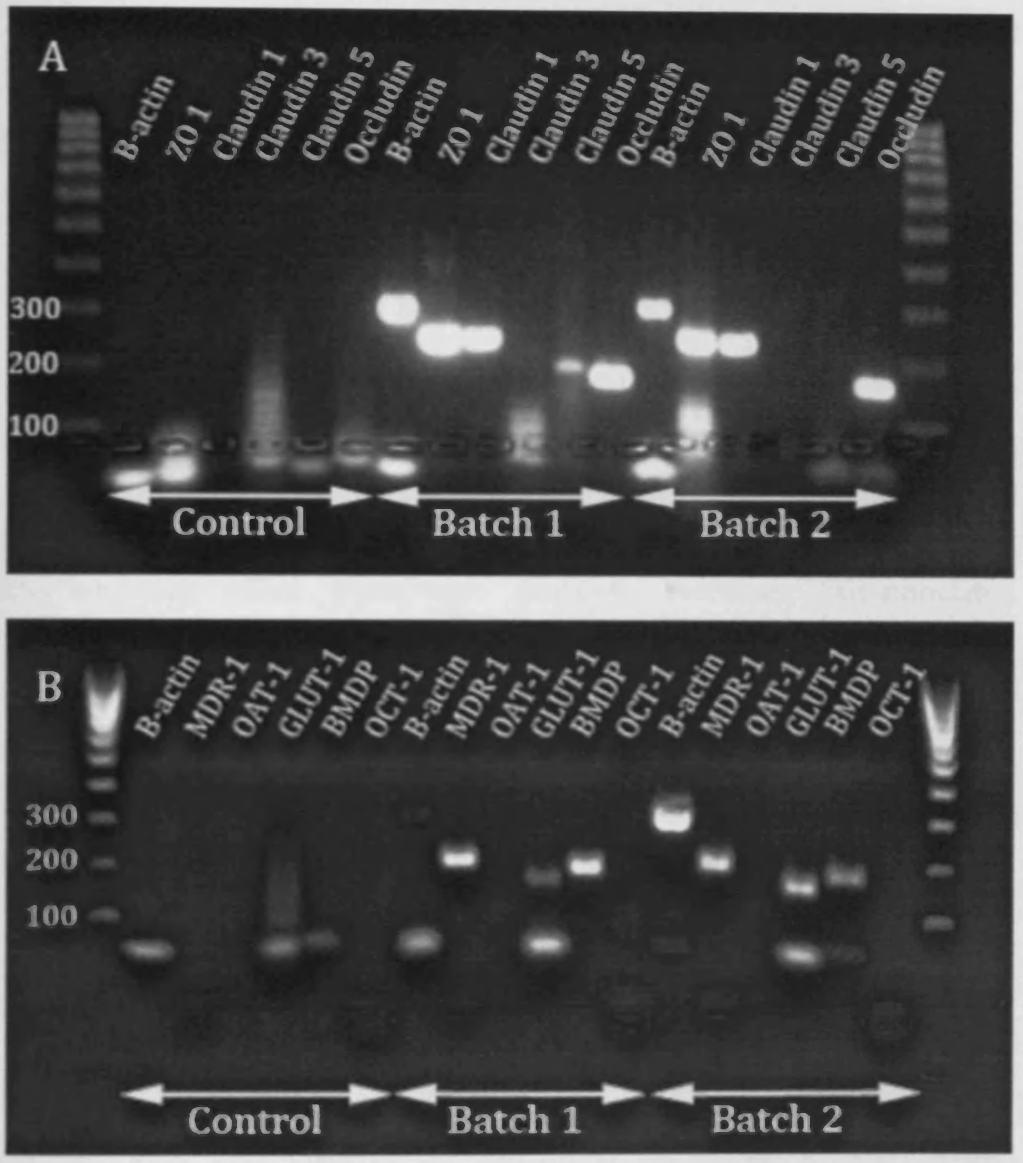

Figure 3.7 mRNA expression of tight junctional elements and transporters within two representative PBMVEC isolations. (A) mRNA transcripts were confirmed for tight junctional elements ZO-1, Claudin-1, Claudin-5 and Occludin but expression of Claudin-3 was not observed in any isolation. (B) Transcripts for the principle glucose transporter GLUT-1 were confirmed as was expression for the multidrug resistance transporters MDR-1 and brain multidrug resistance protein BMDP. Note bands < 100bp in Control are cDNA from RT-PCR minus primers and do not represent mRNA transcripts.

3.4.5 Functional expression of the P-gp efflux transporter in PBMVEC cells

After confirming P-glycoprotein (MDR-1) expression at both the mRNA level using RT-PCR (**Figure 3.7B**) and the protein level using Western analysis (**Figure 3.8 inset**), functional assessment of P-gp mediated efflux within PBMVEC cells grown from frozen stocks was undertaken. This was accomplished using a flow-cytometric assay to monitor accumulation and retention of the fluorescent P-gp substrate rhodamine-123 in the presence and absence of the selective P-gp inhibitor verapamil (40 μM). Verapamil, by inhibiting efflux transporter function, increases cell-associated rhodamine-123 at the end of both accumulation and retention phases in P-gp positive cell lines. **Figure 3.8A** and **3.8B** shows the respective accumulation and retention of rhodamine-123 in PBMVEC cells. Verapamil exposure leads to a significant ($P < 0.05$) increase in rhodamine-123 accumulation of approximately 350%, while at the end of the retention phase, a more sensitive indicator of P-gp functionality, verapamil exposure significantly increased ($P < 0.05$) cell-associated rhodamine-123 by ~ 750%. These data confirm the functional expression of P-gp within PBMVECs.

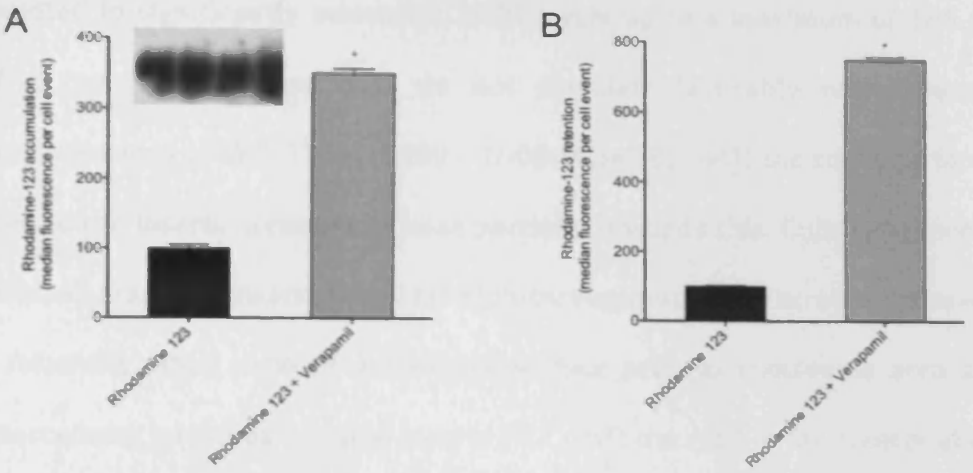

*Figure 3.8 Functional P-gp activity in PBMVEC cells. Intracellular accumulation (A) and retention (B) of rhodamine-123. Accumulation – Cells were incubated for 45 min at 37°C in media containing rhodamine-123 ± verapamil. Retention – After an accumulation phase cells were washed with PBS and rhodamine-123 effluxed over 90 min at 37°C in rhodamine-123-free media ± verapamil. Data are expressed as % of rhodamine-123 control (100%) as mean ± S.D. (n = 6). * signifies a statistically significant (P < 0.05) difference compared to respective control. Inset A: strong and consistent signal strength in Western blot analysis for P-gp in four batches of PBMVECs.*

3.4.6 Permeability assessments in PBMVECs

After confirming that cryopreserved stocks of PBMVECs were responsive to astrocytes, the permeability properties of confluent monolayers of PBMVECs were assessed in the presence or absence of astrocyte co-culture or astrocyte conditioned medium. Exposing PBMVECs to soluble astroglial factors in small Transwell™ inserts (6.5 mm diameter; 0.33 cm^2) resulted in TEER measurements across the monolayers of up to 75.0 ± 1.7 $\Omega.cm^2$ at day 8 post-seeding. Exchanging the culture medium for a 'switch' medium that was serum free but supplemented with physiological concentrations of hydrocortisone (550 nM) and modulators of cAMP for a 24 hr period

resulted in significantly increased TEER levels up to a maximum of 185 ± 16 Ω.cm^2. Whilst these data do not correlate favorably with *in-vivo* measurements of BBB TEER (1500 – 2000 Ω.cm^2[83, 84]) the small surface area of the inserts accounts at least partially towards this. Cultures grown on small diameter inserts (ideal for high-throughput solute screening) have a relatively small ratio of monolayer surface area to transverse area at intercellular junctions. In large inserts (4.7 cm^2) the ratio is far greater and TEER values are significantly higher (in the supervisor's laboratory up to 834 ± 136 Ω.cm^2 with C6 co-culture[85]) and more closely correlate with *in-vivo* TEER.

The discriminative power of a BBB model to paracellular and transcellular probes is often a better measure of monolayer restrictiveness than TEER. Therefore, to further characterize the paracellular barrier within cultured PBMVECs, the permeability of confluent monolayers to the paracellular probe [^{3}H]sucrose and to the transcellular probe [^{14}C]diazepam was determined within the same insert such that the permeability to each probe reflects the same cell monolayer. **Figure 3.9** shows the variability between three different isolations. Whilst all isolations showed significant difference ($p < 0.05$) between sucrose and diazepam permeability coefficients within a given isolation, there was no significant difference in sucrose or diazepam permeabilities between isolations and the isolation protocol developed as detailed in 3.3.3 was thus shown to be highly reproducible.

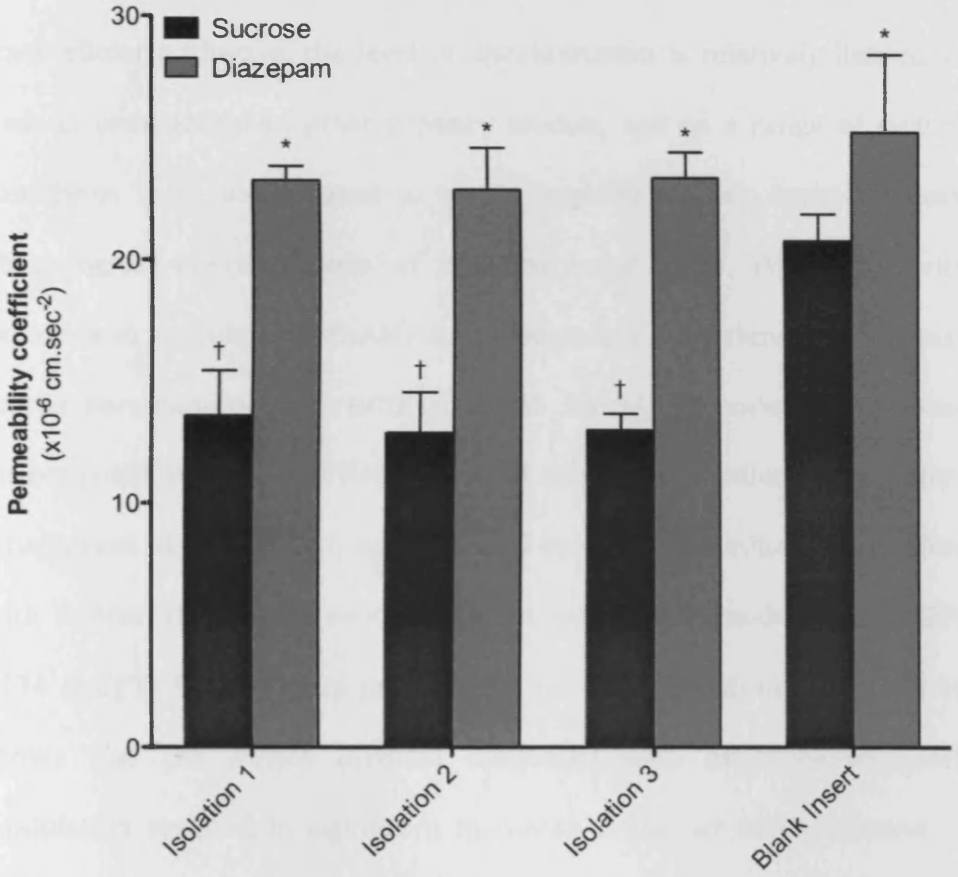

*Figure 3.9 Permeability to sucrose and diazepam probes in three PBMVEC isolations. PBMVECs were thawed from frozen stocks and cultured in growth medium for 7 days. The permeability to sucrose and diazepam was then determined. All isolations show a significant difference ($p<0.05$) between sucrose and diazepam permeability coefficients i.e. discrimination between paracellular and transcellular pathways. However no statistically significant difference was observed between isolation batches. No difference in permeability to diazepam was observed between cell isolations and blank RTCI coated inserts indicative of PBMVECs offering limited resistance to transcellular passage of solutes. Conversely the significant difference in sucrose permeability between isolations and blank inserts shows that PBMVECs restrict paracellular diffusion pathways. Data represent mean ± SD (n = 4-6). * signifies a statistically significant difference ($P < 0.05$) between sucrose and diazepam permeability co-efficients. † signifies a statistically significant difference ($P < 0.05$) between sucrose permeabilities in PBMVECs and blank inserts.*

Whilst the batches showed discrimination between paracellular and transcellular pathways, the level of discrimination is relatively limited, at least in comparison to other primary models, and so a range of culture conditions were investigated to try to improve barrier restrictiveness. Physiological concentrations of hydrocortisone (550 nM) along with exposure to modulators of cAMP have previously been shown to decrease barrier permeability at the BBB[18, 19, 25, 86, 87]. To understand if these factors could improve the PBMVEC model, the culture medium on confluent monolayers (day 7 *in-vitro*) was replaced by a switch medium (serum free with hydrocortisone) or switch medium with cAMP modulators (Ro20-1274 & CPT) for 24 hours prior to the permeability study. **Figure 3.10** shows that the switch medium combined with exposure to cAMP modulators resulted in significant increases in barrier restrictiveness as evidenced by decreases in permeability to sucrose in comparison to non-treated cells. Cells undergoing a switch procedure without cAMP modulators showed numerical but not significant decrease in permeability compared to switch alone.

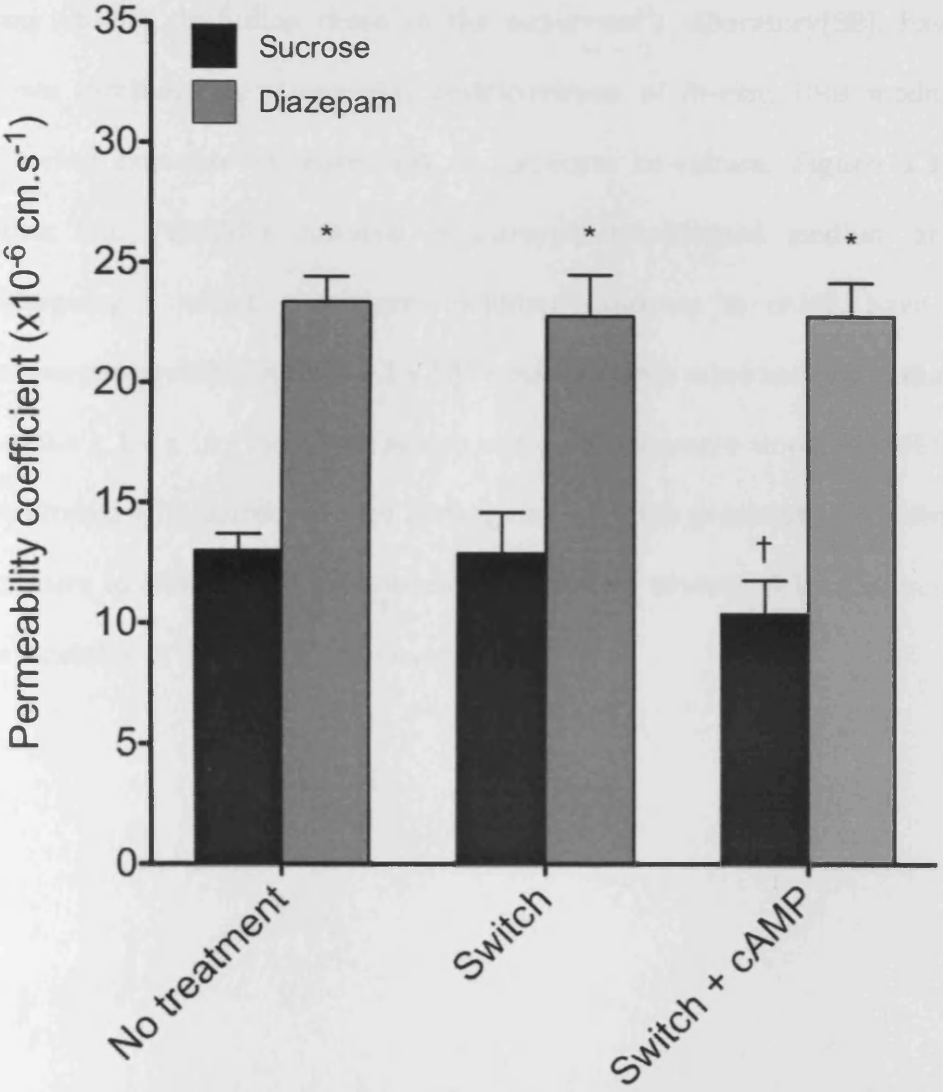

Figure 3.10 *Effect of hydrocortisone and cAMP elevators on the permeability of PBMVECs to paracellular and transcellular probes. After 7 days culture in growth medium, serum was withdrawn from confluent monolayers of PBMVECs and cells were exposed for 24 hours to either hydrocortisone (550 nM; Switch) or hydrocortisone and cAMP elevators (Ro20-1274, 20 μM; CPT, 250 μM; Switch + cAMP). Hydrocortisone alone did not lead to an increase in paracellular restrictiveness. Exposure to hydrocortisone and the cAMP modulators resulted in a statistically significant reduction in sucrose permeability indicative of enhanced paracellular restriction. In all treatments, statistically significant discrimination between paracellular (sucrose) and transcellular (diazepam) probes was observed. Data represent mean ± SD (n = 4). * represents a statistically significant difference (P < 0.05) between sucrose and diazepam permeability co-efficients. † represents a statistically significant difference (P < 0.05) between sucrose permeabilities compared to control untreated cells.*

Many studies, including those in the supervisor's laboratory[88], have shown increases in paracellular restrictiveness of *in-vitro* BBB models following exposure to astrocytes or astrocyte co-culture. **Figure 3.11** shows that PBMVECs cultured in astrocyte conditioned medium and undergoing a switch procedure, including exposure to cAMP, have a sucrose permeability of 8.6 ± 1.1 x 10^{-6} cm.s^{-1} which is more restrictive than the 10.4 ± 1.4 x 10^{-6} cm.s^{-1} for switch and cAMP exposure alone. PBMVECs co-cultured with astrocytes and undergoing a switch procedure, including exposure to cAMP, were even more restrictive as evidenced by a sucrose permeability of 7.5 ± 0.7 x 10^{-6} cm.s^{-1}.

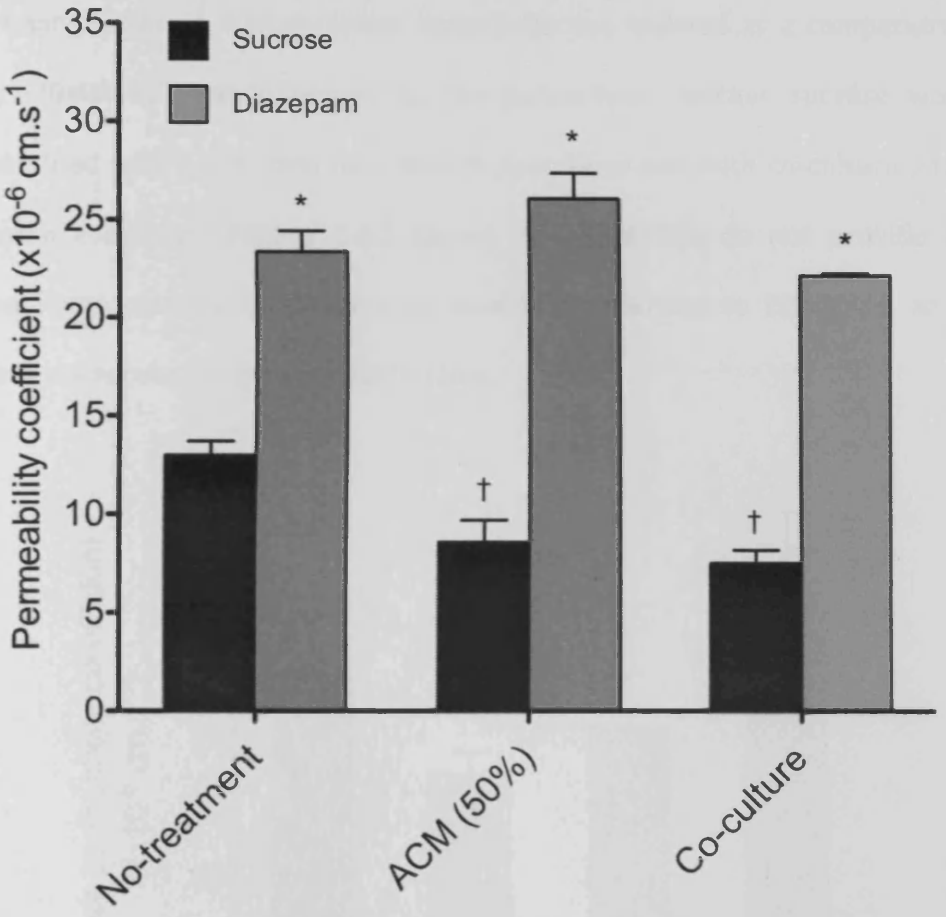

*Figure 3.11 Effect of hydrocortisone and cAMP elevation combined with exposure to astroglial factors or astrocyte co-culture on PBMVEC permeability to paracellular and transcellular probes. PBMVECs were cultured until confluent (7 days) in astrocyte conditioned medium or in the presence of astrocyte co-culture and then switched to a serum free medium containing hydrocortisone and cAMP elevators for 24 hours before transport studies were conducted. In all treatment groups statistically significant discrimination between paracellular and transcellular probes was observed. Exposure of PBMVECs to astrocyte conditioned medium followed by the switch procedure at day 7 resulted in a statistically significant increase in paracellular restrictiveness as evidenced by a reduction in permeability to sucrose. Co-culturing the cells with astrocytes followed by the switch procedure at day 7 resulted in a further significant reduction in sucrose permeability compared to both untreated cells and cells exposed to astroglial factors. Data are mean ± SD (n = 4-6). * represents a statistically significant difference (P < 0.05) between diazepam and sucrose permeability co-efficients. † represents a statistically significant difference (P < 0.05) between sucrose permeabilities compared to control untreated cells.*

Primary rat brain microvascular endothelia was isolated as a comparator for PBMVECs. Restrictiveness to the paracellular marker sucrose was examined with C6 co-culture, a switch procedure and with co-culture and switch combined. **Figure 3.12** shows that RBMVECs do not provide a restrictive paracellular barrier, at least in comparison to PBMVECs, and were unresponsive to astrocytic factors.

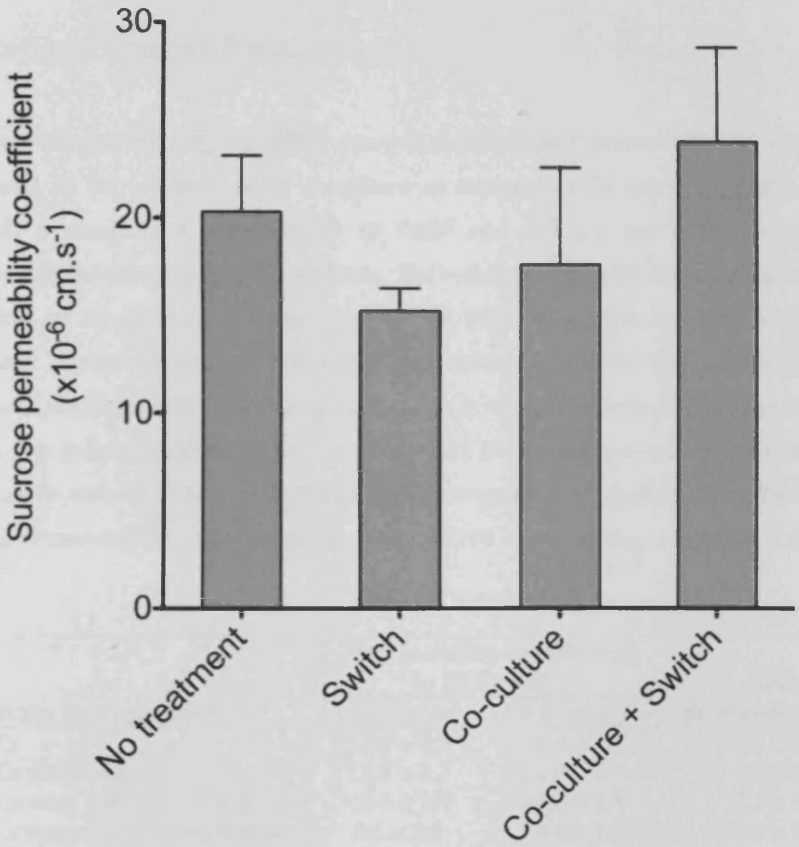

Figure 3.12 Permeability to sucrose in freshly isolated rat primary brain microvascular endothelia. Cells did not exhibit significant paracellular restrictiveness under any of the conditions investigated.

The data in Figures 3.9 – 3.12 are summarised in **Table 3.10** and include sucrose and diazepam permeability data under all conditions tested and

also the ratio between sucrose and diazepam to show the level of discrimination between the paracellular and transcellular pathway. These data clearly indicate that the greatest paracellular restriction is achieved in PBMVECs co-cultured with astrocytes and undergoing a switch procedure with hydrocortisone and modulators of cAMP. However, the discrimination between paracellular and transcellular pathways is the same when the co-culture model or conditioned medium model are exposed to hydrocortisone and cAMP modulators.

Table 3.10 Permeability coefficients for sucrose and diazepam across PBMVEC monolayers grown alone, in the presence of C6 co-culture or exposed to C6 astroglial factors during growth. As a comparator, permeability of RBE4 and primary rat brain microvascular endothelia and the membrane alone is shown. The ratio of permeabilities (diazepam:sucrose) is indicative of the level of discrimination of the BBB model between transcellular and paracellular probes. Untreated PBMVECs discriminate between the paracellular and transcellular pathways although the discrimination is relatively limited (diazepam:sucrose = 1.8 ± 0.6). The greatest discrimination combined with the lowest permeability to sucrose was observed when cells were both co-cultured with astrocytes until confluent and then exposed to hydrocortisone and the cAMP modulators Ro20-1274 and CPT. Data are mean ± SD (n = 4-6).

Blood-brain barrier model	Permeability co-efficient ($\times 10^{-6}$ cm.s^{-1}) [^{14}C]Sucrose	[^{3}H]Diazepam	Ratio diazepam:sucrose
PBMVECs	13.0 ± 0.7	23.4 ± 1.1	1.8 ± 0.6
PBMVECs with switch	12.9 ± 1.7	22.8 ± 1.7	1.8 ± 0.1
PBMVECs with 'switch' + cAMP	10.4 ± 1.4	22.8 ± 1.4	2.2 ± 0.2
PBMVECs exposed to C6 astroglial factors with 'switch' + cAMP	8.6 ± 1.1	26.1 ± 1.3	3.0 ± 0.3
PBMVECs with C6 co-culture and with 'switch' + cAMP	7.5 ± 0.7	22.2 ± 0.1	2.9 ± 0.1
Primary rat BBB with C6 co-culture	17.6 ± 5.0	-	NA
RBE4	45.46 ± 2.5	-	NA
Membrane (polyester, 0.33 cm^2)	21.0 ± 0.73	26.4 ± 0.9	1.3 ± 0.005
Membrane (polyester, 0.33 cm^2) collagen coated	18.6 ± 3.3	24.7 ± 1.5	1.2 ± 0.04

3.4.7 Selection of brain microvascular endothelia cell surface binding peptide-phages

A series of *in-vitro* biopanning experiments, detailed in section 3.3.14, were conducted against confluent monolayers of porcine (PBMVECs), rat (RBE4) and mouse (b.End3) brain microvascular endothelia to identify cell surface binding peptides; preliminary studies revealed that even after short exposure times, *in-vitro* BBB models were not restrictive to the passage of insertless-M13 across cell monolayers. Ph.D.™-C7C library phages were incubated with cell monolayers at 4°C to block endocytic processes that would internalize the phages. After four rounds of panning against each of the respective cell lines, the pool of phages recovered in the final 3rd glycine elution were gene sequenced collectively to identify if a common motif had been selected. If there is sufficient penetration of the phage population with clones displaying a common motif, sequence traces will expose this despite 'contamination' with phages that do not display the motif. In each cell line investigated, the gene sequence for the pool did not indicate a conserved motif or sequence. This is in contrast for example to biopanning studies against streptavidin where sequencing of the collective pool of phage in the 3rd glycine elution of the third round of panning revealed a common sequence of AC-**GTFIHPQ**-CGGGS that was present in sufficient copy number to dominate the population. In addition ELISA studies to monitor phage binding after each round of panning did not reveal any binding above background insertless-phages suggestive of a failed selection protocol (data not shown).

Nevertheless a number of clones from each cell line recovered in glycine elution 3 of round 4 were sequenced individually (see **Table 3.11**) and these were inputted into a BLAST search to identify any homologies with known peptides or proteins that traverse or interact with the BBB.

Table 3.11 Amino acid sequences of brain microvascular endothelial cell surface associated phage clones.

Cell line	Peptide sequence
b.End3	AC-NTSVSKW-CGGGS
	AC-NSPRHWT-CGGGS
	AC-THPIHQM-CGGGS
	AC-SNGFSRS-CGGGS
	AC-PTQGPHN-CGGGS
PBMVEC	AC-NDPLHTT-CGGGS
	AC-NPVGFQY-CGGGS
	AC-KFLQTSC-CGGGS
	AC-DSRATAS-CGGGS
	AC-PSHPQAL-CGGGS
RBE4	AC-NELGHYQ-CGGGS
	AC-KANNHYH-CGGGS
	AC-SIHSPRV-CGGGS
	AC-NLTLKNL-CGGGS
	AC-SPGHGRL-CGGGS
	AC-LDTSPRL-CGGGS

BLAST analysis revealed that sequence NTSVSKW shares significant homology with a region of the V3 loop of HIV GP120, which studies have shown has a role in the cellular uptake of HIV[89]. In studies that parallel those described in detail in chapter 4, this phage clone was co-injected into a rat along with insertless phages to assess brain accumulation but unfortunately the clone did not show any increased entry into the brain compared to insertless phages (data not shown).

3.5 Discussion

The research and development of brain therapeutics and brain targeting vectors would benefit significantly from the availability of a robust and reproducible *in-vitro* cell culture model that mimics the *in-vivo* blood-brain barrier in terms of morphology, barrier restrictiveness and biochemistry that would complement both *in-situ* brain models and *in-silico* assessments of drug physicochemical properties. Classically both industry and academia have utilized immortalized epithelial cell lines for mid to high throughput screening of potential CNS active therapeutics[90]. Unfortunately the non-cerebral origin of these cell lines often limit their use as predictors of CNS penetration since differences in both architecture and biochemistry commonly result in a poor correlation between *in-vitro* and *in-vivo* permeation. An *in-vitro* blood-brain barrier model that more closely resembles the *in-vivo* blood-brain barrier architecture would provide a system to address both fundamental mechanistic aspects of BBB drug transport and quantitative drug permeation. The potential for *in-vitro* BBB models to serve as high throughput permeability screens to determine whether lead compounds that show activity on the bench top are likely to accumulate in the central nervous system at a sufficient concentration to result in a therapeutic effect is of significant interest within the pharmaceutical industry. With many brain microvascular models lacking a sufficiently restrictive paracellular pathway the establishment of a robust and reproducible model remains a continuing challenge. It must be noted that membrane partitioning effects, active influx and efflux transporters

and metabolic systems unique to the BBB phenotype contribute to a dynamic overall barrier permeability and should be accounted for in any model developed. Primary cultures of non-transformed BBB endothelial cells retain the closest phenotype to the *in-vivo* environment however perceived technical challenges and high costs associated with isolation, at least in comparison to transformed cell lines, has dissuaded many researchers from exploiting primary resources. The low cell yield from rat and mice brains and the ethical and tissue constraints associated with isolating human BBB cell models has meant that the isolation of bovine and porcine material has received the most attention. Whilst isolations of bovine and porcine material are time-consuming, a large amount of material is isolated which is often discarded either because the material is not required or because there is insufficient time to culture all the material at once. The ability to store the isolated primary material for extended time periods without loss of cell viability, phenotype or function when recovered would benefit researchers immensely. In this chapter characterization of primary cultures of porcine brain microvascular endothelial cells recovered from cryopreserved stocks was undertaken to assess their usefulness as a pharmaceutical blood-brain barrier model and specifically as a model to afford the selection of phages that bind brain microvasculature. PBMVECs were isolated by enzymatic digestion of homogenates of porcine brain grey matter tissue firstly by dispase and then collagenase/dispase. Density centrifugations through Percoll gradients were used to separate microvascular capillaries from other tissue types after the first digestion

and then to separate microvascular capillary fragments from cellular debris after the second digestion. Each porcine brain (<5 month old pigs) yielded approximately 25 million endothelial cells providing sufficient material for many studies based upon an initial seeding density of 250 $k.cm^{-2}$. The isolated cells were cryopreserved in 10% DMSO, 20% Horse serum and 70% M199 to yield 10 vials per brain i.e. 2.5 million cells per vial. Cells could be recovered from frozen stocks at least 12 months after cryopreservation with no apparent loss in cell viability retaining a plating efficiency of 50-60%. PBMVECs and RBMVECs (isolated as a comparator for PBMVECs) had a clear requirement for an extracellular matrix without which cell colonies did not spread and confluency was never achieved. Coating culture surfaces with rat tail collagen type I at a density of 3 $\mu g.cm^{-2}$ proved successful for all applications used in the studies in this chapter. It must be noted that the source of collagen was critical in establishing optimal growth of PBMVECs and all studies were undertaken using collagen from Roche Applied Biosciences; collagen obtained from alternative suppliers led to inconsistent growth patterns. In addition, the technique of coating was important, with experimentation in the production of collagen gels using ammonia unsuccessful, as were collagen concentrations less than 3 $\mu g.cm^{-2}$ and greater than 5 $\mu g.cm^{-2}$. In contrast to Galla's work, no significant difference was observed in culture reproducibility with different combinations of collagen (Type I/IV), fibronectin or laminin[91].

Microscopic examination of PBMVECs cultured from cryopreserved stocks revealed a gross morphology consistent with endothelial architecture, specifically a spindle-like, squamous and attenuated morphology with cell dimensions typical of other brain microvascular cells. In electron micrographs adjacent endothelial cells were seen to overlap and were 'locked' together by tight-junctional complexes. In support of these observations, RT-PCR confirmed mRNA transcripts for tight-junctional elements including zonnula occludens 1, occludin, claudin-1 and the endothelial specific claudin-5.

Increases in ALP activity when PBMVECs are cultured with C6 astrocytes indicated their responsiveness to astrocytic factors although astrocyte conditioned medium did not result in significant increases in ALP activity. In contrast, exposure of PBMVECs to C6 conditioned medium as well as when co-cultured with C6 astrocytes profoundly increased barrier restrictiveness as evidenced by significant reductions in permeability to the paracellular probe sucrose. In addition, a switch strategy first described by Galla and co-workers[27] was adopted whereby when the monolayer reached confluence (day 7) serum was withdrawn from the culture and supplemented with physiological concentrations of hydrocortisone and with Ro20-1274 and CPT (modulators of cAMP)[27]. Consistent with the findings of Galla et al[27] the switch procedure led to increased barrier restrictiveness particularly when cAMP modulators were incorporated into the switch procedure. It was clear however that the most restrictive

phenotype was observed with PBMVECs co-cultured with C6 astrocytes and undergoing the switch strategy leading to a diazepam:sucrose ratio of ~ 3 compared to ~ 1.8 for cells cultured without any treatments. Whilst the PBMVEC model developed is partially responsive to astrocyte conditioned medium (increases in paracellular restrictivness but unresponsive in ALP assessments), co-culture with astrocytes was deemed superior. Unfortunately, the understanding of the exact identity and concentrations of astrocytic factors required for upregulation of various BBB phenotypic markers remains poorly understood and indeed some research groups have failed to isolate primary BBB cells that respond to astrocytic factors either in conditioned medium or when in co-culture and almost without exception continuous cell lines are unresponsive[88]. It is clear that the dynamic interplay, both physical and biochemical, between astrocytes and brain microvascular endothelia is complex. A full and detailed analysis to characterize both the identity and concentration of soluble factors secreted by astrocytes, using such techniques as mass spectrometry and chromatographic techniques, whilst laborious would prove invaluable in further optimizing BBB models.

In contrast to other investigators the aim of the studies has been to utilize only primary cultures or PBMVECs retrieved from cryopreservation and not early passage cells where phenotypic drift can become an issue. Primary monolayers cultured in the absence of astrocyte factors retained modest barrier restrictivness with sucrose permeabilities > 10 x 10^{-6} $cm.s^{-1}$

and with some discrimination between paracellular and transcellular pathways (ratio sucrose:diazepam ~ 2). This is superior to primary bovine cultures (sucrose permeability 10-24 x 10^{-6} $cm.s^{-1}$), primary rat cultures (sucrose permeability with C6 co-culture 18 x 10^{-6} $cm.s^{-1}$), immortalized rat cells (sucrose permeability ~ 35 x 10^{-6} $cm.s^{-1}$) and immortalized murine models (sucrose permeability with C6 co-culture ~ 20 x 10-6 $cm.s^{-1}$). Co-culturing PBMVECs with astrocyte factors followed by a switch procedure and exposure to modulators of cAMP led to a significant enhancement of paracellular barrier restrictiveness as evidenced by low absolute permeabilities to sucrose of ~ 7.5 x $10^{-6}cm.s^{-1}$ in PBMVECs co-cultured with C6 and subject to the switch procedure. It is worth noting that the permeability and bioelectric properties of PBMVECs examined in this chapter were all made on 'small' Transwell™ inserts (surface area 0.33 cm^2) to provide a high-throughput model of the BBB. Our own studies[85] have shown that when PBMVECs are cultured on large inserts (4.7 cm2), a greater restriction in the paracellular pathway is observed particularly with astrocyte co-culture **Table 3.12**. As previously described this is largely due to the relatively small ratio of monolayer surface area to transverse area at intercellular junctions (leakiest area) in small inserts compared to large.

Table 3.12 Permeability coefficients for sucrose and propranolol across PBMVEC monolayers cultured on large inserts (4.7 cm²) either alone or in the presence of C6 co-culture or exposed to C6 astroglial factors during growth. Adapted from [85]. PBMVECs grown on large inserts co-cultured with C6 and undergoing a switch procedure with cAMP modulation have a transcellular:paracellular discrimination ratio of ~ 11.5 this compares ~ 3 under the same conditions but grown on small inserts.

Blood-brain barrier model	Permeability co-efficient (x 10^{-6} cm.s^{-1})		Ratio propranolol:sucrose
	[14C]Sucrose	[3H]Propranolol	
PBMVECs	12.1 ± 1.3	25.4 ± 1.8	2.1 ± 1.4
PBMVECs exposed to C6 astroglial factors with 'switch' + cAMP	8.8 ± 1.2	26.0 ± 1.3	2.95 ± 1.1
PBMVECs with C6 co-culture and 'switch' + cAMP	1.6 ± 1.0	18.4 ± 0.7	11.5 ± 0.7

Blood-brain barrier specific endocytic, transcytotic and transporter systems that either deliver nutrients into brain parenchyma or efflux potentially toxic xenobiotics away from brain parenchyma are an essential feature of the BBB and their identification in any BBB model is a distinguishing feature compared to *in-vitro* models of non-cerebral origin. Brain microvasculature is highly selective with respect to vesicular mediated transport with morphometric studies revealing a decreased numerical density of vesicles within brain microvasculature. However, highly regulated endocytic and transcytotic processes at the BBB are an essential requirement for the delivery of solutes into brain parenchyma and are a feature of normal BBB physiology. Within PBMVEC cells, membrane vesicles of both caveolae and clathrin coated pit morphology were evident with the apparent density of caveolae greater than clathrin coated pits (although detailed morphometric analysis was not undertaken to confirm this). This is consistent with studies that have shown strong staining of

caveolin-1 at the immunohistochemical level in brain microvascular endothelial cells as a component of the caveolar compartment[81]. Given the effects of astrocytic interaction on PBMVEC cell phenotype, it is not unreasonable then to question if astrocytes have an effect on the expression of caveolin-1 which, given the direct association of this integral membrane protein and key structural element with caveolae, may subsequently lead to changes in numerical density of caveolae vesicles or indeed alterations in topography. Immunoblot analysis of caveolin-1 revealed strong expression in freshly isolated primary, cryopreserved primary and first passage PBMVECs that was not affected by either co-culture with astrocytes or exposure to astrocyte conditioned medium. The phosphorylated form of caveolin-1 demonstrated strong expression in cryopreserved primary and first passage PBMVECs and was not affected by exposure to astrocytic factors. However, expression of phosphorylated caveolin-1 in freshly isolated PBMVECs was consistently negligible. Whilst evidence is beginning to emerge that an up-regulation in phosphorylated caveolin-1 may be associated with BBB breakdown, this is normally accompanied by up-regulation in total caveolin-1[92]. This was not observed in cryopreserved primary or first passage cells. It is curious that in non-brain endothelia, an up-regulation in phosphorylated caveolin-1 (with total caveolin-1 remaining consistent) is associated with increased caveolae vesicle budding and with increased vesicle internalization and therefore reflects the inherent endocytic capacity of the cell[93]. This warrants further investigation in porcine brain microvascular endothelia.

Carrier transporters play a key role in nutrient and drug entry and efflux from the brain. Whilst the pig genome is not fully sequenced, a range of putative genes for carrier transporters of pharmaceutical interest have been identified and mRNA transcripts for these transporters were examined for. Positive expression was confirmed for drug efflux transporters (MDR-1, MRP1 and BMDP), cation transporters (OCT-1) and cationic and neutral amino acid transporters (CAA-1 and NAA-1 respectively). Additionally, positive expression was confirmed for the long form of leptin receptor (OB-Rb), which has a long intracellular domain essential for signal transduction purposes. Ob-Rb, expressed within the cerebellum and hypothalamus on neuropeptidergic neurons, plays a key role in the regulation of food intake and energy expenditure[94, 95]. Its presence within brain microvascular endothelia is curious and requires further exploration since it is the short form, OB-Ra, that is thought to be the predominant receptor form at the BBB and is responsible for leptin transport into the brain[96]. The presence of the organic anion transporting polypeptide transporters OATP-A and OATP-C and the multidrug resistance transporter MRP2 could not be detected. Whether MRP2 is truly absent at the blood-brain barrier is a topic of intense debate with many laboratories failing to detect MRP2 within brain microvascular endothelia either at the mRNA transcript or protein level (reviewed in [97]). However, in certain disease states, for example epilepsy, unequivocal immunohistochemical staining has been observed, particularly in rats[97]. The expression and topography of drug resistance transporters at the BBB

remains a controversial subject since investigations into their presence have often yielded variable and conflicting results depending on both culture conditions and species. A general consensus suggests P-gp, MRP2, MRP4, MRP5 and BCRP are expressed on the luminal membrane pumping xenobiotics out of the brain, whilst MRP1 is located on the basal membrane pumping into the brain parenchyma[98, 99]. It is widely accepted that *in-vitro* brain microvasculature, both primary and continuous, retain relatively poor efflux transporter activity compared to the in-vivo counterpart. Studies to determine P-gp activity in PBMVECs highlighted a strong and active P-gp efflux as evidenced by Western blot signal and functional data using the P-gp substrate rhodamine-123 and the selective P-gp inhibitor verapamil. It is difficult and indeed sometimes misleading to make direct comparisons between *in-vitro* and *in-vivo* transporter activity, however in P-gp knockout mice (mdr1a -/-) an approximate 10-fold greater accumulation of digoxin is observed compared to wild-type mice; the 7-fold greater retention of rhodamine-123 in PBMVECs with P-gp chemically knocked out using verapamil compares favourably with this[100].

Having successfully isolated and characterized a primary BBB model that retained a phenotype similar to the *in-vivo* BBB, a series of phage display studies were conducted against the luminal surface of in-*vitro* monolayers of PBMVECs, and for comparison two immortalized cell models, mouse b.End3 and rat RBE4. In preliminary studies to determine whether monolayers could be used for transendothelial screening of phage display

libraries, BBB models were not found to be restrictive enough to prevent insertless phages crossing the cell monolayers. This was supported by other studies concurrently undertaken within the laboratory by a colleague who showed primary alveolar epithelial monolayers displaying varying TEER of 200 - 1000 $\Omega.cm^2$ afforded varying degrees of translocation of insertless phage from apical (luminal) to basal surfaces. In other words the tighter the paracellular barrier then the less wild-type phage was translocated. In contrast using an ex-vivo lung model where the alveolar barrier is fully intact within the correct 3-dimensional architecture showed the insertless phage were essentially excluded from transport across the barrier[101]. Therefore a series of panning studies were conducted against confluent BBB monolayers with the aim of isolating peptides that bound brain microvasculature to increase residency time of a therapeutic cargo at the BBB. These studies were not particularly successful given that a common peptide or peptide motif was not identified. This probably is not that surprising given the landscape of the apical plasmalemma and all the different proteins and receptors that are on display for interaction. However, of note a peptide with sequence AC-**NTSVSKW**-CGGGS was identified in phage panning studies against b.End3 that shares homology with the V3 loop of HIV GP120. William Banks has shown in a series of elegant *in-vitro* and *in-vivo* studies that GP120 is a potent stimulator of adsorptive endocytosis at the BBB in a species independent manner and is at least partially responsible for free HIV virus uptake into the brain[102-104]. This may only be a partial route of entry given the studies of

Kanmonge which have shown that GP120 is able to downregulate a host of tight junctional proteins that include ZO-1, ZO-2 and occludin which results in loss of paracellular restrictiveness at the BBB[105-107]. Unfortunately, *in-vivo* studies in the rat suggested that peptide AC-**NTSVSKW**-CGGGS does not enhance phage uptake into the brain however a detailed examination of its distribution in mice, the species from which its was identified in phage studies, is probably needed before it can be totally discounted.

In conclusion, this chapter has described the characterisation of a primary cell culture model of the blood-brain barrier derived from porcine tissue. This characterization focused on monolayer barrier properties, specifically the discrimination of the paracellular pathway from the transcellular pathway, and upon endocytic transport pathways and carrier mediated transporters and assessed the influence of various astrocyte co-culture conditions. The astrocyte factors were provided by either co-culture with C6 astroglioma cells or by collecting secreted factors from C6 cells and supplementing growth medium with these factors. The C6 astroglioma cell line is widely used, described in the literature as a surrogate for primary astrocytes. Consistent with previous reports successful isolation and culture of primary brain microvascular endothelial cells was achieved, with cells retaining phenotypic and functional characteristics similar to the *in-vivo* cell type. In contrast to previous reports primary cells were successfully cryopreserved for periods up to 12 months without loss of phenotype. Caveolae membrane vesicles were a prominent feature of the

phenotype as was the formation of tight junctional complexes. The presence of astrocyte factors either within conditioned medium or utilizing co-culture system was essential in generating a highly restrictive barrier capable of discriminating transcellular and paracellular markers. Exposure to astrocyte factors did not appear to overtly affect the morphological appearance or topography of vesicles nor alter the expression of Caveolin-1 although it must be noted that the level of phosphorylated caveolin-1, an important marker of caveolae endocytic function, varied between freshly isolated brain microvascular cells in primary culture or first passage. RT-PCR was used to undertake a comprehensive transport characterization using primers that were designed against known porcine genes and mRNA transcripts were identified for ABC efflux transporters, glucose and amino acid transporters, leptin receptor and tight junctional proteins. Functional expression of P-glycoprotein mediated efflux was also confirmed in this model. These studies progress the characterization of a valuable primary brain microvascular culture model that will find resource with academic and industrial researchers especially since the primary cells can be cryopreserved for extended periods of time and recovered by the user when required without loss in phenotype or functionality. PBMVECs, along with b.End3 and RBE4 cells, were used in phage display studies focusing on identifying peptides that interact with the blood-brain barrier but such studies did not reveal any candidate peptides.

1. Abbott, N.J., P.A. Revest, and I.A. Romero, *Astrocyte-endothelial interaction: physiology and pathology.* Neuropathol Appl Neurobiol, 1992. **18**(5): p. 424-33.

2. Goldstein, G.W., *Endothelial cell-astrocyte interactions. A cellular model of the blood-brain barrier.* Ann N Y Acad Sci, 1988. **529**: p. 31-9.

3. Rubin, L.L. and J.M. Staddon, *The cell biology of the blood-brain barrier.* Annu Rev Neurosci, 1999. **22**: p. 11-28.

4. Stewart, P.A. and M.J. Wiley, *Developing nervous tissue induces formation of blood-brain barrier characteristics in invading endothelial cells: a study using quail--chick transplantation chimeras.* Dev Biol, 1981. **84**(1): p. 183-92.

5. Seulberger, H., F. Lottspeich, and W. Risau, *The inducible blood--brain barrier specific molecule HT7 is a novel immunoglobulin-like cell surface glycoprotein.* EMBO J, 1990. **9**(7): p. 2151-8.

6. Schlosshauer, B. and K.H. Herzog, *Neurothelin: an inducible cell surface glycoprotein of blood-brain barrier-specific endothelial cells and distinct neurons.* J Cell Biol, 1990. **110**(4): p. 1261-74.

7. Hawkins, B.T. and T.P. Davis, *The blood-brain barrier/neurovascular unit in health and disease.* Pharmacol Rev, 2005. **57**(2): p. 173-85.

8. Smith, M.W. and M. Gumbleton, *Endocytosis at the blood-brain barrier: from basic understanding to drug delivery strategies.* J Drug Target, 2006. **14**(4): p. 191-214.

9. Kacem, K., et al., *Structural organization of the perivascular astrocyte endfeet and their relationship with the endothelial glucose transporter: a confocal microscopy study.* Glia, 1998. **23**(1): p. 1-10.

10. Reese, T.S. and M.J. Karnovsky, *Fine structural localization of a blood-brain barrier to exogenous peroxidase.* J Cell Biol, 1967. **34**(1): p. 207-17.

11. Janzer, R.C. and M.C. Raff, *Astrocytes induce blood-brain barrier properties in endothelial cells.* Nature, 1987. **325**(6101): p. 253-7.

12. Nagy, Z., *The barrier and regulatory functions of cerebral endothelium.* Acta Biomed Ateneo Parmense, 1992. **63**(1-2): p. 31-41.

13. Lobrinus, J.A., et al., *Induction of the blood-brain barrier specific HT7 and neurothelin epitopes in endothelial cells of the chick chorioallantoic vessels by a soluble factor derived from astrocytes.* Brain Res Dev Brain Res, 1992. **70**(2): p. 207-11.

14. Tontsch, U. and H.C. Bauer, *Glial cells and neurons induce blood-brain barrier related enzymes in cultured cerebral endothelial cells.* Brain Res, 1991. **539**(2): p. 247-53.

15. Meyer, J., J. Rauh, and H.J. Galla, *The susceptibility of cerebral endothelial cells to astroglial induction of blood-brain barrier enzymes depends on their proliferative state.* J Neurochem, 1991. **57**(6): p. 1971-7.

16. Engelhardt, B., *Development of the blood-brain barrier.* Cell Tissue Res, 2003. **314**(1): p. 119-29.

17. Dehouck, M.P., et al., *An easier, reproducible, and mass-production method to study the blood-brain barrier in vitro.* J Neurochem, 1990. **54**(5): p. 1798-801.

18. Rubin, L.L., et al., *A cell culture model of the blood-brain barrier.* J Cell Biol, 1991. **115**(6): p. 1725-35.

19. Rist, R.J., et al., *F-actin cytoskeleton and sucrose permeability of immortalised rat brain microvascular endothelial cell monolayers: effects of cyclic AMP and astrocytic factors.* Brain Res, 1997. **768**(1-2): p. 10-8.

20. Sobue, K., et al., *Induction of blood-brain barrier properties in immortalized bovine brain endothelial cells by astrocytic factors.* Neurosci Res, 1999. **35**(2): p. 155-64.

21. El Hafny, B., et al., *Modulation of P-glycoprotein activity by glial factors and retinoic acid in an immortalized rat brain microvessel endothelial cell line.* Neurosci Lett, 1997. **236**(2): p. 107-11.

22. Bauer, H.C. and H. Bauer, *Neural induction of the blood-brain barrier: still an enigma.* Cell Mol Neurobiol, 2000. **20**(1): p. 13-28.

23. Abbott, N.J., *Astrocyte-endothelial interactions and blood-brain barrier permeability.* J Anat, 2002. **200**(6): p. 629-38.

24. Tran, N.D., et al., *Transforming growth factor-beta mediates astrocyte-specific regulation of brain endothelial anticoagulant factors.* Stroke, 1999. **30**(8): p. 1671-8.

25. Igarashi, Y., et al., *Glial cell line-derived neurotrophic factor induces barrier function of endothelial cells forming the blood-brain barrier.* Biochem Biophys Res Commun, 1999. **261**(1): p. 108-12.

26. Utsumi, H., et al., *Expression of GFRalpha-1, receptor for GDNF, in rat brain capillary during postnatal development of the BBB.* Am J Physiol Cell Physiol, 2000. **279**(2): p. C361-8.

27. Hoheisel, D., et al., *Hydrocortisone reinforces the blood-brain properties in a serum free cell culture system.* Biochem Biophys Res Commun, 1998. **247**(2): p. 312-5.

28. Dore-Duffy, P., et al., *Pericyte migration from the vascular wall in response to traumatic brain injury.* Microvasc Res, 2000. **60**(1): p. 55-69.

29. Balabanov, R. and P. Dore-Duffy, *Role of the CNS microvascular pericyte in the blood-brain barrier.* J Neurosci Res, 1998. **53**(6): p. 637-44.

30. Risau, W., et al., *Blood-brain barrier pericytes are the main source of gamma-glutamyltranspeptidase activity in brain capillaries.* J Neurochem, 1992. **58**(2): p. 667-72.

31. Healy, D.P. and S. Wilk, *Localization of immunoreactive glutamyl aminopeptidase in rat brain. II. Distribution and correlation with angiotensin II.* Brain Res, 1993. **606**(2): p. 295-303.

32. Alliot, F., et al., *Pericytes and periendothelial cells of brain parenchyma vessels co-express aminopeptidase N, aminopeptidase A, and nestin.* J Neurosci Res, 1999. **58**(3): p. 367-78.

33. Hardebo, J.E., B. Falck, and C. Owman, *A comparative study on the uptake and subsequent decarboxylation of monoamine precursors in cerebral microvessels.* Acta Physiol Scand, 1979. **107**(2): p. 161-7.

34. Thomas, W.E., *Brain macrophages: on the role of pericytes and perivascular cells.* Brain Res Brain Res Rev, 1999. **31**(1): p. 42-57.

35. Hori, S., et al., *A pericyte-derived angiopoietin-1 multimeric complex induces occludin gene expression in brain capillary endothelial cells through Tie-2 activation in vitro.* J Neurochem, 2004. **89**(2): p. 503-13.

36. Dohgu, S., et al., *Brain pericytes contribute to the induction and up-regulation of blood-brain barrier functions through transforming growth factor-beta production.* Brain Res, 2005. **1038**(2): p. 208-15.

37. Gumbleton, M. and K.L. Audus, *Progress and limitations in the use of in vitro cell cultures to serve as a permeability screen for the blood-brain barrier.* J Pharm Sci, 2001. **90**(11): p. 1681-98.

38. Muruganandam, A., et al., *Development of immortalized human cerebromicrovascular endothelial cell line as an in vitro model of the human blood-brain barrier.* FASEB J, 1997. **11**(13): p. 1187-97.

39. Xiao, L., et al., *Plasmodium falciparum: involvement of additional receptors in the cytoadherence of infected erythrocytes to microvascular endothelial cells.* Exp Parasitol, 1996. **84**(1): p. 42-55.

40. Prudhomme, J.G., et al., *Studies of Plasmodium falciparum cytoadherence using immortalized human brain capillary endothelial cells.* Int J Parasitol, 1996. **26**(6): p. 647-55.

41. Ketabi-Kiyanvash, N., et al., *NKIM-6, a new immortalized human brain capillary endothelial cell line with conserved endothelial characteristics.* Cell Tissue Res, 2007. **328**(1): p. 19-29.

42. Weksler, B.B., et al., *Blood-brain barrier-specific properties of a human adult brain endothelial cell line.* FASEB J, 2005. **19**(13): p. 1872-4.

43. Tatsuta, T., et al., *Enhanced expression by the brain matrix of P-glycoprotein in brain capillary endothelial cells.* Cell Growth Differ, 1994. **5**(10): p. 1145-52.

44. Wijsman, J.A. and R.R. Shivers, *Immortalized mouse brain endothelial cells are ultrastructurally similar to endothelial cells and respond to astrocyte-conditioned medium.* In Vitro Cell Dev Biol Anim, 1998. **34**(10): p. 777-84.

45. Asaba, H., et al., *Blood-brain barrier is involved in the efflux transport of a neuroactive steroid, dehydroepiandrosterone sulfate, via organic anion transporting polypeptide 2.* J Neurochem, 2000. **75**(5): p. 1907-16.

46. Williams, R.L., et al., *Endothelioma cells expressing the polyoma middle T oncogene induce hemangiomas by host cell recruitment.* Cell, 1989. **57**(6): p. 1053-63.

47. Roux, F., et al., *Regulation of gamma-glutamyl transpeptidase and alkaline phosphatase activities in immortalized rat brain microvessel endothelial cells.* J Cell Physiol, 1994. **159**(1): p. 101-13.

48. Regina, A., et al., *Dexamethasone regulation of P-glycoprotein activity in an immortalized rat brain endothelial cell line, GPNT.* J Neurochem, 1999. **73**(5): p. 1954-63.

49. Lechardeur, D., et al., *Induction of blood-brain barrier differentiation in a rat brain-derived endothelial cell line.* Exp Cell Res, 1995. **220**(1): p. 161-70.

50. Greenwood, J., et al., *SV40 large T immortalised cell lines of the rat blood-brain and blood-retinal barriers retain their phenotypic and immunological characteristics.* J Neuroimmunol, 1996. **71**(1-2): p. 51-63.

51. Kido, Y., et al., *Functional clarification of MCT1-mediated transport of monocarboxylic acids at the blood-brain barrier using in vitro*

cultured cells and in vivo BUI studies. Pharm Res, 2000. **17**(1): p. 55-62.

52. Mooradian, D.L. and C.A. Diglio, *Production of a transforming growth factor-beta-like growth factor by RSV-transformed rat cerebral microvascular endothelial cells.* Tumour Biol, 1991. **12**(3): p. 171-83.

53. Durieu-Trautmann, O., et al., *Immortalization of brain capillary endothelial cells with maintenance of structural characteristics of the blood-brain barrier endothelium.* In Vitro Cell Dev Biol, 1991. **27A**(10): p. 771-8.

54. Stins, M.F., et al., *Bovine brain microvascular endothelial cells transfected with SV40-large T antigen: development of an immortalized cell line to study pathophysiology of CNS disease.* In Vitro Cell Dev Biol Anim, 1997. **33**(4): p. 243-7.

55. Teifel, M. and P. Friedl, *Establishment of the permanent microvascular endothelial cell line PBMEC/C1-2 from porcine brains.* Exp Cell Res, 1996. **228**(1): p. 50-7.

56. Bowman, P.D., et al., *Brain microvessel endothelial cells in tissue culture: a model for study of blood-brain barrier permeability.* Ann Neurol, 1983. **14**(4): p. 396-402.

57. Audus, K.L. and R.T. Borchardt, *Bovine brain microvessel endothelial cell monolayers as a model system for the blood-brain barrier.* Ann N Y Acad Sci, 1987. **507**: p. 9-18.

58. Nakagawa, S., et al., *A new blood-brain barrier model using primary rat brain endothelial cells, pericytes and astrocytes.* Neurochem Int, 2008.

59. Librizzi, L., et al., *Blood-brain barrier preservation in the in vitro isolated guinea pig brain preparation.* J Neurosci Res, 2001. **66**(2): p. 289-97.

60. Mackic, J.B., et al., *Cereport (RMP-7) increases the permeability of human brain microvascular endothelial cell monolayers.* Pharm Res, 1999. **16**(9): p. 1360-5.

61. Deli, M.A., et al., *Permeability studies on in vitro blood-brain barrier models: physiology, pathology, and pharmacology.* Cell Mol Neurobiol, 2005. **25**(1): p. 59-127.

62. Young, R.C., et al., *Development of a new physicochemical model for brain penetration and its application to the design of centrally acting H2 receptor histamine antagonists.* J Med Chem, 1988. **31**(3): p. 656-71.

63. Abraham, M.H., H.S. Chadha, and R.C. Mitchell, *Hydrogen-bonding. Part 36. Determination of blood brain distribution using octanol-water partition coefficients.* Drug Des Discov, 1995. **13**(2): p. 123-31.

64. Abraham, M.H., H.S. Chadha, and R.C. Mitchell, *Hydrogen bonding. 33. Factors that influence the distribution of solutes between blood and brain.* J Pharm Sci, 1994. **83**(9): p. 1257-68.

65. Abraham, M.H., *The factors that influence permeation across the blood-brain barrier.* Eur J Med Chem, 2004. **39**(3): p. 235-40.

66. van de Waterbeemd, H., et al., *Estimation of blood-brain barrier crossing of drugs using molecular size and shape, and H-bonding descriptors.* J Drug Target, 1998. **6**(2): p. 151-65.

67. Lombardo, F., J.F. Blake, and W.J. Curatolo, *Computation of brain-blood partitioning of organic solutes via free energy calculations.* J Med Chem, 1996. **39**(24): p. 4750-5.

68. Kelder, J., et al., *Polar molecular surface as a dominating determinant for oral absorption and brain penetration of drugs.* Pharm Res, 1999. **16**(10): p. 1514-9.

69. Osterberg, T. and U. Norinder, *Prediction of drug transport processes using simple parameters and PLS statistics. The use of ACD/logP and ACD/ChemSketch descriptors.* Eur J Pharm Sci, 2001. **12**(3): p. 327-37.

70. Osterberg, T. and U. Norinder, *Prediction of polar surface area and drug transport processes using simple parameters and PLS statistics.* J Chem Inf Comput Sci, 2000. **40**(6): p. 1408-11.

71. Norinder, U., P. Sjoberg, and T. Osterberg, *Theoretical calculation and prediction of brain-blood partitioning of organic solutes using MolSurf parametrization and PLS statistics.* J Pharm Sci, 1998. **87**(8): p. 952-9.

72. Norinder, U. and T. Osterberg, *Theoretical calculation and prediction of drug transport processes using simple parameters and partial least squares projections to latent structures (PLS) statistics. The use of electrotopological state indices.* J Pharm Sci, 2001. **90**(8): p. 1076-85.

73. Norinder, U. and M. Haeberlein, *Computational approaches to the prediction of the blood-brain distribution.* Adv Drug Deliv Rev, 2002. **54**(3): p. 291-313.

74. Wang, Q., et al., *Evaluation of the MDR-MDCK cell line as a permeability screen for the blood-brain barrier.* Int J Pharm, 2005. **288**(2): p. 349-59.

75. Franke, H., H. Galla, and C.T. Beuckmann, *Primary cultures of brain microvessel endothelial cells: a valid and flexible model to study drug transport through the blood-brain barrier in vitro.* Brain Res Brain Res Protoc, 2000. **5**(3): p. 248-56.

76. Newman, G.R., et al., *Caveolin and its cellular and subcellular immunolocalisation in lung alveolar epithelium: implications for alveolar epithelial type I cell function.* Cell Tissue Res, 1999. **295**(1): p. 111-20.

77. Goh, L.B., et al., *Endogenous drug transporters in in vitro and in vivo models for the prediction of drug disposition in man.* Biochem Pharmacol, 2002. **64**(11): p. 1569-78.

78. Vorbrodt, A.W., *Ultrastructural cytochemistry of blood-brain barrier endothelia.* Prog Histochem Cytochem, 1988. **18**(3): p. 1-99.

79. Beuckmann, C., S. Hellwig, and H.J. Galla, *Induction of the blood/brain-barrier-associated enzyme alkaline phosphatase in endothelial cells from cerebral capillaries is mediated via cAMP.* Eur J Biochem, 1995. **229**(3): p. 641-4.

80. Stewart, P.A., *Endothelial vesicles in the blood-brain barrier: are they related to permeability?* Cell Mol Neurobiol, 2000. **20**(2): p. 149-63.

81. Virgintino, D., et al., *Expression of caveolin-1 in human brain microvessels.* Neuroscience, 2002. **115**(1): p. 145-52.

82. Arvanitis, D.N., et al., *Membrane-associated estrogen receptor and caveolin-1 are present in central nervous system myelin and oligodendrocyte plasma membranes.* J Neurosci Res, 2004. **75**(5): p. 603-13.

83. Crone, C. and S.P. Olesen, *Electrical resistance of brain microvascular endothelium.* Brain Res, 1982. **241**(1): p. 49-55.

84. Butt, A.M., H.C. Jones, and N.J. Abbott, *Electrical resistance across the blood-brain barrier in anaesthetized rats: a developmental study.* J Physiol, 1990. **429**: p. 47-62.

85. Smith, M., Y. Omidi, and M. Gumbleton, *Primary porcine brain microvascular endothelial cells: biochemical and functional characterisation as a model for drug transport and targeting.* J Drug Target, 2007. **15**(4): p. 253-68.

86. Balyasnikova, I.V., et al., *Cyclic adenosine monophosphate regulates the expression of the intercellular adhesion molecule and the inducible nitric oxide synthase in brain endothelial cells.* J Cereb Blood Flow Metab, 2000. **20**(4): p. 688-99.

87. Rubin, L.L., et al., *Differentiation of brain endothelial cells in cell culture.* Ann N Y Acad Sci, 1991. **633**: p. 420-5.

88. Omidi, Y., et al., *Evaluation of the immortalised mouse brain capillary endothelial cell line, b.End3, as an in vitro blood-brain barrier model for drug uptake and transport studies.* Brain Res, 2003. **990**(1-2): p. 95-112.

89. Seddiki, N., et al., *The V3 loop-mimicking pseudopeptide 5[Kpsi(CH2N)PR]-TASP inhibits HIV infection in primary macrophage cultures.* AIDS Res Hum Retroviruses, 1999. **15**(4): p. 381-90.

90. Garberg, P., et al., *In vitro models for the blood-brain barrier.* Toxicol In Vitro, 2005. **19**(3): p. 299-334.

91. Tilling, T., et al., *Basement membrane proteins influence brain capillary endothelial barrier function in vitro.* J Neurochem, 1998. **71**(3): p. 1151-7.

92. Nag, S., J.L. Manias, and D.J. Stewart, *Expression of endothelial phosphorylated caveolin-1 is increased in brain injury.* Neuropathol Appl Neurobiol, 2009. **35**(4): p. 417-26.

93. Aoki, T., R. Nomura, and T. Fujimoto, *Tyrosine phosphorylation of caveolin-1 in the endothelium.* Exp Cell Res, 1999. **253**(2): p. 629-36.

94. Iqbal, J., et al., *Immunohistochemical characterization of localization of long-form leptin receptor (OB-Rb) in neurochemically defined cells in the ovine hypothalamus.* Brain Res, 2001. **920**(1-2): p. 55-64.

95. Siawrys, G., et al., *Long form leptin receptor mRNA expression in the hypothalamus and pituitary during early pregnancy in the pig.* Neuro Endocrinol Lett, 2005. **26**(4): p. 305-9.

96. Merino, B., et al., *Choroid plexus epithelial cells co-express the long and short form of the leptin receptor.* Neurosci Lett, 2006. **393**(2-3): p. 269-72.

97. Hoffmann, K., et al., *Expression of the multidrug transporter MRP2 in the blood-brain barrier after pilocarpine-induced seizures in rats.* Epilepsy Res, 2006. **69**(1): p. 1-14.

98. Begley, D.J., *ABC transporters and the blood-brain barrier.* Curr Pharm Des, 2004. **10**(12): p. 1295-312.

99. Zhang, Y., et al., *Plasma membrane localization of multidrug resistance-associated protein homologs in brain capillary endothelial cells.* J Pharmacol Exp Ther, 2004. **311**(2): p. 449-55.

100. Schinkel, A.H., et al., *Absence of the mdr1a P-Glycoprotein in mice affects tissue distribution and pharmacokinetics of dexamethasone, digoxin, and cyclosporin A.* J Clin Invest, 1995. **96**(4): p. 1698-705.

101. Morris, C.J. and M. Gumbleton, *Phage display identification of lung epithelial trafficking peptide mediating enhanced transpulmonary absorption.*. Biochem. Soc. Trans., 2006. **25**(I): p. Abstract P010.

102. Banks, W.A., et al., *Adsorptive endocytosis of HIV-1gp120 by blood-brain barrier is enhanced by lipopolysaccharide.* Exp Neurol, 1999. **156**(1): p. 165-71.

103. Banks, W.A., A.J. Kastin, and V. Akerstrom, *HIV-1 protein gp120 crosses the blood-brain barrier: role of adsorptive endocytosis.* Life Sci, 1997. **61**(9): p. PL119-25.

104. Banks, W.A., V. Akerstrom, and A.J. Kastin, *Adsorptive endocytosis mediates the passage of HIV-1 across the blood-brain barrier: evidence for a post-internalization coreceptor.* J Cell Sci, 1998. **111 (Pt 4)**: p. 533-40.

105. Kanmogne, G.D., et al., *HIV-1 gp120 compromises blood-brain barrier integrity and enhances monocyte migration across blood-brain barrier: implication for viral neuropathogenesis.* J Cereb Blood Flow Metab, 2007. **27**(1): p. 123-34.

106. Kanmogne, G.D., C. Primeaux, and P. Grammas, *HIV-1 gp120 proteins alter tight junction protein expression and brain endothelial cell permeability: implications for the pathogenesis of HIV-associated dementia.* J Neuropathol Exp Neurol, 2005. **64**(6): p. 498-505.

107. Kanmogne, G.D., R.C. Kennedy, and P. Grammas, *HIV-1 gp120 proteins and gp160 peptides are toxic to brain endothelial cells and neurons: possible pathway for HIV entry into the brain and HIV-associated dementia.* J Neuropathol Exp Neurol, 2002. **61**(11): p. 992-1000.

Chapter 4 *In-vivo* phage display for the identification of brain targeting peptides

4.1 Introduction

4.1.1 Delivery of peptides to the brain

Macromolecules including peptides and proteins show great potential as therapeutic agents to treat a wide variety of brain disorders. However, for many of these therapeutics the physical and metabolic barriers, as well as the efflux carriers expressed at high levels in the brain microvasculature present a major obstacle to the entry of biologics into the brain. In addition, systemic pharmacokinetic issues such as extensive binding to plasma proteins, high systemic clearance or small volume of distribution which give rise to a short elimination half-life reduce the exposure of a potential therapeutic to the brain microvascular cells. Nevertheless, many endogenous regulatory peptides and proteins do cross the BBB via endocytosis or via specific, saturable transport systems to achieve active concentrations in the brain. As a consequence, the BBB vascular barrier may afford opportunities for the therapeutic delivery of macromolecules not least due to the dense distribution of microvasculature at the BBB (intercapillary distances of ~ 40 μm) that means, with sufficient vascular exposure, peptides and proteins that transcytose the barrier have ready access to the entire brain.

The exposure of brain microvasculature to a therapeutic is largely a function of its systemic pharmacokinetics and some of the difficulties associated with brain delivery can be negated by tailoring the systemic pharmacokinetic (PK) profile of the therapy. Brain-derived neurotrophic

factor (BDNF), a ~ 14 KDa protein that supports the survival, growth and differentiation of new neurons, has a saturable transporter at the BBB delivering BDNF to brain parenchyma[1] but unfavourable systemic PK issues including a short half-life and an unstable enzymatic profile result in limited exposure of brain microvasculature to BDNF[2]. Whilst the development of complex carrier mediated systems for the delivery of BDNF has been an active area of research [3-7], modifying the systemic pharmacokinetic profile of BDNF may lead to significant increases in brain concentrations comparable to targeted BBB delivery vector conjugates.

Whilst for certain therapeutics it may be possible to utilise non-vascular routes into the brain that effectively bypass the BBB such as the nasal passages, the leakier (cf BBB) choroid plexus, the circumventricular organs and via direct intrathecal and intracerebroventricular administration, it is clear from the literature that in the main the exploitation of endocytic, transcytotic and carrier mediated transporter pathways remain the focus of attention in delivering biomacromolecules across the BBB.

4.1.2 Evidence of endocytic activity at the BBB

Morphometric studies have been undertaken to determine microvascular vesicular densities within a broad range of tissues across a range of species (reviewed in [8]). In the main vesicular densities are reported from electron microscopic examination of tissue obtained from whole animals perfused with a fixative. Whilst there are issues in obtaining robust

quantitative data by such an approach due to procedural artefacts, the consensus is that BBB vesicle density ranks amongst the lowest reported for all tissue types (see **Table 4.1**).

Table 4.1 Density of endothelial vesicles in capillaries from various tissues (adapted from[8])

Group	Tissue	Number of vesicles per μm²
Low density	Brain	14.00 ± 13.20
	Testis	8.80 ± 5.02
	Ovary	10.60 ± 3.98
Medium density	Pancreas	41.7 ± 13.74
	Intestine	33.3 ± 12.73
	Lung	30.9 ± 15.52
High density	Cardiac muscle	70.35 ± 20.70
	Skeletal muscle	92.6± 22.41
	Diaphragm	66.4 ± 20.65

A confounding issue in morphometric analysis is that some of the apparent cytoplasmically-free endocytic vesicles remain connected to the plasmalemma. For example three-dimensional reconstructions of ultrathin tissue sections reveal that nearly all of the apparently free vesicles are attached to the cell membrane and most vesicles are fused with each other[9-11]. Nevertheless, electron micrographs of BBB endothelia generally depict individual, free vesicles approximately 50 – 100 nm in diameter, in addition to omega-shaped 'caveolae-like' invaginations of the plasmalemma. Whilst caveolae appear to be the predominant vesicle type at the BBB[12, 13], several studies have reported expression of clathrin and observation of clathrin coated pits within *in-vitro* BBB models and isolated capillaries[12-14]; functionality of these clathrin vesicles at the BBB has been evidenced by the internalisation of transferrin receptor[15-19].

A significant number of studies have been conducted demonstrating a variety of endocytic mechanisms that are evident at the BBB. Using classical markers such as HRP[20], dextran and lucifer yellow[21-23], fluid phase endocytosis has been observed both *in-vitro* and *in-vivo* within brain endothelia. However, the ubiquity of fluid phase endocytosis throughout all tissue cell types coupled with a low rate of turnover does not make for an appealing therapeutic delivery route into the brain. Adsorptive endocytosis (AE) at the BBB is better defined, occurring at both a greater rate and extent than fluid phase; for example, within *in-vivo* mouse brain microvasculature[24] wheat germ agglutinin (WGA), an established marker of AE, undergoes endocytosis at a rate 10-fold greater than HRP. More relevant to therapeutic delivery however, are the diverse range of macromolecules that have been identified to undergo receptor mediated endocytosis and transcytosis (RMT) at the BBB. These include, amongst others, the transferrins, various hormones, cytokines, microorganisms and toxins (for a detailed review see [25]). In principle exploiting an RMT pathway should afford selective and potentially efficient delivery to brain parenchyma. Whilst the development of strategies to exploit endocytic and transcytotic pathways are still in their infancy, impressive results have been documented where the targeting of particular receptors has afforded significant delivery of a therapeutic cargo to the brain (see **Table 4.2** for examples).

Table 4.2 Selection of key studies that highlight the use of RMT to deliver a payload into the brain. TfR - transferrin receptor; OX-26 - mouse MAb to rat TfR; 8D3 - rat MAb to mouse TfR; CRM197 - mutated diphtheria toxin; LRP - low density lipoprotein receptor-related protein; P97 - melanotransferrin; IR - insulin receptor.

Target Receptor	BBB Targeting vector	Study species	Payload	Comments	Ref
Rat TfR	OX-26 MAb (Hydrazone linker)	Rat	Methotrexate (MTX)	Up to 47-fold greater brain penetration with conjugated MTX vs. free MTX	[26]
Rat TfR	OX-26 MAb (Biotin/avidin)	Rat	VIP	65% increase in cerebral blood flow; no increase with free VIP	[27]
Rat TfR	OX-26 MAb (Chemical linkage)	Rat	Nerve growth factor	Prevents loss of striatal choline acetyltransferase immunoreactive neurons following quinolinic acid administration	[28]
Rat TfR	OX-26 MAb (Biotin/avidin)	Rat	Polyamide nucleic acids (PNA)	28-fold increase in brain uptake compared to PNA alone	[29]
Rat TfR	OX-26 MAb (Disulphide bridge)	Primates	Recombinant CD4	5-fold increase in CD4 brain uptake cf. non-conjugated	[30]
Rat TfR	OX-26 MAb (PEGylated liposomes)	Rat	Daunomycin	Increased brain uptake of OX26 conjugated liposomes versus free daunomycin or un-conjugated liposomes	[31]
Rat TfR	OX-26 MAb (PEGylated liposomes)	Rat	Beta galactosidase & luciferase gene	Beta galactosidase expression throughout the brain. Luciferase expression 30-100-fold greater than naked plasmid	[32]
Rat TfR	Rat anti-TfR (IgG3; biotin/avidin)	Rat	Antisense peptide-nucleic acid	Brain uptake of antisense therapy 15-fold greater when conjugated to Ab	[33]
Rat TfR	Human Tf (PEGylated nanoparticles)	Rat	Azidothymidine	3-fold increase in AZT concentration in the brain with Tf conjugated nanoparticles compared to un-conjugated.	[34]
Mouse TfR	8D3 MAb (Biotin/avidin)	Mouse	PNA to huntingtin gene	3-fold increase in brain uptake with conjugated PNA vs. free	[35]
HB-EGF	CRM197 (Primary amine)	Guinea Pig	HRP	2-fold increase in HRP activity within an *in-vitro* model of the BBB when conjugated to CRM917; increased uptake *in-vivo*	[36]
Human IR	83-14 MAb (Biotin/avidin)	Monkey	β-amyloid peptide	10-fold increase in brain volume of distribution compared to free	[37]
LRP	P97 (cross-linking)	Mice	Adriamycin	20-35% increase in survival of mice with intracranial tumours compared to free adriamycin	[38]
LRP	Polysorbate80 apolipoprotein E coating (nanoparticles)	Mice	Dalargin; loperamide, 5-FU	Variety of biological responses within the CNS cf. uncoated nanoparticles	[39, 40]

4.1.3 Cell penetrating peptides

In the early 1990s intense research was ignited into the use of cell penetrating peptides (CPPs) or protein transduction domains (PTDs) as they have been termed, for the intracellular delivery of therapeutic material. This followed the observation that short peptide motifs (16 – 20 AAs) from the homeodomain of Antennapedia protein within *Drosophila* species rapidly transfer across plasma membranes in a receptor-, temperature- and energy- independent manner [41, 42]. CPPs are short amphiphilic amino acid motifs (< 30 amino acid residues) derived from native proteins or modifications thereof and represent the minimum amino acid motif that facilitates membrane translocation. Whilst CPPs are represented by a diverse collection of amino acid motifs, they share several common attributes notably a highly cationic chemistry with preserved amphipathicity. The early cell biology studies that suggested endocytic processes do not play a significant role in CPP internalization [41-44] were soon disputed and it is now recognised that many CPPs do display a temperature- and energy- dependent uptake process characteristic of endocytosis and, at least for some CPPs, endocytosis can be considered the major if not exclusive mechanism of plasma cell membrane translocation[45]. However, there is clear evidence that under certain conditions direct translocation across the plasma membrane can occur (NETS ATJ) Traffic AJ

Surprisingly there are only a handful of reports detailing the exploitation of CPPs to enhance the delivery of therapeutic cargos to the brain despite pharmacokinetic and pathological evidence of a HIV-derived CPP (Tat)

penetrating into brain parenchyma[46]. The BBB associated CPP research to date has been pioneered by Rouselle's laboratory who have reported using various CPPs to enhance brain uptake of the anticancer agent doxorubicin[47-49], the beta-lactam antibiotic benzylpenicillin[50], the encephalin analogue dalargin[51], and the opioid analgesic morphine-6-glucoronide[52]. Perhaps it is the ubiquitous uptake of CPPs by all tissues that has prevented significant investment in optimizing the delivery of CPPs to the CNS.

4.1.4 Phage display and BBB delivery

The molecular diversity of receptors on the luminal endothelial cell surface of different vascular beds represents an exciting opportunity for targeted molecular therapy and imaging [53]. The inherent accessibility of vascular endothelium to the blood coupled with the heterogeneity of receptor expression and localization may allow the selective delivery of therapeutics to particular tissue vasculature. Combinatorial technologies such as phage display can be screened against endothelial surfaces from specific tissue types either *in-vitro* or *in-vivo* and may offer greater diversity for interaction compared to classical techniques such as proteomic or antibody based mapping via mass spectrometry or hybridoma technology. To date a number of vascular beds have been explored by phage display in normal and pathological tissues with varying degrees of success (for detailed reviews see [54-60]). The primary aim of such studies has been the identification of peptides that either (i) increase residency time at a

particular vascular bed or (ii) mediate the transport of a cargo across a biological barrier. A good example of (i) is the phage display identification of peptides that contain an α_v-integrin binding motif (NGR)[61] that is recognised to promote cell adhesion[62]. When coupled to doxorubicin the peptide enhanced drug efficacy against human breast caner xenografts in nude mice and also reduced systemic toxicity[61]. An example of the latter (ii) is the phage display selection of a peptide with sequence CVVWMGFQQVC that interacts with polymeric I receptor[63] that mediates epithelial transcytosis of polymeric immunoglobulins.

4.1.5 Objectives

In this chapter a series of rat *in-vivo* phage display strategies were employed to identify peptides that mediate phage transduction across the blood brain barrier to gain access to the brain parenchyma and specifically to access brain grey matter. Subsequently, whole body tissue distribution studies were undertaken for a select peptide-phage clone compared to that of insertless phages.

In parallel, an *in-silico* physiologically based pharmacokinetic model was developed and utilised to gain a quantitative perspective of the extent of brain delivery that can be expected to be achieved for macromolecules with different systemic pharmacokinetics and with different affinities for brain parenchyma, i.e. as if a BBB targeting vector was active. These *in-silico* data

were used to provide context to the peptide phage tissue distribution studies.

4.2 Materials and methods

4.2.1 Materials

Materials used in phage studies are detailed in Chapter 2.

4.2.2 Animals

Male SD rats (450 - 500 g) were purchased from Harlan Laboratories (Bicester, UK). Rats were housed in regular cages and conditions and were acclimatized for 1 week before studies conducted. All rats had food and water *ad libitum*. All experiments were conducted using protocols approved by Cardiff University Joint Biological Services Unit.

4.2.3 *In-vivo* selection of brain homing peptides

The details of the phage display selection methodologies employed for the identification of brain homing peptides are detailed in **Figure 4.1**.

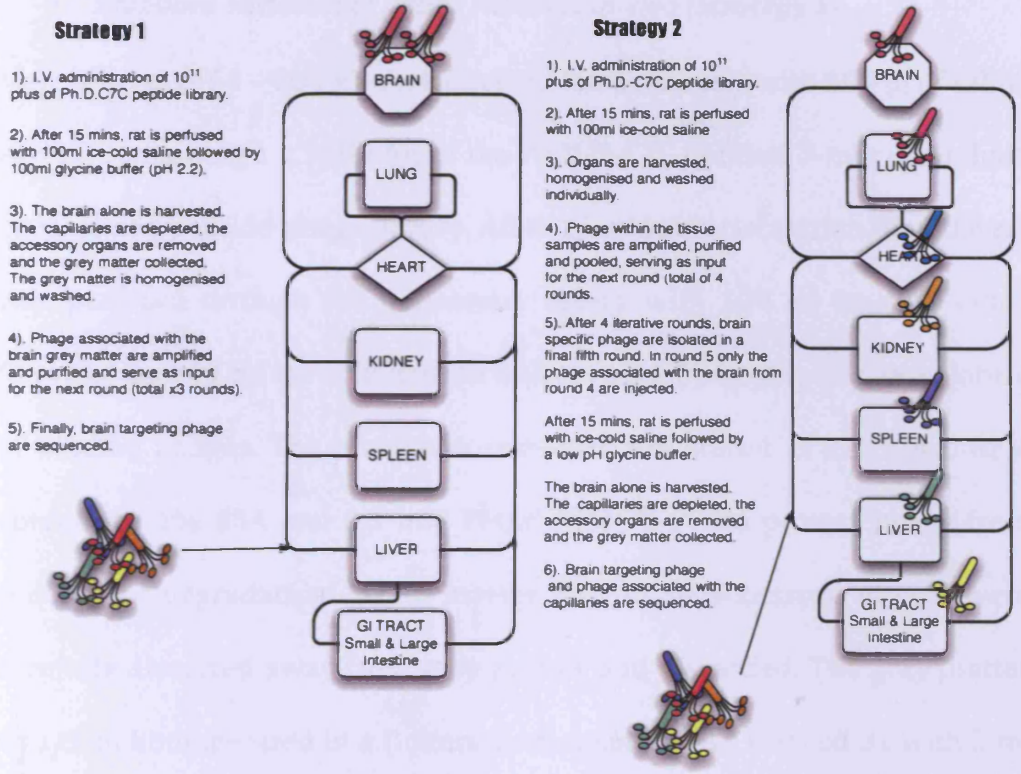

Figure 4.1 Schematic representation of in-vivo biopanning procedures used to isolate brain homing peptide-phages. The Ph.D.™-C7C library was injected into male SD rats then either: (i) In "Strategy 1" the brain was harvested following saline and glycine perfusions to remove vascular bound phage. The accessory organs were removed, the capillaries depleted and the grey matter homogenized and washed. The phages associated with the grey matter were amplified, purified and served as input in the next iterative round (three rounds in total) before phages within grey matter and capillaries were sequenced, OR (ii) In "Strategy 2" all the major organs were harvested, homogenized and washed, phages recovered and then amplified, purified and pooled to serve as input in the next iterative round (four rounds in total). A final fifth round was used to select brain specific peptide phages whereby only the brain-associated peptide phages from round four were injected. The grey matter was isolated from the capillaries and the peptide-phage associated with both grey matter and capillaries sequenced.

- ***Standard selection of phage libraries in-vivo (Strategy 1)***

Male SD rats (450 – 500 g) were injected intravenously with 100 µl of saline (0.9%) containing 1 x 10^{11} pfus of the Ph.D.™-C7C cyclised 7-mer disulphide constrained peptide-phage library. After 15 minutes circulation time the rat was perfused through the pulmonary artery with 100 ml ice-cold saline followed by 100 ml ice-cold glycine buffer (pH 2.2) to strip the vasculature of binding phages. The brain was removed and stored in ice-cold DMEM containing 1% BSA and 0.5 mM PMSF (DMEM-PI) to protect phage from proteolytic degradation. White matter and brain accessory organs were carefully dissected away from grey matter and discarded. The grey matter was then homogenized in a Dounce homogenizer and washed 3x with 5 ml of DMEM-PI; tissue was centrifuged at 3000g for 5 mins between each wash. The vasculature was depleted from the grey matter by centrifuging the tissue on a 33% percoll gradient (6000g, 10 mins) and collecting the grey matter fraction that floats to the surface. The grey matter was then incubated for 15 mins at room temperature with 2ml of an overnight culture of *E. coli* (incubated at least 18 hrs). A 100µl aliquot was removed for plaque assay and the remaining culture added to 20 ml LB broth and incubated for 4.5 hours at 37°C. Phages were purified using a double PEG precipitation as previously described in chapter 2 and inputted into subsequent rounds of selection; in total, three rounds of selection were completed. An aliquot of phages associated with brain grey matter and capillary vasculature from the final round of panning were gene sequenced

using standard Big Dye v3.1 chemistry on an ABI Prism 3100 genetic analyzer.

- ***Synchronous selection of phage libraries in-vivo (Strategy 2)***

Male SD rats (450 – 500 g) were injected intravenously with 100 µL of saline (0.9%) containing 10^{11} plaque forming units (pfus) of the Ph.D.™-C7C library. After 15 mins the rat was perfused with 100ml ice-cold saline through the pulmonary artery. Major organs (brain, lung, heart, liver, kidneys, spleen and testicles) were removed and stored in DMEM-PI over ice. The organs were homogenized individually in a Dounce homogenizer and then amplified separately as described in Strategy 1. Phages were purified by a double PEG precipitation procedure. Amplified phages from each organ (1×10^{10} pfus) were pooled and used for the subsequent round of *in-vivo* selection. After four such rounds, a brain selection round was performed where only brain-associated phages from round 4 were injected (1×10^{11} pfus). After a 100ml ice-cold saline perfusion followed by a 100 ml ice-cold glycine buffer (pH 2.2) perfusion to strip the vasculature of binding phages, the brain was harvested. White matter and brain accessory organs were removed and, as described for Strategy 1, the grey matter was homogenized, the vasculature depleted and the phage associated with grey matter and capillary vasculature recovered. An aliquot of the final fifth round phages associated with brain grey matter or vasculature were gene sequenced using standard Big Dye v3.1 chemistry on an ABI Prism 3100 genetic analyzer.

4.2.4 *In-vivo* distribution of phages

1 x 10^{11} pfus each of a selected library phage clone and insertless-M13 phage were co-injected into male SD rats (total volume 100 µl). At time-points 7, 15, 45, 90 and 180 mins a blood sample was taken and the animal perfused with 100 ml ice-cold saline followed by 100 ml ice-cold glycine buffer. The brain, heart, liver, kidneys, spleen, large intestine (~ 1g), small intestine (~ 1g), muscle (~1g from thigh) and testicles were harvested. The white matter and accessory organs were dissected from the brain grey matter and discarded. The grey matter was homogenized, washed 3x with DMEM-PI and the vasculature isolated using a percoll gradient as previously described. All other tissue was homogenized and washed 3x with DMEM-PI. The tissues were then incubated with 2ml of an overnight culture of ER2738 at room temperature for 15 mins before addition of 8 ml of LB broth for a further 30 mins. Phage content was then determined by plaque formation assay in the presence of IPTG/X-gal in the top agar.

Pharmacokinetic parameters were calculated in Graphpad Prism by fitting phage blood data to a biexponential equation, $C(t) = Ae^{-k_A t} + Be^{-k_B t}$, where C(t) = phage.ml^{-1} of blood. The area under the blood concentration–time curve and tissue concentration-time curve (AUC) was calculated by the linear trapezoidal rule and blood clearance (CL) from CL = Dose / AUC 0–∞.

4.2.5 Phage amplification errors

The expression of peptides on the pIII coat protein of M13 in the Ph.D.™-C7C library may result in amplification defects if the displayed peptides block the interaction of pIII with the f-pilus on *E. coli*. pIII on insertless phages has unrestricted access to the f-pilus such that for the same input of insertless and library phages, amplification in *E. coli* for a given time may result in higher copy numbers of insertless phages. This would overestimate the accumulation of insertless-M13 in a tissue. To address this issue, 100 pfus each of library phages and insertless phages were incubated with 2 ml of an overnight culture of *E. coli* for 15 minutes after which 8ml of LB broth was added and the culture incubated for a further 30 minutes; this parallels the protocol undertaken to quantify phage numbers in tissues during distribution studies. A 1 ml aliquot of culture was then removed and the number of phages determined by plaque formation assays.

4.2.6 Tissue stability

To determine whether phage stability in different tissues impacted upon apparent *in-vivo* accumulation and distribution, the stability of a library phage clone (AC-**SYTSSTM**-CGGGS) and insertless–M13 was determined in *ex-vivo* tissue and blood. Samples of blood (1ml), brain grey matter (1g) and liver (1g) were harvested from a terminally anaesthetised rat. The tissue was then homogenized in 1 ml pre-warmed DMEM (37°C); importantly DMEM did not contain protease inhibitors. To each tissue or blood sample was added 2 x 10^{11} pfus of either library phage clone or insertless-M13. At

pre-determined intervals (15, 45, 90 mins) a 200 µl sample of tissue or 10 µl of blood was removed and the number of phages in the sample determined by plaque formation assay. The number of phages in the tissue or blood sample at each time point was compared to the number of phages in a DMEM only control.

4.2.7 Effects of perfusion on phage numbers

To ensure that saline and glycine perfusion did not damage the integrity of the brain vasculature to result in an apparent increased accumulation of phages, the uptake of peptide-phages (AC-**SYTSSTM**-CGGGS) into grey matter was assessed with and without saline and glycine perfusions. Briefly, 1 x 10^{11} pfus of phage were injected intravenously into two male SD rats. After 15 minutes, one of the rats was perfused with 100ml ice-cold saline followed by 100ml glycine buffer and one rat was not perfused after exsanguination. The brains were then harvested and stored in DMEM-PI over ice. Grey matter was isolated as previously described and the capillaries depleted. Plaque formation assay was used to determine the number of phages in brain grey matter and associated with capillaries.

4.2.8 Physiological based pharmacokinetic (PBPK) simulations

The structure of the PBPK model developed and detailed in **Figure 4.2** is based on a model reported in the literature [64]. Mass balance equations were written for all tissue compartments based on drug partition into the tissue, assuming a well-stirred system with perfusion rate limited

distribution, and drug elimination due to tissue clearance in the eliminating compartment.

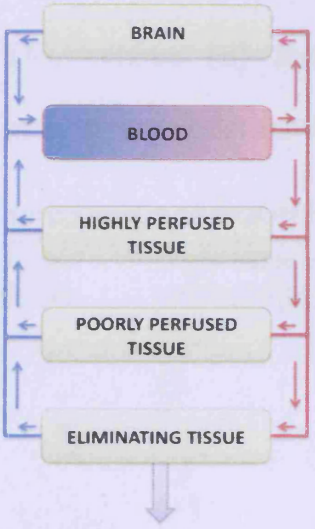

Figure 4.2 Schematic overview of the compartments included in the PBPK model.

For the brain compartment and non-eliminating compartments, the differential equation had the following form:

$$\frac{dC_T}{dt} = \frac{1}{V_T}\left(Q_T.C_{blood} - \frac{Q_T.C_T}{kp} - CL_T.C_{blood}\right) \qquad \textit{Equation 4.1}$$

For the eliminating compartment, the differential equation had the following form:

$$\frac{dC_{EI}}{dt} = \frac{1}{V_{EI}}\left(Q_{EI}.C_{blood} - \frac{Q_{EI}.C_{EI}}{kp} - Q_{EI}.E.C_{blood}\right) \qquad \textit{Equation 4.2}$$

For the blood compartment, the differential equation had the following form:

$$\frac{dC_{Blood}}{dt} = \frac{1}{V_{Blood}}\left(Q_{Heart}(CV - CA)\right) \qquad \textit{Equation 4.3}$$

The parameters in the equation refer to blood flow (Q), concentration (C), volume (V), extraction ratio (E), tissue partition co-efficient (k_p), clearance (CL) and time (t). The subscripts refer to tissue (T), cardiac output (Heart), blood (Blood), arterial (A), venous (B) and eliminating tissue (El). Physiological parameters used in the model are detailed in **Table 4.3**.

Table 4.3 Rat physiological parameters used in whole body PBPK model (adapted from[65])

Organ	Organ volumes per body weight (L/kg)	Organ blood volume (% cardiac output)	Compartment
Brain	0.0057	1.5	Brain
Liver	0.0366	1.6	Eliminating
Kidney	0.0073	19	Eliminating
Heart	0.0033	5	High Perfusion
Lung	0.005	-	High Perfusion
Spleen	0.002	1.7	High Perfusion
Gut	0.027	14.4	High Perfusion
Other	0.1577	9.41	High Perfusion
Muscle, skin, bone	0.636	47	Low Perfusion

Model simulations were conducted in Stella (Version 9.03; Isee Systems, Lebanon, USA) a numerical integration software package that simultaneously solves systems of coupled first-order differential equations; a schematic of the model can be seen in **Figure 4.3**.

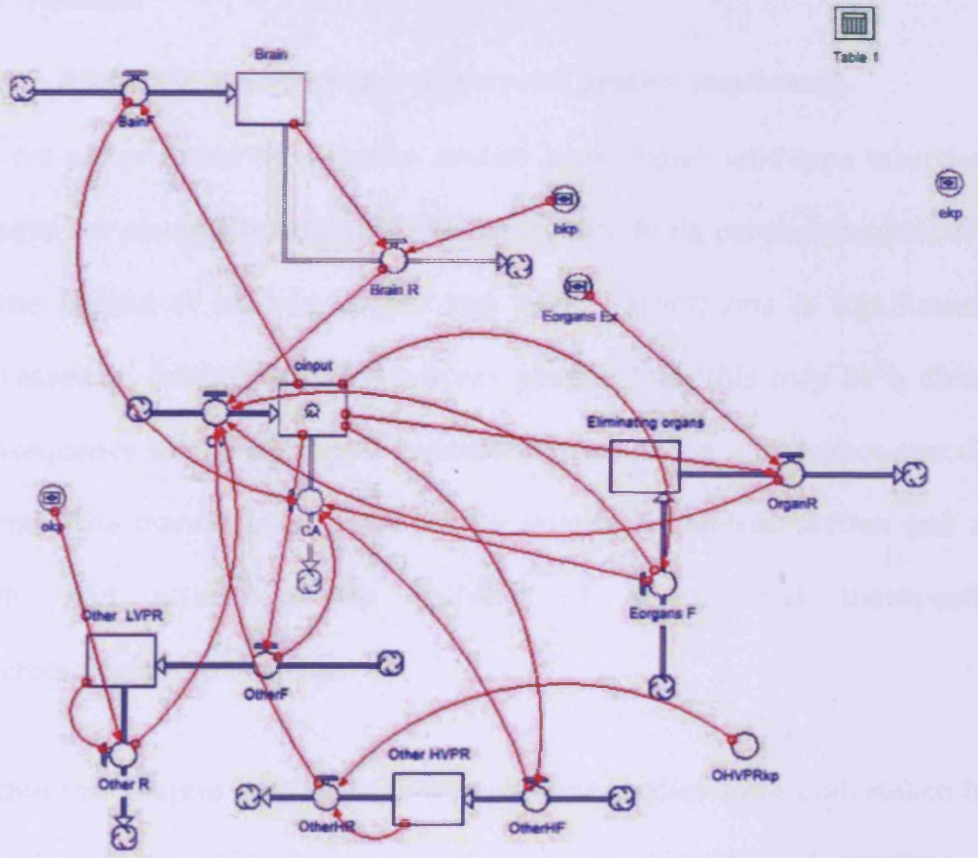

Figure 4.3 Schematic of the pharmacokinetic model built in Stella to predict brain concentrations of drug.

A series of concentration vs. time-course curves were simulated for changing affinity for the brain and changing extraction ratio within the eliminating compartment. The tissue affinities within the highly perfused and poorly perfused compartment were kept at a constant value of 2 based on the assumption that any targeting moiety would increase affinity for brain alone.

4.3 Results

4.3.1 Analysis of in-vivo phage recovery and peptide sequences

In-vivo phage tissue distribution studies have shown wild-type insertless phages are essentially excluded from entry into brain parenchyma[66, 67]. If the uptake of peptide-phages into brain parenchyma is significantly increased in comparison to insertless phages, then this may be a direct consequence of the displayed peptide and would be a sequence-specific event. The translocation process may involve a non-toxic action and as such, find utility in the delivery of experimental therapeutic macromolecules to the brain.

Within this chapter a series of *in-vivo* panning studies were undertaken by injecting peptide phage library into the systemic circulation of rats, the aim of which was to isolate brain homing peptides. Those peptide-phages that may be selectively associated with brain parenchyma were subsequently recovered and the displayed peptides identified. The details of these selection strategies are outlined in **Figure 4.1**. Isolation strategy 1 was designed solely to select for those phages that enter brain parenchyma. In contrast, isolation strategy 2 was designed to simultaneously select for phages that enter different tissues in a single rat. Strategy 2 has previously been exploited by Renata Pasqualini[68] and co-workers who identified peptide motifs that were specific for particular organs. Its reported advantage is the minimization of animal numbers required to identify peptide phages that 'home' to different tissues. In both strategies a saline

perfusion was employed to remove the blood from the tissues and as such the freely circulating peptide-phages. This was followed by a low pH glycine perfusion to strip the vasculature of binding peptide phages. Subsequently the brain was harvested, brain white matter and brain accessory organs (choroid plexus, brain stem, circumventricular organs etc) were removed and brain capillaries were depleted using established techniques[69]. These processes afforded the recovery of phages associated with grey matter and not other areas of the brain; many CNS disorders are localized to grey matter, which contains the neural cell bodies that process sensory and motor information.

Analysis of phage recovery from tissues analysed in isolation strategy 1 rounds 1-3 i.e. where only phages from the brain were harvested and injected in iterative rounds of panning (**Figure 4.4**) showed that there was a progressive increase in the percentage of phage input recovered from brain grey matter. This is in contrast to the other organs harvested that, with the exception of liver, showed decreased accumulation with progressive selection rounds. Combined, these data indicate enrichment for a population of peptide-phages that home to the brain.

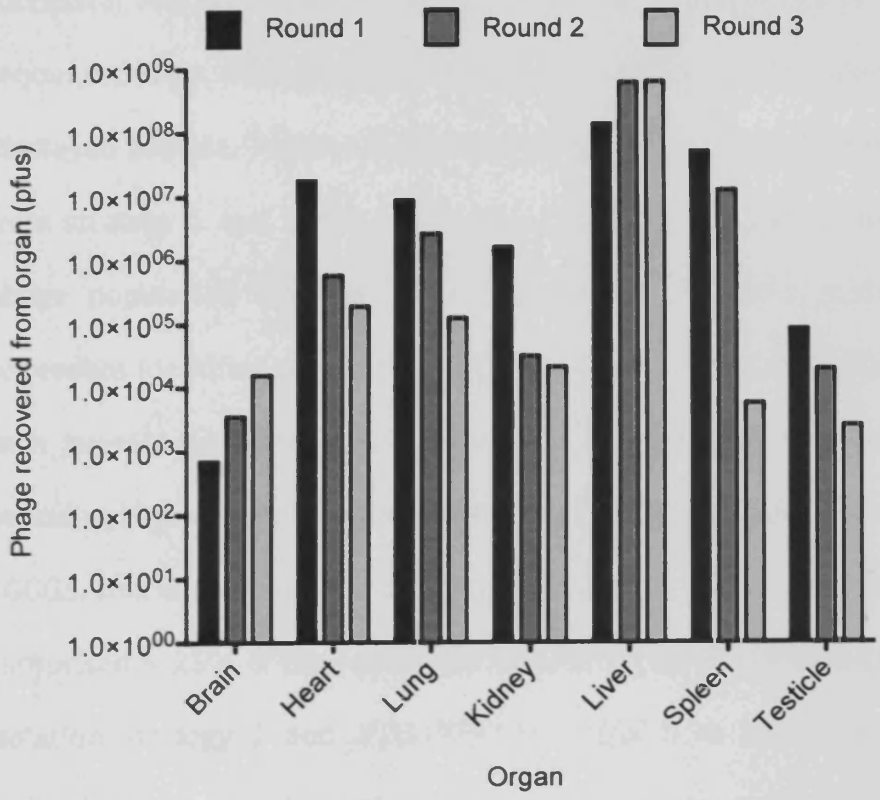

Figure 4.4 Peptide phages recovered from organs in isolation strategy 1. The number of phages recovered from brain grey matter progressively increases between selection rounds. This is in contrast to the other organs harvested where the number of phages decreases. These data imply enrichment of a population of peptide phages that home to the brain.

Analagous data are not presented for isolation strategy 2 because all the phages recovered from each organ were amplified in each panning round. Large variations in the number of phages recovered from each organ would mean that removing samples for titration before amplification would deplete the recovered phages unequally from each organ and may bias later rounds of selection.

Increases in phage recovery with successive rounds of selection in isolation strategy 1 **Figure 4.4** gave confidence that the selection protocol was

successful and therefore an extensive number of phage clones were gene sequenced from strategy 1 and strategy 2 to determine the identity of the displayed peptide. **Table 4.4** highlights a subset of the sequences analysed from strategy 1 and 2 that were present in multiple copy number in the phage population isolated. In isolation strategy 1, the most common sequences identified were AC-**PDVPHPA**-CGGGS and AC-**STASTQA**-CGGGS, each present as 1.5% of the population recovered. In strategy 2, two peptide-phages were recovered AC-**SYTSSTM**-CGGGS and AC-**SNTSSTT**-CGGGS, sharing a common motif AC-**SxTSSTx**-CGGGS and which combined comprised ~ 25% of the recovered population. AC-**PDVPHPA**-CGGGS from isolation strategy 1 and AC-**SYTSSTM**-CGGGS from isolation strategy 2 were also recovered from the depleted brain capillary fraction as well as from brain grey matter. This is a significant find as it supports the hypothesis that phages displaying certain peptide sequences may gain access to grey matter through an intracellular route at the BBB rather than bypassing it via leaky paracellular areas of the BBB or via other barriers such as the choroid plexus.

Table 4.4 Amino acid sequences of brain homing peptides isolated in multiple copy number from strategies 1 and 2. Data are presented as percentage of total colonies sequenced: (i) Strategy 1: ~ 450 colonies sequenced from grey matter and 48 colonies sequenced from microvasculature; (ii) Strategy 2: ~ 150 colonies sequenced from grey matter and 48 colonies sequenced from microvasculature.

Peptide sequence	Frequency		Strategy
	Grey Matter	Brain Microvascular Capillaries	
AC-SYTSSTM-CGGGS	17%	19%	2
AC-SNTSSTT-CGGGS	6%	-	2
AC-TIENPRA-CGGGS	6%	-	2
AC-PDVPHPA-CGGGS	1.5%	13%	1
AC-STASTQA-CGGGS	1.5%	-	1
AC-HTLHGSA-CGGGS	1.3%	-	1
AC-TISFDRY-CGGGS	1.3%	-	1
AC-KQAASQQ-CGGGS	1%	-	1
AC-NARTSLF-CGGGS	1%	-	1
AC-EPEKPRT-CGGGS	1%	-	1
AC-SVSSYNS-CGGGS	<1%	-	1
AC-DATNLTM-CGGGS	<1%	-	1
AC-NRTAAPL-CGGGS	<1%	-	1
AC-SLMKSPE-CGGGS	<1%	-	1
AC-VRANMTA-CGGGS	<1%	-	1
AC-TDPGQSA-CGGGS	<1%	-	1
AC-TRTSHHN-CGGGS	<1%	-	1
AC-DSTQTRQ-CGGGS	<1%	-	1
AC-LPTAQNS-CGGGS	<1%	-	1
AC-PMSQNSL-CGGGS	<1%	-	1
AC-HQGVGTT-CGGGS	<1%	-	1
AC-NREHPNT-CGGGS	<1%	-	1
AC-PVHNARN-CGGGS	<1%	-	1
AC-HNQIYPQ-CGGGS	<1%	-	1
AC-PNSNSKL-CGGGS	<1%	-	1
AC-PNNHSRH-CGGGS	<1%	-	1
AC-TQADLAK-CGGGS	<1%	-	1
AC-HQTSLLM-CGGGS	<1%	-	1
AC-VPHDRTS-CGGGS	<1%	-	1
AC-IPSGLLQ-CGGGS	<1%	-	1
AC-NNMTNTW-CGGGS	<1%	-	1
AC-QGHQSGS-CGGGS	<1%	-	1
AC-TQPARSQ-CGGGS	<1%	-	1
AC-PNSMHSS-CGGGS	<1%	-	1

Increasing affinity for target is generally accompanied by the emergence of a common motif in the amino acid sequences of virtually all the displayed peptides e.g. HPQ for streptavidin binding peptides. To determine any patterns within the amino acid residues of the displayed peptides, an analysis was undertaken to determine the incidence of each amino acid at the seven randomized positions in the displayed peptide. The results for both isolation strategy 1 and isolation strategy 2 of this analysis can be seen in **Figure 4.5** and **Figure 4.6** respectively. It is quite apparent in both strategies that serine (S) and threonine (T) constitute a significant percentage of the total residues for the clones sequenced and particularly serine at residues 1, 4 and 5 i.e. AC-**S**XX**SS**XX-CGGS. Of note, the most common clones identified in strategy 2, AC-**S**Y**TSS**TM-CGGGS and AC-**SNTSS**TT-CGGS, contain serines at these positions. It is also clear that certain residues are not favoured in the sequences, most notably the aromatic amino acids phenylalanine (F), tryptophan (W) and to a lesser extent tyrosine (Y). These findings are not the result of library bias since the amino acids are evenly distributed throughout the seven randomized positions in phage clones in the Ph.D.™-C7C library [70].

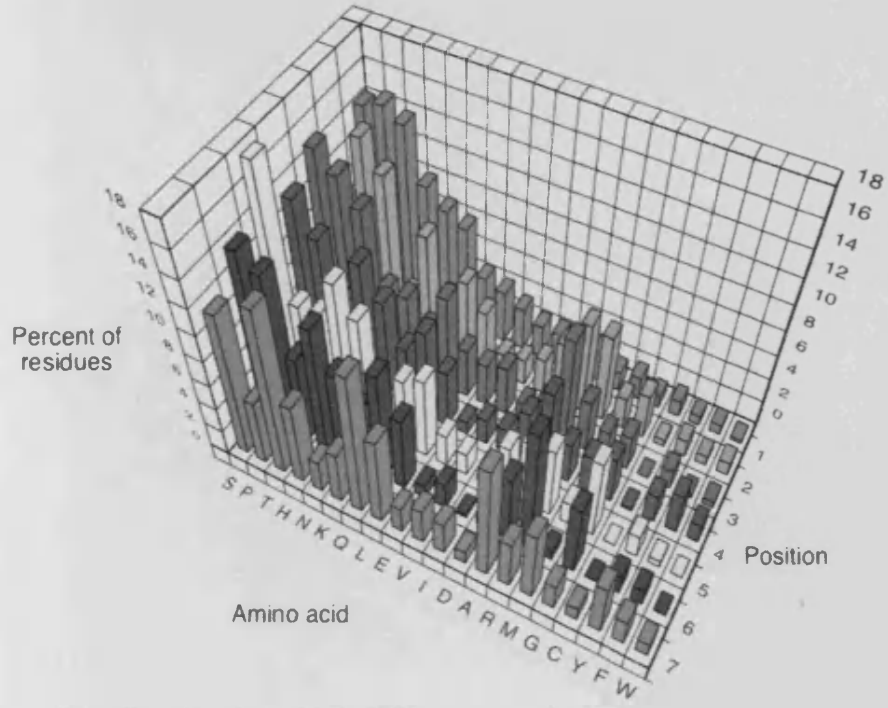

	Percentage occurrence						
	Residue position						
Residue	1	2	3	4	5	6	7
S	14.21	9.35	14.81	13.23	17.66	13.77	11.49
P	14.73	14.29	13.51	10.94	8.05	12.73	5.22
T	13.95	12.21	11.69	6.62	8.05	7.01	13.32
H	10.08	3.64	6.23	10.43	11.17	10.13	6.53
N	8.79	8.83	6.23	8.14	9.09	7.27	2.61
K	8.01	4.68	4.42	5.09	2.86	5.19	4.18
Q	4.65	6.49	7.53	7.12	5.71	8.83	11.49
L	4.13	4.68	3.90	4.58	6.49	5.97	7.05
E	3.36	1.82	3.38	1.02	2.60	1.04	2.09
V	2.58	2.08	3.90	2.04	1.82	2.08	2.87
I	2.58	2.86	1.56	2.04	0.52	0.26	2.61
D	2.84	4.94	2.60	4.33	4.16	0.78	1.04
A	2.58	7.27	8.57	6.87	5.45	5.45	9.40
R	1.55	7.01	4.16	3.31	5.71	10.13	3.92
M	1.81	2.60	2.34	3.05	1.82	0.78	5.74
G	1.03	3.64	2.86	3.82	6.49	5.71	2.09
C	1.29	0.52	0.00	0.25	0.00	0.00	1.04
Y	0.78	1.30	1.56	2.29	1.82	1.56	4.18
F	0.78	0.78	0.26	3.31	0.52	1.30	2.09
W	0.26	1.04	0.52	1.53	0.00	0.00	1.04

Figure 4.5 Distributions of amino acids observed at seven randomized positions in phages recovered from brain grey matter in isolation strategy 1.

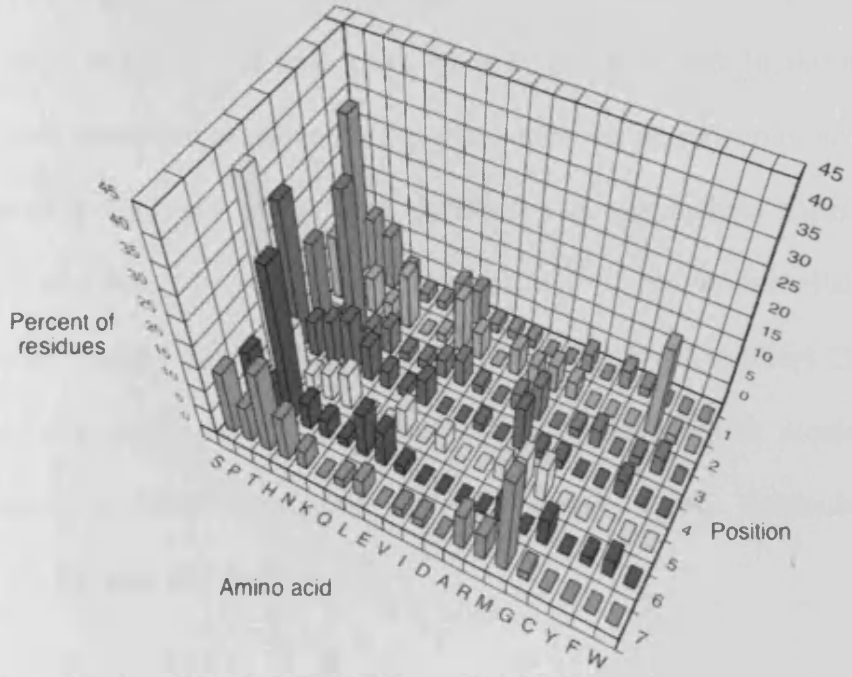

	Percentage occurrence						
	Residue position						
Residue	1	2	3	4	5	6	7
S	33.33	13.73	17.65	31.37	41.18	11.76	13.73
P	13.73	1.96	1.96	7.84	11.76	5.88	7.84
T	11.76	7.84	31.37	9.80	3.92	33.33	17.65
H	5.88	3.92	3.92	11.76	5.88	5.88	9.80
N	1.96	11.76	5.88	7.84	7.84	3.92	3.92
K	1.96	0.00	1.96	3.92	0.00	1.96	0.00
Q	7.84	1.96	1.96	1.96	0.00	9.80	1.96
L	7.84	11.76	3.92	5.88	5.88	7.84	3.92
E	1.96	5.88	5.88	0.00	0.00	1.96	0.00
V	1.96	0.00	1.96	0.00	3.92	0.00	1.96
I	1.96	5.88	0.00	1.96	0.00	0.00	1.96
D	0.00	3.92	3.92	0.00	0.00	0.00	0.00
A	0.00	5.88	7.84	9.80	3.92	0.00	7.84
R	3.92	3.92	0.00	1.96	7.84	5.88	5.88
M	0.00	0.00	1.96	1.96	7.84	0.00	21.57
G	3.92	0.00	3.92	0.00	0.00	5.88	1.96
C	1.96	0.00	0.00	0.00	0.00	0.00	0.00
Y	0.00	19.61	1.96	3.92	0.00	1.96	0.00
F	0.00	1.96	3.92	0.00	0.00	3.92	0.00
W	0.00	0.00	0.00	0.00	0.00	0.00	0.00

Figure 4.6 Distributions of amino acids observed at seven randomized positions in phages recovered from brain grey matter in isolation strategy 2.

An analysis of the physicochemical properties of the high frequency clones identified in strategy 1 and 2 can be seen in **Table 4.5.** In the main, the peptides identified were not primarily composed of hydrophobic residues suggesting they are unlikely to partition into the plasma membrane to affect translocation of the phage particle into the endothelial cell by diffusion. In any case diffusion seems unlikely given the short 15 minute phage circulation before perfusion and harvesting which would not be sufficient to afford significant diffusion across a cell, particularly of a particle the size of a phage.

Table 4.5 Physicochemical properties of high frequency clones identified in isolation studies. Calculations were made using a peptide property calculator from Innovagen (Innovagen AB, Lund, Sweden).

Sequence	Net Charge at pH 7.0	pI	Average hydrophilicity	% hydrophilic residues
AC-SYTSSTM-CGGGS	0	5.9	-0.5	43%
AC-PDVPHPA-CGGGS	-0.9	4.9	0.1	14%
AC-STASTQA-CGGGS	0	6	-0.1	43%
AC-HTLHGSA-CGGGS	0.2	8	-0.5	14%
AC-TISFDRY-CGGGS	0	6.7	-0.1	43%
AC-KQAASQQ-CGGGS	1	10.1	0.4	71%
AC-NARTSLF-CGGGS	1	11	-0.2	43%
AC-EPEKPRT-CGGGS	0	7.1	1.7	57%
AC-SVSSYNS-CGGGS	0	5.9	-0.3	71%
AC-DATNLTM-CGGGS	-1	3.1	-0.2	29%
AC-NRTAAPL-CGGGS	1	11	0	29%
AC-SLMKSPE-CGGGS	0	6.9	0.5	57%
AC-TQADLAK-CGGGS	0	6.7	0.4	43%
AC-HQTSLLM-CGGGS	0.1	7.8	-0.8	29%
AC-VPHDRTS-CGGGS	0.1	7.8	0.6	43%
AC-IPSGLLQ-CGGGS	0	6	-0.7	29%
AC-NNNTNTW-CGGGS	0	6	-0.5	57%
AC-VRANMTA-CGGGS	1	11	-0.1	29%
AC-TDPGQSA-CGGGS	-1	3.1	0.4	43%
AC-TRTSHHN-CGGGS	1.2	11	0.2	43%
AC-DSTQTRQ-CGGGS	0	6.8	0.8	71%
AC-LPTAQNS-CGGGS	0	6	-0.3	43%
AC-PMSQNSL-CGGGS	0	6	-0.3	57%
AC-HQGVGTT-CGGGS	0.1	7.8	-0.4	14%
AC-NREHPNT-CGGGS	0.1	7.9	0.8	57%
AC-PVHWARN-CGGGS	1.1	11	-0.4	29%
AC-HNQIYPQ-CGGGS	0.1	7.8	-0.6	43%
AC-PNSNSKL-CGGGS	1	10.1	0.3	71%
AC-PNNHSRH-CGGGS	1.2	11	0.4	57%
AC-QGHQSGS-CGGGS	0.1	7.8	0.1	57%
AC-TQPARSQ-CGGGS	0.1	11	0.4	57%
AC-PNSMHSS-CGGGS	0.1	7.8	-0.1	57%

There was also a pattern in the isoelectric point of the peptides displayed on the phages recovered in isolation strategies 1 and 2 (**Figure 4.7**) with the majority (over 90%) contained within a bimodal pattern having a pI of either 6-8 or 9-11. Virtually none of the displayed peptides had a pI between 8 and 9.

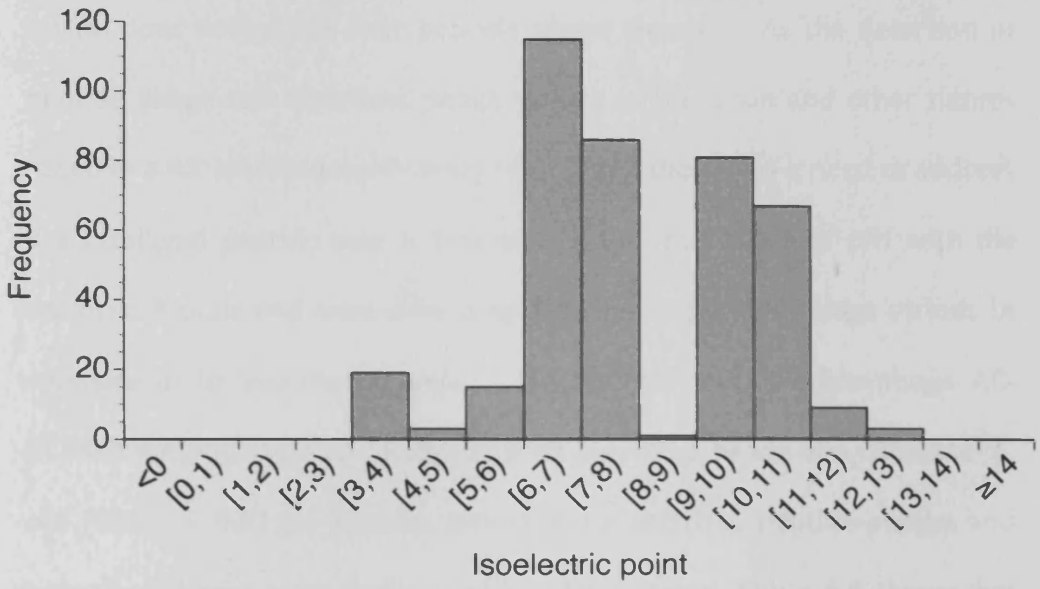

Figure 4.7 Distribution of isoelectric points of phage peptide motifs identified in isolation strategies 1 and 2.

From the sequence analysis detailed above for the original panning strategies three peptide-phage clones were taken forward to determine their potential in homing to the brain: (i) AC-**PDVPHPA**-CGGGS; isolated in strategy 1 and displaying the highest frequency in both brain grey matter and capillary fractions, (ii) AC-**SYTSSTM**-CGGGS; isolated in strategy 2 displaying the highest frequency in both brain grey matter and capillary fractions and (iii) AC-**TQPARSQ**-CGGGS; isolated in strategy 1 and having a pI of 11 which is similar to the cell penetrating peptides.

4.3.2 Phage amplification errors

Before undertaking brain homing studies of the three clones detailed above, the relative amplification of library phages was compared to insertless phages. Insertless phages represent an almost ideal control, however, the insertless phage may display some preferential differences in its interactions with *E.coli* over peptide phage clones. As the detection of peptide phage and insertless phage virions in the brain and other tissues requires a 45-minute amplification with *E. coli* there was a need to address if a displayed peptide may interfere with the interaction of pIII with the bacterial F-pilus and thus slow amplification of peptide phage virions in comparison to insertless phage. To address this, peptide-phage AC-**SYTSSTM**-CGGGS was co-incubated with insertless phage in a culture of *E. coli* (OD_{600} ~ 0.5) for 45 mins before the number of peptide-phages and insertless phages were determined by plaque assay. **Table 4.6** shows that for the same input of peptide phage library and insertless phages, the rate of growth of insertless phages is some 2.4 ± 0.4 times faster than library phages. This clearly has major implications in tissue distribution studies since the amount of insertless phages that enter a given tissue (as determined by plaque formation assay) will be an overestimate by a factor of 2.4. Therefore, the results described for the relative (viz insertless) phage tissue distribution studies in this chapter have been corrected to account for the relative amplification rates of insertless and library phages over 45 mins.

Table 4.6 shows comparison of the amplification of SYTSSTM-M13 with insertless phages. Peptide- and insertless- phages were co-infected in equal quantities into a culture of E. coli. After 45 minutes, the number of insertless phages was 2.4 ± 0.4 times greater than peptide phages. This methodology parallels that used to recover phages from tissue.

	Number of SYTSSTM-M13	Number of insertless-M13	Ratio of insertless phages to peptide phages
Study 1	140	340	2.4
Study 2	200	400	2.0
Study 3	140	380	2.7
Mean	160 ± 35	373 ± 31	2.4 ± 0.4

4.3.3 Ex-vivo stability of SYTSSTM-M13 and insertless-M13

Proteases have been shown to significantly reduce the infectivity of phages by cleaving the N-terminal globular domain of the pIII protein preventing interaction with the F-pilus[71-73]. Since phage tissue distribution was monitored by plaque forming assay which measures viable phage particles there is the concern that *in-vivo* exposure to rat proteases would degrade phages and therefore the number of phages recovered from a tissue would significantly underestimate the true number entering the tissue. This could be different for different tissues and therefore undermine any tissue-selectivity assessments. Further, the fact that the displayed peptide is fused to pIII raises the question as to whether the displayed peptide would protect pIII from proteolytic digestion leading to the higher recovery of library phages from tissue compared to insertless. To address these issues, phages were incubated (37°C) with fresh homogenates of liver and brain and with blood. The recovery of peptide or insertless phages from these tissue samples after set periods of time (15, 45 and 90 mins) was compared to the recovery from phages similarly incubated in DMEM; stability of both library and insertless phages has been confirmed in DMEM over 24 hours

(data not shown). Whilst the recovery of phages from tissue was variable (as a result of the inherent errors in phage titration techniques which have been estimated as ~ 25%[74]), **Figure 4.8** shows that, in comparison to phages similarly incubated in DMEM, there was no significant decrease in either library or insertless phage viability in any of the tissues investigated.

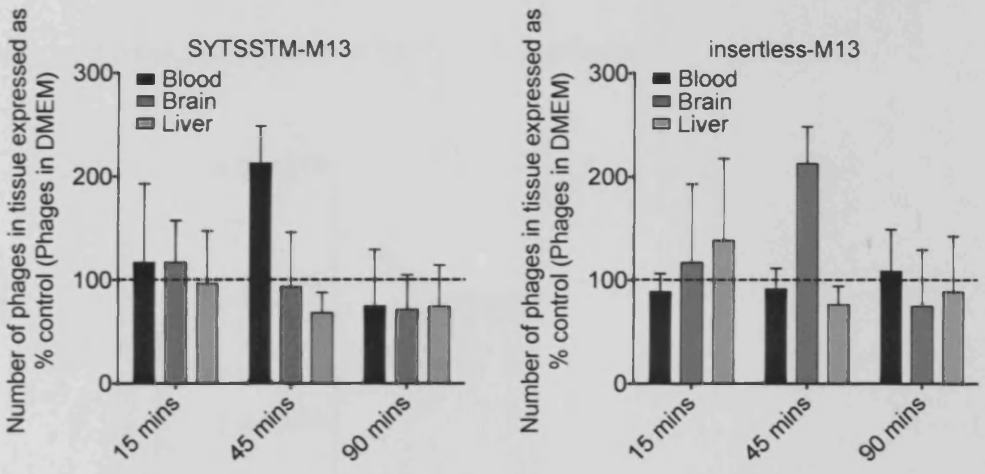

Figure 4.8 Ex-vivo stability of SYTSSTM-M13 and insertless-M13. Brain and liver were excised from terminally anesthetised rats and a blood sample was removed. Brain and liver were homogenized in DMEM (37°C) and then 1ml aliquots of tissue and blood were incubated with phages, either SYTSSTM-M13 or insertless-M13. At the indicated time-points a sample of tissue and blood was collected and the number of phages determined by plaque formation assay. Comparison of the number of phages recovered with a sample of phages similarly incubated in DMEM alone revealed that there was no significant degradation at any time point investigated. Data are means ± SD expressed as percentage control (n = 3).

4.3.4 Effects of perfusion on phage numbers

There was some concern that perfusion procedures would result in damage to the brain microvasculature allowing phages that ordinarily would not enter the brain to 'leak' in. The recovery of phages from brain grey matter and capillary fractions was therefore determined in two animals, one

perfused with saline and glycine and the other not perfused. **Figure 4.9** shows that saline and glycine perfusions drastically reduce the number of phages recovered from grey matter and the brain capillary fraction. This suggests two points, firstly saline and glycine do not appear to damage the BBB to allow phages to 'leak' into the brain and secondly, the perfusion strategy is successful in removing phages from residual blood within the brain and from the surface of the brain capillaries.

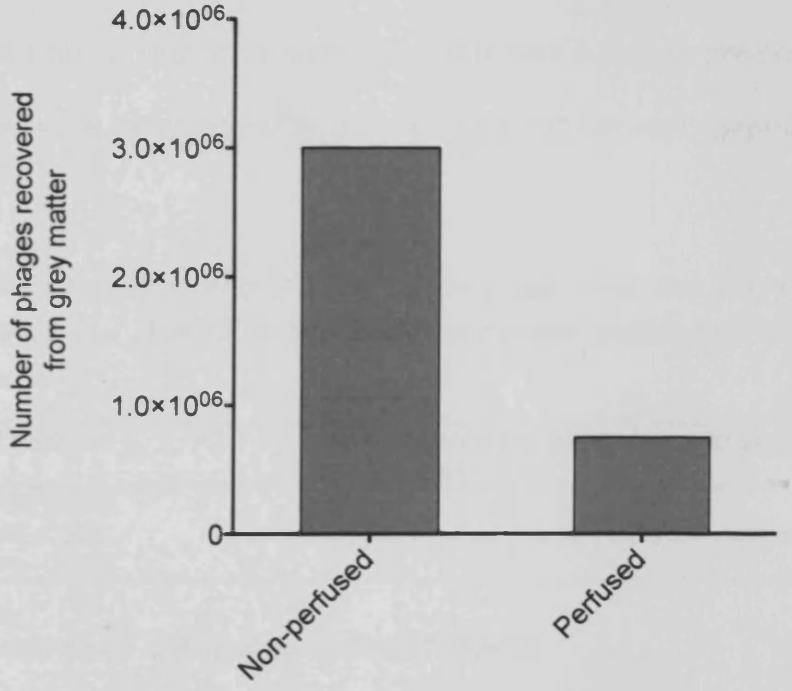

Figure 4.9 Effects of perfusion on phage recovery from grey matter. Saline and glycine perfusion (perfused on histogram) remove freely circulating phages and phages attached to vasculature resulting in reduced recovery from grey matter.

4.3.5 Fifteen minute brain uptake of selected peptide-phage clones

To analyse the capacity of selected phage clones AC-**PDVPHPA**-CGGGS, AC-**SYTSSTM**-CGGS and AC-**TQPARSQ**-CGGGS to home to the brain, each clone

was co-injected, with an equal number of insertless phage, into a rat and allowed to circulate for 15 minutes before the animal was sacrificed and perfused with saline and glycine. The brain was harvested, the white matter removed and the capillaries depleted before the number of peptide and insertless phages in grey matter was determined by plaque formation assay. **Table 4.7** shows the ratio of peptide-M13 phage to insertless-M13 phage for each of the three peptide-phage investigated. Only SYTSSTM-M13 preferentially enter brain compared to insertless-M13 after a 15-minute circulation time. It should be noted that this was a simple pre-screen and these data were only determined in a single rat for each peptide phage clone.

Table 4.7 Brain homing capacity of select peptide phage clones. Only phage clone AC-SYTTSTM-CGGGS was observed to enter brain grey matter preferentially compared to insertless phage.

Displayed Peptide	Ratio Peptide-Phage:Wild-type in grey matter at 15 mins (n = 1)
AC-SYTSSTM-CGGGS	8
AC-TQPARSQ-CGGGS	0.3 (i.e. > 3-fold greater insertless enter the brain)
AC-PDVPHPA-CGGGS	1

4.3.6 In-vivo tissue distribution of SYTSSTM-M13

With SYTSSTM-M13 showing greater uptake at 15 minutes compared to insertless-M13, extensive *in-vivo* tissue distribution studies were undertaken to construct a detailed *in-vivo* pharmacokinetic profile. Equal quantities of SYTSSTM-M13 and insertless-M13 were co-injected into rat, allowed to circulate for 7, 15, 45, 90 or 180 minutes before the rats were terminally anaesthetised and perfused with saline and glycine to clear blood and vasculature of circulating phage. After harvesting the brain grey

matter and other major organs the number of SYTSSTM-M13 recovered from each tissue was compared to the recovery of insertless-M13; each time point was undertaken in triplicate (i.e. n= 3 animals) on the same day using the same prepared dose of phage. **Figure 4.10** shows the distribution of SYTSSTM-M13 and insertless-M13 in brain grey matter and **Figure 4.11** shows the distribution in blood, heart, lung, liver, kidney, spleen, testicles, small and large intestine, and muscle. The data reveal that only in brain grey matter is the peak concentration of SYTSSTM-M13 significantly greater than insertless-M13 ($p < 0.05$) with a mean ratio of 3.4 (corrected for amplification error). It is clear however that in comparison to other tissues analysed, the uptake of phages into brain grey matter is relatively minor with the peak concentration of SYTSSTM-M13 representing just 2.1×10^{-4} % of injected dose; this compares to 18% of injected dose in the liver although the liver is recognized as the primary elimination route for phages[66]. Further, phages did not appear to persist in brain grey matter, or most of the other organs, for any significant time with after 180 minutes neither SYTSSTM-M13 nor insertless-M13 detectable in brain grey matter.

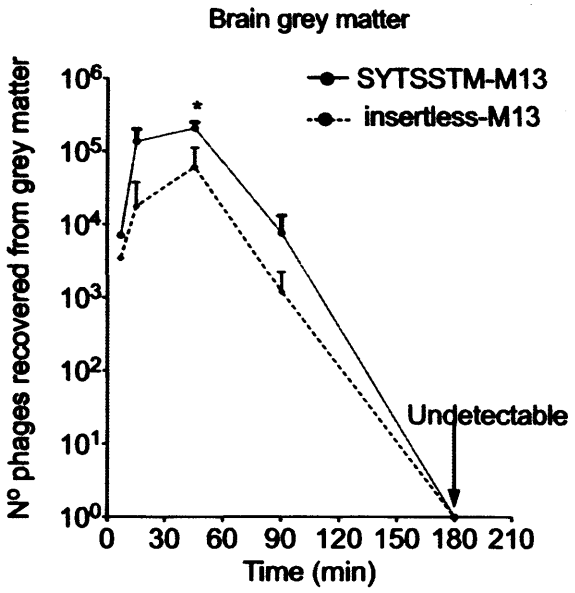

*Figure 4.10 Pharmacokinetic profile of SYTSSTM-M13 and insertless-M13 in brain grey matter of male SD rats. 1x10[11] pfus of SYTSSTM-M13 and insertless-M13 were co-injected intravenously into male SD rats. At the indicated time intervals, rats were terminally anaesthetized before perfusion with ice-cold saline and ice-cold glycine (pH2.2). The brain and major organs were then harvested. The white matter and accessory organs were separated from the rest of the brain and discarded. The capillaries were extracted from the grey matter using density centrifugation. The number of phage particles in brain grey matter was then determined by plaque formation assay. The experimentally determined Cmax (45 mins) for SYTSSTM-M13 was found to be significantly greater than insertless-M13. * represents a statistically significant difference (P < 0.05) compared to insertless-M13. Data are presented as mean ± SD (n=3 for each timepoint) and incorporate an amplification error factor of 2.4.*

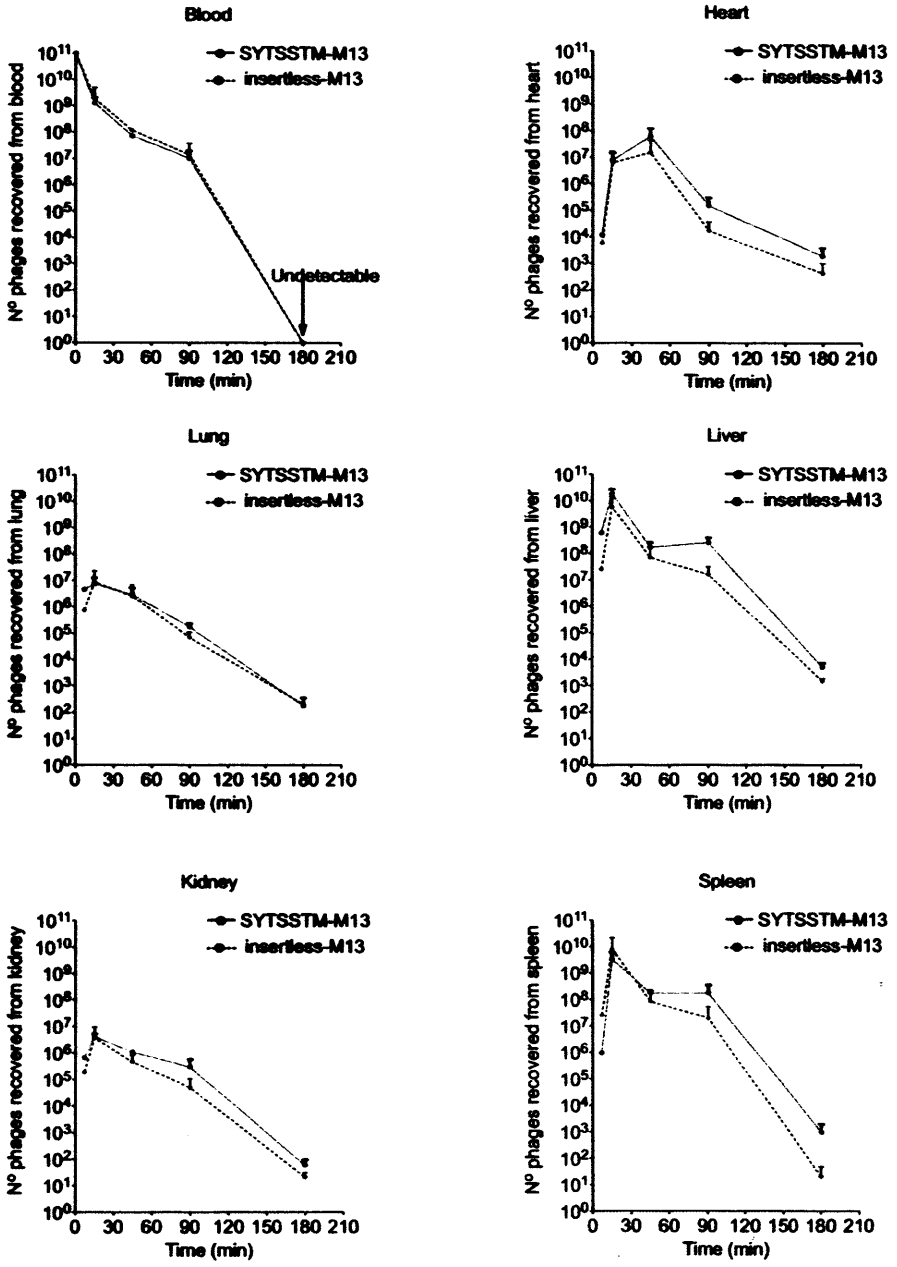

Figure 4.11 Pharmacokinetic profile of SYTSSTM-M13 and insertless-M13 in the major organs of male SD rats (continued on next page). 1 x 10^{11} pfus of SYTSSTM-M13 and insertless-M13 were co-injected intravenously into male SD rats. At the indicated time intervals, the animals were terminally anaesthetized before perfusion with ice-cold saline and ice-cold glycine (pH2.2). The number of phage particles in each tissue was then determined by plaque assay. No significant difference was observed between Cmax for SYTSSTM-M13 and insertless-m13. Data are presented as mean (n=3 for each timepoint) and incorporate amplification error factor.

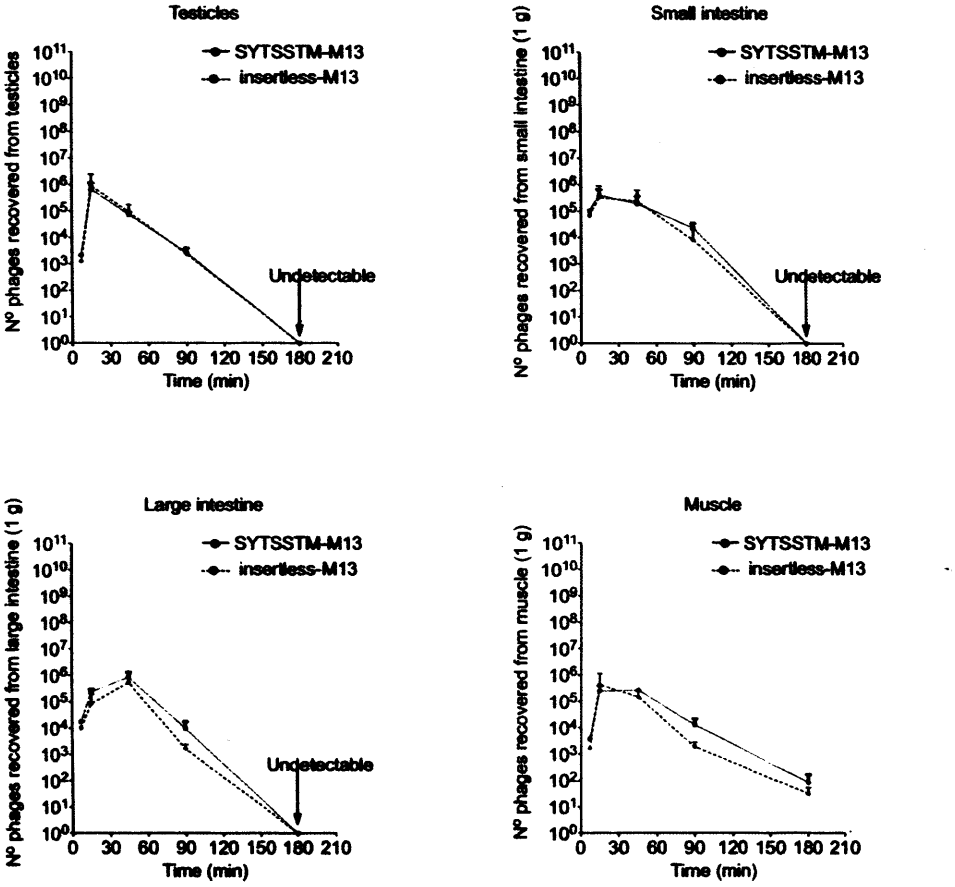

Figure 4.11 continued. Pharmacokinetic profile of SYTSSTM-M13 and insertless-M13 in the major organs of male SD rats.

Other points to note are the exact same PK profile of SYTSSTM-M13 and insertless-M13 in the blood (see **Table 4.8**) with both phage types undetectable at 180 minutes. These are an important find since they show that SYTSSTM-M13 does not circulate for longer in the blood to provide greater opportunity for uptake.

Table 4.8 Blood pharmacokinetic parameters of SYTSSTM-M13 and insertless-M13 following intravenous administration. Parameters were determined using equations detailed in 4.2.4.

	SYTSSTM-M13	insertless-M13
AUC pfus.ml^{-1}.min	7.78 x 10^{11}	7.89 x 10^{11}
k_1 ml.min^{-1}	0.086	0.087
K_2 ml.min^{-1}	0.3711	0.3740
$t_{1/2,1}$ min	1.868	1.853
$t_{1/2,2}$ min	8.021	7.923
Cl ml.min^{-1}.rat^{-1}	0.129	0.127
r^2	0.9996	0.9978

A better measure of phage uptake into a tissue than Cmax is the area under the curve (AUC). AUC gives a measure of the total exposure of a given tissue to phages, for example a long, low concentration exposure may be as important as a shorter but higher concentration. **Table 4.9** shows the total AUCs, calculated from mean phage data, for SYTSSTM-M13 and insertless-M13 in each of the tissues investigated. Once again the AUC data reinforces the view that the brain is a relatively minor distribution route for phages. However, comparison of the ratio of brain AUCs reveals a substantially greater uptake of SYTSSM-M13 in comparison to insertless-M13 (~ 4-fold greater uptake). Notably, uptake is also substantially greater for heart (~ 3.6 fold) and liver (~ 3.3 fold) but the ratio of AUC in blood is ~ 1. Data are corrected for amplification errors in insertless-M13.

Table 4.9 AUCs calculated from experimentally determined tissue distributions of SYTSSTM-M13 and insertless-M13. The fold increase in AUC of SYTSSTM-M13 compared to insertless-M13 is greatest for brain although considerable increases were also observed for heart and liver. Of note, the AUC for blood is the same for SYTSSTM-M13 and insertless-M13. AUCs were calculated using the trapezoid rule from mean distribution data.

Tissue	$AUC_{SYTSSTM-M13(0-\infty)}$ (pfus.min)	$AUC_{insertless-M13(0-\infty)}$ (pfus.min)	Ratio $AUC_{SYTSSTM-M13} : AUC_{insertless-M13}$
Brain	1.09×10^{7}	0.27×10^{7}	4.018
Lung	2.82×10^{8}	2.66×10^{8}	1.062
Heart	2.47×10^{9}	0.69×10^{9}	3.557
Liver	3.74×10^{11}	1.12×10^{11}	3.336
Kidneys	1.44×10^{8}	0.91×10^{8}	1.582
Spleen	0.80×10^{11}	1.53×10^{11}	0.525
Large intestine (1 g)	3.77×10^{7}	2.16×10^{7}	1.745
Small intestine (1 g)	1.69×10^{7}	1.61×10^{7}	1.052
Muscle (1 g)	1.57×10^{7}	1.38×10^{7}	1.138
Testicle	1.51×10^{7}	2.16×10^{7}	0.734
Blood (1ml)	7.78×10^{11}	7.89×10^{11}	0.985

In comparison to some tissues, the rate of perfusion of the brain is moderate and since rate of perfusion determines exposure of a tissue to phages, AUCs reported in **Table 4.9** will always indicate that highly perfused tissues accumulate greater quantities of phages. To compensate for this AUCs were standardized for perfusion rate, the results of which are shown in **Table 4.10** (ratios of SYTSSTM-M13:insertless-M13 remain the same); rat organ perfusion rates were obtained from[75]. These data now suggest that the uptake of SYTSSTM-M13 into the brain is not as minor a route of distribution as would at first be suggested. This is demonstrated by comparing the AUC of SYTSSTM in the tissues with the AUC of SYTSSTM in the lung; lung was chosen for comparison because the whole of the cardiac output passes through the lungs and yet, corrected for perfusion, very little SYTSSTM is taken up in comparison to the other organs. Even when corrected for perfusion, uptake of insertless phages into the brain is less

than the other tissues investigated. **Figure 4.12** is a graphical representation of the data presented in **Table 4.9** and **Table 4.10**.

Table 4.10 Perfusion adjusted AUCs calculated from experimentally determined tissue distributions of SYTSSTM-M13 and insertless-M13. AUCs have been corrected for exposure of tissues to phages, since highly perfused rat tissues will be exposed to greater quantities of phages per unit time than poorly perfused rat tissues. Whilst the ratio of AUC SYTSSTM-M13 to AUC insertless-M13 does not change, the tissue distribution is altered. AUCs are calculated using the trapezoid rule from mean distribution data and perfusion values were obtained from [75].

Tissue	$AUC_{SYTSSTM\text{-}M13(0\text{-}\infty)}$ (pfus.g^{-1}.ml^{-1}.min^{2})	$AUC_{insertless\text{-}M13(0\text{-}\infty)}$ (pfus.g^{-1}.ml^{-1}.min^{2})	Ratio AUC SYTSSTM Tissue: AUC SYTSSTM Lung
Brain	7.50×10^{5}	1.87×10^{5}	5.7
Lung	1.32×10^{5}	1.24×10^{5}	-
Heart	1.98×10^{7}	0.56×10^{7}	150
Liver	4.41×10^{8}	1.32×10^{8}	3341
Kidneys	4.44×10^{5}	2.8×10^{5}	3.3
Spleen	1.11×10^{9}	2.12×10^{9}	8409
Large intestine (1 g)	1.92×10^{6}	1.11×10^{6}	14.5
Small intestine (1 g)	5.69×10^{5}	5.41×10^{5}	4.3
Muscle (1 g)	3.03×10^{6}	2.66×10^{6}	22.7
Testicle	6.86×10^{6}	7.30×10^{6}	52
Blood	7.78×10^{11}	7.89×10^{11}	-

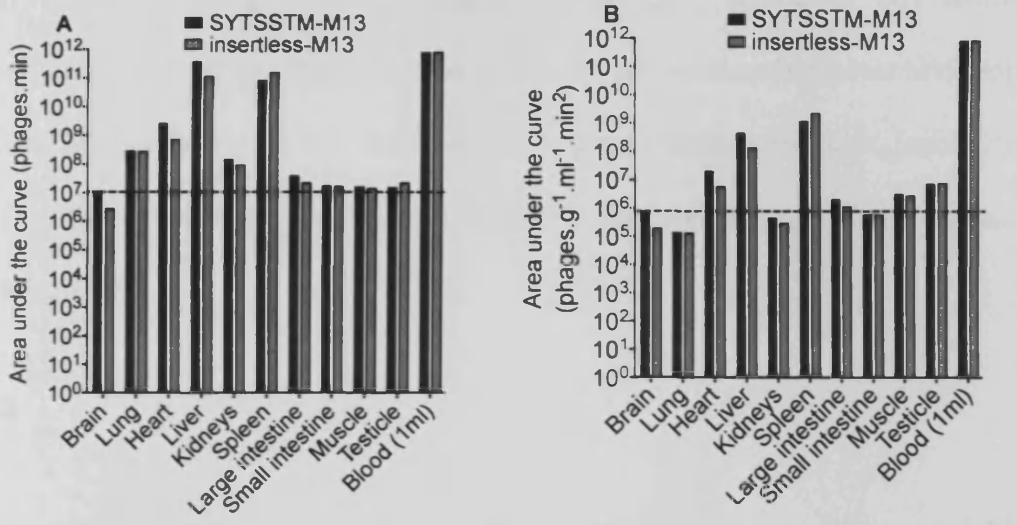

Figure 4.12 AUC in major organs and tissues for SYTSSTM-M13 and insertless-M13 co-administered to male SD rats. (A) Total AUC of SYTSSTM-M13 compared to insertless-M13. (B) AUCs of SYTSSTM-M13 and insertless-M13 adjusted for rat tissue perfusion. Perfusion governs exposure of a tissue to phages and given that the rate of brain perfusion is relatively low in comparison to other tissues[75] this reduces the exposure of brain microvasculature to phages.

4.3.7 Pharmacokinetic simulations of brain uptake

To explore how various pharmacokinetic parameters may impact on the accumulation of phages in brain parenchyma, a physiologically based pharmacokinetic model (PBPK) was constructed in Stella the details of which can be seen in **Figure 4.2** and **Figure 4.3**. The PBPK model was based on the structure of the rat circulatory system and used published values for rat organ masses and rates of perfusion to reflect convective transport of a molecule to the brain via blood flow. The model was simplified at the organ level to assume transfer between well-stirred compartments such that the effects of intravascular dispersion and diffusion are not modelled. Simulations were run to assess the accumulation of molecule in the brain through:

(a) varying affinity for brain tissue (K_p[brain] = 0.2, 2 or 20) while maintaining a constant extraction ratio in the eliminating compartment (simulations run at E = 0.1 and 1) and a constant tissue affinity (K_p[other] = 2) in the other highly perfused and poorly perfused compartments in the PBPK model

OR

(b) varying extraction ratio in the eliminating compartment while maintaining a constant affinity for brain tissue (simulations run for either K_p[brain] = 0.2 and 20) and constant tissue affinity for highly perfused and poorly perfused compartments (K_p[other] = 2). The results of these simulations can be seen graphically in **Figure 4.13** and summarized in **Table 4.11** and **Table 4.12.**

The modelling provided insights into the effects of changing PK on brain accumulation. Firstly, for the same extraction ratio in the eliminating compartment, any increase in affinity for brain tissue (K_p[brain]) is directly reflected by a proportional increase in brain AUC(total) i.e. a 10-fold increase in K_p[brain] leads to a 10-fold increase in brain AUC(total) (see **Table 4.11**). The same is not true for peak concentration (Cmax), indeed the increase in Cmax may be considerably smaller than the increase in K_p[brain], for example with an extraction ratio of 1 in the eliminating compartment (i.e. a rapidly eliminated molecule), a 100-fold increase in K_p[brain] (0.2 – 20) only results in an 8.2 fold increase in Cmax. The

simulations also show that AUC(total) and Cmax can be increased if peripheral pharmacokinetics are modified to extend circulation time. Even with a poor affinity for brain tissue (K_p[brain] = 0.2), reducing the extraction ratio from 1 to 0.1 (i.e. changing from a rapidly eliminated to a slowly eliminated molecule) results in an approximate 9-fold increase in brain AUC and only a small 1.25-fold increase in Cmax. Together the simulations demonstrate that modifying both peripheral pharmacokinetics and central affinity will achieve the greatest brain accumulation although changes in tissue affinity are the most influential factor. For example increasing brain affinity from 0.2 to 2 and reducing extraction ratio from 1 to 0.1 results in a 53-fold increase in brain AUC and a 9-fold increase in Cmax. The simulations also show that increasing Cmax is challenging since even with a 100-fold increase in K_p[brain] and a reduction in extraction ratio from 1 to 0.1 Cmax is only increased by approximately 31-fold. Clearly this presents an issue when a minimum concentration threshold must be reached in the brain (Cmax) for a therapeutic effect.

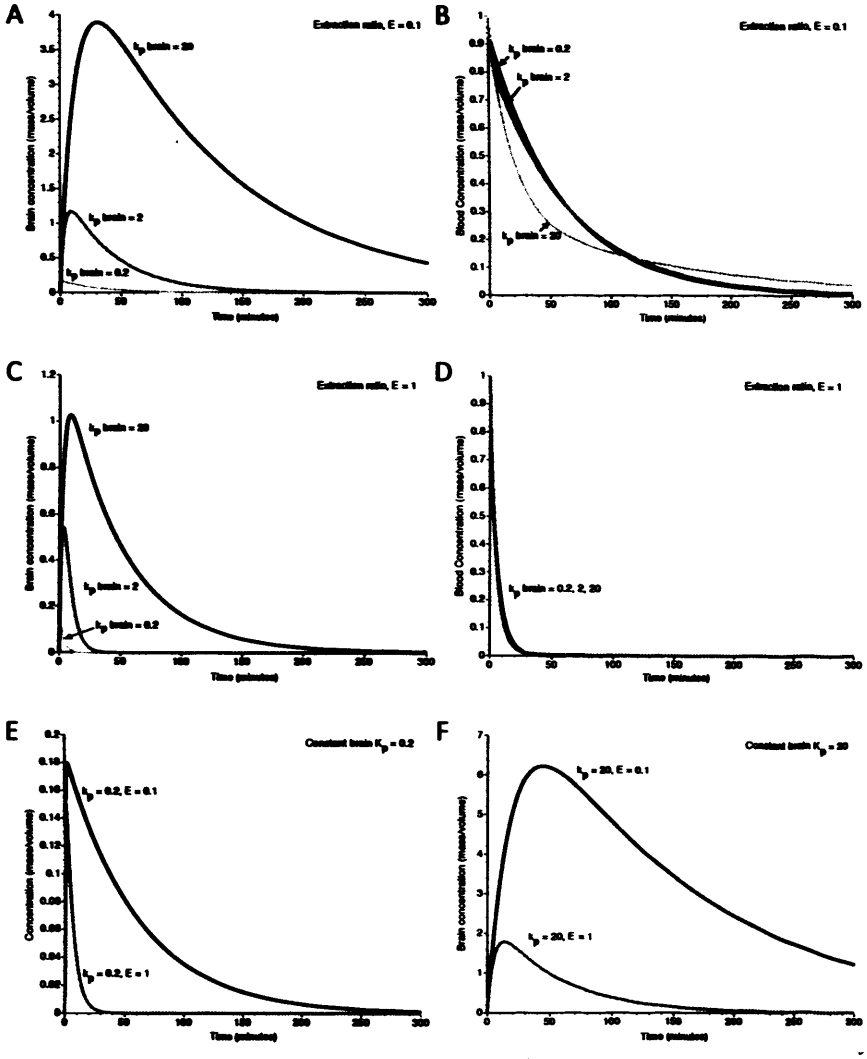

Figure 4.13 Brain and blood compartment PBPK simulations. (A) Change in brain pharmacokinetic profile with increasing affinity for brain tissue (kp = 0.2, 2 and 20) when the extraction ratio in the eliminating compartment is low (E = 0.1). (B) Change in blood pharmacokinetic profile with increasing affinity for brain tissue (kp = 0.2, 2 and 20) when the extraction ratio in the eliminating compartment is low (E = 0.1). (C) Change in brain pharmacokinetic profile with increasing affinity for brain tissue (kp = 0.2, 2 and 20) when the extraction ratio in the eliminating compartment is high (E = 1). (D) Change in blood pharmacokinetic profile with increasing affinity for brain tissue (kp = 0.2, 2 and 20) when the extraction ratio in the eliminating compartment is high (E = 1). (E) Change in brain pharmacokinetic profile with decreasing extraction ratio in the eliminating compartment (E = 0.1, 1) for a peptide with low brain affinity (kp = 0.2). (F) Change in brain pharmacokinetic profile with decreasing extraction ratio in the eliminating compartment (E = 0.1, 1) for a peptide with high brain affinity (kp = 20). A 10-fold decrease in E results in ~ 3.7-fold increase in Cmax.

Table 4.11 Brain pharmacokinetic parameters calculated from PBPK simulations.

Input Model Parameters		Model Predictions				
Extraction ratio eliminating organs	K_p Brain	MRT (mins)	AUC Blood$_{(0-\infty)}$ (Conc. units.mins)	AUC Brain$_{(0-\infty)}$ (Conc. units.mins)	C_{MAX} Brain (Conc. units)	t_{MAX} Brain (mins)
0.1	0.2	34.41	28.64	5.73	0.1551	2
0.1	2	39.15	28.64	57.28	1.1278	10
0.1	20	90.23	28.64	572.8	3.8341	32
1	0.2	3.34	3.05	1.08	0.1238	1
1	2	3.81	3.05	11.07	0.5343	4
1	20	8.40	3.05	110.6	1.0204	9

Table 4.12 Changes in brain pharmacokinetic parameters with increasing brain affinity and eliminating compartment extraction ratio.

Extraction ratio (E)	Change in Brain Kp	Fold change in brain AUC	Fold change in Brain C_{MAX}
0.1	0.2 to 2 (x10-fold)	10	7.3
0.1	2 to 20 (x10-fold)	10	3.4
0.1	0.2 to 20 (x100-fold)	100	24.7
1	0.2 to 2 (x10-fold)	10	4.3
1	2 to 20 (x10-fold)	10	1.9
1	0.2 to 20 (x100-fold)	100	8.2

Brain kp	Change in extraction ratio (E)	Fold change in brain AUC	Fold change in Brain C_{MAX}
0.2	1 to 0.1	5.3	1.25
2	1 to 0.1	5.3	2.11
20	1 to 0.1	5.3	3.75

The simulations also highlighted that care must be taken in interpreting differences in tissue concentrations at arbitrary timepoints. **Figure 4.14A** shows the difference in concentration for a given time-point between two molecules, both with a K_p[brain] of 20 but with extraction ratios in the eliminating organs of 0.1 and 1 respectively (brain concentrations for the two molecules are shown in **Figure 4.14B**). The difference in Cmax between the molecules is 3.75-fold and the difference in AUCs is 5.3 fold (see **Table 4.11**), however the difference in tissue concentration for a given timepoint increases exponentially even when the amount of drug remaining in tissue is very small and perhaps of no intrinsic therapeutic value.

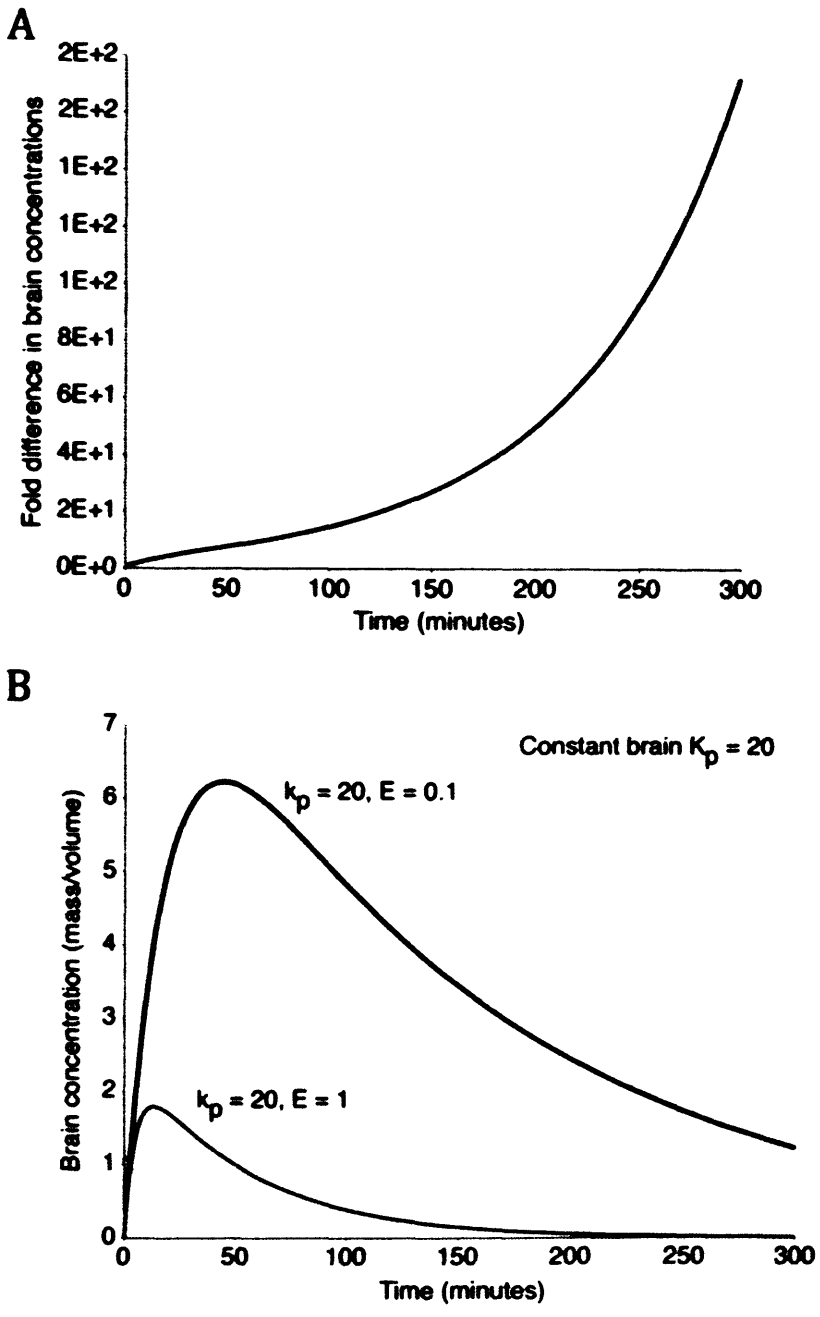

Figure 4.14 Difference in tissue concentration at a given timepoint between a drug with K_p[brain] of 20 and extraction ratio of 0.1 in the eliminating organs and a drug with K_p[brain] of 20 and extraction ratio of 1 in the eliminating organs. (A) With increasing time, differences in brain tissue concentration exponentially increase even when brain tissue concentrations may be negligible. (B) Tissue concentration profile of drugs modelled show that differences in AUC and Cmax are only modestly different (5.3-fold and 3.75-fold respectively).

The simulations provide some interesting context to the phage studies undertaken. Since the blood pharmacokinetic profile for SYTSSTM-M13 and insertless-M13 were found to be identical, their extraction ratios within the eliminating organs must be similarly identical. Therefore the increases observed in brain AUC with STYSSTM-M13 must reflect an increase in affinity for brain tissue and given the ratio of brain AUCs for SYTSSTM-M13 and insertless-M13 was 4 this implies SYTSSTM-M13 has a 4-fold increase in affinity for brain tissue compared to insertless-M13. Of course this similarly suggests that the affinity of SYTSSTM-M13 for liver and heart is respectively 3.3- and 3.6- fold greater than insertless-M13.

4.4 Discussion

Whilst considerable progress has been made in developing vectors for the efficient delivery of biologics across many biological barriers, delivery across the BBB and into the brain remains a significant challenge. To overcome the limiting nature of the BBB a range of methods have been proposed for the effective delivery of therapeutics including the transient opening of the BBB with osmotic agents[76-78] or bradykinin analogs[76] and exploitation of specific transport systems at the BBB such as transferrin receptor, insulin receptor, monocarboxylate, amine and neutral amino acid transporters. More recently interest has grown in the use of peptides as drug delivery vectors. Such peptides include peptides designed against specific receptors such as LRP[79] or the more general CPPs such as SynB1 and SynB4 peptides, a new class of vectors derived from the

antimicrobial protein protegrin 1 originally isolated from porcine leucocytes[80-82] and products of pathogens that have the capacity to traverse the plasmalemma such as Antennapedia and Tat peptides from human immunodeficiency virus. Indeed in studies detailed in chapter 3, a peptide sharing significant homology with the V3 loop of HIV GP 120 was recovered in panning experiments against mouse BBB endothelia; GP 120 has been implicated in the entry of HIV into CD4 -/- cells.

Generally the cell penetrating peptides investigated to date are highly positively charged and as such stimulate adsorptive mediated endocytosis, a ubiquitous route of entry into the cell that occurs within all vascular beds. To afford site-specific delivery of biologics, many researchers are seeking to identify peptides that interact with vascular addresses on capillary endothelia within the tissue of interest. Phage display has shown promise in surveying the molecular landscape within such vascular beds to identify unique peptides and peptide motifs that promote cell binding and potentially transcytosis.

In the studies described in this chapter, two strategies were employed to identify peptides that home to the brain and specifically to brain grey matter. In both strategies male SD rats were injected with a peptide-phage library that contains 1.2 x 10^9 unique phage peptide clones and after 15 minutes circulation time the rats were perfused with ice-cold saline to flush the blood from the animal and then a low pH glycine buffer (pH 2.2) to strip the vasculature of binding peptides; glycine has been shown to non-

specifically disrupt phage peptide interactions without rendering the phages non-infective. Both saline and glycine buffer were checked prior to each study to ensure they were iso-osmotic and therefore unlikely to damage vasculature. The low pH of the glycine perfusion may have been expected to damage the vasculature but experiments that examined the effects of saline and glycine perfusion on phage uptake did not suggest this was so. In strategy 1, three rounds of selection were undertaken in which only phages from the brain served as input into iterative rounds of selection. Specifically, the brain was harvested, the white matter removed and the capillaries depleted to leave grey matter from which phages were recovered. Of note, the accumulation of phages within the brain increased with each iterative round whilst the accumulation in the other organs harvested decreased. In strategy 2 a synchronous selection process was undertaken based on the studies detailed by Pasqualini and co-workers[68]. In the first four rounds of panning, library phages were recovered from brain, heart, lung, kidney, liver, spleen and testicle, amplified and pooled for the next iterative round of panning. A final fifth panning round was undertaken where only the phages recovered from grey matter in round 4 were injected. Whilst the overall aim in strategy 2 was to identify peptides that mediate the traversal of phages across the BBB and into the brain, the phages recovered from the other organs harvested in isolation strategy 2 are stored ready for future analysis. This strategy would be particularly advantageous in continuing the *in-vivo* human studies

pioneered by Wadih Arap and co-workers[53] where it may be critical to identify tissue homing peptides to a variety of organs in a single screen.

Gene sequencing of an extensive number of phages recovered from the brain in the final rounds of selection in strategies 1 and 2 revealed some peptide motifs present in higher frequency. Strategy 2 in particular resulted in the isolation of clones present as a significant fraction of the phage population, with AC-**SYTSSTM**-CGGGS and AC-**SNTSSTT**-CGGGS combined present as ~ 25% of the pool sequenced; notably, these two peptides share a common motif AC-**SxTSSTx**-CGGS. In isolation strategy 1 the most frequent clones in the population were present at around 1.5% of the pool sequenced (AC-**PDVPHPA**-CGGGS and AC-**STASTQA**-CGGGS). These results raise the question why does strategy 2 appear to be more successful in selecting a common motif and clones occurring in higher frequency than strategy 1? One would imagine recovering peptide phages from the brain alone (strategy 1) would be more efficient in selecting brain homing phages than pooling phages recovered from multiple organs (strategy 2). It is difficult to address this issue satisfactorily although there may be issues surrounding the number of panning rounds undertaken, three for strategy 1 versus five for strategy 2 and in hindsight it may have been better to undertake further selection rounds in strategy 1. However, a frequency analysis of the amino acids at the seven random positions in the peptides identified in strategies 1 and 2 suggested consistency between the two panning strategies indicating that serine residues at positions 1, 4 and 5

may be important for brain homing. Coincidentally serine residues at positions 1, 4 and 5 are in agreement with in the highest frequency binders AC-**SYTSSTM**-CGGGS and AC-**SNTSSTT**-CGGGS. A population of phages associated with the capillary fraction of the brain were also sequenced and within this population AC-**SYTSSTM**-CGGGS and AC-**PDVPHPA**-CGGGS were identified with a frequency of 19% and 13% respectively. These data suggested that AC-**SYTSSTM**-CGGGS and AC-**PDVPHPA**-CGGGS may gain access to the brain via the microvasculature.

Physicochemical analysis of the primary amino acid sequences of the all the peptide-phage clones recovered from the brain in isolation strategies 1 and 2 (600 sequences in total) revealed the displayed peptides were largely composed of hydrophilic residues. This probably suggests that the peptides would not diffuse through the plasma membrane. Of note, the isoelectric points of the peptides recovered were mainly between 6 and 8 and 9 and 11. It is interesting to note that the population of phages with pI 9-11 will be highly cationic in nature, a feature in common with the cell penetrating peptides that are thought to interact with anionic domains on the plasmalemmal glycocalyx to stimulate adsorptive endocytosis as a consequence of their isoelectric point[83, 84]. It is recognized that the interactions of peptides and proteins with surface receptors is dictated by pH and pI. For example lactoferrin binds specific receptors on the surface of human monocytes to affect iron deposition. When the iron has been deposited, there is a subtle change in the pI of lactoferrin from 8.8 to 8.9

which grossly impairs the rebinding of lactotransferrin to its cognate receptor[85]. The pI data obtained for the peptides would therefore at the very least discount the peptides from binding certain receptors where these pIs would be unfavourable. Those peptides with pIs greater than 9 were not extensively investigated in tissue distribution studies because it was envisaged that they may act as cell penetrating peptides and enhance phage uptake ubiquitously in all tissue types. Notably, sequences AC-**SYTSSTM**-CGGGS, AC-**SNTSSTT**-CGGGS and AC-**PDVPHPA**-CGGGS, identified in the highest frequency in grey matter and/or capillary fraction, are not highly cationic at neutral pH and are therefore unlikely to stimulate adsorptive endocytosis.

A search of the SWISSPROT database using the BLAST search engine did not reveal any homologies of note with the most commonly identified peptides from the selection strategies only corresponding with hypothetical proteins, proteins that are predicted from genomic sequencing but the expression of which have not been confirmed. This is not uncommon in phage display against cellular targets that express a significant diversity of receptors and surface markers. Arguably, the goal of phage display is to identify novel peptide sequences that interact with target and although this gives no indication of the nature of the target, methods such as immuno-precipitation can be used subsequently to identify the binding partner.

Based on the results of the initial panning strategies the brain uptake of AC-**SYTSSTM**-CGGS (the most common clone in strategy 2), AC-**PDVPHPA**-

CGGGS (high frequency in capillary fraction and grey matter in strategy 1) and AC-**TQPARSQ**-CGGGS (recovered in isolation strategy 1 and highly cationic) was compared to the uptake of insertless-M13 15 minutes after intravenous administration. The results of these studies suggested that only phages displaying AC-**SYTSSTM**-CGGGS were taken up to a greater extent than insertless phages. Whilst the failure of clones PDVPHPA-M13 and TQPARSQ-M13 to gain enhanced access to the brain was disappointing, the ~ 8 fold greater uptake of SYTSSTM-M13 (corrected for amplification errors) was encouraging. Some thought was given to using *in-vitro* BBB models to determine permeability co-efficients for SYTSSTM-M13 and insertless-M13 but as detailed in chapter 3, the establishment of a highly restrictive rat BBB model proved elusive. Therefore, an extensive *in-vivo* distribution study of SYTSSTM-M13 was undertaken. 1×10^{11} pfus of SYTSSTM-M13 and insertless-M13 were co-injected intravenously and the number of phages accumulating in the major organs of the body assessed at various timepoints from which the AUCs were calculated for each of the tissues. In agreement with *in-vivo* assessments of the biodistribution of M13 phages in mice, accumulation was primarily observed in the liver and spleen with relatively little uptake in the brain[67]. Nevertheless, the brain AUC of SYTSSTM-M13 was found to be ~ 4-fold greater than insertless-M13 which suggests a ~ 4-fold greater affinity for brain than insertless-M13. An increase in tissue uptake was also observed in the heart (3.6-fold) and liver (3.3-fold), although to a lesser extent than the brain, with the remaining tissues showing comparable uptake of SYTSSTM-M13 and insertless-M13.

The increased uptake in tissues other than the brain is not entirely unexpected since few receptors or cell surface markers are found exclusively in a single vascular bed. For example OX-26 a monoclonal antibody that binds transferrin receptor has been intensively investigated for the delivery of therapeutic cargos into the brain (see **Table 4.2** for examples). The density of transferrin receptor at the BBB has been estimated as ~ 60,000 receptors per cell[15] whilst for liver it is ~ 120,000 receptors per cell[86]. Therefore, increases in brain uptake of therapeutic cargos conjugated to OX-26 are paralleled in the liver. Indeed, comparison of OX-26 uptake with isotypic control results in an 18-fold greater uptake in the brain and a 13-fold greater uptake in the liver 5 hours post administration[87]. In cases where the sole objective is increased brain uptake and accompanying increases in peripheral uptake are not important, arguably this doesn't matter. Conversely if a therapeutic cargo is highly toxic, for example a chemotherapeutic agent, site specific rather than site selective delivery may be of greater import. A limiting aspect of the studies undertaken is that accumulation of phage cannot be monitored over time within the same animal rather each timepoint requires a separate animal (in triplicate for each timepoint). Inherent biological variability between animals coupled with the inaccuracy in phage titers results in relatively large standard deviations in the data making statistical analysis difficult. Nevertheless, only within brain was the peak concentration (Cmax) of phages significantly greater (~ 3.4-fold) for SYTSSTM-M13 compared to insertless-M13.

Few phage display studies have sought to identify peptides that mediate the traversal of the BBB. Pasqualini and co-workers[68] described a tri-peptide motif, RGF, that was present in ~ 3.5% of the clones sequenced after a third round of selection however subsequent measurements of brain accumulation of clones displaying this motif were not undertaken. Fan and co-workers[88] utilized a cyclic 7-mer T7 phage display library to identify peptides that home to mouse brain; T7 is a lytic phage that infects *E. coli*. A peptide sequence CAGALCY was demonstrated to accumulate in the brain approximately 1000-fold greater than insertless-T7 at 2 hours post administration; no AUC data was reported. Whilst these results demonstrate the utility of phage in selecting brain homing peptides some care must be taken in their interpretation. The mice in the study were not perfused with any agent to strip the microvasculature of binding phages and the white matter, accessory organs and capillaries were left in-situ. Therefore the phages recovered represent accumulation in the whole brain. Friden[26] and Moos and Morgan[89] demonstrated in the early 1990s that only a small fraction of material associated with whole brain actually reaches the parenchyma (5 - 10%). In the phage studies undertaken in this chapter, only brain parenchyma was collected and analysed and perhaps therefore, whilst the results described are more modest they may better reflect true brain uptake.

To contextualise the peptide phage results obtained, a physiologically based pharmacokinetic model was constructed. In their simplest form, the

simulations showed that increases in affinity for brain tissue are directly proportional to increases in AUC, however this was not the case for peak concentration Cmax and even relatively large increases in brain affinity may only result in modest increases in peak concentration. The simulations also highlighted the need for researchers to report AUCs and Cmax not just differences in concentration at an arbitrary time-point which can unwittingly exaggerate the true enhancement in uptake. More importantly, the model reinforced the concept that a combination of increasing brain affinity AND increasing circulation time is the optimal strategy for improving brain accumulation. These data reaffirm that strategies such as PEGylation of a therapeutic entity to prolong circulation half-life coupled with conjugation to a targeting vector is a considered approach to improving brain penetration.

In summary, the aim of the studies in this chapter was to identify peptides that home to the brain. A peptide with sequence AC-**SYTSSTM**-CGGGS modestly increased the accumulation of a supramacromolecular entity into the brain with an approximate 4-fold increase in brain AUC. Further characterization of this peptide within *in-situ* brain perfusion models and brain microdialysis systems would help to examine brain transport kinetics without interference from whole body disposition processes. Clearly, the work detailed in this chapter is not at a conclusion and with more time many exciting studies can be designed to further investigate the true utility of the identified peptide to deliver therapeutics to the brain.

Reference List

1. Pan, W., et al., *Transport of brain-derived neurotrophic factor across the blood-brain barrier.* Neuropharmacology, 1998. **37**(12): p. 1553-61.

2. Poduslo, J.F. and G.L. Curran, *Permeability at the blood-brain and blood-nerve barriers of the neurotrophic factors: NGF, CNTF, NT-3, BDNF.* Brain Res Mol Brain Res, 1996. **36**(2): p. 280-6.

3. Zhang, Y. and W.M. Pardridge, *Blood-brain barrier targeting of BDNF improves motor function in rats with middle cerebral artery occlusion.* Brain Res, 2006. **1111**(1): p. 227-9.

4. Pardridge, W.M., *Blood-brain barrier drug targeting enables neuroprotection in brain ischemia following delayed intravenous administration of neurotrophins.* Adv Exp Med Biol, 2002. **513**: p. 397-430.

5. Zhang, Y. and W.M. Pardridge, *Neuroprotection in transient focal brain ischemia after delayed intravenous administration of brain-derived neurotrophic factor conjugated to a blood-brain barrier drug targeting system.* Stroke, 2001. **32**(6): p. 1378-84.

6. Zhang, Y. and W.M. Pardridge, *Conjugation of brain-derived neurotrophic factor to a blood-brain barrier drug targeting system enables neuroprotection in regional brain ischemia following intravenous injection of the neurotrophin.* Brain Res, 2001. **889**(1-2): p. 49-56.

7. Pardridge, W.M., Y.S. Kang, and J.L. Buciak, *Transport of human recombinant brain-derived neurotrophic factor (BDNF) through the rat blood-brain barrier in vivo using vector-mediated peptide drug delivery.* Pharm Res, 1994. **11**(5): p. 738-46.

8. Stewart, P.A., *Endothelial vesicles in the blood-brain barrier: are they related to permeability?* Cell Mol Neurobiol, 2000. **20**(2): p. 149-63.

9. Bundgaard, M., *Vesicular transport in capillary endothelium: does it occur?* Fed Proc, 1983. **42**(8): p. 2425-30.

10. Frokjaer-Jensen, J., *Three-dimensional organization of plasmalemmal vesicles in endothelial cells. An analysis by serial sectioning of frog mesenteric capillaries.* J Ultrastruct Res, 1980. **73**(1): p. 9-20.

11. Frokjaer-Jensen, J., *The plasmalemmal vesicular system in striated muscle capillaries and in pericytes.* Tissue Cell, 1984. **16**(1): p. 31-42.

12. Smith, M., Y. Omidi, and M. Gumbleton, *Primary porcine brain microvascular endothelial cells: biochemical and functional*

characterisation as a model for drug transport and targeting. J Drug Target, 2007. **15**(4): p. 253-68.

13. Omidi, Y., et al., *Evaluation of the immortalised mouse brain capillary endothelial cell line, b.End3, as an in vitro blood-brain barrier model for drug uptake and transport studies.* Brain Res, 2003. **990**(1-2): p. 95-112.

14. Gragera, R.R., E. Muniz, and R. Martinez-Rodriguez, *Molecular and ultrastructural basis of the blood-brain barrier function. Immunohistochemical demonstration of Na+/K+ ATPase, alpha-actin, phosphocreatine and clathrin in the capillary wall and its microenvironment.* Cell Mol Biol (Noisy-le-grand), 1993. **39**(8): p. 819-28.

15. Pardridge, W.M., J. Eisenberg, and J. Yang, *Human blood-brain barrier transferrin receptor.* Metabolism, 1987. **36**(9): p. 892-5.

16. Banks, W.A., et al., *Studies of the slow bidirectional transport of iron and transferrin across the blood-brain barrier.* Brain Res Bull, 1988. **21**(6): p. 881-5.

17. Bradbury, M.W., *Transport of iron in the blood-brain-cerebrospinal fluid system.* J Neurochem, 1997. **69**(2): p. 443-54.

18. Moos, T. and E.H. Morgan, *Evidence for low molecular weight, non-transferrin-bound iron in rat brain and cerebrospinal fluid.* J Neurosci Res, 1998. **54**(4): p. 486-94.

19. Malecki, E.A., et al., *Existing and emerging mechanisms for transport of iron and manganese to the brain.* J Neurosci Res, 1999. **56**(2): p. 113-22.

20. Westergaard, E., *The blood-brain barrier to horseradish peroxidase under normal and experimental conditions.* Acta Neuropathol, 1977. **39**(3): p. 181-7.

21. Guillot, F.L. and K.L. Audus, *Angiotensin peptide regulation of fluid-phase endocytosis in brain microvessel endothelial cell monolayers.* J Cereb Blood Flow Metab, 1990. **10**(6): p. 827-34.

22. Guillot, F.L. and K.L. Audus, *Angiotensin peptide regulation of bovine brain microvessel endothelial cell monolayer permeability.* J Cardiovasc Pharmacol, 1991. **18**(2): p. 212-8.

23. Guillot, F.L., K.L. Audus, and T.J. Raub, *Fluid-phase endocytosis by primary cultures of bovine brain microvessel endothelial cell monolayers.* Microvasc Res, 1990. **39**(1): p. 1-14.

24. Banks, W.A. and R.D. Broadwell, *Blood to brain and brain to blood passage of native horseradish peroxidase, wheat germ agglutinin, and*

albumin: pharmacokinetic and morphological assessments. J Neurochem, 1994. **62**(6): p. 2404-19.

25. Smith, M.W. and M. Gumbleton, *Endocytosis at the blood-brain barrier: from basic understanding to drug delivery strategies.* J Drug Target, 2006. **14**(4): p. 191-214.

26. Friden, P.M., et al., *Anti-transferrin receptor antibody and antibody-drug conjugates cross the blood-brain barrier.* Proc Natl Acad Sci U S A, 1991. **88**(11): p. 4771-5.

27. Bickel, U., et al., *Pharmacologic effects in vivo in brain by vector-mediated peptide drug delivery.* Proc Natl Acad Sci U S A, 1993. **90**(7): p. 2618-22.

28. Kordower, J.H., et al., *Intravenous administration of a transferrin receptor antibody-nerve growth factor conjugate prevents the degeneration of cholinergic striatal neurons in a model of Huntington disease.* Proc Natl Acad Sci U S A, 1994. **91**(19): p. 9077-80.

29. Pardridge, W.M., R.J. Boado, and Y.S. Kang, *Vector-mediated delivery of a polyamide ("peptide") nucleic acid analogue through the blood-brain barrier in vivo.* Proc Natl Acad Sci U S A, 1995. **92**(12): p. 5592-6.

30. Walus, L.R., et al., *Enhanced uptake of rsCD4 across the rodent and primate blood-brain barrier after conjugation to anti-transferrin receptor antibodies.* J Pharmacol Exp Ther, 1996. **277**(2): p. 1067-75.

31. Huwyler, J., D. Wu, and W.M. Pardridge, *Brain drug delivery of small molecules using immunoliposomes.* Proc Natl Acad Sci U S A, 1996. **93**(24): p. 14164-9.

32. Shi, N., et al., *Brain-specific expression of an exogenous gene after i.v. administration.* Proc Natl Acad Sci U S A, 2001. **98**(22): p. 12754-9.

33. Penichet, M.L., et al., *An antibody-avidin fusion protein specific for the transferrin receptor serves as a delivery vehicle for effective brain targeting: initial applications in anti-HIV antisense drug delivery to the brain.* J Immunol, 1999. **163**(8): p. 4421-6.

34. Mishra, V., et al., *Targeted brain delivery of AZT via transferrin anchored pegylated albumin nanoparticles.* J Drug Target, 2006. **14**(1): p. 45-53.

35. Lee, H.J., et al., *Imaging gene expression in the brain in vivo in a transgenic mouse model of Huntington's disease with an antisense radiopharmaceutical and drug-targeting technology.* J Nucl Med, 2002. **43**(7): p. 948-56.

38. Gabathuler, R., et al., *Development of a potential protein vector (NeuroTrans) to deliver drugs across the blood-brain barrier.* International Congress Series, 2005. **1277**: p. 171-184.

39. Kreuter, J., *Influence of the surface properties on nanoparticle-mediated transport of drugs to the brain.* J Nanosci Nanotechnol, 2004. **4**(5): p. 484-8.

40. Lode, J., et al., *Influence of surface-modifying surfactants on the pharmacokinetic behavior of 14C-poly (methylmethacrylate) nanoparticles in experimental tumor models.* Pharm Res, 2001. **18**(11): p. 1613-9.

41. Derossi, D., et al., *Cell internalization of the third helix of the Antennapedia homeodomain is receptor-independent.* J Biol Chem, 1996. **271**(30): p. 18188-93.

42. Derossi, D., et al., *The third helix of the Antennapedia homeodomain translocates through biological membranes.* J Biol Chem, 1994. **269**(14): p. 10444-50.

43. Vives, E., P. Brodin, and B. Lebleu, *A truncated HIV-1 Tat protein basic domain rapidly translocates through the plasma membrane and accumulates in the cell nucleus.* J Biol Chem, 1997. **272**(25): p. 16010-7.

44. Fischer, R., et al., *Break on through to the other side-biophysics and cell biology shed light on cell-penetrating peptides.* Chembiochem, 2005. **6**(12): p. 2126-42.

45. Richard, J.P., et al., *Cellular uptake of unconjugated TAT peptide involves clathrin-dependent endocytosis and heparan sulfate receptors.* J Biol Chem, 2005. **280**(15): p. 15300-6.

46. Banks, W.A., S.M. Robinson, and A. Nath, *Permeability of the blood-brain barrier to HIV-1 Tat.* Exp Neurol, 2005. **193**(1): p. 218-27.

47. Rousselle, C., et al., *New advances in the transport of doxorubicin through the blood-brain barrier by a peptide vector-mediated strategy.* Mol Pharmacol, 2000. **57**(4): p. 679-86.

48. Mazel, M., et al., *Doxorubicin-peptide conjugates overcome multidrug resistance.* Anticancer Drugs, 2001. **12**(2): p. 107-16.

49. Rousselle, C., et al., *Enhanced delivery of doxorubicin into the brain via a peptide-vector-mediated strategy: saturation kinetics and specificity.* J Pharmacol Exp Ther, 2001. **296**(1): p. 124-31.

50. Rousselle, C., et al., *Improved brain delivery of benzylpenicillin with a peptide-vector-mediated strategy.* J Drug Target, 2002. **10**(4): p. 309-15.

51. Rousselle, C., et al., *Improved brain uptake and pharmacological activity of dalargin using a peptide-vector-mediated strategy.* J Pharmacol Exp Ther, 2003. **306**(1): p. 371-6.

52. Temsamani, J., et al., *Improved brain uptake and pharmacological activity profile of morphine-6-glucuronide using a peptide vector-mediated strategy.* J Pharmacol Exp Ther, 2005. **313**(2): p. 712-9.

53. Arap, W., et al., *Steps toward mapping the human vasculature by phage display.* Nat Med, 2002. **8**(2): p. 121-7.

54. Li, X.B., H.J. Schluesener, and S.Q. Xu, *Molecular addresses of tumors: selection by in vivo phage display.* Arch Immunol Ther Exp (Warsz), 2006. **54**(3): p. 177-81.

55. Kolonin, M., R. Pasqualini, and W. Arap, *Molecular addresses in blood vessels as targets for therapy.* Curr Opin Chem Biol, 2001. **5**(3): p. 308-13.

56. Hajitou, A., R. Pasqualini, and W. Arap, *Vascular targeting: recent advances and therapeutic perspectives.* Trends Cardiovasc Med, 2006. **16**(3): p. 80-8.

57. Zurita, A.J., W. Arap, and R. Pasqualini, *Mapping tumor vascular diversity by screening phage display libraries.* J Control Release, 2003. **91**(1-2): p. 183-6.

58. Pasqualini, R., W. Arap, and D.M. McDonald, *Probing the structural and molecular diversity of tumor vasculature.* Trends Mol Med, 2002. **8**(12): p. 563-71.

59. Trepel, M., W. Arap, and R. Pasqualini, *In vivo phage display and vascular heterogeneity: implications for targeted medicine.* Curr Opin Chem Biol, 2002. **6**(3): p. 399-404.

60. Becerril, B., M.A. Poul, and J.D. Marks, *Toward selection of internalizing antibodies from phage libraries.* Biochem Biophys Res Commun, 1999. **255**(2): p. 386-93.

61. Arap, W., R. Pasqualini, and E. Ruoslahti, *Cancer treatment by targeted drug delivery to tumor vasculature in a mouse model.* Science, 1998. **279**(5349): p. 377-80.

62. Koivunen, E., D.A. Gay, and E. Ruoslahti, *Selection of peptides binding to the alpha 5 beta 1 integrin from phage display library.* J Biol Chem, 1993. **268**(27): p. 20205-10.

63. Braathen, R., et al., *Identification of a polymeric Ig receptor binding phage-displayed peptide that exploits epithelial transcytosis without dimeric IgA competition.* J Biol Chem, 2006. **281**(11): p. 7075-81.

64. Poulin, P. and F.P. Theil, *Prediction of pharmacokinetics prior to in vivo studies. II. Generic physiologically based pharmacokinetic models of drug disposition.* J Pharm Sci, 2002. **91**(5): p. 1358-70.

65. Poulin, P. and F.P. Theil, *Prediction of pharmacokinetics prior to in vivo studies. 1. Mechanism-based prediction of volume of distribution.* J Pharm Sci, 2002. **91**(1): p. 129-56.

66. Molenaar, T.J., et al., *Uptake and processing of modified bacteriophage M13 in mice: implications for phage display.* Virology, 2002. **293**(1): p. 182-91.

67. Zou, J., et al., *Biodistribution of filamentous phage peptide libraries in mice.* Mol Biol Rep, 2004. **31**(2): p. 121-9.

68. Kolonin, M.G., et al., *Synchronous selection of homing peptides for multiple tissues by in vivo phage display.* FASEB J, 2006. **20**(7): p. 979-81.

69. Yu, C., et al., *Gamma glutamyl transpeptidase is a dynamic indicator of endothelial response to stroke.* Exp Neurol, 2007. **203**(1): p. 116-22.

70. NEB, *Ph.D.™ Phage Display Libraries. Instruction Manual.* 2009.

71. Armstrong, J., R.N. Perham, and J.E. Walker, *Domain structure of bacteriophage fd adsorption protein.* FEBS Lett, 1981. **135**(1): p. 167-72.

72. Gray, C.W., R.S. Brown, and D.A. Marvin, *Adsorption complex of filamentous fd virus.* J Mol Biol, 1981. **146**(4): p. 621-7.

73. Deng, L.W. and R.N. Perham, *Delineating the site of interaction on the pIII protein of filamentous bacteriophage fd with the F-pilus of Escherichia coli.* J Mol Biol, 2002. **319**(3): p. 603-14.

74. Fridholm, H. and E. Everitt, *Rapid and reproducible infectivity end-point titration of virulent phage in a microplate system.* J Virol Methods, 2005. **128**(1-2): p. 67-71.

75. Folkow, B., *Circulation.* 1971, New York: Oxford University Press.

76. Kroll, R.A. and E.A. Neuwelt, *Outwitting the blood-brain barrier for therapeutic purposes: osmotic opening and other means.* Neurosurgery, 1998. **42**(5): p. 1083-99; discussion 1099-100.

77. Haluska, M. and M.L. Anthony, *Osmotic blood-brain barrier modification for the treatment of malignant brain tumors.* Clin J Oncol Nurs, 2004. **8**(3): p. 263-7.

78. Demeule, M., et al., *Involvement of the low-density lipoprotein receptor-related protein in the transcytosis of the brain delivery vector Angiopep-2.* J Neurochem, 2008. **106**(4): p. 1534-1544.

79. Rapoport, S.I., *Osmotic opening of the blood-brain barrier: principles, mechanism, and therapeutic applications.* Cell Mol Neurobiol, 2000. **20**(2): p. 217-30.

80. Kokryakov, V.N., et al., *Protegrins: leukocyte antimicrobial peptides that combine features of corticostatic defensins and tachyplesins.* FEBS Lett, 1993. **327**(2): p. 231-6.

81. Harwig, S.S., et al., *Determination of disulphide bridges in PG-2, an antimicrobial peptide from porcine leukocytes.* J Pept Sci, 1995. **1**(3): p. 207-15.

82. Aumelas, A., et al., *Synthesis and solution structure of the antimicrobial peptide protegrin-1.* Eur J Biochem, 1996. **237**(3): p. 575-83.

83. Fittipaldi, A. and M. Giacca, *Transcellular protein transduction using the Tat protein of HIV-1.* Adv Drug Deliv Rev, 2005. **57**(4): p. 597-608.

84. Wadia, J.S. and S.F. Dowdy, *Transmembrane delivery of protein and peptide drugs by TAT-mediated transduction in the treatment of cancer.* Adv Drug Deliv Rev, 2005. **57**(4): p. 579-96.

85. Birgens, H.S. and L.O. Kristensen, *Impaired receptor binding and decrease in isoelectric point of lactoferrin after interaction with human monocytes.* Eur J Haematol, 1990. **45**(1): p. 31-5.

86. Rudolph, J.R., E. Regoeczi, and S. Southward, *Quantification of rat hepatocyte transferrin receptors with poly- and monoclonal antibodies and protein A.* Histochemistry, 1988. **88**(2): p. 187-92.

87. Pardridge, W.M., J.L. Buciak, and P.M. Friden, *Selective transport of an anti-transferrin receptor antibody through the blood-brain barrier in vivo.* J Pharmacol Exp Ther, 1991. **259**(1): p. 66-70.

88. Fan, X., et al., *An in vivo approach to structure activity relationship analysis of peptide ligands.* Pharm Res, 2007. **24**(5): p. 868-79.

89. Moos, T. and E.H. Morgan, *Restricted transport of anti-transferrin receptor antibody (OX26) through the blood-brain barrier in the rat.* J Neurochem, 2001. **79**(1): p. 119-29.

Chapter 5 Caveolin-1: a novel drug target in Glioma

5.1 Introduction

5.1.1 The functional role of caveolin-1 in oncogenesis and metastatic disease

In recent years, the role of caveolae and caveolins in human health and disease has received significant attention in such areas as cancer, muscular dystrophy, diabetes, atherosclerosis, Alzheimer's disease and HIV (reviewed in [1]). However, it is within the field of oncology and specifically the pathogenesis of cancer that their study has been particularly focused. Traditionally caveolin-1 has been viewed as a tumour suppressor protein given its absence in breast, lung and ovarian cancer cell lines derived from tumour tissue and not least its ability to inhibit the EGF-R/RAS/ERK growth signaling pathway when recombinantly re-expressed in respective *in-vitro* models [1-3]. Further, the gene encoding caveolin-1 is mapped to chromosome 7q31.1, a locus frequently deleted, amplified or mutated in a variety of common cancers such as those of the breast, prostate and kidney[4, 5]. More recently, however, two seminal papers[6, 7] were published that described the up-regulation of caveolin-1 in clinical specimens of prostate cancer. In these specimens, caveolin-1 was shown to drive the aggressive features of prostate cancer including invasion and development of androgen resistance[6, 7]. Following on from this a succession of clinical papers were published correlating caveolin-1 over-expression with disease progression in a diverse range of cancer types including amongst others lung, pancreas, kidney and colon[2, 8].

Despite significant studies into the role of caveolin-1 in cancer development and progression, its precise function remains complex and controversial; caveolin-1 has been described variously as a tumour suppressor or tumour promoter depending on the tumour type and disease stage. This dual function is perhaps best exemplified in breast cancer. Studies undertaken with caveolin-1 knockout mice [9, 10] and cells derived from breast carcinomas [11, 12] have shown that the loss of caveolin-1 from mammary cells is sufficient to promote the pathogenesis of breast cancer. These pathological features include activation of the EGF-R/RAS/ERK signaling pathway, increased cell proliferation, initiation of mammary hyperplasia and enhanced anchorage independent growth leading to invasion and metastasis. On the other hand, several clinico-pathological studies, including those within the supervisor's laboratory[13], have shown that caveolin-1 over-expression correlates with the aggressive features of certain breast cancers, most notably the basal-like and inflammatory invasive subtypes[14-16]. **Table 5.1** shows the cancers in which caveolin-1 expression is elevated in primary tumours compared to matched normal tissue and positively correlates with poor clinical outcome. Notably, positive expression of caveolin-1 correlates with post-operative disease recurrence, increased invasive and metastatic potential and increased chemotherapeutic resistance, that, altogether are suggestive of an aggressive phenotype.

Table 5.1 Carcinomas in which raised caveolin-1 expression correlates with poor clinical prognosis (adapted from [17]).

Tissue	Tumour type	Ref
Esophagus	Squamous cell carcinoma (oral cavity)	[18-20]
Pancreas	Ductal adenocarcinoma	[21]
	Intraductal papillary-mucinous tumour	[22]
Colon	Adenocarcinoma	[23]
Liver	Hepatocellular carcinoma from cirrhotic liver	[24-26]
Kidney	Clear cell renal carcinoma	[27-30]
Bladder	Urothelial carcinoma	[29-32]
	Squamous cell carcinoma	[30, 32]
Prostate	Androgen sensitive and insensitive adenocarcinoma	[6, 33-38]
Breast	Ductal carcinoma	[6, 39]
	Basal-like carcinoma	[39, 40]
Lung	Non-small-cell lung cancer	[41, 42]
	Pleomorphic carcinoma	[43]
	Squamous cell carcinoma	[44, 45]
	Adenocarcinoma	[46]
Thyroid	Papillary carcinoma	[47, 48]
Brain	Glioma	[49, 50]
	Meningioma	[51]
Mesenchyme	Ewing's sarcoma	[52]

Caveolin-1, a scaffolding protein, primarily exerts its actions through a cytoplasmically oriented scaffolding domain (CSD; AAs 82-101) that binds partner proteins that contain a caveolin binding motif[53]. Caveolin-1 thereby compartmentalizes signaling molecules within caveolae serving as a checkpoint for signaling cascades. This signaling is controlled through direct interaction of partner proteins with CSD. Specifically caveolin-1 is considered to serve as a molecular brake which inhibits the intrinsic kinase activity of a diverse range of signaling molecules via the action of the CSD. [54]. Many signaling molecules and growth factor receptors have been shown to interact with CSD including tyrosine kinases (Src family), glycoslyl phosphatidylinositol-linked proteins, endothelial nitric oxide synthetase (eNOS), PKC isoforms and H-Ras, heterotrimeric G protein [55].

In addition, caveolin-1 has been shown to regulate a number of genes involved in tumourigenesis and tumour progression notably BRCA1, IGFR, cyclin D1, ERα and survivin[56]. Such interactions in cell signaling and gene pathways confer on caveolin-1 a regulatory role in tumour proliferation, differentiation, apoptosis and invasion.

5.1.2 Molecular mechanisms of caveolin-1 in cancer progression

Whilst the precise role of caveolin-1 in cancer progression remains to be fully elucidated a number of key molecular mechanisms have been described. Caveolin-1 appears to promote metastatic potential through a general role in cell motility, recycling membrane material on the receding face and inserting membrane material into the leading edge thus providing cellular locomotion[57]. Additionally, a number of *in-vitro* studies have revealed a positive interaction of caveolin-1 with GTPases that are critical in promoting cell motility [58-60]. Further, caveolin-1 probably plays some role in the loss of cell-cell contacts in invasive carcinomas; caveolin-1 localises to both adherens (zonula adherens) and tight (zonula occludens) junctions to stabilize epithelial and endothelial barriers[61, 62]. Intracellular sequestration of membranous caveolin-1 has been shown at least *in-vitro* to increase invasive capacity[63].

The subcellular localization of caveolin-1 is influenced by post-translational modifications of various domains within the protein which in turn serves to modify the overall function of caveolin-1 [64]. Phosphorylation of tyrosine,

most notably tyrosine 14, via src-family kinases results in the redistribution of cavolin-1 to integrin-rich focal-adhesion zones and the recruitment of a c-src/grb-7 signaling complex which leads to activation of the RAS/RAF/ERK cascade and uncontrolled proliferation[65, 66]. Also phosphorylation of caveolin-1 at serine 80 has been shown to shuttle caveolin-1 into a secretory pathway resulting in a loss of intracellular caveolin-1, an event that is proposed to subvert tumour suppressive activity[67]. There is evidence to suggest secreted caveolin-1 may act as an autocrine or paracrine tumour-promoting factor in prostate cancer. Specifically, caveolin-1 secreted by high-grade androgen insensitive prostate cancer cells can be taken up by low grade, caveolin-1 negative and androgen sensitive prostate cancer cells where it increases both cell viability and clonal growth[68, 69]. Further, this secreted caveolin-1 can also be taken up by tumour endothelial cells leading to a number of angiogenic activities such as tubule formation, cell migration and nitric oxide production [70].

Metastatic spread requires a relaxation of cell-cell and cell-matrix interactions. Caveolin-1 links extracellular matrix components to the cytoskeleton and thus influences matrix-dependent growth. In normal tissue, caveolin-1 appears to act as a sensor for cell detachment which triggers caveolin-1 endocytosis, down regulation of integrin signaling leading to detachment induced apoptosis[71, 72]. Overexpression of caveolin-1 allows tumour cells to escape anchorage-dependent growth

through an integrin-mediated mechanism that results in up-regulation of survival pathways that include IGF-1/PI3K/AKT[73, 74]. Caveolin-1 is also involved in the remodeling and proteolysis of extracellular matrix. A number of proteases and their regulatory partners, co-localise to caveolae and/or are activated by caveolin-1 including cathepsin B, pro-urokinase plasminogen activator (pro-uPA), GPI-anchored urokinase-receptor (uPAR)[75, 76], matrix metalloproteases (MT1-MMP,MMP-2/9/11/13) and its inducer EMM-PRIN(CD147)[77-79]. Dysregulation of these components can lead to unrestricted degradation of extracellular matrix and increased invasive capacity.

5.1.3 Caveolin-1 and astrocytomas

Whilst the number of published articles reporting the function of caveolin-1 in the pathogenesis of cancer (breast, prostate, lung, RCC, and colon; see table **Table 5.1**) has increased dramatically during the last decade, the number that have specifically focused on its role in glioblastoma are few. Several independent gene expression and immunohistochemical studies conducted with human tissue have consistently reported the up-regulation of caveolin-1 in advanced astrocytomas [49, 50, 80-82]. In these studies caveolin-1 was mostly associated with grade III oligoastrocytomas and grade IV glioblastomas [49] but was reported as absent from the grade II oligodendrogliomas. However, recent work by Cassoni and co-workers [50] utilized an extended cohort (n = 65) of oligodendroglioma specimens and found that caveolin-1 expression could be detected in 22% of all cases

of this glioma subtype. Specifically, patients with oligodendrogliomas that stained positive for caveolin-1 had significantly poorer survival than those patients whose tumours were caveolin-1 negative. Collectively, these clinico-pathological studies support the premise that caveolin-1 serves as a tumour promoter in astrocytoma[50].

Surprisingly, only two papers to date have specifically set out to examine, mechanistically, the contribution of caveolin-1 to the phenotype of astrocytoma. The first published by Abulrob in 2004 [83] reported the expression of caveolin-1 and its association with wtEGF-R and recombinant EGF-RvIII in the U87-MG cell line (a grade IV glioblastoma cell line). Here they describe the association of wtEGF-R but not the constitutively active mutated/truncated EGF-RvIII form. Further, treatment of U87-MG cells with specific inhibitors of EGF-R caused an increase in receptor association with caveolin-1 and caveolae domains. These results allude to the possibility of caveolin-1 serving as a tumour suppressor, at least in this cell line. However, the authors were ambivalent in their conclusion as to the exact role of caveolin-1 in glioblastoma. A second report by Martin et al [84], again using the U87-MG cell line, examined the effect of siRNA mediated caveolin-1 down-regulation by employing a combination of gene array analyses and functional assays. In this work the loss of caveolin-1 caused an increase in ERK activity, cell proliferation and cell migration[84]. Additionally, integrins were identified as the main set of genes affected by caveolin-1 silencing, with an up-regulation of $\alpha 5\beta 1$ (a marker for glioma

aggressiveness) reported. This latter study proposes that caveolin-1 serves as a tumour suppressor and not tumour promoter in glioblastoma.

Evidently, the *in-vitro* work conducted so far contradicts the clinico-pathological studies undertaken. However, it must be noted that the two *in-vitro* studies conducted to date have both utilized the U87-MG cell line. This is a cell line that has certain characteristic features including a wt p53 status i.e. p53 positive and an absence of EGF-RvIII. Mutations in p53 and the presence of EGF-RvIII occur in up to 30% and 60% of all glioblastomas respectively, and are associated with the more aggressive clinical features of the disease[85, 86]. Therefore, inferences using the U87-MG cell line concerning the role of caveolin-1 in pathogenesis of glioma should be treated with caution. Clearly, comparative studies of caveolin-1 contribution to the glioblastoma phenotype are needed in a panel of glioma cells with different genetic backgrounds and which reflect a broader clinical spectrum i.e. cell lines that carry p53 and phosphatase and tensin homolog (PTEN) mutations and possess varying levels of EGFR and EGF-RvIII.

5.1.4 Objectives

The aim of this chapter was to investigate the expression and functionality of caveolin-1 with respect to the pathobiology of a panel of grade IV glioblastoma cell lines and to establish if caveolin-1 represents a novel target for the treatment of glioblastoma. Four cells were selected that vary in their known p53 and PTEN status. Mechanistic studies were undertaken

in an attempt to delineate the signaling pathways responsible for the reported up-regulation of caveolin-1 occurring in human glioblastoma.

5.2 Materials & Methods

5.2.1 Materials

Rapamycin was obtained from Cabiochem, (Nottingham, UK). PD 98059 was obtained from InvivoGen, (Wiltshire, UK). DMSO; glycine; bovine serum albumin (BSA); leupeptin; aprotinin; sodium molybdate; phenylarsine oxide; $NaVO_4$; NaF and EGTA were obtained from Sigma-Aldrich Company Ltd, (Poole,UK). Isotone II diluent was obtained from Beckman Coulter, (High Wycombe, UK). All siRNAs were obtained from Eurofins MWG/Operon (Ebersberg, Germany). All cell culture mediums and Lipoprotein 2000™ were obtained from Invitrogen, (Paisley, UK). Acrylamide; ammonium persulphate; SDS; TEMED and Tween 20 were obtained from Pharmacia Biotech, (St. Albans, UK). Rabbit anti-human phospho-S6 polyclonal; rabbit anti-human caveolin-1 polyclonal; rabbit anti-human phospho-ERK polyclonal and rabbit anti-human phospho-caveolin-1 antibodies were obtained from Cell Signalling Technology, New England Biolabs, (Hitchin, UK). HRP conjugated anti-rabbit was obtained from Amersham, (Cardiff, UK). Nitrocellulose membranes and Supersignal West Dura were obtained from Pierce, (Rockford, USA). Triton-x 100 was obtained from ICN Biomedicals Inc, (Ohio, USA). Matrigel® was obtained from BD Technologies, (Oxford, UK). Vectashield containing DAPI was obtained from Vector Laboratories, Inc. (California, USA).

5.2.2 Cell lines

The human glioblastoma cell lines U373 MG (p53 mut; PTEN –ve) and T98-G (p53 mut; PTEN +ve) were seeded at 1.3 x 10^4 cells.cm^{-2} whilst U-87 MG (p53 wt; PTEN –ve), A172 (p53 wt; PTEN –ve) were seeded at 2 x 10^4 cells.cm^{-2}. All cells were maintained in culture medium comprising DMEM supplemented with 10% heat inactivated FBS and the antibiotics penicillin G (100 units.ml^{-1}) and streptomycin sulfate (100 μg.ml^{-1}). Cultures were maintained at 37°C in a humidified atmosphere (5% CO_2/95% air) with culture medium replenished every 48 hours.

5.2.3 siRNA transfections

As previously described in the literature [87, 88], a synthetic siRNA duplex (21 nucleotides) targeting the caveolin-1 mRNA sequence 5'-AACCAGAAGGGACACACAGUU-3' was used to down-regulate caveolin-1 protein expression and an siRNA duplex targeting the firefly luciferase (GL2) mRNA sequence 5'-AACGUACGCGGAAUACUUCGA-3' was used as a negative control. The duplexes were purchased from MWG/Eurofins (Ebersberg, Germany) as unprotected, desalted, and purified siRNA.

U373-MG and T98-G cells were seeded at 1.3 x 10^4 cells.cm^{-2}, whilst A172 and U87-MG cells were seeded at 2.0 x 10^4 cells.cm^{-2} in 24 well and 6 well formats, for growth and Western blot analysis, respectively. After 24h, all cells were transfected with 70 nmol (0.6ug) for the 24 well format or 350nmol (3.5μg) for the 6 well format of siRNA complexed with

Lipofectamine™ 2000 for 4h as recommended by the manufacturer. Briefly for 24 well plates (per well) 1 µl of lipofectamine in 50 µl of Optimem was complexed with siRNA (70 nmol in 50 µl of Optimem) for 20 mins before addition to wells containing 60 µl of Optimem. For 6 well plates (per well) 5 µl of lipofectamine in 250 µl of Optimem was complexed with siRNA (350nmol in 250 µl of Optimem) for 20 mins before addition to wells containing 100 µl of Optimem. Four hours after transfection the cells were supplemented with Optimem containing serum (FBS) to a final concentration of 10%. The cells were harvested 90hrs after transfection for cell counts and immunoblotting.

5.2.4 Cell growth analysis

Cell population growth was evaluated by means of trypsin dispersion of the cell monolayers (performed in triplicate) following a 72h incubation with PD 98059 (10 – 50 µM) or rapamycin (1 nM – 1 µM) or a 90 hour exposure to siRNA. Controls were incubated for the same period of time with appropriate vehicle or control siRNA (luciferase). Cell counts were undertaken by use of a Coulter-counter (Luton, UK). All proliferation studies were performed at least three times.

5.2.5 Western blot analysis

5.2.5.1 Preparation of cell lysates

Glioblastoma cell lines, cultured in 6-well plates (surface area 10cm^2 per well), were incubated at 4°C with 200 µl of lysis buffer (50 mM Tris (pH

7.5), 1% Triton-X, 5 mM EGTA, 150 mM NaCl, 60 mM n-octyl-glucoside) containing protease inhibitors (PMSF, aprotinin, leupeptin, sodium fluoride, phenylarsine, sodium molybdate and sodium pervandate). After 15 mins, the lysate was collected and centrifuged (13,500g; 15 mins) to pellet cellular debris. Lysate was aspirated and stored at -20°C until required.

5.2.5.2 Lysate protein determination

Total protein in cell lysates was quantified using a Bicinchoninic Acid (BCA) assay kit (Sigma-Aldrich Company Ltd, Poole, UK) essentially as described in [89] but with modifications. Assay reagent was prepared immediately before addition to cell lysates by mixing one part BCA solution to fifty parts of a 4% w/v solution of $CuSO_4.5H_2O$. After adding 200 µl of assay reagent to 25 µl of cell lysate, samples were incubated at 37°C for 30 mins. The absorbance of the resultant copper-I-BCA complex was measured at 560 nm using an Anthos htll microtiter reader (Labtech International, East Sussex, U.K). Calibration standards of BSA were prepared in the range 200 – 1000 $\mu g.ml^{-1}$ in lysis buffer and measured concurrently with lysate samples.

5.2.5.3 Gel electrophoresis

Gel electrophoresis was undertaken using the Mini-protean II apparatus from Biorad (Hertfordshire, UK). The gel casting apparatus was assembled using 1.5 mm spacers and filled with a 12 % SDS polyacrylamide running gel solution (**Table 5.2**)

Table 5.2 Composition of 12 % SDS polyacrylamide running gel solution.

Constituent	Volume
Tris-HCl, 1.5 M pH 8.8	5 ml
SDS, 12 % w/v	0.1 ml
Acrylamide, 30 % w/v	8 ml
Ammonium persulphate, 10% w/v	0.1 ml
TEMED	0.012 ml
ddH2O	6.6 ml

During polymerization, gels were overlaid with isopropanol to prevent atmospheric interference during the cross-linking reaction. Once the running gel had set (~ 15 min), the isopropanol was removed using blotting paper. The running gel was then overlaid with a 4% SDS stacking gel **(Table 5.3)**

Table 5.3 Composition of 4 % SDS polyacrylamide stacking gel solution.

Constituent	Volume
Tris-HCl, 0.5 M pH 6.8	2.5 ml
SDS, 4 % w/v	0.1 ml
Acrylamide, 30 % w/v	1.3 ml
Ammonium persulphate, 10% w/v	0.1 ml
TEMED	0.01 ml
ddH2O	6.1 ml

Volumes of cell lysate corresponding to 20µg of total protein for each experimental variable were diluted in an equal volume of 2 x sample loading buffer **(Table 5.4)** which were then heated for 5 mins at 95°C. Lysates and molecular markers were then carefully loaded into the gel.

Table 5.4 Composition of loading buffer.

Constituent	Volume
SDS, 10% w/v	4ml
Glycerol, 20% v/v	2ml
Tris-HCl, 0.2M pH 6.8	2ml
Bromophenol Blue, 0.01% v/v	
DTT, 10 mM	
ddH2O	1.6 ml

The gel assembly was removed from the casting apparatus and placed carefully into a running tank. The tank was filled with running buffer (0.025 M Tris base; 0.192 M Glycine) until the gel was completely submerged (~800 ml). Gels were electrophoresed at 200 V for 50 mins.

5.2.5.4 Western blot

Gels were removed from the electrophoretic tank and submerged in ice-cold blotting buffer (0.025 M Tris base, 0.192 M Glycine, 20% v/v methanol) for 5 mins before protein was transferred from SDS-PAGE gel onto nitrocellulose membrane. Nitrocellulose membrane was cut to size and prepared for transfer by soaking in blotting buffer for 15 mins. The gel was removed from the blotting buffer and the nitrocellulose membrane gently placed onto the gel. The gel was then sandwiched firstly between filter paper and then between Scotch brite pads. The whole complex was then locked inside a transfer cassette and loaded into a gel tank surrounded by ice. The tank was filled with blotting buffer and the protein transferred over 90 mins by electrophoresis with a constant current of 400 mA. The nitrocellulose membrane was removed and washed (NaCl, 100 mM; Tris, 10mM pH 7.5; 0.1% v/v Tween 20) before being submerged in blocking buffer (5% w/v non-fat milk in wash buffer) for 1 hr. The membrane was then incubated overnight at 4°C with primary antibody (1:1000 dilution in blocking buffer). The following day the primary antibody was aspirated and the membrane was washed 6x with washing buffer before incubating with secondary antibody (1:7000 dilution of swine anti-rabbit HRP) for 1 hr at

room temperature. Finally the membrane was washed 6x with washing buffer. Detection was made in a dark room using SuperSignal® Ultra. Detection reagent was prepared as per the manufacturers protocol and was spread thinly over the membrane for upto 5 mins. The membrane was loaded into an autoradiography cassette and a section of Hyperfilm ECL was laid over the membrane before the cassette was sealed. Signal was accumulated for 1 minute before the film was developed and fixed. Image acquisition was undertaken on a GS-700 densitometer with Molecular Analyst Software (Bio-Rad, Hemel Hempstead, UK).

5.2.6 Cell invasion assays

The invasive potential of glioblastoma cell lines U373 MG and U-87 MG, was investigated in a Matrigel™ invasion chamber. Matrigel™ is a basement membrane extract from the Engelbreth-Holm-Swarm (EHS) mouse sarcoma, a tumor abundant in ECM proteins particularly laminin, collagen IV, heparan sulfate proteoglycans and entactin. Matrigel™ invasion chambers have been widely used to study the metastatic potential of tumour cells[90-92]. Invasion chambers were prepared by coating Transwell™ inserts (8 μm pore size) with 50 μl of a 1:3 dilution of Matrigel™ in RPMI and incubated at 37°C for 2 hrs. Cells were prepared for invasion assays by seeding in 6 well plates for 24 hrs before exposure to siRNA or rapamycin. After 72 hrs exposure (total of 96 hrs *in-vitro*) cell monolayers were disaggregated with trypsin and each invasion chamber was seeded with 50,000 cells (total volume 200 μl). Following a 24 hr

incubation (total time *in-vitro* of 120 hrs), the Matrigel™ coating was carefully removed from the chamber membrane using a sterile cotton bud and the chamber was submerged in 3.7% formaldehyde for 10 mins to fix the cells. After washing the inserts in PBS, the membrane was carefully excised with a scalpel. Once removed, the membrane was mounted cell side up on a microscope slide with DAPI Vectashield. Cells were counted from micrographs recorded following microscopic examination.

5.2.7 Statistical analysis

Statistical analysis was performed using Graphpad Prism (Graphpad Software; California, USA). Results were expressed as mean ± standard deviation (SD) unless otherwise stated. Statistical significance between multiple groups was assessed using a two-way ANOVA followed by a post hoc Bonferroni test. Single group differences were determined using a one-way ANOVA followed by Dunnett's post hoc or by two-tailed Student's t-test. $P < 0.05$ was considered significant.

5.3 Results

Western blotting of lysates from four cell lines routinely used as in-vitro models of grade IV gliomas confirmed the presence of caveolin-1 under normal basal conditions (see **Figure 5.1**) Phosphorylated caveolin-1 was also confirmed in A172 (p53 wt; PTEN –ve), U373-MG (p53 mt; PTEN –ve) and T 98 G (p53 mt; PTEN +ve) but not in U87-MG (p53 wt; PTEN –ve) (see **Figure 5.1**). Of note, the relative expression of total caveolin-1 in A172 was low compared to the other cell lines investigated but the phosphorylated

caveolin-1 signal was intense and is suggestive that virtually all the caveolin-1 is phosphorylated within A172 under basal conditions.

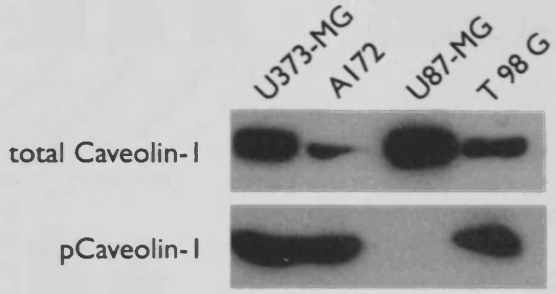

Figure 5.1 Western blot analysis of caveolin-1 and phosphorylated caveolin-1 expression in human glioma cell lines. Data are representative of at least three separate experiments.

To assess the role of caveolin-1 in human glioblastoma, its expression was modulated in the panel of four cell lines, U373-MG, U87-MG, A172 and T 98 G. The siRNA mediated depletion was confirmed at the protein level within each cell line using Western blotting (**Figure 5.2**); a control siRNA sequence against luciferase did not result in any significant change in caveolin-1. Histograms in **Figure 5.2** show that in both p53 wt (U87-MG and A172) and p53 mt (U373-MG and T 98 G) cell lines, down-regulation of caveolin-1 results in a significant ($p < 0.05$) reduction in cellular proliferation. It should be noted that the control siRNA sequence did however also result in a significant reduction in growth (particularly for the U87-MG and U373-MG cell lines) probably as a result of transfection lipid and is not an uncommon feature of siRNA studies examining the effect upon cell growth. When re-expressed as a % of control siRNA, then knockdown of caveolin-1 had a statistically significant ($p < 0.05$) effect upon cell growth compared to the control siRNA treatments.

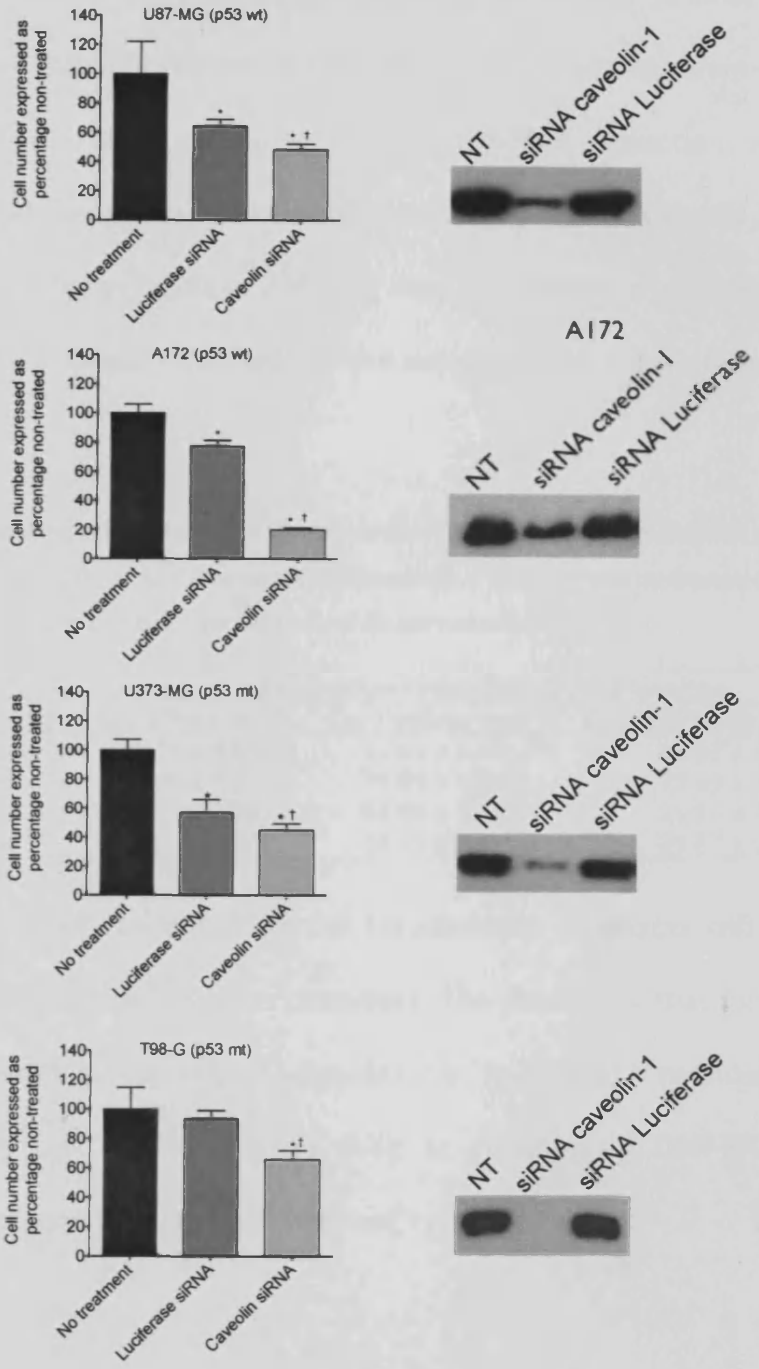

*Figure 5.2 Effect of siRNA-mediated down-regulation of caveolin-1 on cell growth of p53-poistive glioma cell lines U87-MG and A172 and p53 mt cell lines U373-MG and T 98 G. Treatments are caveolin-1 siRNA or control luciferase siRNA. Representative Western blots of caveolin-1 are shown for each cell line. Results are expressed as mean ± SD (n = 4). * denotes significance ($p < 0.05$) versus no-treatment control. † denotes significance ($p < 0.05$) versus control luciferase siRNA.*

Table 5.5 shows the percentage reduction in cellular proliferation as a result of the down-regulation of caveolin-1. At a minimum, down-regulation of caveolin-1 results in a ~ 20% (U373-MG) reduction in cellular proliferation compared to similarly treated control siRNA cells and in the case of A172 by as much as 74%. Of note, the effects of caveolin-1 down-regulation on cellular proliferation did not appear to correlate with p53 or PTEN status.

*Table 5.5 Effects of siRNA mediated down-regulation of caveolin-1 on cellular proliferation. Data are mean ± SD (n=4). * denotes significance ($p < 0.05$) versus no-treatment control. † denotes significance ($p < 0.05$) versus control luciferase siRNA.*

	Percentage reduction in proliferation		
	Luc-siRNA vs NT	**Cav1-siRNA vs NT**	**Cav1 siRNA vs Luc-siRNA**
U87-MG (p53 wt)	35.76 ± 4.54*	51.61 ± 3.79*	24.67 ± 5.89†
A172 (p53 wt)	22.86 ± 4.09*	79.89 ± 1.29*	73.93 ± 1.67†
U373-MG (p53 mt)	42.77 ± 8.63*	54.89 ± 4.31*	21.17 ± 7.53†
T 98 G (p53 mt)	6.45 ± 5.36*	34.11 ± 5.93*	29.57 ± 6.34†

The influence of caveolin-1 on the invasiveness of glioma cell lines was measured in Matrigel invasion chambers. The data show that for U373-MG cells, depletion of caveolin-1 significantly ($p < 0.05$) reduces invasive capacity by up to 80% (**Figure 5.3**); in contrast, in U87-MG cells no reduction of invasiveness was observed.

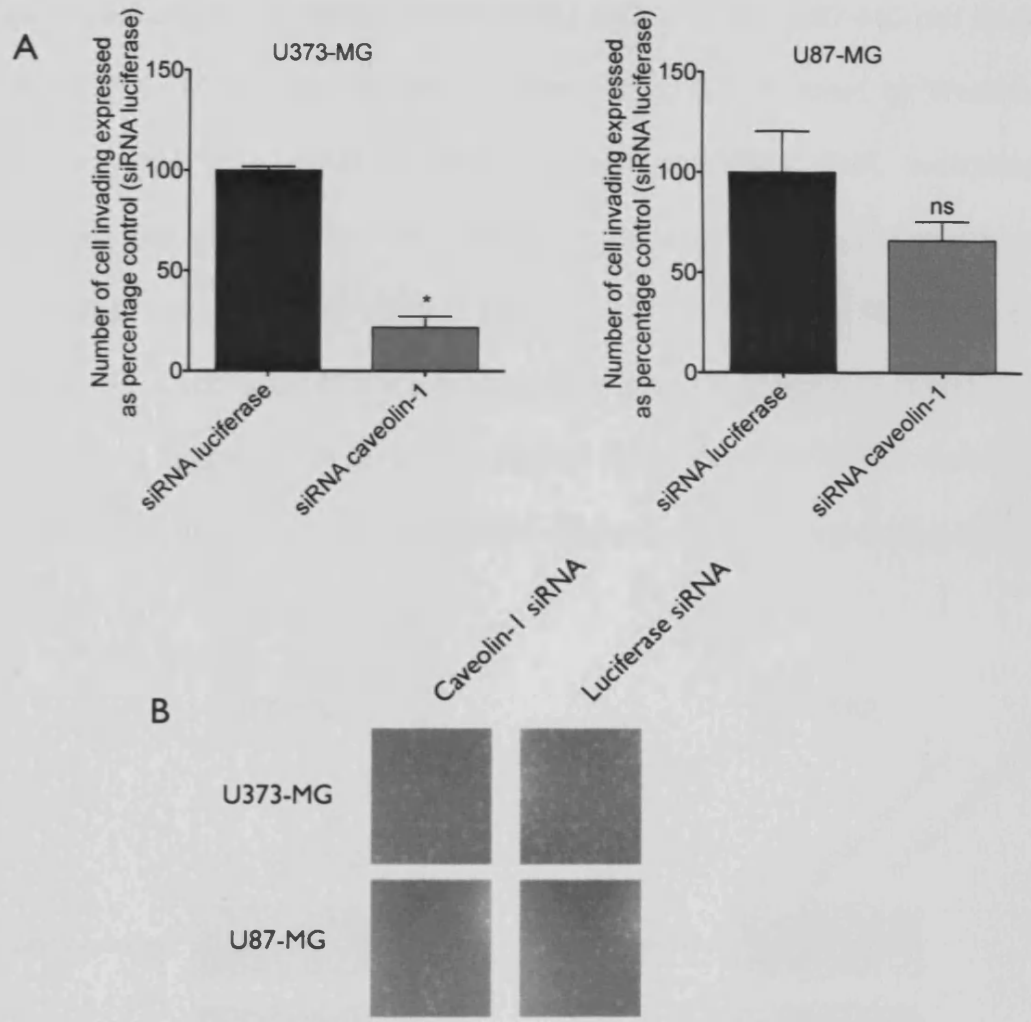

*Figure 5.3 Effect of siRNA-mediated down-regulation of caveolin-1 on invasion of glioma cell lines U87-MG and U373-MG through Matrigel. (A) Down-regulation of caveolin-1 in U373-MG cells treated with caveolin-1 siRNA results in reduced invasive capacity compared to cells treated with luciferase siRNA (~ 80% reduction). Down-regulation of caveolin-1 in U87-MG cells treated with caveolin-1 siRNA had no affect on invasive capacity. Data are mean ± SEM for 5 fields of view (n = 2 chambers) expressed as percentage control (luciferase siRNA). * denotes significance ($p < 0.05$) versus luciferase siRNA. (B) Representative fields of view of Matrigel invasion chambers (x 20 magnification) reveal that U373-MG are generally more invasive than U87-MG.*

Having shown in cell growth studies (**Figure 5.2**) and invasion studies (**Figure 5.3**) that elevated caveolin-1 expression correlates with glioma aggressiveness, efforts were made to dissect the pathways through which caveolin-1 acts. **Figure 5.4** shows the effects of caveolin-1 down-regulation

on phosphorylated (activated) ERK in the U373-MG and U87-MG cell lines. In the U87-MG cell line, depletion of caveolin-1, as confirmed by Western blot, resulted in a similar depletion in phosphorylated ERK, indicating reduced ERK activity. This result demonstrates that caveolin-1 is upstream of ERK i.e. caveolin-1 potentiates ERK activity. For cell line U373-MG no reduction in activated ERK accompanied the down-regulation of caveolin-1. This result suggests that caveolin-1 has no direct effect on ERK or that ERK is upstream of caveolin-1 i.e that ERK drives caveolin-1 expression in this cell line.

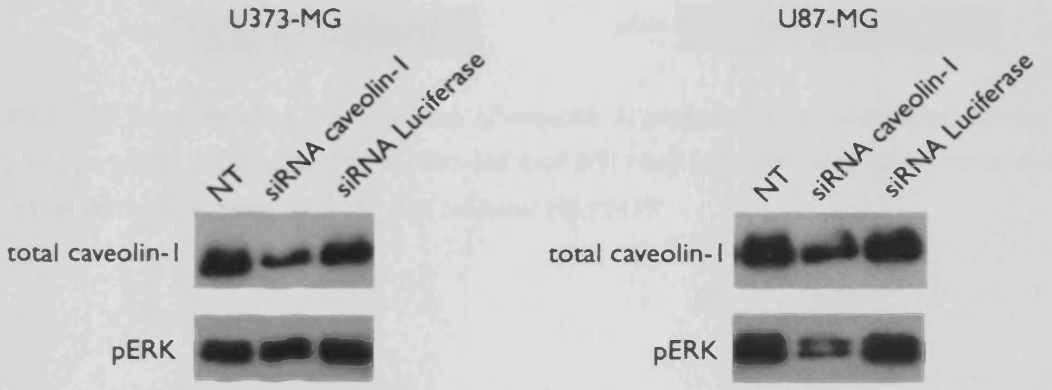

Figure 5.4 Protein expression of total caveolin-1 and activated (phosphorylated) ERK in U87-MG, U373-MG, A172 and T 98 G following siRNA-mediated down-regulation of caveolin-1. Western blots are representative of at least three separate experiments.

Figure 5.6 shows the effects on U373-MG and U87-MG cell growth of the ERK inhibitor PD 98059 and **Figure 5.5** shows representative Western analyses for total caveolin-1 and activated (phosphorylated) ERK following exposure to PD 98059. In both cell lines, PD 98059 resulted in concentration dependent inhibition of cell growth (**Figure 5.6**). In U87-MG cells, PD 98059 reduced expression of phosphorylated (activated) ERK but

had no effect on total caveolin-1 levels. This result is consistent with that shown in **Figure 5.4** indicating that caveolin-1 is upstream of ERK in the U87-MG cell line. In U373-MG, PD 98059 exposure resulted in losses in activated (phosphorylated) ERK and total caveolin-1 indicating that ERK is upstream of caveolin-1 i.e. ERK activity potentiates caveolin-1 expression.

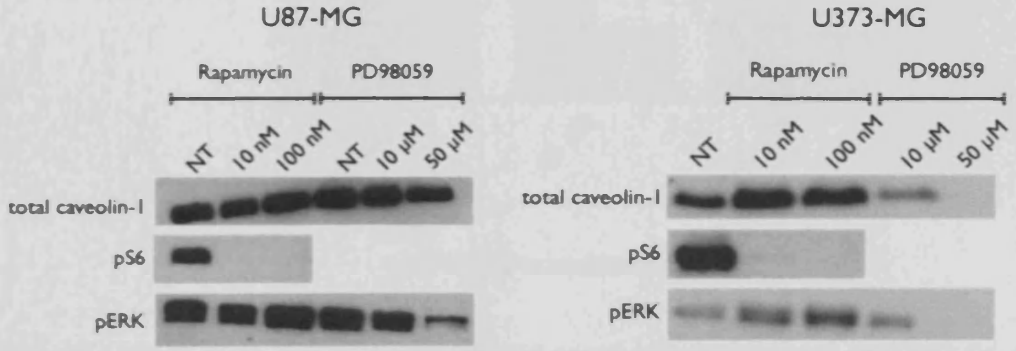

Figure 5.5 *Representative Western blots of caveolin-1, phosphorylated (activated) S6 and phosphorylated (activated) ERK in U87-MG and U373-MG cells following exposure to the mTOR inhibitor Rapamycin or the ERK inhibitor PD 98059.*

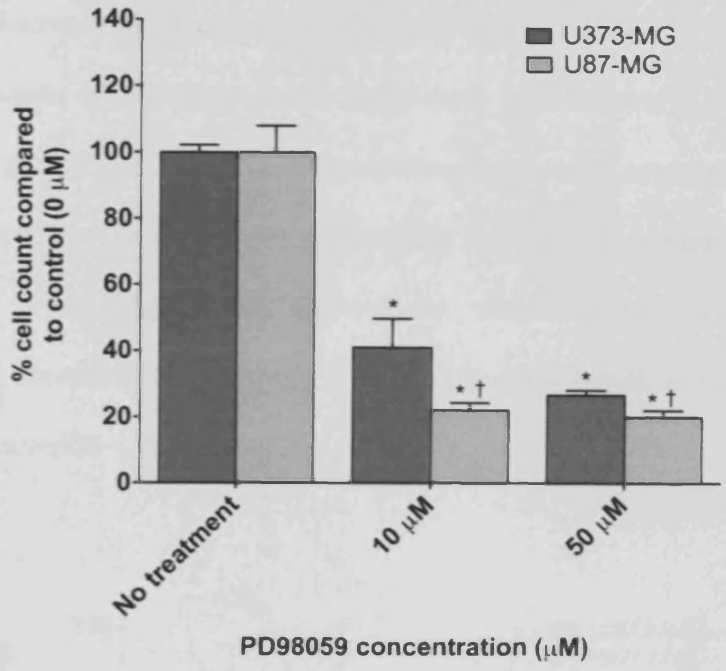

*Figure 5.6 Effects of the ERK inhibitor PD 98059 on cell growth in U87-MG and U373-MG cell lines. Results are expressed as mean ± SD (n = 4). * denotes significance (p < 0.05) versus no-treatment control. † denotes significance (p < 0.05) versus respective U373-MG treatment.*

Figure 5.7 shows the effects on cell growth of U373-MG and U87-MG following exposure to the mTOR inhibitor rapamycin and **Figure 5.5** shows representative Western analyses for total caveolin-1, phosphorylated S6 (activated), a downstream marker in the mTOR pathway, and phosphorylated (activated) ERK in cells exposed to rapamycin. In both cell lines rapamycin resulted in concentration-dependent inhibition of cell growth and loss of activated S6. However, it is noted that U373-MG cells were significantly more resistant to the growth inhibitory effects of rapamycin than U87-MG cells at all doses examined. Strikingly, rapamycin had no effect on total-caveolin-1 in the U87-MG but caused a significant increase in total caveolin-1 expression in U373-MG. The rapamycin

mediated increase in caveolin-1 in U373-MG was paralleled by increases in the expression of phosphorylated (activated) ERK **Figure 5.5**. This is a result consistent with ERK activity driving caveolin-1 expression in the U373-MG cell line given that PD 98059 (ERK inhibitor) treatments reduced caveolin-1 levels **Figure 5.5**. Collectively, these results conclude that rapamycin increases ERK activity in U373-MG cells, which in turn further increases caveolin-1 expression.

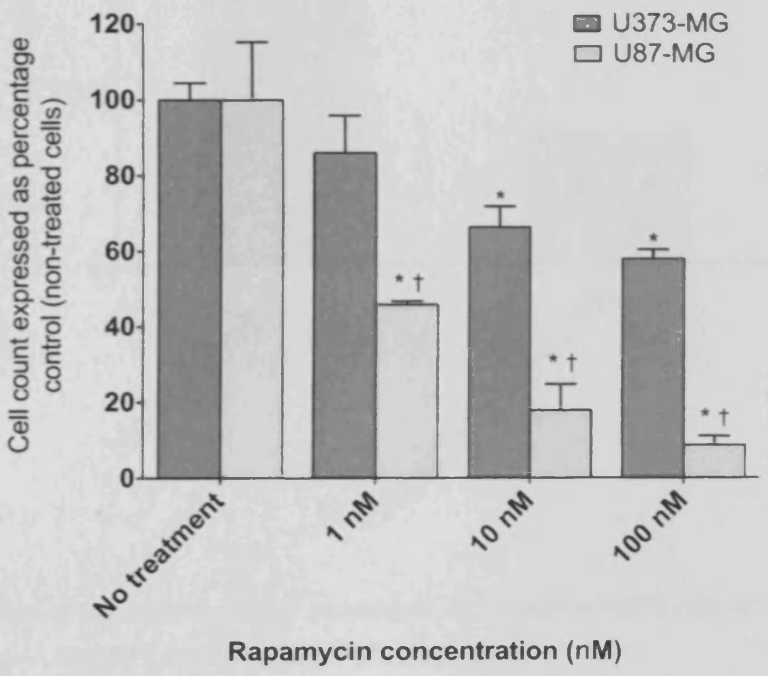

*Figure 5.7 Effects of the mTOR inhibitor rapamycin on cell growth in U87-MG and U373-MG cell lines. Results are expressed as mean ± SD (n = 4). * denotes significance (p < 0.05) versus no-treatment control. † denotes significance (p < 0.05) versus respective U373-MG treatment.*

Given then that U373-MG cells exposed to rapamycin result in an upregulation in caveolin-1 (**Figure 5.5**) and that caveolin-1 promotes invasion in U373-MG cells (**Figure 5.3**) it was hypothesized that rapamycin

treatment of U373-MG may promote invasion. **Figure 5.8** shows that despite an up-regulation of caveolin-1 following rapamycin treatment, the invasiveness of U373-MG is actually reduced following rapamycin treatment.

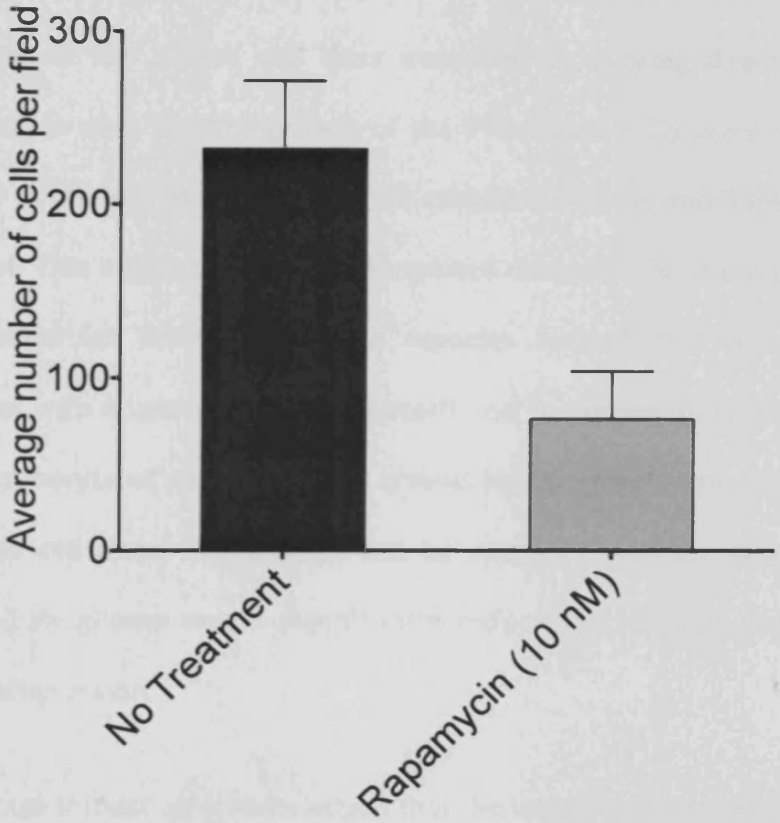

Figure 5.8 Effect of the mTOR inhibitor Rapamcyin on invasion of U373 cells into Matrigel™. Data are mean ± SEM for 5 fields of view (n = 2 chambers).

5.4 Discussion

Examination of caveolin-1 and phosphorylated caveolin-1 in a panel of glioblastoma cell lines revealed different degrees of expression of both isoforms between the four cell lines. This is the first study to identify phosphorylated caveolin-1 in glioma cell lines and is a finding that has

profound implications for the role of caveolin-1 in tumour pathobiology and glioma disease progression *per se*. Comparing total levels of caveolin-1 to its phosphorylated form in each of the cell lines it can be concluded that the caveolin-1 in both the T98-G and A172 cell lines is virtually all phosphorylated. Although treatment with caveolin-1 siRNA affected the growth of all the glioma cell lines examined to varying degrees, it is interesting to note that the growth of the T98-G and A172 were the most sensitive to the loss of caveolin-1, with respectively 29% and 74% growth inhibition. This suggests that phosphorylated caveolin-1 in these cell lines is important for their proliferative capacity. Indeed, this is a finding consistent with a recent study by Felicetti and co-workers[93] who found that phosphorylated caveolin-1 was critical for the proliferation of human melanoma cell lines. Therefore it can be reasoned that the targeting of caveolin-1 in glioma would significantly reduce tumour size and retard disease progression.

At this stage it must be acknowledged that the targeted down-regulation of caveolin-1 in the U87-MG cell line also inhibited growth by 24.6%, a finding in contrast to Martin et al 2009[84]. These latter workers actually found that the loss of caveolin-1 increased growth by up to 50%, a finding which led them to conclude that caveolin-1 serves as a tumour suppressor in this cell line[84]. Of note, these researchers used a biochemical assay of proliferation as their end point instead of cell counts as conducted in this study. However, the most plausible explanation of the differences reported

in this study and that of Martin et al is that different sub-lines of U87-MG exist between laboratories. Well documented examples of different cancer cell sub-lines giving varying results exist, these reflect subtle differences in their molecular profiles and hence phenotype. Perhaps the most notable being the MCF-7 breast cancer cell line[94] and the LnCap prostate cancer cell line[68]. The different sub-clones of U87-MG that are indicated to exist probably result from cell heterogeneity within the original U87-MG parental cell cultures [95]. Indeed, five distinct populations could be cloned from the parental U87-MG cell culture based upon their expression of tissue factors alone [95]. Each of these populations differed in their growth rate and led the authors to conclude that such cell culture heterogeneity can complicate experiments using molecular manipulation [95]. Nevertheless, the reduced U87-MG cell growth following caveolin-1 siRNA treatment presented in this present study is consistent with the accompanied loss of activated ERK (a growth promoting signaling component) following caveolin-1 down-regulation (**Figure 5.4**). Further, no inverse relationship between caveolin-1 and ERK was demonstrated in any of the four cell lines examined. Coupled with the reduced growth rates evident in all cell lines following caveolin-1 knockdown, collectively these results strongly support a role for caveolin-1 as a tumour promoter in glioma and not a tumour suppressor. This is in agreement with the immuno-histochemical studies conducted with clinical glioma specimens that show increased caveolin-1 expression correlates with adverse disease parameters [49, 50, 80-82]. Also it can be concluded from these studies that the contribution of caveolin-1 to

the growth of glioblastomas does not occur in a p53 and PTEN dependant manner. Hence these studies identify caveolin-1 as novel drug target for the treatment of glioma in general, irrespective of their genetic background.

Invasion studies were conducted in the U373-MG and U87-MG cell lines to examine the potential role of caveolin-1 in the process of cellular invasion. Clearly the targeted down-regulation of caveolin-1 in the U373-MG resulted in a dramatic inhibition of 78.25% ± 19.5 compared to control luciferase siRNA treated cells. No significant effect of caveolin-1 down-regulation on invasion in the U87-MG was observed. It is interesting to note that the more invasive U373-MG cells contained phosphorylated caveolin-1. This is consistent with the reported role of phosphorylated caveolin-1 in the increased invasion of human melanoma[93] and breast cancer cells [58]. In these studies the knockdown of caveolin-1 or transfection with a caveolin-1 mutant that cannot be phosphorylated inhibited invasion and formation of foci in semisolid medium [93] and altered focal adhesion kinase signaling (FAK) disrupting focal adhesion dynamics which are critical for the invasion and metastasis of cancer cells [58]. Caveolin-1 over-expression has also been linked to invasion and metastasis to lymph nodes and distant sites in several cancers including kidney [27], breast [14] prostate [96] and lung[45], although the phosphorylation status of caveolin-1 in these latter clinico-pathological studies was not examined.

Metastasis of gliomas to distant organs is rare and therefore is not a clinical issue. However, invasive growth and local infiltration into surrounding

nerve tissue is a well known characteristic of glioblastomas and a phenomena that limits the success of treatment strategies[97]. Further the diffuse nature of malignant glioma within brain parenchyma has long been recognized by neurosurgeons when super-radical hemispherectomies failed to fully eradicate tumours [98]. Re-growth of tumour from locally invaded cells nearly always occurs and is associated with chemo- and radio-resistance, giving rise to the possibility that locally invasive glioma cells activate cell signaling pathways that mediate resistance to such conventional therapies[98]. Therefore based upon the invasion results obtained in the U373-MG cell line it can be proposed that caveolin-1 may represent a valid target and an alternative treatment strategy for inhibiting such localized infiltration and treatment resistance. Interestingly, it is increasingly realized that invasive glioma cells show a decreased proliferation rate[98]. The loss of caveolin-1 in the U373-MG cell line did not retard growth to the same extent as in the other glioma cells lines (albeit marginally when compared to U87-MG). This may be reconciled by the fact that caveolin-1, or specifically, phosphorylated caveolin-1 has a more predominant role in driving invasion than proliferation in the U373-MG cell line, as opposed to the A172 cell line where its role may be that of driving proliferation. However, it is acknowledged that further work on the contribution of caveolin-1 in the A172 and T98-G cell lines are needed in order to support this conjecture.

It is important to consider factors that may drive caveolin-1 phosphorylation in glioma cells, given the present study shows that the phosphorylation status of caveolin-1 differs between glioma cell lines. This may convey different cellular properties and hence impact upon outcomes for glioma patients. Src kinase is a well established molecule that mediates the phosphorylation of caveolin-1 at tyrosine 14 [65]. This src-mediated caveolin-1 phosphorylation is reported to stimulate the subcellular trafficking of activated EGF-R to increase cell migration and invasion[66, 99]. Also src-mediated caveolin-1 phosphorylation is in turn regulated by EGF-R. For example in human squamous and epidermoid carcinoma cells caveolin-1 is phosphorylated via src kinase upon EGF-R activation[100]. In addition aberrant EGF-R status is also shown to induce the src kinase-mediated phosphorylation of caveolin-1. Specifically, cells that over-express EGF-R or carry EGF-R forms exhibiting mutated truncations within the intracellular c-terminus have phosphorylated caveolin-1[101]. Indeed, caveolin-1 phosphorylation is maximal when the EGF-R is truncated since these forms of the receptor are constitutively activated[101].

These above studies clearly indicate that under certain conditions caveolin-1 and EGF-R co-operate to modulate cell behaviour. It is perhaps this relationship between EGF-R status and caveolin-1 phosphorylation that is most important for glioma and disease progression. Amplification of the EGF-R gene and over-expression of EGF-R protein is the most common genetic alteration and occurs in about 40% of all primary glioblastomas. Of

these, up to 75% harbour EGF-R gene rearrangements resulting in the increased expression of both wild type and mutated EGF-R forms [86]. The most common EGF-R mutation in glioblastomas is known as EGF-RvIII and is associated with increased cell proliferation[102], invasion [103], tumour angiogenesis[104] and chemo-resistance[105]. The EGF-R status of the four glioma cell lines used in this study is currently unknown but it can be rationalised that their phosphorylated caveolin-1 status may reflect underlying alterations in EGF-R. Indeed, the A172 cell line has been previously fully characterized with respect to EGF-R status by others and found to contain EGF-R tandem duplication mutations which, similar to EGF-RvIII, arise from rearrangements between introns[106]. It must be noted that of the four cell lines used in this study, the A172 cell line displayed the highest levels of phoshorylated caveolin-1 when compared to total caveolin-1 levels. Given these lines of evidence it is envisaged that a caveolin-1 inhibitor would effectively disrupt the EGF-R-caveolin-1 axis in glioma tumour cells and therefore limit the disease parameters of glioblastomas.

One element of this chapter was a preliminary investigation into the signaling pathways that may drive the over-expression of caveolin-1 in glioma cell lines, namely that of the ERK and mTOR signaling pathways. In the U87-MG cell line, PD 98059 a specific inhibitor of ERK did not inhibit caveolin-1 expression at any of the doses examined, despite reductions in phosphorylated (activated) ERK. This result clearly indicates that in the

U87-MG cell line, caveolin-1 is not affected by ERK activity. Further, it can be concluded that caveolin-1 lies upstream of ERK and serves to potentiate ERK activity; since it was shown that caveolin-1 down-regulation results in reduced levels of phosphorylated ERK. How caveolin-1 potentiates ERK activity in glioma is unknown but two mechanisms are possible. Firstly, caveolin-1 may, as previously mentioned, serve to traffic EGF-R, the major upstream activator of ERK and hence allow optimal EGF-R function. Secondly, caveolin-1 may increase levels of phosphorylated ERK via the inhibition of inhibitory phosphatases such as PP1 and PP2A, for which a function for caveolin-1 has been demonstrated in prostate cancer cells [107].

Conversely, in the U373-MG cell lines, PD 98059 caused a dramatic reduction in caveolin-1 expression, demonstrating that in this glioma cell line, caveolin-1 expression is actually driven by ERK activity. Interestingly, rapamycin, a specific inhibitor of mTOR, caused up-regulation of caveolin-1, an increase that was paralleled by increases in phosphorylated (activated) ERK (**Figure 5.5**). Therefore it can also be concluded that in the U373-MG cell line inhibition of the mTOR signaling pathway results in a compensatory up-regulation of the ERK signaling pathway leading to enhanced caveolin-1 expression. This phenomenon may explain why mTOR inhibitors such as rapamycin have met with limited success in clinical trails for glioma[108]. Indeed, the U373-MG cell line (in which mTOR inhibition caused an up-regulation of ERK activity and increased caveolin-1

expression) was a lot less sensitive to the growth inhibitory effects of rapamycin than the U87-MG. This reveals an as yet unidentified pathway that limits the action of mTOR inhibitors in glioma. Similar compensatory pathways following mTOR inhibition are seen in prostate cancer cells [109], although the effects on mTOR inhibition on caveolin-1 expression have not been described. Collectively, the results from the inhibitor work conducted in the U373-MG and U87-MG cell lines show that caveolin-1 is differentially regulated in different glioma subtypes.

In conclusion the work undertaken in this chapter describes for the first time that caveolin-1 serves to potentiate the growth and invasion of glioblastoma cells and as such serves as a tumour promoter. Its involvement in these two different pathological parameters make it an ideal and much needed novel drug target for the treatment of glioblastomas. In this chapter was also shown how caveolin-1 expression affects and is affected by key signaling pathways (a proposed schematic of the role of caveolin-1 in the prgression of glioblastoma multiforme can be found in **Appendix 2**). These insights also provide valuable information regarding treatment decisions when using molecular targeted therapies such as mTOR inhibitors and tyrosine kinase inhibitors for the treatment of glioblastomas.

Reference List

1. Campbell, L., M. Gumbleton, and K. Ritchie, *Caveolae and the caveolins in human disease.* Advanced Drug Delivery Reviews, 2001. **49**(3): p. 325-335.

2. Williams, T.M. and M.P. Lisanti, *Caveolin-1 in oncogenic transformation, cancer, and metastasis.* Am J Physiol Cell Physiol, 2005. **288**(3): p. C494-506.

3. Cohen, A.W., et al., *Role of caveolae and caveolins in health and disease.* Physiol Rev, 2004. **84**(4): p. 1341-79.

4. Engelman, J.A., X.L. Zhang, and M.P. Lisanti, *Genes encoding human caveolin-1 and -2 are co-localized to the D7S522 locus (7q31.1), a known fragile site (FRA7G) that is frequently deleted in human cancers.* FEBS Lett, 1998. **436**(3): p. 403-10.

5. Engelman, J.A., et al., *Chromosomal localization, genomic organization, and developmental expression of the murine caveolin gene family (Cav-1, -2, and -3). Cav-1 and Cav-2 genes map to a known tumor suppressor locus (6-A2/7q31).* FEBS Lett, 1998. **429**(3): p. 330-6.

6. Yang, G., et al., *Elevated expression of caveolin is associated with prostate and breast cancer.* Clin Cancer Res, 1998. **4**(8): p. 1873-80.

7. Nasu, Y., et al., *Suppression of caveolin expression induces androgen sensitivity in metastatic androgen-insensitive mouse prostate cancer cells.* Nat Med, 1998. **4**(9): p. 1062-4.

8. Goetz, J.G., et al., *Caveolin-1 in tumor progression: the good, the bad and the ugly.* Cancer Metastasis Rev, 2008. **27**(4): p. 715-35.

9. Williams, T.M., et al., *Caveolin-1 gene disruption promotes mammary tumorigenesis and dramatically enhances lung metastasis in vivo. Role of Cav-1 in cell invasiveness and matrix metalloproteinase (MMP-2/9) secretion.* J Biol Chem, 2004. **279**(49): p. 51630-46.

10. Park, D.S., et al., *Caveolin-1-deficient mice show accelerated mammary gland development during pregnancy, premature lactation, and hyperactivation of the Jak-2/STAT5a signaling cascade.* Mol Biol Cell, 2002. **13**(10): p. 3416-30.

11. Engelman, J.A., et al., *Reciprocal regulation of neu tyrosine kinase activity and caveolin-1 protein expression in vitro and in vivo. Implications for human breast cancer.* J Biol Chem, 1998. **273**(32): p. 20448-55.

12. Lee, S.W., et al., *Tumor cell growth inhibition by caveolin re-expression in human breast cancer cells.* Oncogene, 1998. **16**(11): p. 1391-7.

13. Thomas, N.B., et al., *Growth of hormone-dependent MCF-7 breast cancer cells is promoted by constitutive caveolin-1 whose expression is lost in an EGF-R-mediated manner during development of tamoxifen resistance.* Breast Cancer Res Treat, 2009.

14. Hayashi, K., et al., *Invasion activating caveolin-1 mutation in human scirrhous breast cancers.* Cancer Res, 2001. **61**(6): p. 2361-4.

15. Pinilla, S.M., et al., *Caveolin-1 expression is associated with a basal-like phenotype in sporadic and hereditary breast cancer.* Breast Cancer Res Treat, 2006. **99**(1): p. 85-90.

16. Perrone, G., et al., *Caveolin-1 expression in human breast lobular cancer progression.* Mod Pathol, 2009. **22**(1): p. 71-8.

17. Burgermeister, E., et al., *Caveats of caveolin-1 in cancer progression.* Cancer Lett, 2008. **268**(2): p. 187-201.

18. Hung, K.F., et al., *The biphasic differential expression of the cellular membrane protein, caveolin-1, in oral carcinogenesis.* J Oral Pathol Med, 2003. **32**(8): p. 461-7.

19. Ando, T., et al., *The overexpression of caveolin-1 and caveolin-2 correlates with a poor prognosis and tumor progression in esophageal squamous cell carcinoma.* Oncol Rep, 2007. **18**(3): p. 601-9.

20. Kato, K., et al., *Overexpression of caveolin-1 in esophageal squamous cell carcinoma correlates with lymph node metastasis and pathologic stage.* Cancer, 2002. **94**(4): p. 929-33.

21. Suzuoki, M., et al., *Impact of caveolin-1 expression on prognosis of pancreatic ductal adenocarcinoma.* Br J Cancer, 2002. **87**(10): p. 1140-4.

22. Terris, B., et al., *Characterization of gene expression profiles in intraductal papillary-mucinous tumors of the pancreas.* Am J Pathol, 2002. **160**(5): p. 1745-54.

23. Fine, S.W., et al., *Elevated expression of caveolin-1 in adenocarcinoma of the colon.* Am J Clin Pathol, 2001. **115**(5): p. 719-24.

24. Yokomori, H., et al., *Enhanced expression of endothelial nitric oxide synthase and caveolin-1 in human cirrhosis.* Liver, 2002. **22**(2): p. 150-8.

25. Yokomori, H., et al., *Elevated expression of caveolin-1 at protein and mRNA level in human cirrhotic liver: relation with nitric oxide.* J Gastroenterol, 2003. **38**(9): p. 854-60.

26. Yerian, L.M., et al., *Caveolin and thrombospondin expression during hepatocellular carcinogenesis.* Am J Surg Pathol, 2004. **28**(3): p. 357-64.

27. Campbell, L., M. Gumbleton, and D.F. Griffiths, *Caveolin-1 overexpression predicts poor disease-free survival of patients with clinically confined renal cell carcinoma.* Br J Cancer, 2003. **89**(10): p. 1909-13.

28. Joo, H.J., et al., *Increased expression of caveolin-1 and microvessel density correlates with metastasis and poor prognosis in clear cell renal cell carcinoma.* BJU Int, 2004. **93**(3): p. 291-6.

29. Horiguchi, A., et al., *Impact of caveolin-1 expression on clinicopathological parameters in renal cell carcinoma.* J Urol, 2004. **172**(2): p. 718-22.

30. Fong, A., et al., *Expression of caveolin-1 and caveolin-2 in urothelial carcinoma of the urinary bladder correlates with tumor grade and squamous differentiation.* Am J Clin Pathol, 2003. **120**(1): p. 93-100.

31. Kunze, E., et al., *Transitional cell carcinomas and nonurothelial carcinomas of the urinary bladder differ in the promoter methylation status of the caveolin-1, hDAB2IP and p53 genes, but not in the global methylation of Alu elements.* Int J Mol Med, 2006. **17**(1): p. 3-13.

32. Rajjayabun, P.H., et al., *Caveolin-1 expression is associated with high-grade bladder cancer.* Urology, 2001. **58**(5): p. 811-4.

33. Yang, G., et al., *Combined c-Myc and caveolin-1 expression in human prostate carcinoma predicts prostate carcinoma progression.* Cancer, 2005. **103**(6): p. 1186-94.

34. Yang, G., et al., *Caveolin-1 expression in clinically confined human prostate cancer: a novel prognostic marker.* Cancer Res, 1999. **59**(22): p. 5719-23.

35. Karam, J.A., et al., *Caveolin-1 overexpression is associated with aggressive prostate cancer recurrence.* Prostate, 2007. **67**(6): p. 614-22.

36. Satoh, T., et al., *Caveolin-1 expression is a predictor of recurrence-free survival in pT2N0 prostate carcinoma diagnosed in Japanese patients.* Cancer, 2003. **97**(5): p. 1225-33.

37. Tahir, S.A., et al., *Development of an immunoassay for serum caveolin-1: a novel biomarker for prostate cancer.* Clin Cancer Res, 2003. **9**(10 Pt 1): p. 3653-9.

38. Tahir, S.A., et al., *Preoperative serum caveolin-1 as a prognostic marker for recurrence in a radical prostatectomy cohort.* Clin Cancer Res, 2006. **12**(16): p. 4872-5.

39. Savage, K., et al., *Caveolin 1 is overexpressed and amplified in a subset of basal-like and metaplastic breast carcinomas: a morphologic, ultrastructural, immunohistochemical, and in situ hybridization analysis.* Clin Cancer Res, 2007. **13**(1): p. 90-101.

40. Garcia, S., et al., *Poor prognosis in breast carcinomas correlates with increased expression of targetable CD146 and c-Met and with proteomic basal-like phenotype.* Hum Pathol, 2007. **38**(6): p. 830-41.

41. Sunaga, N., et al., *Different roles for caveolin-1 in the development of non-small cell lung cancer versus small cell lung cancer.* Cancer Res, 2004. **64**(12): p. 4277-85.

42. Ho, C.C., et al., *Caveolin-1 expression is significantly associated with drug resistance and poor prognosis in advanced non-small cell lung cancer patients treated with gemcitabine-based chemotherapy.* Lung Cancer, 2008. **59**(1): p. 105-10.

43. Moon, K.C., et al., *Expression of caveolin-1 in pleomorphic carcinoma of the lung is correlated with a poor prognosis.* Anticancer Res, 2005. **25**(6C): p. 4631-7.

44. Yoo, S.H., et al., *Expression of caveolin-1 is associated with poor prognosis of patients with squamous cell carcinoma of the lung.* Lung Cancer, 2003. **42**(2): p. 195-202.

45. Kato, T., et al., *Difference of caveolin-1 expression pattern in human lung neoplastic tissue. Atypical adenomatous hyperplasia, adenocarcinoma and squamous cell carcinoma.* Cancer Lett, 2004. **214**(1): p. 121-8.

46. Ho, C.C., et al., *Up-regulated caveolin-1 accentuates the metastasis capability of lung adenocarcinoma by inducing filopodia formation.* Am J Pathol, 2002. **161**(5): p. 1647-56.

47. Ito, Y., et al., *Caveolin-1 overexpression is an early event in the progression of papillary carcinoma of the thyroid.* Br J Cancer, 2002. **86**(6): p. 912-6.

48. Ito, Y., et al., *Caveolin-1 and 14-3-3 sigma expression in follicular variant of thyroid papillary carcinoma.* Pathol Res Pract, 2005. **201**(8-9): p. 545-9.

49. Cassoni, P., et al., *Caveolin-1 expression is variably displayed in astroglial-derived tumors and absent in oligodendrogliomas: concrete*

premises for a new reliable diagnostic marker in gliomas. Am J Surg Pathol, 2007. **31**(5): p. 760-9.

50. Senetta, R., et al., *Caveolin 1 expression independently predicts shorter survival in oligodendrogliomas.* J Neuropathol Exp Neurol, 2009. **68**(4): p. 425-31.

51. Barresi, V., et al., *Caveolin-1 in meningiomas: expression and clinico-pathological correlations.* Acta Neuropathol, 2006. **112**(5): p. 617-26.

52. Tirado, O.M., et al., *Caveolin-1 (CAV1) is a target of EWS/FLI-1 and a key determinant of the oncogenic phenotype and tumorigenicity of Ewing's sarcoma cells.* Cancer Res, 2006. **66**(20): p. 9937-47.

53. Couet, J., et al., *Identification of peptide and protein ligands for the caveolin-scaffolding domain. Implications for the interaction of caveolin with caveolae-associated proteins.* J Biol Chem, 1997. **272**(10): p. 6525-33.

54. Razani, B., S.E. Woodman, and M.P. Lisanti, *Caveolae: from cell biology to animal physiology.* Pharmacol Rev, 2002. **54**(3): p. 431-67.

55. Shaul, P.W. and R.G. Anderson, *Role of plasmalemmal caveolae in signal transduction.* Am J Physiol, 1998. **275**(5 Pt 1): p. L843-51.

56. Sathornsumetee, S., et al., *Molecularly targeted therapy for malignant glioma.* Cancer, 2007. **110**(1): p. 13-24.

57. Grande-Garcia, A. and M.A. del Pozo, *Caveolin-1 in cell polarization and directional migration.* Eur J Cell Biol, 2008. **87**(8-9): p. 641-7.

58. Joshi, B., et al., *Phosphorylated caveolin-1 regulates Rho/ROCK-dependent focal adhesion dynamics and tumor cell migration and invasion.* Cancer Res, 2008. **68**(20): p. 8210-20.

59. Grande-Garcia, A., et al., *Caveolin-1 regulates cell polarization and directional migration through Src kinase and Rho GTPases.* J Cell Biol, 2007. **177**(4): p. 683-94.

60. Lin, M., et al., *Regulation of pancreatic cancer cell migration and invasion by RhoC GTPase and caveolin-1.* Mol Cancer, 2005. **4**(1): p. 21.

61. Miotti, S., et al., *Simultaneous expression of caveolin-1 and E-cadherin in ovarian carcinoma cells stabilizes adherens junctions through inhibition of src-related kinases.* Am J Pathol, 2005. **167**(5): p. 1411-27.

62. Song, L., S. Ge, and J.S. Pachter, *Caveolin-1 regulates expression of junction-associated proteins in brain microvascular endothelial cells.* Blood, 2007. **109**(4): p. 1515-23.

63. Orlichenko, L., et al., *Caveolae Mediate Growth Factor-induced Disassembly of Adherens Junctions to Support Tumor Cell Dissociation.* Mol Biol Cell, 2009.

64. Nomura, R. and T. Fujimoto, *Tyrosine-phosphorylated caveolin-1: immunolocalization and molecular characterization.* Mol Biol Cell, 1999. **10**(4): p. 975-86.

65. Li, S., R. Seitz, and M.P. Lisanti, *Phosphorylation of caveolin by src tyrosine kinases. The alpha-isoform of caveolin is selectively phosphorylated by v-Src in vivo.* J Biol Chem, 1996. **271**(7): p. 3863-8.

66. Lee, H., et al., *Constitutive and growth factor-regulated phosphorylation of caveolin-1 occurs at the same site (Tyr-14) in vivo: identification of a c-Src/Cav-1/Grb7 signaling cassette.* Mol Endocrinol, 2000. **14**(11): p. 1750-75.

67. Schlegel, A., P. Arvan, and M.P. Lisanti, *Caveolin-1 binding to endoplasmic reticulum membranes and entry into the regulated secretory pathway are regulated by serine phosphorylation. Protein sorting at the level of the endoplasmic reticulum.* J Biol Chem, 2001. **276**(6): p. 4398-408.

68. Tahir, S.A., et al., *Secreted caveolin-1 stimulates cell survival/clonal growth and contributes to metastasis in androgen-insensitive prostate cancer.* Cancer Res, 2001. **61**(10): p. 3882-5.

69. Li, L., et al., *Caveolin-1 mediates testosterone-stimulated survival/clonal growth and promotes metastatic activities in prostate cancer cells.* Cancer Res, 2001. **61**(11): p. 4386-92.

70. Tahir, S.A., et al., *Tumor cell-secreted caveolin-1 has proangiogenic activities in prostate cancer.* Cancer Res, 2008. **68**(3): p. 731-9.

71. Del Pozo, M.A. and M.A. Schwartz, *Rac, membrane heterogeneity, caveolin and regulation of growth by integrins.* Trends Cell Biol, 2007. **17**(5): p. 246-50.

72. del Pozo, M.A., et al., *Phospho-caveolin-1 mediates integrin-regulated membrane domain internalization.* Nat Cell Biol, 2005. **7**(9): p. 901-8.

73. Ravid, D., et al., *Caveolin-1 inhibits cell detachment-induced p53 activation and anoikis by upregulation of insulin-like growth factor-I receptors and signaling.* Oncogene, 2005. **24**(8): p. 1338-47.

74. Glait, C., et al., *Caveolin-1 up-regulates IGF-I receptor gene transcription in breast cancer cells via Sp1- and p53-dependent pathways.* Exp Cell Res, 2006. **312**(19): p. 3899-908.

75. Cavallo-Medved, D., et al., *Caveolin-1 mediates the expression and localization of cathepsin B, pro-urokinase plasminogen activator and their cell-surface receptors in human colorectal carcinoma cells.* J Cell Sci, 2005. **118**(Pt 7): p. 1493-503.

76. Stahl, A. and B.M. Mueller, *The urokinase-type plasminogen activator receptor, a GPI-linked protein, is localized in caveolae.* J Cell Biol, 1995. **129**(2): p. 335-44.

77. Lopez-Rivera, E., et al., *Matrix metalloproteinase 13 mediates nitric oxide activation of endothelial cell migration.* Proc Natl Acad Sci U S A, 2005. **102**(10): p. 3685-90.

78. Labrecque, L., et al., *Src-mediated tyrosine phosphorylation of caveolin-1 induces its association with membrane type 1 matrix metalloproteinase.* J Biol Chem, 2004. **279**(50): p. 52132-40.

79. Annabi, B., et al., *Hyaluronan cell surface binding is induced by type I collagen and regulated by caveolae in glioma cells.* J Biol Chem, 2004. **279**(21): p. 21888-96.

80. Sallinen, S.L., et al., *Identification of differentially expressed genes in human gliomas by DNA microarray and tissue chip techniques.* Cancer Res, 2000. **60**(23): p. 6617-22.

81. Van Meter, T., et al., *Microarray analysis of MRI-defined tissue samples in glioblastoma reveals differences in regional expression of therapeutic targets.* Diagn Mol Pathol, 2006. **15**(4): p. 195-205.

82. Ross, D.T., et al., *Systematic variation in gene expression patterns in human cancer cell lines.* Nat Genet, 2000. **24**(3): p. 227-35.

83. Abulrob, A., et al., *Interactions of EGFR and caveolin-1 in human glioblastoma cells: evidence that tyrosine phosphorylation regulates EGFR association with caveolae.* Oncogene, 2004. **23**(41): p. 6967-79.

84. Martin, S., et al., *Caveolin-1 regulates glioblastoma aggressiveness through the control of alpha(5)beta(1) integrin expression and modulates glioblastoma responsiveness to SJ749, an alpha(5)beta(1) integrin antagonist.* Biochim Biophys Acta, 2009. **1793**(2): p. 354-67.

85. Nozaki, M., et al., *Roles of the functional loss of p53 and other genes in astrocytoma tumorigenesis and progression.* Neuro Oncol, 1999. **1**(2): p. 124-37.

86. Gan, H.K., A.H. Kaye, and R.B. Luwor, *The EGFRvIII variant in glioblastoma multiforme.* J Clin Neurosci, 2009. **16**(6): p. 748-54.

87. Cho, K.A., et al., *Morphological adjustment of senescent cells by modulating caveolin-1 status.* J Biol Chem, 2004. **279**(40): p. 42270-8.

88. Shin, J., et al., *Caveolin-1 is associated with VCAM-1 dependent adhesion of gastric cancer cells to endothelial cells.* Cell Physiol Biochem, 2006. **17**(5-6): p. 211-20.

89. Smith, P.K., et al., *Measurement of protein using bicinchoninic acid.* Anal Biochem, 1985. **150**(1): p. 76-85.

90. Albini, A., *Tumor and endothelial cell invasion of basement membranes. The matrigel chemoinvasion assay as a tool for dissecting molecular mechanisms.* Pathol Oncol Res, 1998. **4**(3): p. 230-41.

91. Repesh, L.A., *A new in vitro assay for quantitating tumor cell invasion.* Invasion Metastasis, 1989. **9**(3): p. 192-208.

92. Thompson, E.W., et al., *Supernatants of acquired immunodeficiency syndrome-related Kaposi's sarcoma cells induce endothelial cell chemotaxis and invasiveness.* Cancer Res, 1991. **51**(10): p. 2670-6.

93. Felicetti, F., et al., *Caveolin-1 tumor-promoting role in human melanoma.* Int J Cancer, 2009. **125**(7): p. 1514-22.

94. Zivadinovic, D. and C.S. Watson, *Membrane estrogen receptor-alpha levels predict estrogen-induced ERK1/2 activation in MCF-7 cells.* Breast Cancer Res, 2005. **7**(1): p. R130-44.

95. Carson, S.D. and S.J. Pirruccello, *Tissue factor and cell morphology variations in cell lines subcloned from U87-MG.* Blood Coagul Fibrinolysis, 1998. **9**(6): p. 539-47.

96. Ayala, G.E., et al., *Stromal antiapoptotic paracrine loop in perineural invasion of prostatic carcinoma.* Cancer Res, 2006. **66**(10): p. 5159-64.

97. Tonn, J.C. and R. Goldbrunner, *Mechanisms of glioma cell invasion.* Acta Neurochir Suppl, 2003. **88**: p. 163-7.

98. Giese, A., et al., *Cost of migration: invasion of malignant gliomas and implications for treatment.* J Clin Oncol, 2003. **21**(8): p. 1624-36.

99. Khan, E.M., et al., *Epidermal growth factor receptor exposed to oxidative stress undergoes Src- and caveolin-1-dependent perinuclear trafficking.* J Biol Chem, 2006. **281**(20): p. 14486-93.

100. Kim, Y.N., P. Dam, and P.J. Bertics, *Caveolin-1 phosphorylation in human squamous and epidermoid carcinoma cells: dependence on ErbB1 expression and Src activation.* Exp Cell Res, 2002. **280**(1): p. 134-47.

101. Kim, Y.N., et al., *Epidermal growth factor-stimulated tyrosine phosphorylation of caveolin-1. Enhanced caveolin-1 tyrosine phosphorylation following aberrant epidermal growth factor receptor status.* J Biol Chem, 2000. **275**(11): p. 7481-91.

102. Horvath, S., et al., *Analysis of oncogenic signaling networks in glioblastoma identifies ASPM as a molecular target.* Proc Natl Acad Sci U S A, 2006. **103**(46): p. 17402-7.

103. Lal, A., et al., *Mutant epidermal growth factor receptor up-regulates molecular effectors of tumor invasion.* Cancer Res, 2002. **62**(12): p. 3335-9.

104. Wu, J.L., et al., *IkappaBalphaM suppresses angiogenesis and tumorigenesis promoted by a constitutively active mutant EGFR in human glioma cells.* Neurol Res, 2004. **26**(7): p. 785-91.

105. Nagane, M., et al., *Human glioblastoma xenografts overexpressing a tumor-specific mutant epidermal growth factor receptor sensitized to cisplatin by the AG1478 tyrosine kinase inhibitor.* J Neurosurg, 2001. **95**(3): p. 472-9.

106. Ciesielski, M.J. and R.A. Fenstermaker, *Oncogenic epidermal growth factor receptor mutants with tandem duplication: gene structure and effects on receptor function.* Oncogene, 2000. **19**(6): p. 810-20.

107. Li, L., et al., *Caveolin-1 maintains activated Akt in prostate cancer cells through scaffolding domain binding site interactions with and inhibition of serine/threonine protein phosphatases PP1 and PP2A.* Mol Cell Biol, 2003. **23**(24): p. 9389-404.

108. Omuro, A.M., S. Faivre, and E. Raymond, *Lessons learned in the development of targeted therapy for malignant gliomas.* Mol Cancer Ther, 2007. **6**(7): p. 1909-19.

109. Grant, S., *Cotargeting survival signaling pathways in cancer.* J Clin Invest, 2008. **118**(9): p. 3003-6.

Chapter 6 Phage display identification of peptides that bind caveolin-1 scaffolding domain

6.1 Introduction

In recent years it has become apparent that caveolin-1 plays a key role in the modulation of signal transduction events[1, 2]. As a corollary any alteration in the expression or functioning of caveolin-1 will result in modified cell signaling potentially leading to pathology[3]. Reports in the literature have shown that alteration in expression or functioning of caveolin-1 contributes to the aetiology of a wide range of diseases that include cancer[4, 5], diabetes[6], degenerative muscular dystrophies[7], cirrhosis[8], pulmonary fibrosis[9], atherosclerosis[10, 11], and Alzheimer's disease[12]. Indeed the studies detailed in Chapter 5 of this thesis demonstrated the positive correlation of caveolin-1 with cellular proliferation and invasiveness in glioblastoma multiforme. In addition, caveolin-1 plays a role in the pathology of a variety of infectious diseases including HIV[13, 14], neonatal meningitis[15, 16], Chlamydia[17], human papilloma virus[18, 19] and prion disease[20].

Many of the functions of caveolin-1 are mediated through a small scaffolding domain (caveolin-scaffolding domain; CSD) located within the oligomerisation domain (see **Figure 6.1** for the location of the scaffolding domain within caveolin-1). The significant role of CSD in caveolin-1 function was first demonstrated in 1995 when Li and co-workers[21] showed that CSD inhibits heterotrimeric G-proteins in GTP hydrolysis assays. Subsequently, various laboratories have shown that CSD from caveolin-1 not only interacts with G-proteins but with a variety of disparate

signaling molecules that include EGF-R, Src family tyrosine kinases, PKC iso-forms, H-Ras, Neu, and eNOS (a detailed list of these molecules can be found in [22]); generally reports have shown the interaction of a signaling molecule with caveolin-1 CSD inhibits downstream signaling.

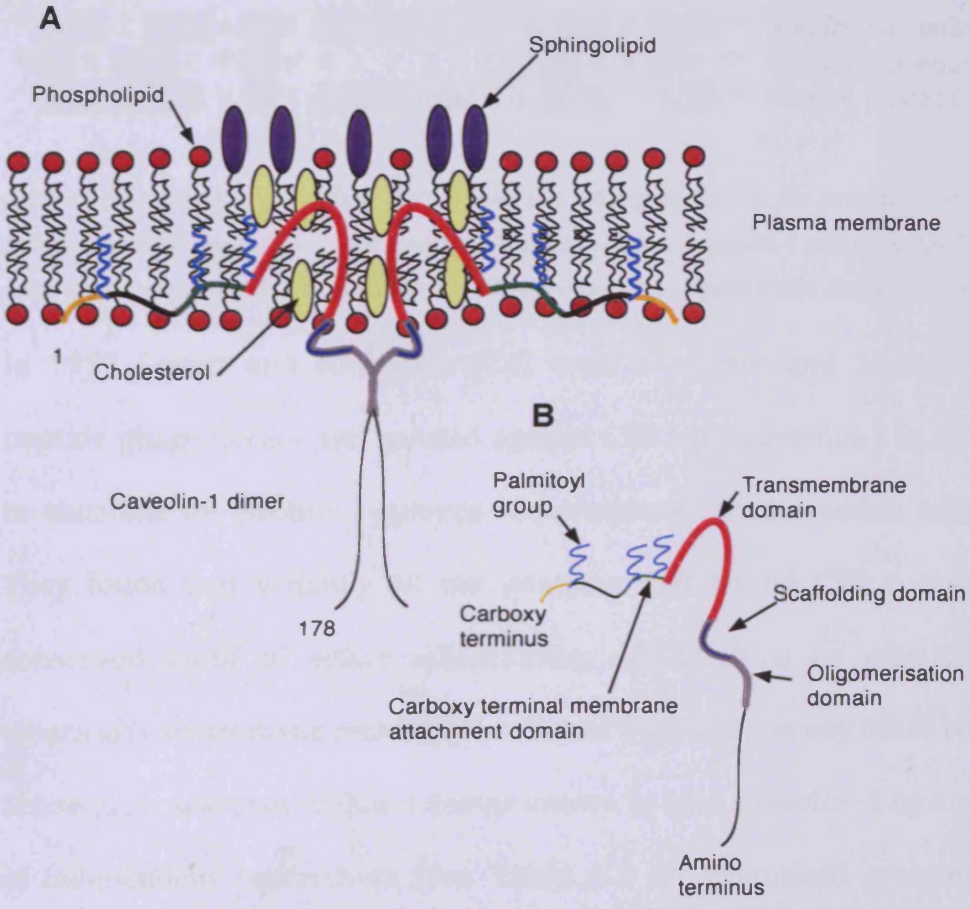

Figure 6.1 Structure and topology of caveolin-1. (A) Membrane topology of caveolin-1. Depicted are two caveolin-1 monomers interacting through the scaffolding domain (within the oligomerisation domain) to form a dimer. In reality 14-16 monomers interact to form a homodimer or if interaction is with caveolin-2, a heterodimer. (B) Schematic of the various domains within caveolin-1. Adapted from[23].

Whilst a caveolin scaffolding domain can be found in all members of the caveolin family (caveolin-1, -2, -3), there is only significant homology of amino acid sequence between caveolin-1 and caveolin-3 (75%

conservation); CSD within caveolin-2 is divergent with only 37% of the amino acids conserved with respect to either caveolin-1 or caveolin-3 (see **Figure 6.2**). The studies in this chapter are only concerned with the scaffolding domain within caveolin-1.

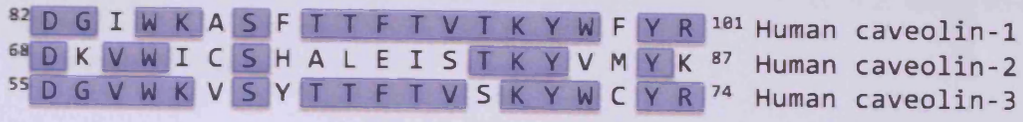

Figure 6.2 Sequence alignment of the caveolin scaffolding domain in the human caveolin gene family. Identical residues are boxed and highlighted in blue. Caveolin-1 and caveolin-3 are the most closely related (75% conservation) with caveolin-2 divergent (35% conservation).

In 1997 Couett and co-workers[24] used a 10-mer and 15-mer linear peptide phage library and panned against CSD from caveolin-1 in an effort to elucidate the protein sequence requirements for interaction with CSD. They found that virtually all the peptides that bound CSD contained a conserved motif of either ωXωXXXXω, ωXXXXωXXω or ωXωXXωXXω where ω is an aromatic residue (Phe, Trp or Tyr) and X is any other residue. Subsequent searches within proteins known to bind caveolin -1 by a variety of independent researchers (see **Table 6.1** for examples) revealed that such proteins invariably contain one of these 'caveolin binding domains' (CBD) within their primary sequence (reviewed in [22]).

Table 6.1 Caveolin binding domains identified in key signaling molecules.

Protein	Caveolin binding domain
Gi2α	**F**T**F**KDLY**F**KM**F**
eNOS	**F**SAAP**F**SG**W**
SRC family kinase	**W**S**F**GILL**Y**
EGF-R	**W**S**Y**GVTV**W**
PKCα	**W**A**Y**GVLL**Y**

It is important to note however, that the presence of a caveolin binding domain within a protein is not an absolute predicator of interaction with CSD and it is clear that surface exposure of the CBD on the protein is a key determinant for interaction. Further, if any such interactions occur they may be very short-lived such that biochemical determination is likely to be extremely difficult.

The mechanism by which the caveolin binding domain interacts with caveolin-1 CSD remains to be fully elucidated since, to date, CSD from caveolin-1 has not been crystallised either alone or with a binding partner on-board. However, 'shotgun scanning' of the scaffolding domain with phage displaying closely related homologs of CSD from caveolin-1, reveal that residues 82, 90, 91, 95, and 97,which form a helical wheel on the face of CSD, are important for interaction with eNOS and PKCα[25]. Some studies have also suggested that the oligomerisation and deoligomerisation through CSD is critical for the modulation of binding affinity to partner proteins[26]. As a result any agent that interferes with oligomerization processes may inhibit binding of partner proteins and therefore potentially alter downstream signaling.

More recently elegant *in-vitro* and *in-vivo* studies have been undertaken to elucidate the role of the caveolin-1 scaffolding domain (as opposed to the entire caveolin-1 protein) in human health and disease. This has generally taken the form of modulating signaling pathways through the intracellular delivery of caveolin-1 scaffolding domain via attachment to cell penetrating

peptides. Bucci and co-workers[27] produced a chimeric protein (AP-CSD) of caveolin-1 scaffolding domain (CSD) and the cell penetrating peptide Antennapedia (AP). After demonstrating that exposure of aortic rings to AP-CSD inhibited acetycholine-induced relaxation of blood vessels and eNOS derived production of nitric oxide, AP-CSD was administered by intraperitoneal injection into a mouse model of foot-pad inflammation (carrageenan, injection into the foot pad). Only the AP-CSD sequence, and not the respective AP-scrambled CSD control sequence reduced carrageenan-induced foot-pad oedema through the attenuation of eNOS-dependant blood-flow.

Neonatal meningitis, an infectious disorder of the CNS is associated with the entry of *Escherichia coli* K1 into brain parenchyma. Dissemination of the bacterium follows transcytosis across brain microvascular endothelium within caveolae[16, 28, 29, 30]. Studies have shown that the interaction of caveolin-1 with PKCα at the site of *E. coli* K1 attachment is essential for invasion of the brain endothelia[15, 31]. Sukumaran and co-workers[15] have demonstrated that invasion can be blocked either by the over-expression of a dominant negative form of caveolin-1 that has been mutated within the scaffolding domain such that it does not bind PKCα or by exposure of brain microvasculature to AP-CSD which competes for PKCα.

6.1.1 Objectives

In this chapter a phage display study was undertaken to identify novel peptides that bind the caveolin-1 scaffolding domain. Peptides that bind the caveolin-1 scaffolding may have utility in modulating caveolin-1 function. The panning experiments used a two-step protocol (see chapter 2) where a caveolin- 1 scaffolding domain biotin conjugate, in solution, was the biopanning target before subsequent capture of the conjugate, plus bound phages, onto streptavidin paramagnetic beads. The interaction of the peptide-phages with caveolin-1 scaffolding domain was subsequently assessed on an individual clonal basis using an ELISA assay before those clones showing maximal binding were gene sequenced to identify the displayed peptides. The peptide sequence of those strongly binding phages will serve as a chemical framework of a future research program to develop small molecule peptidomimetics interacting with CSD to modulate caveolin-1 functioning.

6.2 Materials

Materials used in this chapter have previously been detailed in Chapter 2.

6.3 Methods

The general methods for panning and ELISA studies were as described in Chapter 2 as used for panning against streptavidin target on magnetic beads.

6.3.1 Preparation of CSD-biotin

CSD-biotin was suspended in 50:50 acetonitrile:H_2O containing 0.1% TFA to a concentration of 1mg.ml^{-1}; stock was protected from light and stored at 4°C for a period of up to 1 month. Stability of this CSD-biotin stock at 1 month was confirmed using Matrix-assisted laser desorption/ionization mass spectroscopy (MALDI-TOF). Samples and matrix for mass spectroscopy were prepared by Dr Christopher Morris (Welsh School of Pharmacy) and processed in Cardiff University Chemistry department using a Waters micro MX MALDI-TOF.

6.3.2 Panning

The Ph.D.-C7C™ cyclised 7-mer disulphide constrained peptide phage library was used in panning experiments against CSD-biotin. A schematic of the panning experiment can be seen in **Figure 6.3**. Specifically, streptavidin Magnesphere™ paramagnetic particles (SA-PMPs) were washed three times with phosphate buffered saline immediately prior to use. Panning experiments were conducted in 1.5 ml microcentrifuge tubes that were blocked with Superblock™ (guaranteed biotin-free) prior to use; of note we have observed, in contrast to the use of Superblock™, phage display experiments conducted with standard BSA or non-fat milk blocking buffers result in a tendency for selection of streptavidin binding peptides (HPQ motif). Plastic binding peptide phages were deleted from the library by adding 2 x 10^{11} pfus of peptide-phages to a microcentrifuge tube. After 1 hour, the non-binding phages i.e. those remaining in supernatant were

transferred to a microcentrifuge tube containing 10 mg of SA-PMPs and incubated at room temperature for 1 hour with gentle rocking. The SA-PMPs with bound streptavidin binding phage were then pelleted using a rare earth metal magnet (neodymium). The supernatant was then transferred to a microcentrifuge tube containing 40 pmoles (~0.12μg) of CSD-Biotin in 100 μl of TBS; CSD being the primary target. After 1 hour, 10 mg of SA-PMPs were added to bind the biotin on the CSD and thereby afford the collection of peptide-phage binders to the CSD-biotin target; 10mg of SA-PMPs binds 47 pmoles of biotin which should be sufficient to bind every molecule of CSD-biotin (40 pmoles) in the supernatant. After a 15 minute incubation, the SA-PMPs were pelleted by magnet. The SA-PMPs were washed 10x with TBS-T(0.5%) before being exposed to 3x 5 minute glycine buffer elutions (200 μL) during which the SA-PMPs were sonicated. The glycine elutions containing eluted peptide phages were neutralized, pooled and amplified to serve as input into the next iterative panning round. A total of four panning rounds were completed.

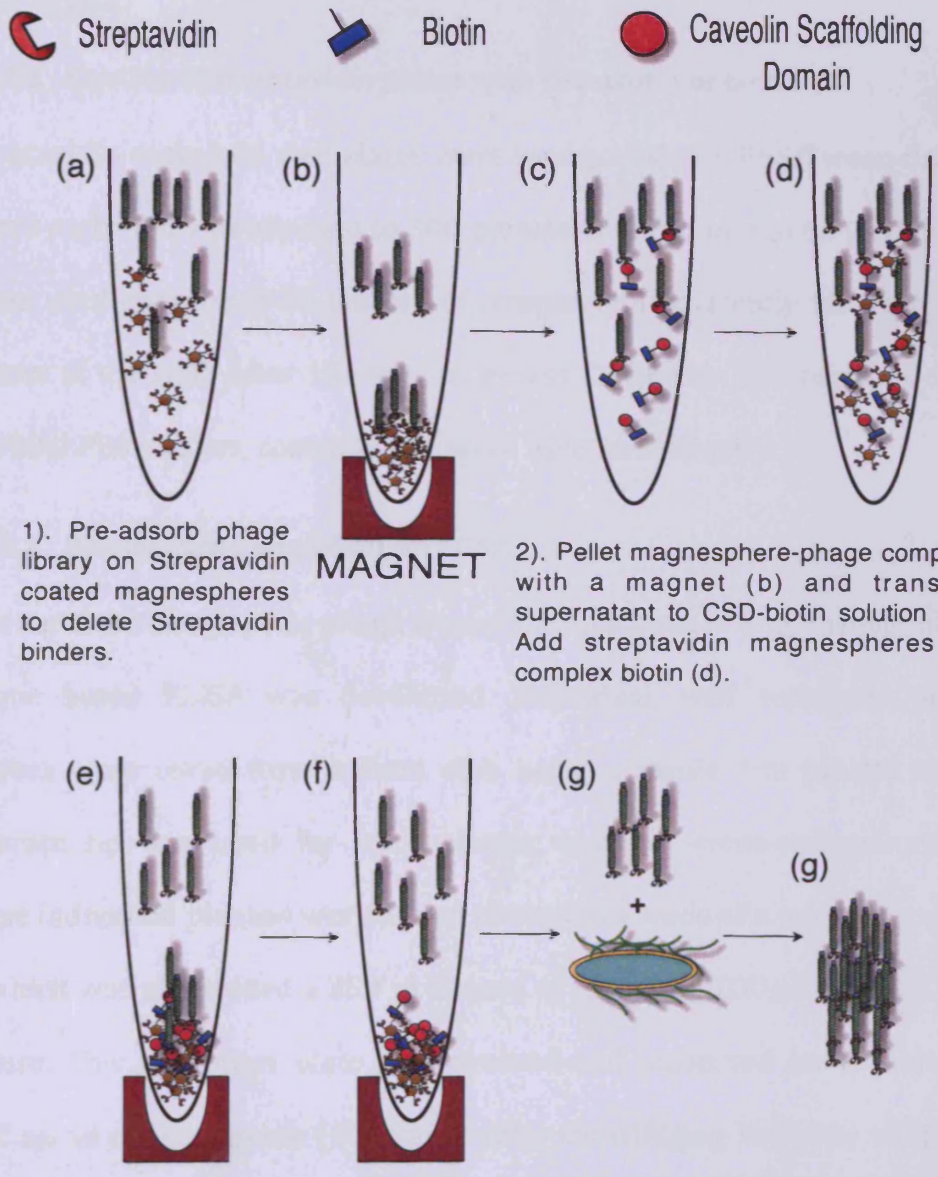

Figure 6.3 Schematic of phage panning procedure to isolate peptides that bind caveolin-1 scaffolding domain.

6.3.3 ELISA

6.3.3.1 Coating of streptavidin plates with CSD-biotin or biotin

Streptavidin coated 96 well plates were washed 3x with PBS-Tween-0.05% before each well was exposed to 300 pmoles of CSD-biotin in 60 µl TBS; the plates used comprised 30 pmoles of streptavidin covalently bound to the bottom of the well. After 15 minutes, excess CSD-biotin was removed with 3x 200µl PBS washes; coated plates were used immediately.

6.3.3.2 Plaque based amplification ELISA

In order to screen peptide phage clones with medium to high throughput, a plaque based ELISA was developed. Individual, well separated phage plaques were cored from a Petri dish using a sterile 1ml pipette tip (a separate tip was used for each plaque to avoid cross-contamination). These individual plaques were added to separate wells of a microtiter plate to which was also added a 250 µl aliquot of log-phase (OD_{600} ~ 0.6) *E. coli* culture. This microtiter plate was covered and incubated for 4 hours at 37°C on an orbital shaker (100 rpm). After centrifuging the plate at 1500g for 10 mins to pellet the *E. coli*, 100 µl samples of phage-containing supernatant were transferred from each well into a corresponding well of a 96 well microtiter plate that had been coated with CSD-biotin and which serves as the plate for ELISA; the remaining supernatant was stored at 4 – 8°C to serve as a stock for future experiments. After 1 hour the supernatant was aspirated from the CSD-coated wells and the wells were then washed 6x with TBS-T(0.5%). Thereafter, the ELISA protocol detailed in Chapter 2

was followed. Negative control was insertless phage (n = 4 per plate) and a positive control was peptide-phage with sequence AC-**GSYWHPQ**-CGGGS (streptavidin binding; n = 4 per plate) binding to uncoated streptavidin wells. A further sequence, AC-**PPTHGRH**-CGGGS, isolated from glycine elution 3 of round 3 of the panning studies was included as an inter-plate control (n = 4 per plate). A total of 1008 clones were analysed using this plaque based assay (12 microtiter plates in total). Phage clones resulting in absorbance signal at least six-fold greater than insertless phages were deemed to be strong binders (moderate binders were classed as a ratio of 3-6 fold greater than insertless and < 3 fold were classed as weak binders).

6.3.3.3 Sequencing

A random selection of 58 phage clones designated as strong binders based on ELISA data (6-fold greater absorbance than insertless phages) were gene sequenced to identify the displayed peptide. The preparation of DNA samples from phage clones and the subsequent gene sequencing protocol has previously been described in chapter 2.

6.4 Results

6.4.1 Stability of CSD-biotin

To assess the stability of a stock of CSD-biotin (1 $mg.ml^{-1}$ in 50:50 acetonitrile:H2O; 0.1% TFA), MALDI-TOF mass spectra were generated following 1 month storage in the dark at 4°C. The expected mass of CSD-biotin was 2990 Da and the observed mass was 2991.8 Da (**Figure 6.4**). These data indicated stability under the tested conditions and therefore

panning experiments were undertaken with stocks prepared and stored in this way. After 1 month, any unused stock was discarded.

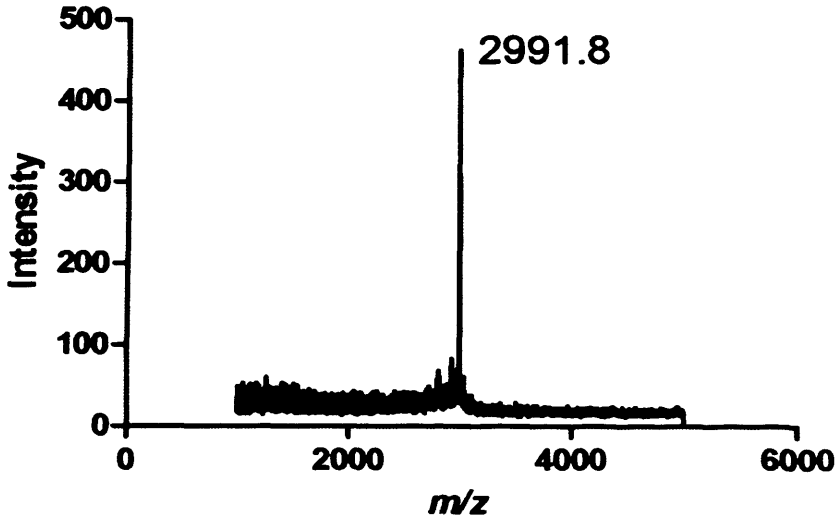

Figure 6.4 MALDI-TOF spectrograph of CSD-biotin stock stored for 1 month at 4°C. Predicted mass is 2990 Da, observed mass was 2991.8 Da.

6.4.2 Identification of peptide ligands for the caveolin-1 scaffolding domain using phage display

Phage panning studies were undertaken using the Ph.D.™-C7C cyclic 7-mer constrained library to identify novel peptides that bind CSD. The panning methodology used was based on similar studies detailed in chapter 2 to identify peptides that bind streptavidin. Essentially, CSD-biotin was exposed to phage library in a solution phase before capture of the phage-CSD-biotin complex on streptavidin coated paramagnetic beads. In total, four rounds of panning were undertaken. The number of phages recovered from glycine elutions 1-3 in panning rounds 1-4 are shown in **Figure 6.5**. Of note, for the same initial input, the number of phages recovered in each

glycine elution increases from round 1 through 3 indicating enrichment for a binding population. In round 4, the number of phages recovered in glycine elutions 2 and 3 decreased compared to the previous round (glycine elutions 2 and 3 are assumed to contain the highest affinity binders) which indicates the selection process plateaus in round 3, and as a result round 4 phages were discarded.

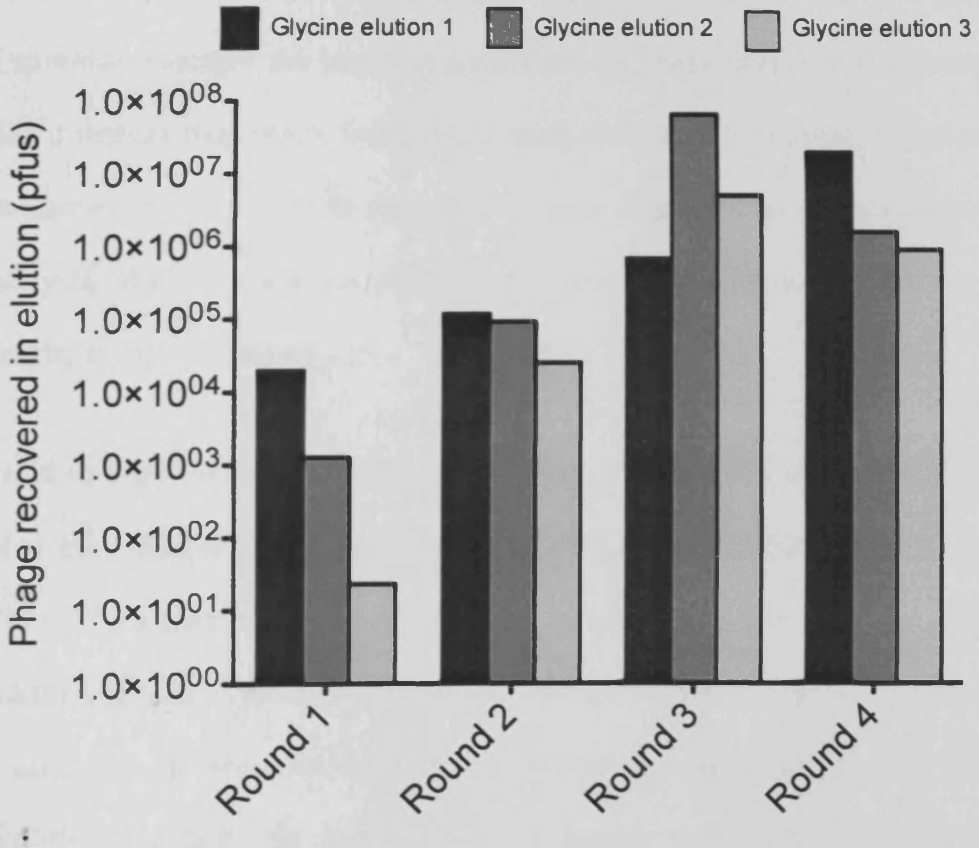

Figure 6.5 Number of phage recovered in glycine elution 1-3 in panning rounds 1 through 4 against CSD-biotin as target. In rounds 1 through 3, the number of phages recovered in each glycine elution increased indicating enrichment for CSD binding peptide phages. In round 4, a decrease in recovery in glycine elutions 2 and 3 was observed indicating enrichment had reached a plateau.

6.4.3 ELISA analysis

The data presented in **Figure 6.5** is indicative of enrichment for a population of CSD-binding peptides. In previous chapters where phage display has been undertaken, a large random sample of phages from the final panning round were gene sequenced to identify conserved peptides or peptide motifs. Those conserved motifs were then taken forward to assess whether they were 'functional'; the assumption is that with the emergence of common motif(s) the panning procedure has been successful. To avoid false positives that result from sequencing data, in this chapter, functional assessment was made of an extensive number of phage clones isolated from the cyclic library in glycine elution 3 of round 3 before gene sequencing to identify the displayed peptide.

A mid to high-throughput ELISA assay was developed in which individual colonies of phages were cored from agar plates and deposited into a culture of *E. coli* in a well of a 96-well microtiter plate. The phages were amplified and then served as input into a standard phage ELISA experiment with CSD as target. In previous ELISA studies detailed in this thesis, phages were amplified, purified and titered before a known amount of phages were inputted into the ELISA. This takes significant time and whilst in the high-throughput screen that was developed, the exact number of input phages was not known, a sample of 6 wells collected from 6 different plates revealed remarkable consistency with the number of phages present in the order of $1 \times 10^6 \pm 10\%$. On each microtiter plate three controls were

included (n = 4 for each), an insertless phage, a streptavidin binding phage (sequence AC-**GSYWHPQ**-CGGGS) and a randomly selected phage from glycine elution 3 of round 3 (AC-**PPTHGRH**-CGGGS) to serve as a measure of plate to plate variability. In total, 1008 clones were assessed using this high-throughput ELISA screening. **Figure 6.6** is a photograph of a representative plate that results from the ELISA. Of note insertless-M13 do not yield any signal (B2, E6, B10, G12) whilst for the library phages there are a range of absorbances from weak e.g. D4, D7, F8 through to intense e.g. F2, B6, B12.

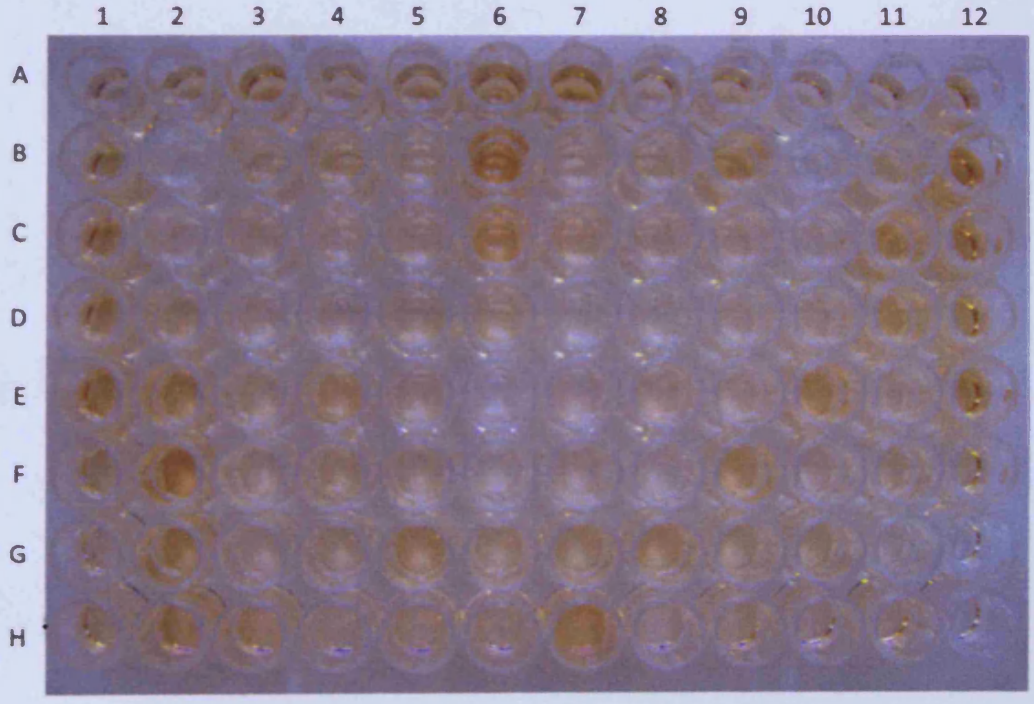

Figure 6.6 Representative high-throughput ELISA screening plate to discriminate peptide-phages that bind CSD with high affinity from those that only moderately bind. Note the intense signal in certain wells e.g. F2, B6, B12 etc which indicates high affinity binding. Plate controls were insertless phages (B2, E6, B10, G12), streptavidin binding phage (C2, F6, C10, H12) and a peptide-phage from glycine elution 3, round 3 (D2, G6, D10, F12).

After completing ELISA studies, the ratio of peptide-phage ELISA signal to insertless phage ELISA signal was calculated for each of the individual colonies analysed (1008 in total). This data was then plotted against the observed frequency of a range of ratios (**Figure 6.7**); in the main a gaussian distribution was observed.

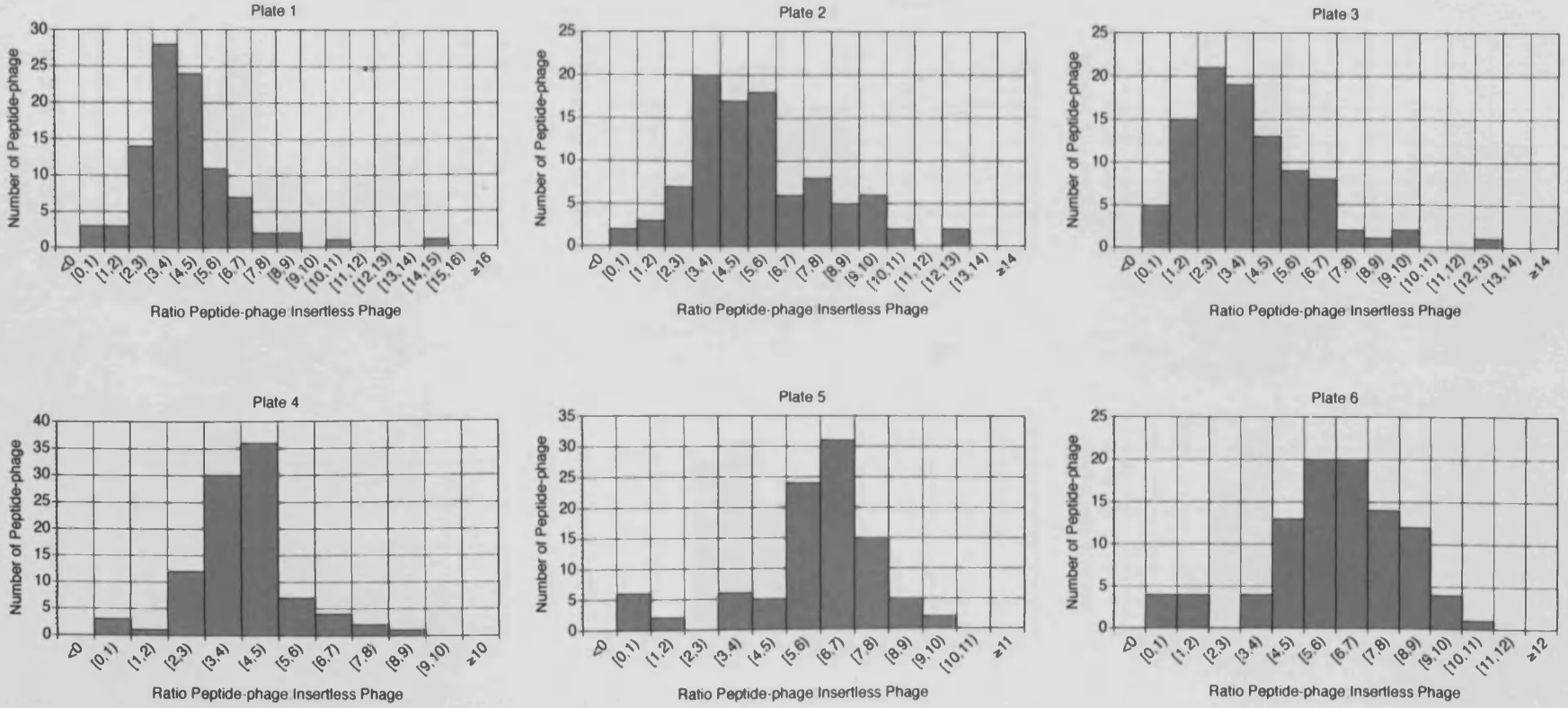

Figure 6.7 ELISA analysis of the binding of 1008 individual peptide-phage clones to CSD. X-axis represents ELISA signal as a ratio of peptide-phage clone to insertless signal and the y-axis is the number of peptide-phage clones generating a given ratio. High affinity binders were defined as those generating an ELISA signal at least 6-fold greater than insertless phage.

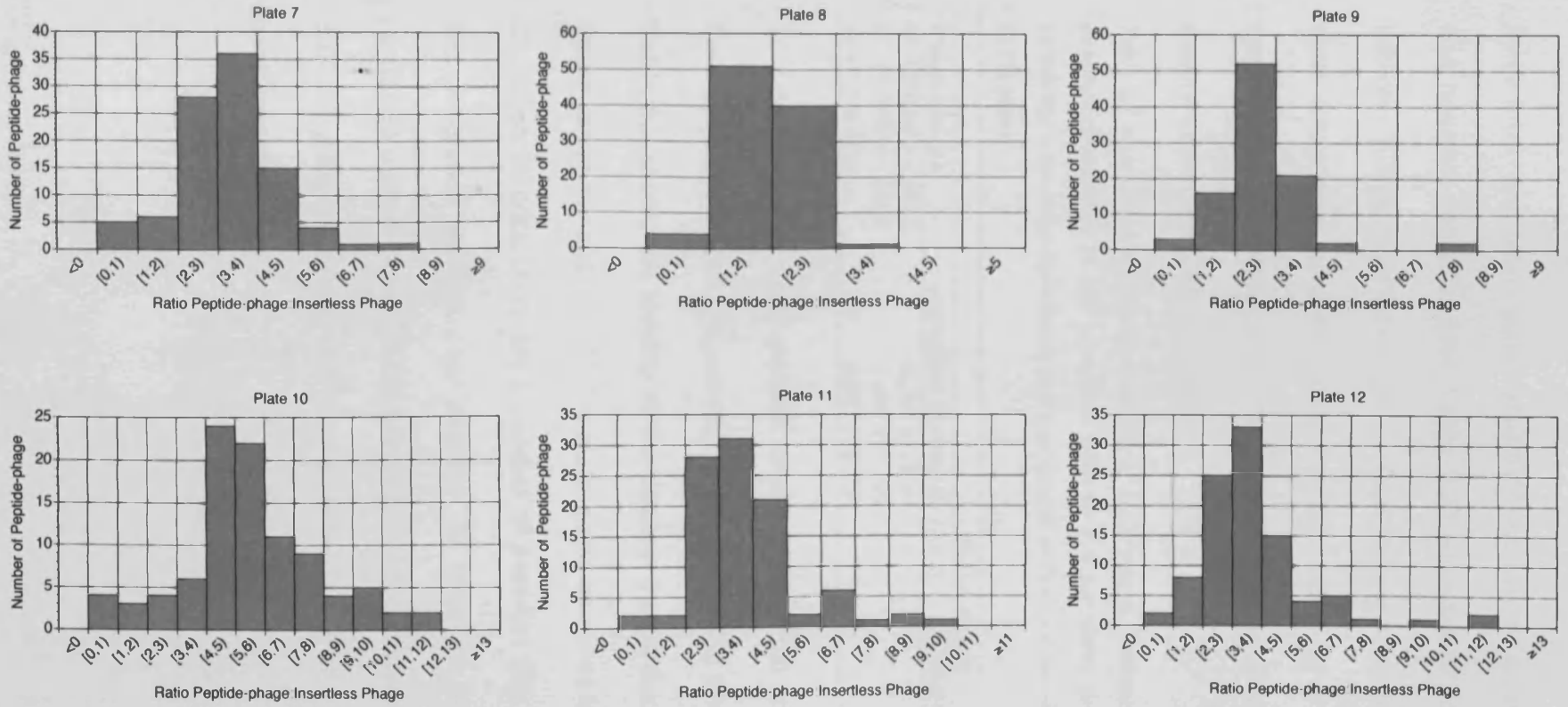

Figure 6.7 continued.

Since intra- and inter- plate variability was low, as determined by positive and negative controls (see **Table 6.2**), absorbance readings across and between plates could be compared. As a consequence, high affinity binders were categorised as those clones having a 6-fold or greater ELISA signal compared to insertless phages; this accounts for approximately 20% of the colonies analysed (200 colonies).

Table 6.2 Inter- and intra- plate variability of ELISA assays. Interplate assays are the mean absorbance readings (± SD) of control wells (n = 4 per plate) for 12 plates. Intraplate variability is the mean absorbance (± SD) of control wells (n = 4 per plate) of a representative ELISA assay.

	ELISA signal	
Phage sample	**Intraplate variability (n=4)**	**Interplate variability (n=48)**
AC-GSYWHPQ-CGGGS	0.209 ± 0.056	0.224 ± 0.068
AC-PPTHGRH-CGGGS	0.402 ± 0.058	0.301 ± 0.177
Insertless-M13	0.087 ± 0.013	0.094 ± 0.029

To date 58 of the ~ 200 samples deemed to be high affinity binders have been gene sequenced (sequencing of the remaining phages is underway). **Table 6.3** shows the identity of the displayed peptides, the ratio of ELISA signal achieved and the ELISA plate number in which the colony was identified. Of note, there are a number of peptides that are present within the population in high copy number. In addition, these peptides were identified from different ELISA plates that were analysed on different days indicating the high frequency of the clones is not as a result of any cross contamination.

Table 6.3 Peptide sequences isolated from a cyclic 7-mer library that bind CSD with high affinity.

Plate	Sequence	ELISA signal (peptide-M13:insertless-M13)	Plate	Sequence	ELISA signal (peptide-M13:insertless-M13)
12	EPTFSPY	11.916	11	SLPKPML	6.269
15	GNTPLNG	7.125	4	SLPKPML	6.007
2	HLAVETL	7.218	11	SLPKPML	6.179
11	HLAVETL	7.962	5	SLYEKWD	8.438
4	HLAVETL	8.898	5	SLYEKWD	7.219
2	IPSWWHL	6.540	1	SLYEKWD	7.490
6	LHSNSVT	7.1971	1	SLYEKWD	7.704
3	LMWPQSV	9.810	11	SLYEKWD	6.115
10	LPVDLYQ	8.801	5	SPNPNAL	7.145
4	MSTFWVV	6.944	5	SPNPNAL	6.479
5	MTLNAQN	7.125	5	SPNPNAL	9.441
6	NAGKAPP	4.853	5	STIAWHH	8.889
5	NAGKAPP	6.707	5	SVTASLQ	7.434
5	PHTPTLT	6.626	10	SVTASLQ	9.828
2	PHTPTLT	6.368	5	SVTASLQ	6.667
5	PHTPTLT	6.069	5	SVTASLQ	6.316
10	PPFDLGH	10.071	10	TNHGLGL	6.532
4	PPFDLGH	7.591	10	TNHGLGL	8.165
1	PPFDLGH	6.061	10	VGPYDHR	6.674
4	PSVNLLT	6.812	10	VINSLHH	7.903
10	PSVNLLT	7.453	10	VINSLHH	6.577
5	PSVNLLT	8.539	10	VINSLHH	6.082
1	PSVNLLT	6.061	5	VINSLHH	7.556
10	PSVNLLT	6.494	6	VINSLHH	7.602
7	PSVNLLT	6.234	5	VINSLHH	6.633
6	QAAAHIW	9.442	12	VINSLHH	6.438
10	QAAAHIW	7.236	10	VINSLHH	7.693
5	RAPLPSF	6.343	1	VINSLHH	6.010
3	RAPLPSF	6.524	3	VNLLTWG	8.365

Table 6.4 shows the frequency of the recovered peptides, the mean ELISA signal ratio of peptide-M13 to insertless-M13 and the number of separate plates the clone was identified on. The most common peptide-phage, VINSLHH, was observed with a frequency of 15.5 % and a mean ELISA ratio of 7.1 ± 0.7. Whilst sequencing of a selection of phages that were deemed to be poor (ratio < 3) or moderate (ratio 3-6) binders of CSD remains to be completed, the small variability in ELISA signal between multiple copies of

the same peptide (in most cases < 10%) suggests that these high frequency clones will not be present amongst the poor to moderate binding clones.

Table 6.4 Frequency and mean ELISA ratio for high affinity CSD binding phages.

Sequence	Frequency within the 58 sequenced	ELISA Mean ratio peptide-M13:insertless-M13	Number of plates clone identified on
VINSLHH	9 (15.5%)	7.1 ± 0.7	5
PSVNLLT	6 (10.3%)	7.0 ± 1.0	5
SLYEKWD	5 (8.6%)	7.4 ± 0.8	3
SVTASLQ	4 (6.9%)	7.6 ± 1.6	2
HLAVETL	3 (5.2%)	8.0 ± 0.8	3
PHTPTLT	3 (5.2%)	6.4 ± 0.3	2
PPFDLGH	3 (5.2%)	7.9 ± 2.0	3
SLPKPML	3 (5.2%)	6.2 ± 0.1	2
SPNPNAL	3 (5.2%)	7.7 ± 1.6	1
NAGKAPP	2 (3.4%)	6.8 ± 0.1	2
QAAAHIW	2 (3.4%)	8.3 ± 1.6	2
RAPLPSF	2 (3.4%)	6.4 ± 0.1	2
TNHGLGL	2 (3.4%)	7.3 ± 1.2	1
EPTFSPY	1 (1.7%)	11.9	1
GNTPLNG	1 (1.7%)	7.1	1
IPSWWHL	1 (1.7%)	6.5	1
LHSNSVT	1 (1.7%)	7.2	1
LMWPQSV	1 (1.7%)	9.8	1
LPVDLYQ	1 (1.7%)	8.8	1
MSTFWVV	1 (1.7%)	6.9	1
MTLNAQN	1 (1.7%)	7.1	1
STIAWHH	1 (1.7%)	8.9	1
VGPYDHR	1 (1.7%)	6.7	1
VNLLTWG	1 (1.7%)	8.4	1

6.5 Discussion

The experiments and results described in this chapter represent the foundation of a program of work to identify peptides that bind caveolin-1 scaffolding domain with high affinity. The program has as its ultimate aim, the development of small molecule peptidomimetics that interact with CSD to interfere with the functioning of caveolin-1. As discussed within the introduction to this chapter, such molecules will represent a novel therapeutic approach in the treatment of disease states where over-expression of caveolin-1 dysregulates signaling pathways resulting in

pathobiological processes. The studies in this chapter represent the very early stages of this program of work and therefore this discussion will focus on future works needed to progress the program.

Cyclic 7mer libraries exposed to caveolin-1 CSD showed increasing affinity for target with progressive rounds of panning until this affinity plateaued in round 3. A cyclic library was chosen because, in comparison to linear peptides, cyclic peptides that have a more constrained secondary structure not only interact with target with higher affinity but are also potentially easier structures from which to design small molecule peptidomimetics.

High-throughput ELISA studies were able to discriminate between peptide-phage clones that bound CSD-biotin with poor, moderate or high affinity at least in comparison to insertless phages. In the panning studies, CSD was attached to biotin and so in the next stage of work those clones identified to bind CSD with high affinity will be examined to ensure that they do not bind biotin and that they bind to CSD in the absence of biotin. A preliminary study using an amplified pool of cyclic 7mer phages from glycine elution 3 of panning round 3 gave an ELISA signal against CSD of 0.221 ± 0.040 versus 0.149 ± 0.027 for insertless phages which indicates minimal binding within the population to biotin. In addition, the peptides so far identified do not match the generic sequence of peptides that bind biotin (CXWXPPF(K/R)XXC)[32]. Whilst this does not necessarily preclude certain clones within the library binding biotin the high affinity binders would be unexpected to do so. This is because biotin must fit some 9Å

inside the streptavidin molecule to access its binding site. In panning studies, any phages interacting with biotin would likely have been displaced when the streptavidin magnespheres were exposed to CSD-biotin (the binding affinity for biotin to streptavidin (kD ~ 10^{-15}M) will not be competed by phage peptides) and therefore subsequently removed during washing stages. In addition in the ELISA studies where CSD-biotin was pre-imobilised before exposure to phage, the biotin should be already 'hidden' and unavailable for interaction.

Once it has been definitively confirmed that the phages do not bind biotin, a series of cell free assays will be undertaken to determine if the peptide phages selected can prevent CSD mediated inhibition of PKC; Oka and co-workers[33] have shown that CSD from both caveolin-1 and -3 inhibit the kinase activity and autophosphorylation of PKCα in cell free assays. In addition, given the importance of caveolin-1 oligomerisation (through CSD) a series of studies will be undertaken to assess whether identified peptides can inhibit oligomerisation. The primary technique that will be used is circular dichroism spectroscopy[34], a technology for measuring differential absorption of left- and right- handed circularly polarized light, that gives information about protein secondary structure and oligomerisation state[35-37].

Subsequently, a measure of the affinity of the peptides for CSD will be made (without the phages on board) using techniques such as surface plasmon resonance[38] and quartz crystal microbalances[39]. Studies have shown

that the affinities of peptides identified from phage display for target are typically in the order of 10 – 100 μM[40-42]. This can be improved by screening focused libraries i.e. phage libraries that contain homologs of the originally identified binding peptide[43]. However, construction of a focused library is time consuming and relatively inefficient. Given that the structure of CSD is known and can therefore be modeled *in-silico*, the next stage of the work will be to use computational design models to modulate the peptide-CSD interaction to improve affinity. There is already some in-house experience with *in-silico* molecular modeling of peptides which was used to explore the interaction of a 4-AAP binding peptide (identified in chapter 2) with 4-AAP[44]. Improvements in affinity in the *in-silico* environment will be translated to the laboratory bench following synthesis of designed peptides. These peptides will have utility in their own right but the complex issues that surround the *in-vivo* administration of peptides will predicate the design of small molecule mimics of the peptides; discussions with potential collaborators are already underway to explore the feasibility of such an approach.

In summary, the studies conducted in this chapter have provided some exciting and encouraging data that suggest a number of peptides have been identified which bind the caveolin scaffolding domain. Ongoing studies are seeking to characterize the capacity of these peptides to modulate the function of CSD. Such peptides and small molecular peptidomimetics designed from them may have utility as novel therapeutics in glioblastoma

multiforme and other disease states where over-expression of the caveolins has a negative effect on human health.

Reference List

1. Anderson, R.G., *The caveolae membrane system.* Annu Rev Biochem, 1998. **67**: p. 199-225.

2. Lajoie, P., et al., *Lattices, rafts, and scaffolds: domain regulation of receptor signaling at the plasma membrane.* J Cell Biol, 2009. **185**(3): p. 381-5.

3. Campbell, L., M. Gumbleton, and K. Ritchie, *Caveolae and the caveolins in human disease.* Adv Drug Deliv Rev, 2001. **49**(3): p. 325-35.

4. Goetz, J.G., et al., *Caveolin-1 in tumor progression: the good, the bad and the ugly.* Cancer Metastasis Rev, 2008. **27**(4): p. 715-35.

5. Burgermeister, E., et al., *Caveats of caveolin-1 in cancer progression.* Cancer Lett, 2008. **268**(2): p. 187-201.

6. Cohen, A.W., et al., *Role of caveolin and caveolae in insulin signaling and diabetes.* Am J Physiol Endocrinol Metab, 2003. **285**(6): p. E1151-60.

7. Galbiati, F., B. Razani, and M.P. Lisanti, *Caveolae and caveolin-3 in muscular dystrophy.* Trends Mol Med, 2001. **7**(10): p. 435-41.

8. Mohammadi, M.S., et al., *Possible mechanisms involved in the discrepancy of hepatic and aortic endothelial nitric oxide synthases during the development of cirrhosis in rats.* Liver Int, 2009. **29**(5): p. 692-700.

9. Gosens, R., et al., *Caveolae and caveolins in the respiratory system.* Curr Mol Med, 2008. **8**(8): p. 741-53.

10. Frank, P.G., S. Pavlides, and M.P. Lisanti, *Caveolae and transcytosis in endothelial cells: role in atherosclerosis.* Cell Tissue Res, 2009. **335**(1): p. 41-7.

11. Frank, P.G. and M.P. Lisanti, *Caveolin-1 and caveolae in atherosclerosis: differential roles in fatty streak formation and neointimal hyperplasia.* Curr Opin Lipidol, 2004. **15**(5): p. 523-9.

12. Gaudreault, S.B., D. Dea, and J. Poirier, *Increased caveolin-1 expression in Alzheimer's disease brain.* Neurobiol Aging, 2004. **25**(6): p. 753-9.

13. Benferhat, R., et al., *The immunogenic CBD1 peptide corresponding to the caveolin-1 binding domain in HIV-1 envelope gp41 has the capacity to penetrate the cell membrane and bind caveolin-1.* Mol Immunol, 2008. **45**(7): p. 1963-75.

14. Huang, J.H., et al., *Identification of the HIV-1 gp41 core-binding motif in the scaffolding domain of caveolin-1.* J Biol Chem, 2007. **282**(9): p. 6143-52.

15. Sukumaran, S.K., M.J. Quon, and N.V. Prasadarao, *Escherichia coli K1 internalization via caveolae requires caveolin-1 and protein kinase Calpha interaction in human brain microvascular endothelial cells.* J Biol Chem, 2002. **277**(52): p. 50716-24.

16. Xie, Y., K.J. Kim, and K.S. Kim, *Current concepts on Escherichia coli K1 translocation of the blood-brain barrier.* FEMS Immunol Med Microbiol, 2004. **42**(3): p. 271-9.

17. Stuart, E.S., W.C. Webley, and L.C. Norkin, *Lipid rafts, caveolae, caveolin-1, and entry by Chlamydiae into host cells.* Exp Cell Res, 2003. **287**(1): p. 67-78.

18. Smith, J.L., S.K. Campos, and M.A. Ozbun, *Human papillomavirus type 31 uses a caveolin 1- and dynamin 2-mediated entry pathway for infection of human keratinocytes.* J Virol, 2007. **81**(18): p. 9922-31.

19. Smith, J.L., et al., *Caveolin-1-dependent infectious entry of human papillomavirus type 31 in human keratinocytes proceeds to the endosomal pathway for pH-dependent uncoating.* J Virol, 2008. **82**(19): p. 9505-12.

20. Michel, V. and M. Bakovic, *Lipid rafts in health and disease.* Biol Cell, 2007. **99**(3): p. 129-40.

21. Li, S., et al., *Evidence for a regulated interaction between heterotrimeric G proteins and caveolin.* J Biol Chem, 1995. **270**(26): p. 15693-701.

22. Razani, B., S.E. Woodman, and M.P. Lisanti, *Caveolae: from cell biology to animal physiology.* Pharmacol Rev, 2002. **54**(3): p. 431-67.

23. Williams, T.M. and M.P. Lisanti, *The caveolin proteins.* Genome Biol, 2004. **5**(3): p. 214.

24. Couet, J., et al., *Identification of peptide and protein ligands for the caveolin-scaffolding domain. Implications for the interaction of caveolin with caveolae-associated proteins.* J Biol Chem, 1997. **272**(10): p. 6525-33.

25. Levin, A.M., et al., *Double barrel shotgun scanning of the caveolin-1 scaffolding domain.* ACS Chem Biol, 2007. **2**(7): p. 493-500.

26. Levin, A.M., et al., *Exploring the interaction between the protein kinase A catalytic subunit and caveolin-1 scaffolding domain with shotgun scanning, oligomer complementation, NMR, and docking.* Protein Sci, 2006. **15**(3): p. 478-86.

27. Bucci, M., et al., *In vivo delivery of the caveolin-1 scaffolding domain inhibits nitric oxide synthesis and reduces inflammation.* Nat Med, 2000. **6**(12): p. 1362-7.

28. Kim, K.J., et al., *The K1 capsule modulates trafficking of E. coli-containing vacuoles and enhances intracellular bacterial survival in human brain microvascular endothelial cells.* Cell Microbiol, 2003. **5**(4): p. 245-52.

29. Wang, Y. and K.S. Kim, *Role of OmpA and IbeB in Escherichia coli K1 invasion of brain microvascular endothelial cells in vitro and in vivo.* Pediatr Res, 2002. **51**(5): p. 559-63.

30. Huang, S.H., M.F. Stins, and K.S. Kim, *Bacterial penetration across the blood-brain barrier during the development of neonatal meningitis.* Microbes Infect, 2000. **2**(10): p. 1237-44.

31. Maruvada, R., Y. Argon, and N.V. Prasadarao, *Escherichia coli interaction with human brain microvascular endothelial cells induces signal transducer and activator of transcription 3 association with the C-terminal domain of Ec-gp96, the outer membrane protein A receptor for invasion.* Cell Microbiol, 2008. **10**(11): p. 2326-38.

32. Saggio, I. and R. Laufer, *Biotin binders selected from a random peptide library expressed on phage.* Biochem J, 1993. **293 (Pt 3)**: p. 613-6.

33. Oka, N., et al., *Caveolin interaction with protein kinase C. Isoenzyme-dependent regulation of kinase activity by the caveolin scaffolding domain peptide.* J Biol Chem, 1997. **272**(52): p. 33416-21.

34. Whitmore, L. and B.A. Wallace, *Protein secondary structure analyses from circular dichroism spectroscopy: methods and reference databases.* Biopolymers, 2008. **89**(5): p. 392-400.

35. Edgcomb, S.P., et al., *Protein structure and oligomerization are important for the formation of export-competent HIV-1 Rev-RRE complexes.* Protein Sci, 2008. **17**(3): p. 420-30.

36. Natalello, A., et al., *Role of flavin mononucleotide in the thermostability and oligomerization of Escherichia coli stress-defense protein WrbA.* Biochemistry, 2007. **46**(2): p. 543-53.

37. Rajan, S., C. Horn, and E.C. Abraham, *Effect of oxidation of alphaA- and alphaB-crystallins on their structure, oligomerization and chaperone function.* Mol Cell Biochem, 2006. **288**(1-2): p. 125-34.

38. Piliarik, M., H. Vaisocherova, and J. Homola, *Surface plasmon resonance biosensing.* Methods Mol Biol, 2009. **503**: p. 65-88.

39. Dixon, M.C., *Quartz crystal microbalance with dissipation monitoring: enabling real-time characterization of biological materials and their interactions.* J Biomol Tech, 2008. **19**(3): p. 151-8.

40. Katz, B.A. and R.T. Cass, *In crystals of complexes of streptavidin with peptide ligands containing the HPQ sequence the pKa of the peptide histidine is less than 3.0.* J Biol Chem, 1997. **272**(20): p. 13220-8.

41. Hao, J., et al., *Identification and rational redesign of peptide ligands to CRIP1, a novel biomarker for cancers.* PLoS Comput Biol, 2008. **4**(8): p. e1000138.

42. Sato, A.K., et al., *Development of mammalian serum albumin affinity purification media by peptide phage display.* Biotechnol Prog, 2002. **18**(2): p. 182-92.

43. Pal, G., et al., *Alternative views of functional protein binding epitopes obtained by combinatorial shotgun scanning mutagenesis.* Protein Sci, 2005. **14**(9): p. 2405-13.

44. Smith, M.W., et al., *Phage display identification of functional binding peptides against 4-acetamidophenol (Paracetamol): an exemplified approach to target low molecular weight organic molecules.* Biochem Biophys Res Commun, 2007. **358**(1): p. 285-91.

Chapter 7 General discussion

The incidence of central nervous system disorders is steadily rising and now represents a major component of overall healthcare spend. This is largely a result of rapidly increasing life expectancies in industrialised countries that have resulted in ageing populations. For example it is estimated that by 2050 approximately 20% of the US population will be 65 or over[1]. Given that age remains the most significant non-genetic risk factor contributing to CNS disorders, and that improvements in diagnostic techniques coupled with growing coverage within the media have resulted in greater awareness of CNS disorders amongst the public, there is a growing pressure to deliver new therapeutics to the market.

The pharmaceutical industry recognises the potential for market growth in the treatment of CNS disorders; in 2005 fifteen pharmaceutical companies generated CNS sales in excess of $1 billion and this is forecast to rise in the next five years[2]. However, the global market for CNS-related therapies is dominated by the development of 'me too' small molecule drugs for the treatment of depression (30% market share)[2]. Whilst the development of new classes of anti-depressants is lucrative it does not address the pressing need to develop novel therapeutics for the treatment of complex CNS disorders such as neurodegenerative disorders, neuroAIDS and brain cancers. The slow adaptation of the pharmaceutical industry to the development of new therapeutics for such diseases is partly as a result of the failure rate for CNS drugs in development to reach the clinic. Whilst US statistics show that approximately 11% of drugs that enter clinical trials

reach the market, for CNS therapeutics it is only 3-4% and therefore by extension CNS drugs are far more costly to develop[3].

The high failure rate in clinical trials of new therapies for CNS disorders is as a consequence of many factors but particularly the relative failure to forecast the extent of transport of drug across the BBB into the brain[4] as well as the paucity of predictive animal models for complex CNS disorders such as Alzheimer's disease, brain cancers or neuroAIDs where there is no single dominant mechanism for disease[5]. As such it is difficult to interpret the value of translational research from cell model to animal model to human. For example it may be some time before a consensus is reached as to whether therapies that reduce amyloid plaque formation outperform therapies that stimulate neurotransmitter function in Alzheimer's disease[6].

It is fair to assume that the treatment of complex CNS disorders will benefit from a shift in focus from small molecule therapies to biomacromolecules that include peptides, proteins, antibodies, enzymes and genes. It is unfortunate then that many biomacromolecules displaying promising therapeutic effects *in-vitro* all too often prove ineffective when administered to animals or humans. This is often due to the limiting nature of the blood-brain barrier, which effectively excludes any molecule that is not small and lipophilic, i.e. the very antithesis of a biomacromolecule.

The development of new CNS therapies can essentially be simplified to three issues: (i) identifying a druggable target within a CNS disorder that drives disease; (ii) identifying biomacromolecules that functionally interact with the druggable target to elicit a therapeutic effect; and (iii) designing strategies to enhance the penetration of such biomacromolecules into the CNS.

Recent methodological advances in areas such as gene microarrays, immuno-histochemical analyses and transgenic animals have afforded the molecular dissection of various disease pathways leading to the identification of new druggable targets in a host of CNS disorders. In addition there has been a maturation in polypeptide display systems that afford rapid identification of peptides, proteins, antibodies and enzymes that interact with molecular targets. A range of strategies have also been proposed to enhance the delivery of novel biomacromolecules to the brain including peptidergic[7] and proteinergic[8] delivery vectors that mediate traversal of macromolecules across the blood brain barrier. Phage display is a powerful combinatorial technology that affords the selection of peptides that bind to a target of interest and may therefore have application in the discovery of novel peptidergic therapies and delivery vectors within the field of brain disorders. As a consequence, the research conducted in this thesis has been focused on exploiting phage display for the discovery of peptides that will have utility within experimental therapeutics of brain disorders.

Having no in-house experience of phage display, Chapter 2 detailed the validation of a cyclic 7-mer library against two molecules, streptavidin and paracetamol (4-AAP); the selection of these molecules was carefully considered. Streptavidin, a large macromolecule (~ 53 KDa), has been extensively probed with peptide phage libraries and there is a clear consensus in the literature that peptides containing a HPQ tripeptide motif bind with high affinity within the biotin-binding pocket of the streptavidin molecule[9-11]. In-house selection experiments against streptavidin coated on either magnetic beads or on a plastic surface yielded a series of peptide sequences that contained the HPQ motif. As evidenced by ELISA assay, these peptide phages bound with high affinity to Streptavidin. Separate experiments against streptavidin immobilised on different solid supports resulted in the selection of a common series of peptides and demonstrated robustness in the selection technique.

4-AAP, a low molecular weight entity, was selected for its simplicity and because it has two structural isomers that differ from the parent molecule only by the orientation of the hydroxyl group around the benzene ring. 4-AAP has a very limited number of functional groups and it was therefore used as a proof of principle to examine if a phage library could identify peptides that interact with such a simple molecule. Immobilisation of 4-AAP to a solid support through one of its limited functional groups would reduce the number of points for peptide interaction and therefore a strategy of selecting phages against insoluble complexes of the molecule

was devised. Whilst such complexes will present a heterogeneous surface, all the functional groups should be on display and available for interaction.

A peptide phage displaying sequence AC-**NPNNLSH**-CGGGS was identified to bind 4-AAP. In a peptide sequence-dependant manner AC-**NPNNLSH**-CGGGS phages were able to prevent the *in-vitro* hepatotoxicity of 4-AAP but not its isomer 3-AAP. In addition, the peptide phage reduced by ~ 20% the permeability of 4-AAP across a semi-permeable membrane. Since the publication of this work[12], the methodology of selecting against insoluble complexes has been repeated by Yu and co-workers to identify peptides that bind dexamethasone[13]. Whilst this strategy of selecting against insoluble complexes may not prove applicable to a wide range of molecules, peptides that bind low molecular weight entities should have utility in biological and environmental sensing applications and as therapeutics in their own right.

The increasing emphasis on early consideration of issues surrounding the delivery of candidate drug molecules to the brain within CNS drug discovery programs would benefit from the availability of robust *in-vitro* models of the *in-situ* blood brain barrier. This would complement investigations of *in-vivo* drug transport and predictions based on *in-silico* assessments of physico-chemical properties of candidate molecules[14-16]. Given the unique phenotype of BBB endothelia, it is somewhat of an anachronism then that the pharmaceutical industry rely on cell models that are neither cerebral in origin nor are endothelial in nature. It is true that

considerable experience has been obtained in translating data garnered from epithelial cell lines (e.g. MDCK) to predict *in-vivo* brain uptake, but epithelial cell lines of non-cerebral origin cannot account for the unique cellular architecture, transport-, metabolic- and receptor- systems on brain endothelia. A better model would more closely resemble the *in-vivo* phenotype and would therefore provide a system in which to study quantitative permeation as well as mechanistic aspects of BBB transport and pathobiological processes.

A number of immortalised brain capillary endothelial cells lines have been developed both commercially and within academic laboratories (recently reviewed in [4, 16]) but so far these models have failed to generate a sufficiently restrictive paracellular architecture and therefore their value in high-throughput permeability screens of candidate molecules is limited. In contrast, primary or 1st passage cultures of freshly isolated brain microvasculature appear to retain many of the morphological and biochemical properties of the *in-vivo* phenotype. In chapter 3 the development and characterisation of a primary porcine brain microvascular capillary endothelia cell model was described. A porcine model was developed because of the limited availability and ethical constraints associated with using human brain tissue and regulatory restrictions on the use of bovine material that has accompanied the emergence of BSE. Attempts to establish a restrictive primary rat model were complicated by issues surrounding low cell yield and culture purity.

In common with studies cited in the literature[17-19], introduction of puromycin into culture medium increased purity for rat endothelial cells however, monolayers failed to present a paracellular barrier that was significantly more restrictive than immortalised rat models. Nevertheless the primary rat model presented may still be of value in mechanistic uptake studies at the BBB.

The development of the porcine model, based on the methods of Galla[20], was more successful. Micrographs of confluent monolayers of PBMVECs revealed the cells adopt a spindle-like, squamous and attenuated phenotype that is consistent with endothelial microvasculature. Ultrastructural examination using T.E.M. revealed the presence of tight-junctional complexes at cell margins and vesicular structures consistent with caveolae and clathrin coated pits; on a subjective basis caveolae were more abundant. Primary cultures of PBMVECs were responsive to astrocyte factors as demonstrated by up-regulation in alkaline phosphatase activity when monolayers were co-cultured with the astroglioma cell line C6. Whilst C6 are commonly used in co-culture systems to improve paracellular restrictiveness it would be interesting to explore the effect of primary porcine astrocytes on the model. This would provide an isogenic model that may better represent the *in-vivo* BBB.

Monolayers of PBMVECs generated a restrictive barrier to solute permeability and discriminated between the permeability of transcellular and paracellular probes. In common with reports in the literature[21-27],

the restrictiveness of the model was significantly improved by exposure to astrocytic factors either in the form of astrocyte conditioned medium or astrocyte co-culture, with the co-culture resulting in the greatest restrictiveness. Paracellular restrictiveness was improved by a 'switch' procedure that involved withdrawal of serum from the cultures for a period of 24 hours prior to the permeability study and supplementation with physiological concentrations of hydrocortisone[28] and cAMP modulators[29, 30]. The final model which comprised astrocyte co-culture and the 'switch' procedure resulted in a sucrose paracellular permeability co-efficient of ~ 7.5 x 10^{-6} $cm.s^{-1}$. This is significantly more restrictive than immortalised brain microvascular models.

Expression of mRNA transcripts was confirmed for a number of key tight junctional elements (ZO-1, occludin, claudin-1 and claudin 5) and a series of transporters known to be expressed at the BBB including the multi-drug efflux transporter P-glycoprotein (P-gp) that presents a significant obstacle to the treatment of many CNS disorders[31-33]. Following confirmation of P-gp expression at the protein level using Western analysis, functional expression was determined. In accumulation-retention assays, the P-gp substrate rhodamine-123 was retained by PBMVECs around 7-fold greater in the presence of the P-gp inhibitor verapamil.

Issues that have prevented adoption of primary BBB models within industry include the time and technical resources required for model development, batch to batch variability and material wastage when only

limited amounts of the isolated material are required for planned studies. Characterisation of the PBMVEC model has demonstrated that batch-to-batch variability is negligible and efforts to cryopreserve the cells were successful with little loss in paracellular restrictiveness when cells were recovered from frozen after 1 year.

At the end of chapter 3, the PBMVEC model along with immortalised mouse (bEnd3) and rat (RBE4) BBB models were used in phage selection studies for the identification of peptides that bind brain microvasculature. A series of studies was undertaken with the phage library exposed to confluent monolayers of BBB cultures maintained at 4°C throughout the experiment to prevent internalisation of the phages; the intent of the studies was to identify a series of peptides that increase residency time at the BBB. Discovering a peptide vector that specifically effects transcytosis at the BBB is a major and unmet challenge and it was hypothesised that it may prove easier to increase the local concentration of a drug at the brain by identifying a peptide that essentially 'sticks' to brain microvasculature. This was corroborated by the significant transmigration of insertless phages across confluent BBB monolayers within 5 minutes of phage exposure suggesting that *in-vitro* monolayers are less than ideal for identifying peptides that mediate transvascular transport of cargo across the BBB, an aim probably best accomplished through the use of *in-vivo* phage panning experiments against brain tissue. Nevertheless, peptides that increase the exposure of brain microvasculature to a cargo through binding to the

luminal surface of brain microvasculature should be effective in increasing the brain concentrations of the respective cargo even when BBB permeability to the cargo is relatively poor. However, the *in-vitro* phage studies did not result in the occurrence of a common peptide or conserved motif within any of the panning results from the brain microvascular cell lines examined and ELISA studies, used to monitor the binding of the selected phages to cell monolayers suggested a failure to identify 'true' binders to the luminal surface of the brain microvascular cells. However, a peptide was identified in the panning studies against the bEND3 monolayers with sequence of AC-**NTSVSKW**-CGGGS. This sequence shares significant homology with a region of the V3 loop of HIV GP120 glycoprotein (NISVSKW). Deletion and mutational analyses have yet to be undertaken to elucidate the exact region of GP120 that interacts with the brain microvascular surface but William Banks has shown that the uptake of free HIV virus at the BBB is mediated by GP120 probably by stimulating adsorptive endocytosis[34-37]. Of note this uptake is not CD4-dependant and ignores species barriers. The isoelectric point (pI = 10.1) of the peptide identified in panning experiments against bEnd3, AC-**NTSVSKW**-CGGGS, indicates the peptide to be cationic and would therefore be expected to interact with cell surfaces. However, an *in-vivo* single clone pharmacokinetic study to assess the brain uptake of phages displaying AC-**NTSVSKW**-CGGGS revealed that it does not enhance brain uptake to any greater extent beyond insertless phage.

Chapter 4 describes experiments to select peptides that mediate traversal of phages across the *in-vivo* BBB. The BBB has been shown to effectively exclude phages from the brain and therefore any phages recovered from brain parenchyma would be assumed to arrive there as a result of the displayed peptide. In two separate strategies rats were intravenously administered phage library followed by a series of perfusions to remove circulating phages and phages bound to the vasculature. In the first strategy only phages from the brain were recovered for iterative panning rounds. In the second strategy phages were recovered from all the major organs and pooled to serve as input in subsequent panning rounds. After sequencing an extensive selection of phages associated with brain grey matter from the final round of each of the above described strategies, a number of peptides were identified in the population in high copy number, notably AC-**PDVPHPA**-CGGGS from strategy 1 and AC-**SYTSSTM**-CGGS and AC-**SNTSSTT**-CGGGS from strategy 2. Of note both AC-**PDVPHPA**-CGGGS and AC-**SYTSSTM**-CGGS were also associated with brain capillary fractions. Analysis of the amino acid distributions amongst all the peptides sequenced (~ 600 peptides sequenced) suggested that serine at positions 1, 4 and 5 may be important for brain penetration. Extensive single phage clone *in-vivo* distribution studies revealed that the peptide sequence AC-**SYTSSTM**-CGGS enhanced the partitioning of phages into the brain by approximately 4-fold (as evidenced by measures of total brain AUC). An absence of basic residues and an isoelectric point of 5.9 indicates AC-**SYTSSTM**-CGGS would not be expected to stimulate adsorptive endocytosis like the cell

penetrating peptides. In a departure from other studies that have looked at peptide uptake into the brain the studies detailed in this chapter only assessed phages associated with grey matter and not whole brain. This is important since estimates suggest only a small fraction of material that reaches the brain is associated with brain parenchyma (~ 5 - 10%)[38]. Significant work remains to be undertaken to elucidate the nature of the interaction of this peptide with the BBB.

To contextualise the extent of brain uptake of AC-**SYTSSTM**-CGGGS a series of physiologically based pharmacokinetic simulations were undertaken. The simulations highlighted some of the errors that can occur when comparing treatments with respect to concentrations in a single tissue at one particular timepoint. Currently it is more common to report the difference in tissue concentration at some arbitrary time-point. Whilst this can give the impression that a significant enhancement in uptake has occurred, researchers need to make comparisons with respect to total AUC in the tissue of interest.

Chapter 5 examined the role of caveolin-1 in glioblastoma and hence the validity of targeting caveolin-1 for treatment of this aggressive brain tumour type. These studies served as a forerunner to the use of phage-based strategies for the discovery and development of novel peptides that interact with caveolin-1 scaffolding domain, the main functional component of the caveolin-1 protein, and ultimately serve to inhibit function. To date the exact role of caveolin-1 in glioma is uncertain since several independent

clinical studies correlate positive caveolin-1 expression with aggressive disease whilst the limited *in-vitro* studies conducted in glioma cell lines are equivocal on a role for caveolin-1. In chapter 5 caveolin-1 siRNA was used to downregulate caveolin-1 and led to reduced glioma cell growth and invasion. For the first time caveolin-1 was shown to serve as a tumour promoter in *in-vitro* models of glioma driving two fundamentally important parameters of tumorigenesis, that of cellular proliferation and invasion.

Therefore caveolin-1 was identified as a novel drug target for gliomas and whose inhibition may serve to invoke treatment responses or at the very least limit disease progression. Such achievements would significantly increase the poor median survival rates that currently are under 1 year from the point of diagnosis[39]. Gliomas are traditionally highly resistant to chemo- and radio- therapies, especially upon recurrence after surgical resection. Hence an anti-caveolin-1 peptide or small molecule peptide mimetic would represent a novel addition to traditional treatments. Further, for reasons of pathobiology it is envisaged that an anti-caveolin molecule may actually serve to restore sensitivity to the standard chemo- and radio- therapies. For example, in A549 and FuDu cells, a non-small cell lung carcinoma cell line and a squamous head/neck cancer cell line respectively, ionizing radiation is shown to invoke src kinase stabilisation, activation and phosphorylation of caveolin-1. This results in the caveolin-1-mediated nuclear transport of EGF-R, DNA-PK activation and subsequent repair of DNA damage [40]. Additional lines of evidence that support a role

for caveolin-1 in DNA repair in glioma following chemo- or radio- therapy include (i) the critical function of EGFRvIII and DNA-PK in glioma cell lines[41] and (ii) caveolin-1 knockout mice are less resistant to whole body gamma radiation than their caveolin-1 positive wild type counterparts [42] and (iii) caveolin-1 has very recently been shown to mediate radio-resistance of pancreatic cancer cells in 3D cell models with increases in double stranded DNA breaks reported in cancer cells following caveolin-1 knockdown [43]. Further, glioma is one of the most highly vascularised forms of solid tumours and as such has been the subject of intense focus for anti-angiogenic therapies [39, 44, 45]. Considerable evidence exits for the role of caveolin-1 in mediating tumour blood vessel formation. Correlative evidence from clinical samples indicate that caveolin-1 mediates angiogenesis in RCC[46], prostate cancer[47] and meningiomas [48]. Therefore it is highly likely that an anti-caveolin-1 molecule would exhibit anti-angiogenic properties in glioblastoma. In summary this chapter presents caveolin-1 as a novel drug target in glioblastoma and suggests that an anti-caveolin-1 molecule could inhibit multiple processes of glioma pathology, namely (i) proliferation (ii) invasion (iii) angiogenesis and (iv) chemo- and radio- resistance.

Having identified caveolin-1 as a potential therapeutic target in glioblastoma, chapter 6 details phage display selections to identify peptides that interact with the caveolin scaffolding domain. Phage libraries were exposed to caveolin-scaffolding domain that had a biotin tag attached.

Subsequently, phage-CSD-biotin complexes were captured on streptavidin coated magnetic beads that were washed and the phages recovered using low pH washes. Increasing phage titers in iterative panning rounds indicated enrichment of a CSD binding population. Examination of the binding of over 1000 individual phage clones to CSD using ELISA indicated around 20% of the population bound with high affinity (> 6-fold ratio of peptide phage ELISA signal compared to insertless phage ELISA signal). Sequencing of a subset of these phages revealed a number of common peptides notably AC-**VINSLHH**-CGGS (15% of the high affinity population), AC-**SLYEKWD**-CGGGS and AC-**PSVNLLT**-CGGGS (both 9% of the high affinity population). These peptides are currently undergoing further analysis in cell free assays to determine if they can prevent the caveolin-1 mediated inhibition of PKCα phosphorylation. It is hoped that these peptides will serve as a starting point for the rational design of small molecule anti-caveolin-1 therapies. This strategy is not without precedent. In many cancers, over-expression of MDM2 blocks p53 tumour suppressor activity by binding p53 at its transactivation domain[49]. X-ray crystallography of the MDM2-p53 complex revealed MDM2 interacts with a hydrophobic cleft on p53 through just three side chains of the helical region of p53 (Phe19, Leu26, and Trp23). Following high throughput chemical library screening and rational design, a series of *cis*-imidazoline analogues were developed called Nutilins that bind MDM2[50]. X-ray crystallography studies revealed that the Nutilins bind MDM2 by mimicking the helical region of the hydrophobic cleft of p53. Displacement of p53 from MDM2

increase p53 activity resulting in reduced proliferation and enhanced apoptosis in a range of cancers[50, 51].

In conclusion the results described in this thesis have explored issues surrounding the characterisation of druggable targets within brain disorders and the discovery of peptides that either interact with a druggable target or have utility as delivery vectors to mediate the traversal of biologics across the BBB. The work presented had ambitious aims and was intellectually stimulating. It has made a contribution towards a greater understanding of how over-expression of caveolin-1 increases the proliferation and invasiveness of gliomas. The *in-vitro* BBB cell model developed has been successfully commercialised and hopefully will find utility in the hands of other researchers in addressing health issues surrounding the brain. A peptide was identified that modestly increases the uptake of phages into the brain in a sequence specific manner and provides a foundation for further mechanistic studies to address how it enhances uptake. Such a peptide may find utility in the delivery of therapeutic cargos to the brain. Finally, a series of peptides were identified that appear to bind caveolin-1 scaffolding domain with high affinity. These peptides are currently being further characterised and there is significant expectation that they will be useful in developing anti-caveolin-1 therapeutics.

Reference List

1. Wiener, J.M. and J. Tilly, *Population ageing in the United States of America: implications for public programmes.* Int J Epidemiol, 2002. **31**(4): p. 776-81.
2. *CNS Market Trends, 2007 to 2010 : Key Market Forecasts and Growth Opportunities*, U. Publishing, Editor. 2007.
3. Pritchard, J.F., *Risk in CNS drug discovery: focus on treatment of Alzheimer's disease.* BMC Neurosci, 2008. **9 Suppl 3**: p. S1.
4. Gumbleton, M. and K.L. Audus, *Progress and limitations in the use of in vitro cell cultures to serve as a permeability screen for the blood-brain barrier.* J Pharm Sci, 2001. **90**(11): p. 1681-98.
5. Tsaioun, K., M. Bottlaender, and A. Mabondzo, *ADDME - Avoiding Drug Development Mistakes Early: central nervous system drug discovery perspective.* BMC Neurol, 2009. **9 Suppl 1**: p. S1.
6. Sapra, M. and K.Y. Kim, *Anti-amyloid treatments in Alzheimer's disease.* Recent Pat CNS Drug Discov, 2009. **4**(2): p. 143-8.
7. Liu, Y., et al., *Brain-targeting gene delivery and cellular internalization mechanisms for modified rabies virus glycoprotein RVG29 nanoparticles.* Biomaterials, 2009. **30**(25): p. 4195-202.
8. Bickel, U., T. Yoshikawa, and W.M. Pardridge, *Delivery of peptides and proteins through the blood-brain barrier.* Adv Drug Deliv Rev, 2001. **46**(1-3): p. 247-79.
9. Katz, B.A., *Binding to protein targets of peptidic leads discovered by phage display: crystal structures of streptavidin-bound linear and cyclic peptide ligands containing the HPQ sequence.* Biochemistry, 1995. **34**(47): p. 15421-9.
10. Katz, B.A., *Streptavidin-binding and -dimerizing ligands discovered by phage display, topochemistry, and structure-based design.* Biomol Eng, 1999. **16**(1-4): p. 57-65.
11. Katz, B.A. and R.T. Cass, *In crystals of complexes of streptavidin with peptide ligands containing the HPQ sequence the pKa of the peptide histidine is less than 3.0.* J Biol Chem, 1997. **272**(20): p. 13220-8.
12. Smith, M.W., et al., *Phage display identification of functional binding peptides against 4-acetamidophenol (Paracetamol): an exemplified approach to target low molecular weight organic molecules.* Biochem Biophys Res Commun, 2007. **358**(1): p. 285-91.
13. Yu, X., et al., *Screening of phage displayed human liver cDNA library against dexamethasone.* J Pharm Biomed Anal, 2007. **45**(5): p. 701-5.
14. Podlogar, B.L., I. Muegge, and L.J. Brice, *Computational methods to estimate drug development parameters.* Curr Opin Drug Discov Devel, 2001. **4**(1): p. 102-9.

15. Keseru, G.M. and L. Molnar, *High-throughput prediction of blood-brain partitioning: a thermodynamic approach.* J Chem Inf Comput Sci, 2001. **41**(1): p. 120-8.

16. Vastag, M. and G.M. Keseru, *Current in vitro and in silico models of blood-brain barrier penetration: a practical view.* Curr Opin Drug Discov Devel, 2009. **12**(1): p. 115-24.

17. Perriere, N., et al., *A functional in vitro model of rat blood-brain barrier for molecular analysis of efflux transporters.* Brain Res, 2007. **1150**: p. 1-13.

18. Perriere, N., et al., *Puromycin-based purification of rat brain capillary endothelial cell cultures. Effect on the expression of blood-brain barrier-specific properties.* J Neurochem, 2005. **93**(2): p. 279-89.

19. Calabria, A.R., et al., *Puromycin-purified rat brain microvascular endothelial cell cultures exhibit improved barrier properties in response to glucocorticoid induction.* J Neurochem, 2006. **97**(4): p. 922-33.

20. Franke, H., H. Galla, and C.T. Beuckmann, *Primary cultures of brain microvessel endothelial cells: a valid and flexible model to study drug transport through the blood-brain barrier in vitro.* Brain Res Brain Res Protoc, 2000. **5**(3): p. 248-56.

21. Neuhaus, J., W. Risau, and H. Wolburg, *Induction of blood-brain barrier characteristics in bovine brain endothelial cells by rat astroglial cells in transfilter coculture.* Ann N Y Acad Sci, 1991. **633**: p. 578-80.

22. Isobe, I., et al., *Astrocytic contributions to blood-brain barrier (BBB) formation by endothelial cells: a possible use of aortic endothelial cell for in vitro BBB model.* Neurochem Int, 1996. **28**(5-6): p. 523-33.

23. Hayashi, Y., et al., *Induction of various blood-brain barrier properties in non-neural endothelial cells by close apposition to co-cultured astrocytes.* Glia, 1997. **19**(1): p. 13-26.

24. Duport, S., et al., *An in vitro blood-brain barrier model: cocultures between endothelial cells and organotypic brain slice cultures.* Proc Natl Acad Sci U S A, 1998. **95**(4): p. 1840-5.

25. Scism, J.L., et al., *Evaluation of an in vitro coculture model for the blood-brain barrier: comparison of human umbilical vein endothelial cells (ECV304) and rat glioma cells (C6) from two commercial sources.* In Vitro Cell Dev Biol Anim, 1999. **35**(10): p. 580-92.

26. Sobue, K., et al., *Induction of blood-brain barrier properties in immortalized bovine brain endothelial cells by astrocytic factors.* Neurosci Res, 1999. **35**(2): p. 155-64.

27. Tan, K.H., et al., *A comparison of the induction of immortalized endothelial cell impermeability by astrocytes.* Neuroreport, 2001. **12**(7): p. 1329-34.

28. Hoheisel, D., et al., *Hydrocortisone reinforces the blood-brain barrier properties in a serum free cell culture system.* Biochem Biophys Res Commun, 1998. **244**(1): p. 312-6.

29. Rist, R.J., et al., *F-actin cytoskeleton and sucrose permeability of immortalised rat brain microvascular endothelial cell monolayers: effects of cyclic AMP and astrocytic factors.* Brain Res, 1997. **768**(1-2): p. 10-8.

30. Rubin, L.L., et al., *A cell culture model of the blood-brain barrier.* J Cell Biol, 1991. **115**(6): p. 1725-35.

31. Linnet, K. and T.B. Ejsing, *A review on the impact of P-glycoprotein on the penetration of drugs into the brain. Focus on psychotropic drugs.* Eur Neuropsychopharmacol, 2008. **18**(3): p. 157-69.

32. Rapposelli, S., M. Digiacomo, and A. Balsamo, *P-gp transporter and its role in neurodegenerative diseases.* Curr Top Med Chem, 2009. **9**(2): p. 209-17.

33. Ebinger, M. and M. Uhr, *ABC drug transporter at the blood-brain barrier: effects on drug metabolism and drug response.* Eur Arch Psychiatry Clin Neurosci, 2006. **256**(5): p. 294-8.

34. Banks, W.A., et al., *Adsorptive endocytosis of HIV-1gp120 by blood-brain barrier is enhanced by lipopolysaccharide.* Exp Neurol, 1999. **156**(1): p. 165-71.

35. Banks, W.A., A.J. Kastin, and V. Akerstrom, *HIV-1 protein gp120 crosses the blood-brain barrier: role of adsorptive endocytosis.* Life Sci, 1997. **61**(9): p. PL119-25.

36. Banks, W.A., et al., *Transport of human immunodeficiency virus type 1 pseudoviruses across the blood-brain barrier: role of envelope proteins and adsorptive endocytosis.* J Virol, 2001. **75**(10): p. 4681-91.

37. Banks, W.A., V. Akerstrom, and A.J. Kastin, *Adsorptive endocytosis mediates the passage of HIV-1 across the blood-brain barrier: evidence for a post-internalization coreceptor.* J Cell Sci, 1998. **111 (Pt 4)**: p. 533-40.

38. Moos, T. and E.H. Morgan, *Restricted transport of anti-transferrin receptor antibody (OX26) through the blood-brain barrier in the rat.* J Neurochem, 2001. **79**(1): p. 119-29.

39. Marx, G.M., et al., *Phase II study of thalidomide in the treatment of recurrent glioblastoma multiforme.* J Neurooncol, 2001. **54**(1): p. 31-8.

40. Dittmann, K., et al., *Radiation-induced caveolin-1 associated EGFR internalization is linked with nuclear EGFR transport and activation of DNA-PK.* Mol Cancer, 2008. **7**: p. 69.

41. Mukherjee, B., et al., *EGFRvIII and DNA double-strand break repair: a molecular mechanism for radioresistance in glioblastoma.* Cancer Res, 2009. **69**(10): p. 4252-9.

42. Li, J., et al., *Loss of caveolin-1 causes the hyper-proliferation of intestinal crypt stem cells, with increased sensitivity to whole body gamma-radiation.* Cell Cycle, 2005. **4**(12): p. 1817-25.

43. Hehlgans, S., et al., *Caveolin-1 mediated radioresistance of 3D grown pancreatic cancer cells.* Radiother Oncol, 2009.

44. Reardon, D.A., et al., *The emerging role of anti-angiogenic therapy for malignant glioma.* Curr Treat Options Oncol, 2008. **9**(1): p. 1-22.

45. Argyriou, A.A., E. Giannopoulou, and H.P. Kalofonos, *Angiogenesis and anti-angiogenic molecularly targeted therapies in malignant gliomas.* Oncology, 2009. **77**(1): p. 1-11.

46. Joo, H.J., et al., *Increased expression of caveolin-1 and microvessel density correlates with metastasis and poor prognosis in clear cell renal cell carcinoma.* BJU Int, 2004. **93**(3): p. 291-6.

47. Yang, G., et al., *Correlative evidence that prostate cancer cell-derived caveolin-1 mediates angiogenesis.* Hum Pathol, 2007. **38**(11): p. 1688-95.

48. Barresi, V., S. Cerasoli, and G. Tuccari, *Correlative evidence that tumor cell-derived caveolin-1 mediates angiogenesis in meningiomas.* Neuropathology, 2008. **28**(5): p. 472-8.

49. Kussie, P.H., et al., *Structure of the MDM2 oncoprotein bound to the p53 tumor suppressor transactivation domain.* Science, 1996. **274**(5289): p. 948-53.

50. Vassilev, L.T., et al., *In vivo activation of the p53 pathway by small-molecule antagonists of MDM2.* Science, 2004. **303**(5659): p. 844-8.

51. Klein, C. and L.T. Vassilev, *Targeting the p53-MDM2 interaction to treat cancer.* Br J Cancer, 2004. **91**(8): p. 1415-9.

Appendix 1

Methods

Hep3B growth curve

A growth curve study of Hep3B cultures was undertaken to assess growth characteristics and to determine the optimal time to conduct toxicity studies with 4-AAP and its isomers. Hep3B cells were seeded onto a 24 well culture plate at a seeding density of $3x10^4$ cells.cm^{-2}. The plate was incubated at 37°C for 24 hours to allow cells to adhere. Subsequently, at 24 hour intervals for 5 days, four wells were washed 2x with pre-warmed PBS and cell detachment affected by the addition of pre-warmed trypsin/EDTA (200 µl); cell detachment was monitored under an inverted light microscope. When the cells were completely detached, 300 µl of complete media was added to each well to neutralize the trypsin/EDTA. Two 20 µl aliquots from each well were counted using a Reichert Brightline haemocytometer (Hausser Scientific, USA). The mean counts ± SD from each day were used to construct a growth curve. The cell population doubling time was determined using linear regression of the exponential phase of growth and the time to 80% confluency calculated from the point of plateau in growth.

Micrographs

Hep3B cells were seeded on 24 well culture plates at a seeding density of $3x10^4$ cells.cm^{-2} and grown to 80% confluency before exposure to 1, 5, 10 or 20 mM 4-AAP for 6, 24, 48 or 96 hours. Gross morphology was observed using a Leica DM IRB inverted light microscope (Leica Microsystems Ltd, Milton Keynes, UK) at 10x magnification. Micrographs were captured using

Openlab™ (Improvision Limited, Coventry, UK). Contrast and brightness adjustments were made in Adobe Photoshop CS4.

Reactive oxygen species

The production of reactive oxygen species (ROS) was evaluated using 2',7'-dichlorofluorescein diacetate (DCF-DA) and flow cytometry. DCF-DA diffuses into the intracellular environment where it is hydrolysed by intracellular esterases and oxidised by ROS to dichlorofluorescein (DCF), a highly fluorescent compound. Following 4-AAP treatment (1, 5, 10 and 20 mM) ± NAC (10 mM), medium was aspirated and cells were incubated with 5 μm DCF-DA in DMEM:F12 (DCF-DA diluted from a 10 mM stock solution in DMSO) for 30 minutes at 37°C; final DMSO concentrations were always 1%. Following incubation, the supernatant was aspirated and the cells detached with trypsin/EDTA as described previously. Cells were recovered in 300 μl of fresh complete media and then washed 3x with PBS. Cellular fluorescence intensity was measured using a FacsCalibur flow cytometer (Becton Dickinson, New Jersey, USA) set to collect fluorescent events in the FL-1 channel and with forward scatter (FSC) and side scatter (SSC) optimized to afford sampling from a single uniform cell population. A total of 10,000 events were recorded for each sample. FlowJo (Tree Star Inc, Oregon, USA) was used to analyse the data which were expressed as median fluorescence and percentage of respective controls ± NAC.

LDH leakage

LDH is a stable cytosolic enzyme released from the cytoplasm when the integrity of the cellular membrane is lost. LDH released to culture supernatant was measured using a CytoTox 96® (Promega, Madison, USA) 30 minute coupled enzyme assay which results in the conversion of a tetrazolium salt into a red formazan product in the presence of LDH. The manufacturers protocol was followed but with minor modifications. Briefly, after incubation with 4-AAP (1, 5, 10 and 20 mM) ± NAC (10 mM) for 24 or 48 hours, the culture supernatant was collected and centrifuged for 5 minutes (4°C; 150g) to pellet any cellular debris. Supernatants were stored at -20°C for no longer than 7 days before being assayed. The maximum LDH activity in Hep3B cells was determined by extracting LDH from untreated cells by freeze-thaw lysis in a known volume of fresh culture medium. A 50 µl aliquot of Substrate Mix was added to each sample and incubated for 30 minutes at room temperature. A stop solution was added and the absorbance recorded at 490 nm. Background LDH in fresh culture medium was also measured and subtracted from sample results. LDH leakage was expressed as percentage of untreated cells i.e. cells not exposed to 4-AAP or NAC.

Results

Hep3B growth curve

Hep3B cell growth studies were undertaken to determine when cell monolayers of Hep3B reached 80% confluency, the point at which cell

cultures would be exposed to 4-AAP. **Supplementary Figure 1** shows the growth characteristics of Hep3B over a five day period.

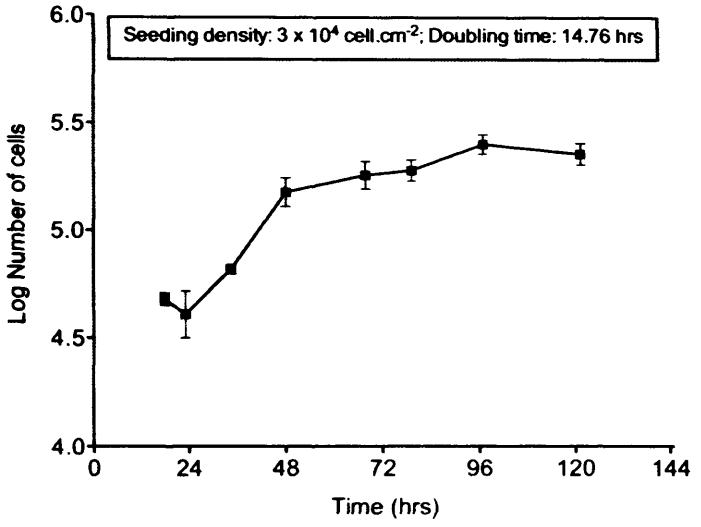

Supplementary figure 1. Five day growth curve of the Hep3B cell line. Using linear regression of the exponential phase of growth cell doubling time was determined to be 14.76 hours and 80% confluency was reached at 56 hours. Data are mean ± SD (n = 3).

The cell doubling time, calculated using linear regression of the exponential growth phase, was 14.76 hours and the time at which the cells were 80% confluent was 56 hours (~ 2.3 days). Therefore, in all *in-vitro* toxicity assays that follow, Hep3B cultures were exposed to 4-AAP or its isomers after 2 days *in-vitro*.

Micrographs

The effects of 4-AAP toxicity on the *in-vitro* viability of the hepatocyte cell line HEP3B were observed microscopically and micrographs recorded. **Supplementary figure 2** shows a series of time lapsed micrographs of confluent Hep3B monolayers exposed to different concentrations of 4-AAP.

After a 5 hour exposure, a reduction in cell number was observed at concentrations greater than and including 5 mM 4-AAP. Further, in cells exposed to 20 mM 4-AAP for 5 hours, gross changes in cell morphology were evident with the cells becoming 'rounder' in shape. After a 24 hour exposure loss of monolayer confluency was overtly visible in cells exposed to 4-AAP concentrations 5 – 20mM and at 48 and 96 hour time-points, nearly all cells exposed to these concentrations were lost from the culture surface. A 4-AAP concentration of 1 mM did not appear visibly toxic to Hep3B cells at any time-point investigated.

Supplementary figure 2. Light micrographs showing time and concentration dependent effects of 4-AAP on Hep3B cells.

Reactive oxygen species

The effect of 4-AAP on the levels of reactive oxygen species in Hep3B cells is shown in **Supplementary figure 3**. Preliminary studies revealed 4-AAP at a concentration of 20 mM leads to greater ROS production as assessed by increases in hepatocyte fluorescence intensity using the fluorogenic marker DCFDA (**Supplementary figure 3a**). In contrast co-incubation with NAC totally abolished ROS generation (**Supplementary figure 3b**). The concentration dependent effects of 5 hour exposure to 4-AAP on ROS production were then assessed (**Supplementary figure 3c**). The maximal increase in levels of ROS occurred after exposure to 20 mM 4-AAP with a measured intensity of DCF fluorescence 183.71 ± 10.45 % of control ($p < 0.05$). Exposure to 4-AAP concentrations of 5 and 10 mM for 5 hours also increased ROS levels by 132 ± 17.41 and 135 ± 18.17% respectively ($p < 0.05$). The production of ROS was abrogated at all concentrations following co-incubation with 20 mM NAC. The time dependent effects of 4-AAP exposure revealed that in the main, longer exposure to 4-AAP leads to reduced levels of ROS compared to control cells as ROS precursors are depleted as cell viability reduces (**Supplementary figure 3d**) which is in agreement with results observed by other research groups[1]

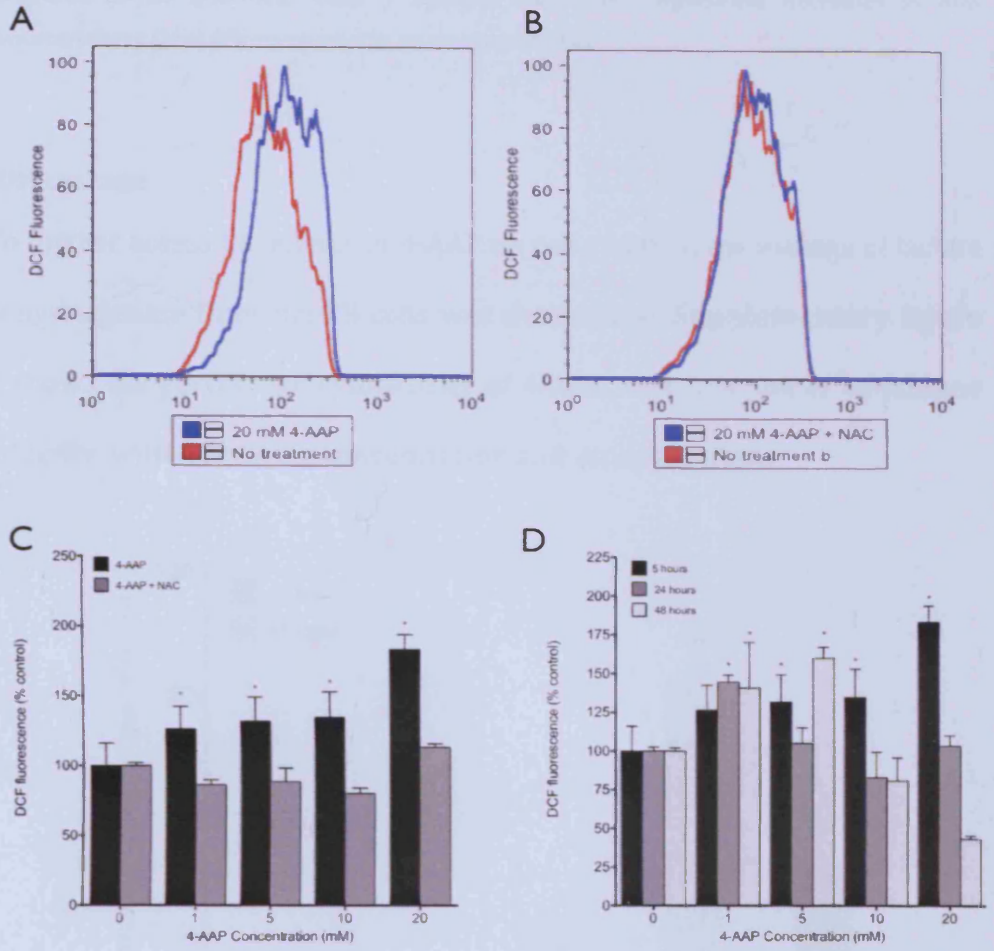

*Supplementary figure 3. Effects of 4-AAP exposure on intracellular production of reactive oxygen species (ROS). (A) After 5 hours exposure to 4-AAP an increase in DCF-DA fluorescence (blue line) is observed compared to non-treated cells (red line) signifying increased levels of intracellular ROS in the presence of 4-AAP. (B) After 5 hours co-incubation of 4-AAP with NAC (10 mM; blue line) the levels of cellular associated DCF-DA fluorescence are no different to non-treated cells (red) indicating no difference in intracellular ROS. (C) Concentration dependent elevation in intracellular ROS levels was observed in Hep3B cells exposed to 4-AAP; co-incubation with NAC prevented production of ROS. Results are presented as mean ± SD where n =4. * Signifies statistically significant difference (p <0.05) compared to no treatment cells. (D) Time dependent effects of 4-AAP on intracellular levels of ROS. Continuing exposure to 4-AAP (24 and 48 hours) generally led to reductions in intracellular concentrations of ROS compared to non-treated cells and is as a result of depletion of ROS precursors as cell viability continues to decline. Results are presented as mean ± SD (n=4). * signifies statistically significant increases in ROS concentrations (p <0.05)*

compared to no treatment cells. † signifies statistically significant decreases in ROS concentrations (p <0.05) compared to no treatment cells.

LDH Leakage

To further assess the effects of 4-AAP on cell viability, the leakage of lactate dehydrogenase from Hep3B cells was determined. **Supplementary figure 4** shows the percentage cytotoxicity of 4-AAP, as a function of membrane integrity, with increasing concentration and exposure time.

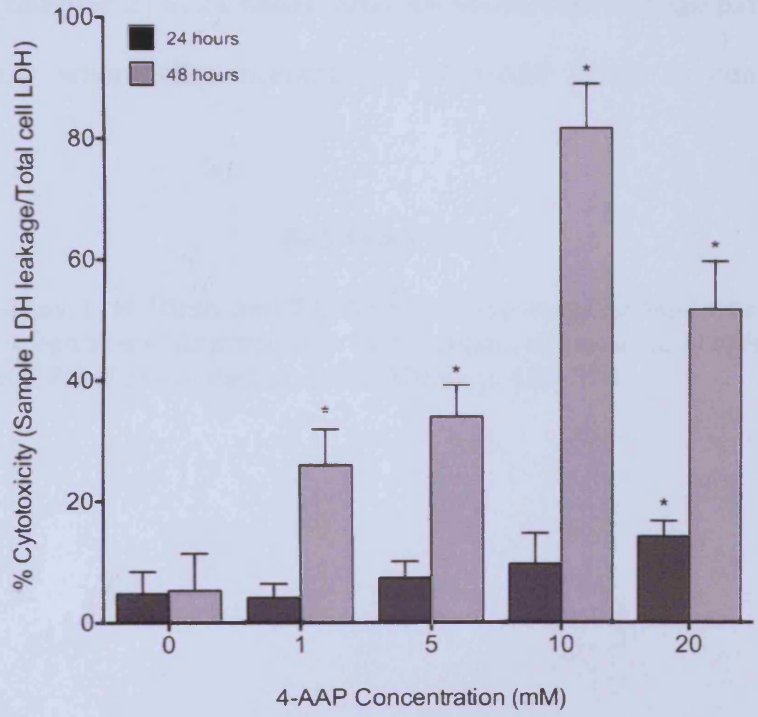

*Supplementary figure 4. LDH leakage from 4-AAP treated Hep3B cells. LDH levels were measured in supernatant and expressed as percentage cytotoxicity i.e. the ratio of LDH in supernatant to the total cellular LDH content. The data at 24 hours showing little toxicity indicates that loss in cellular membrane integrity is a late event in 4-AAP induced cytotoxicity. The results are presented as mean ± SD (n=4). * signifies statistically significant difference (p < 0.05) compared to no treatment cells.*

The cytotoxicity is calculated as a ratio of LDH leakage from sample to the maximum LDH released when a population of untreated Hep3B cells is lysed. Whilst this data reinforces previous results that 4-AAP toxicity is both time and concentration dependent, the loss in cell membrane integrity, the cause of LDH leakage, appears to be a late event in the toxicological cascade with 24 hour exposures to 4-AAP only resulting in significant toxicity at 4-AAP concentrations of 20 mM. This contrasts with MTT studies where as low as 5 mM concentrations result in significant toxicity (**Chapter 2**) at 24 hours. After 48 hours, LDH leakage parallels the MTT assay where all concentrations of 4-AAP result in considerable toxicity.

Reference List

1. Manov, I., M. Hirsh, and T.C. Iancu, *Acetaminophen hepatotoxicity and mechanisms of its protection by N-acetylcysteine: a study of Hep3B cells.* Exp Toxicol Pathol, 2002. **53**(6): p. 489-500.

Appendix 2

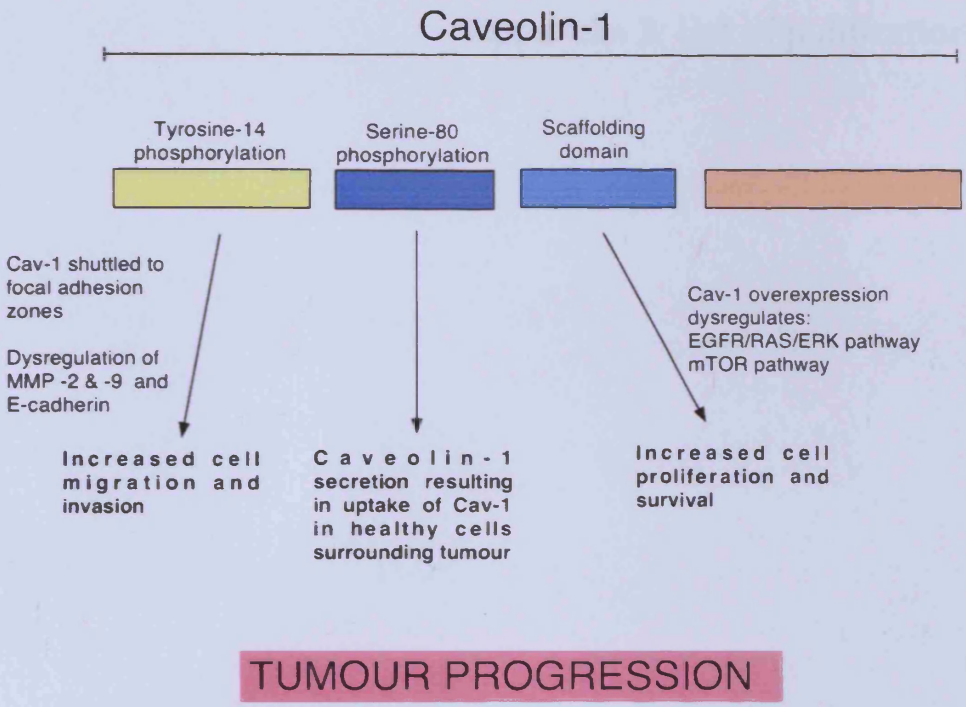

Figure A2: Model of the structure and function of caveolin-1 in the pathogenesis of glioblastoma multiforme. In astrocytomas, upregulation of caveolin-1 combined with post-translational modifications (caveolin-1 phosphorylation) result in altered subcellular compartmentalisation and loss of caveolin-1 mediated tumour suppressive activity that together subvert normal tissue homeostasis.

Appendix 3: List of publications

J Drug Target. 2006 May;14(4):191-214.

Endocytosis at the blood-brain barrier: from basic understanding to drug delivery strategies.

Smith MW, Gumbleton M.

Pharmaceutical Cell Biology, Welsh School of Pharmacy, Cardiff University, Redwood Building, Cardiff CF10 3XF, UK.

The blood-brain barrier (BBB) protects the central nervous system (CNS) from potentially harmful xenobiotics and endogenous molecules. Anatomically, it comprises the brain microvasculature whose functionality is nevertheless influenced by associated astrocyte, pericyte and neuronal cells. The highly restrictive paracellular pathway within brain microvasculature restricts significant CNS penetration to only those drugs whose physicochemical properties afford ready penetration into hydrophobic cell membranes or are capable of exploiting endogenous active transport processes such as solute carriers or endocytosis pathways. Endocytosis at the BBB is an essential pathway by which the brain obtains its nutrients and affords communication with the periphery. The development of strategies to exploit these endocytic pathways for the purposes of drug delivery to the CNS is still an immature field although some impressive results have been documented with the targeting of particular receptors. This current article initially provides an overview of general endocytosis processes and pathways showing evidence of their functional existence within the BBB. Subsequent sections provide, in an entity-specific manner, comprehensive reviews on BBB transport investigations of endocytosis involving: transferrin and the targeting of the transferrin receptor; hormones; cytokines; cell penetrating peptides; microorganisms and toxins, and nanoparticles aimed at more effectively delivering drugs to the CNS.

Biochem Biophys Res Commun. 2007 Jun 22;358(1):285-91. Epub 2007 Apr 27.

Phage display identification of functional binding peptides against 4-acetamidophenol (Paracetamol): an exemplified approach to target low molecular weight organic molecules.

Smith MW, Smith JW, Harris C, Brancale A, Allender CJ, Gumbleton M.

Biomaterials and Biological Interfaces, Welsh School of Pharmacy, Redwood Building, Cardiff University, Cardiff CF10 3XF, UK.

Peptide-phage display has been widely used to explore protein-protein interactions, however, despite the potential range of applications the use of this technology to identify peptides that bind low molecular weight organic molecules has not been explored. In this current study, we identified a phage clone (PARA-061) displaying the cyclic 7-mer peptide sequence N' AC-NPNNLSH-CGGGS C' that binds the low molecular weight organic molecule 4-acetamidophenol (4-AAP; paracetamol). To avoid occupancy of key functional groups on the target 4-AAP molecule our panning strategy was directed against insoluble complexes of 4-AAP rather than against the target linked to a stationary support or bearing an affinity tag. To augment the panning procedure we deleted phage that also bound the 4-AAP isomers, 2-AAP and 3-AAP. The identified PARA-061 peptide-phage clone displayed functional binding properties against 4-AAP in solution, able in a peptide sequence-dependant manner to prevent the in vitro hepatotoxicity of 4-AAP and reduce (approximately 20%) the permeability of 4-AAP across a semi-permeable membrane. Molecular dynamic simulations generated a stable binding conformation between the PARA-061 peptide sequence and 4-AAP. In conclusion, we show that a phage display library can be used to identify peptide sequence-specific clones able to modulate the functional binding of a low molecular weight organic molecule. Such peptides may be expected to find utility in the next generation of hybrid polymer-based biosensing devices.

J Drug Target. 2007 May;15(4):253-68.

Primary porcine brain microvascular endothelial cells: biochemical and functional characterisation as a model for drug transport and targeting.

Smith M, Omidi Y, Gumbleton M.

Pharmaceutical Cell Biology, Welsh School of Pharmacy, Cardiff University, Cardiff, UK.

The blood-brain barrier (BBB) remains a significant obstacle to the delivery of therapeutic agents into the central nervous system (CNS). Primary cell cultures of brain capillary endothelial cells represent the closest possible phenotype to the in vivo BBB cell providing a convenient model for the study of transport systems and events that mediate solute delivery to the CNS. In this investigation we have characterized an in vitro primary BBB model from porcine brain microvascular endothelial capillary (PBMVEC) cells after recovery from cryopreservation of upto 12 months and studied their modulation by astrocytes. Co-cultures of PBMVECs with astrocytes (C6 astroglioma) resulted in trans-endothelial electrical resistance of up to approximately 900Omega cm2 and marked discrimination between the para- and trans- cellular markers sucrose and propranolol. Micrographs of confluent monolayers of PBMVECs showed the presence of tight junction complexes and vesicles with the morphological characteristics of either caveolae or clathrin coated pits. Extensive RT-PCR evaluation highlighted the expression of tight junction transcripts, ABC transporters, leptin receptor and select nutrient transporters. Functional studies examined the kinetics of transport of glucose, large neutral amino acids and p-glycoprotein (P-gp). Our findings indicate primary PBMVECs retain many barrier characteristics and transport pathways of the in vivo BBB. Further, primary cells can be stored as frozen stocks which can be thawed and cultured without phenotypic drift many months after isolation. Frozen PBMVECs therefore serve as a robust and convenient in vitro cell culture tool for research programs involving CNS drug delivery and targeting and in studies addressing blood-brain barrier transport mechanisms.